Plasma-arc Cutting control: Investigations into machine vision, modelling and cutting head kinematics

A thesis presented in partial fulfilment of the requirements for the degree of

Doctor of Philosophy

In

Engineering

at Massey University, Manawatu,

New Zealand

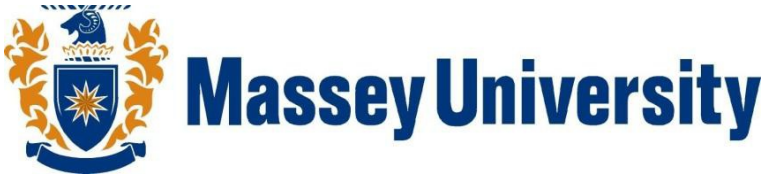

Mathew Flemmer

2018

Abstract

Plasma-arc cutting (PAC) is widely used in industry, but it is an under-researched fabrication tool. A review of the literature reveals much study is needed to improve the PAC process regarding efficiency, quality, stability and accuracy. This research investigated a novel control method for PAC. The PAC process was investigated to identify the gaps, and develop feasible methods, methodologies and systems to improve the PAC cutting quality and process control using machine vision. An automated, visual-inspection algorithm was successfully developed. The algorithm uses NC code to path plan and perform kerf width measurement. This visual inspection facilitated research into several aspects of PAC such as the extent of radiative heat transfer, the significance of kerf asymmetry, and a model describing the slope of the leading edge of the kerf-with respect to feed rate and material thickness. A kinematic investigation was conducted on 3 bevel capable plasma heads to complete the elements of a novel control method.

An automated, visual-inspection (AVI) system for PAC was designed that consists of a vision unit and a mounting rig. This system is able to perform real-time, kerf width measurement reaching an accuracy of 0.1mm. The methodology was validated by experiment, testing cuts on parts with varying size, shape and complexity. The outcomes of this research were published in the International Journal of Mechanical and Production Engineering and the proceedings of the 2017 Mechatronics and Machine Vision in Practice (M2VIP) international conference.

With this developed vision rig, further research was conducted such as an empirical investigation into the relationship between kerf angle and kerf width with respect to torch height, feed rate and material thickness. This investigation was comprised of 35 combinations of the process parameters with 9 replicates for each. A relationship between the process parameters and quality measures was developed, and the magnitudes of kerf asymmetries were quantified.

The understanding of the phenomenology of PAC is deficient in several areas. An experimental study was undertaken that reduced the effects of heat transfer by conduction and convection in order to estimate the contribution by radiative heat transfer. This experimental study maintained an arc between a water-cooled anode and plasma torch for 15 seconds. A test piece was specifically designed with imbedded, resistance-temperature-device thermometers positioned around the transferred arc and the temperature was measured. This investigation was able to estimate the effects of radiation from the plasma-arc. The study found radiative heat transfer is less than 3% of the total power input.

Another experimental study obtained information on the shape of the leading edge of the kerf. For this study slots were cut into steel plates of 6, 8 and 10mm thickness, at feed rates between 350 and 2000mm/min with a torch height of 1.5mm. Edge points for the centre axis of the leading profile were obtained. A relationship between surface angle and material thickness and feed rate was established and is validated through the test range.

A study on obtaining cutting profile data on the front face of the kerf was also undertaken. Slots were cut into plates of 6 and 10mm thickness. Edge points were obtained for the front 180 degrees of the kerf face at sections in 2mm increments. A 3D representation of the shape of the face was then able to be presented.

Finally, the kinematics for 3 bevel capable PAC heads was developed. Two of the heads are existing industrial heads, and the third head is being developed by Kerf Ltd. The kinematics investigation produced the DH parameters and transformation matrices for the forwards kinematics. These were validated using MATLAB®. The resulting dynamics were also produced.

In conclusion, PAC is a complicated process. This research carried out several studies and has addressed several literature gaps with the proposed methods, methodologies and systems, developed through machine vision and PAC head kinematic study.

This research was funded by Callaghan Innovation PhD research funding and received financial support from Kerf Ltd. Callaghan Innovation is a New Zealand government research funding body. Kerf Ltd. is a New Zealand PAC machine manufacturer and distributor.

Acknowledgements

The success of this research is in no small part due to the assistance of my peers and friends.

I'm grateful to my supervisors, Dr Liqiong Tang and Professor Subhas Muhkopadyay, for their patient guidance throughout the project. Without them the balance between an industrial research and academic endeavour could not have been achieved.

This research would not have been possible without the funding from Callaghan Innovation and Kerf Ltd. I am specifically grateful to Mr. Glen Gray who sacrificed much time energy to assist me. Kerf Ltd. provided the means with which to conduct my experiments, the ideas that sparked the research efforts and a lot of answers to a lot of stupid questions.

Throughout the project I've had a lot of assistance from the Massey workshop staff and administration team at the School of Engineering and Advanced Technology. Without them solving my many varied and mundane problems this project could have taken far longer.

My parents have provided support throughout this endeavour and I don't believe I could have finished it without them.

Finally, my girlfriend's unwavering belief in me, and her positive outlook helped provide the impetus to cross the finish line.

Thanks for everything.

Table of Contents

Nomenclature

Symbol	Variable	Description	Units
A_{i+1}^{i}	homography matrix		-
A_{rtd}	RTD coefficient 1	coefficient 1 in RTD relationship	-
B_{rtd}	RTD coefficient 2	coefficient 2 in RTD relationship	-
M_u	molar mass		$kgmol^{-1}$
c_V	specific volume		m^3kg^{-1}
c_p	specific heat capacity	specific heat capacity	$Jkg^{-1}K^{-1}$
${}_{i+1}^{i}R$	rotation matrix		-
$\acute{m}$	mass flow rate		kgs^{-1}
$\vec{\boldsymbol{C}}$	camera offset	distance between camera center and torch center	mm
$\vec{\boldsymbol{c}}$	disk center	location of the disk center in the camera reference fame	pixels
$\vec{\boldsymbol{d}}$	disk center	location of the center of the callibration disk	m
$\vec{\boldsymbol{e}}$	edge point coordinate	coordinate of the edge point on circle circumference	pixels
$\vec{\boldsymbol{f}}$	force vector		N
$\vec{\boldsymbol{t}}$	torch head location	location of the center of the torch	m
α_f	fisheye parameter 1	first constant in the equation for fisheye scaling	-
α_t	connicity, kerf angle	the deviation of the kerf wall from 90 degrees	degrees
α_d	thermal diffusivity		$Jm^{-2}K^{-1}$
β_f	fisheye parameter 2	second constant in the equation for the fisheye scaling	-
δ_z	change in height	change in height from a set point	m
h	torch height	the distance between the torch nozzle and plate	m
Γ	scaling parameter		-
A	quadratic coefficient 1		-
Ar	area	the area being considered	m^2
B	quadratic coefficient 2		-
C	quadratic coefficient 3		-
E	energy		J
HAZ	Heat Affected Zone width	the width of the area affected by the heat of plasma cutting	m
I	current		A
J	Jacobian		-
KW	kerf width	distance between two edges of kerf	m
L	latent heat		J
M	mach number		-
MRR	mass removal rate	the rate at cut material is removed	kgs^{-1}
Nu	Nusselt number		-
P	pressure		Pa

Po	power		W
Pr	Prandtl number		-
Q	Heat	the energy transferred via heat	J
R	ideal gas constant	8.314	$Jmol^{-1}K^{-1}$
Re	Reynold's number		-
SR	surface roughness	density of surface deviations from the average surface	µm
T	temperature		K
V	voltage		V
a	slope	slope in line equation	-
b	intercept	intercept in line equation	-
c	speed of sound	the speed of sound	ms^{-1}
d	distance		m
f	feed rate	rate of torch advancement	ms^{-1}
g	plenum pressure	the pressure of the pl asma in the plenum	Pa
i	horizontal pixel count	horizontal pixel coordinate	pixels
j	vertical pixel count	vertical pixel coordinate	pixels
m	mass		kg
pm_0	pixel scaling constant	constant for linear scaling relationship between pixels andmm.	$Pixmm^{-1}$
pm_h	pixel scaling factor	rate of change of scaling factor with respect to height	$Pixmm^{-1}$
r	radius	distance from center	-
r'	adjusted radius	radius adjusted for fisheye compensation	-
res	resistance		Ω
s	distance	distance between two points	m
th	plate thickness	thickness of plate	m
u	surface unevenness	the amount of deviation in the surface from its average level	m
v	velocity		ms^{-1}
x	X coordinate		m
y	Y coordinate		m
z	Z coordinate		m
α, θ	rotation		rad
γ	specific heat ratio	specific heat / specific volume	-
κ	thermal conductivity	thermal conductivity	$Wm^{-1}K^{-1}$
μ	viscocity		Pas^{-1}
ρ	density		kgm^{-3}
τ	torque		Nm
ω	angular velocity		$rads^{-1}$
ϵ	emmisivity	the effectivenes sin emitting energy via radiation	-

List of Figures

List of Tables

1 Introduction

This research thesis describes the work done at the behest of Kerf Ltd. to advance the field of plasma-arc cutting (PAC). There are two main areas of research. The first area is the development of an automated, visual-inspection system. This is a novel system that will provide value to Kerf Ltd. in future endeavours, as well as provide a tool to aid in empirical investigations for PAC. The second area of research is an investigation into the phenomenology of the PAC process. The PAC process is fundamentally complex, and many key areas are still under-investigated. This work explores the formation of the kerf profile from first principles.

1.1 Background

Plasma-arc cutting (PAC) is a fabrication process that developed from plasma welding in 1955 (Gage, 1957). It is a thermal cutting method where an arc is established between a torch and the work piece by plasma that flows out of the nozzle in a jet. The arc is concentrated, to increase the thermal density, by a shield cap. A secondary gas is often used to further increase the thermal density and increase arc stability. A localized area at the attachment point of the arc is heated rapidly and melts. The molten material is removed by the plasma jet.

Over the last 50 years PAC has developed to make use of different cutting gasses, perform more effectively with its operating parameters, and produce higher quality more accurate cuts. These improvements have often been the result of technological advances that increase the rigidity, stability and density of the jet. Today PAC is a high throughput fabrication process that is commonly used by industry due to its low capital cost when compared to its competitors -- laser - and water-jet cutting -- and high accuracy and throughput compared to oxy-fuel cutting and metal-on-metal methods. Most metal cutting shops in New Zealand and the world take advantage of the high throughput and low cost.

Currently New Zealand's PAC industry primarily serves a redistribution purpose. Companies in the U.S. and Europe (such as Koike, AKSCutting and Hypertherm) develop and produce PAC systems. Companies in New Zealand such as Kerf Ltd. distribute these products to fabricators who make use of the technology. Kerf Ltd. is looking to expand their role in the market by developing some novel products of their own. Kerf Ltd.'s aim for development has two main areas. Firstly, they currently only distribute 3-axis machines. They would like to develop their own 5-axis kinematic head, and the capability to control such a head. This would allow them to offer bevel cutting capability to their customers. The second area is in the use of machine vision to tune the PAC parameters in real time and perform supplementary functions.

Machine vision has been identified as the most suitable option to provide feedback to a control methodology that would tune PAC operating parameters. This is due to its ability to provide large amounts of data quickly, and perform metrology to the desired accuracy. In addition to this, the technology is relatively inexpensive, and due to the popularity of the field, numerous libraries and packages exist to aid development. All these attributes lend a flexibility to the implementation of machine vision as a feedback method. Alternatives to machine vision include time of flight scanning systems, and coordinate measuring machines (CMM), however machine vision offers advantages in speed over CMm and cost over scanning systems.

1.1.1 Value Added

This research aims to add value to both New Zealand and the world. The value to New Zealand comes directly from providing value to PAC machine designers, manufacturers and distributors such as Kerf Ltd. Development of novel solutions to problems in the PAC industry will give them a competitive edge in the market. Further, rather than merely redistributing products from overseas PAC developers, they will have some of their own products with high-tech features to distribute. This will increase value by reducing lead times in distribution and servicing. New Zealand also benefits as the PAC community benefits.

The value to the PAC community is made by increases in the efficiency for PAC. PAC is a widely used fabrication technology and slight improvements in the use of material, speed of production or ease of use will have a large effect. The time spent in post processing for PAC is relatively large compared to its competing cutting processes, and improvements in this area are very valuable.

For example, whilst a nest of parts can be plasma cut in 20 minutes, the post processing operations required to bring the parts to user specifications may take a skilled technician days of labour. Some parts may be over cut significantly or be cut closely to size with a large kerf angle. This might require finishing with an end mill, a linisher or other relatively time-consuming solutions. Alternatively, parts that are undercut may not even be salvageable. Due to the high throughput of PAC, even slight reductions in error can substantially reduce waste and post processing operations. Some PAC systems utilize multiple tools, such as an attached water-jet cutting head. This demonstrates the necessity of being able to conveniently post process PAC parts, and the potential value of improvements in this area.

Finally, this research aims to add value by adding to the literature. PAC is a relatively established technology; but the literature does not reflect this. Various researchers have pointed out that research in this area is limited (Nemchinsky & Severance, 2006), and often only undertaken by industry where there is a focus on application rather than understanding.

1.1.2 Stakeholders

Aside from the industrial stakeholders, this research will also provide value to the PAC research community. The literature suggests that key phenomena behind the PAC process are still insufficiently understood. The PAC process is viewed as a highly complex system that requires a skilled operator to tune the process parameters correctly. With such an operator, it often requires a trial and error approach to arrive at a set of parameters that are acceptable. Even so, the process parameters are rarely ideal. This research provides useful insights and experimental data to further this understanding. Specifically, the mechanism behind cutting with respect to heat transfer is investigated, as well as the shape of the leading edge of the cut profile.

This research was funded in part by Kerf Ltd. The objective described by Kerf Ltd. was to develop a control system for a 5-axis plasma cutting machine. This would follow on from the research work sponsored by Kerf Ltd. to improve the control and extend the capability of a PAC machine for a novel PAC machine head structure that tilted the torch to an angle. As the project progressed, it became apparent that a real-time machine vision system has great potential for PAC process quality control. As a result, this research largely focused on the investigation and development of a machine vision system that could perform measurements for PAC.

1.2 Literature gaps

The main area of research is an investigation into the phenomenology of the PAC process. The second area of research is in the field of machine vision. A review of the literature lays out in detail the state of each of these areas, and the gaps that are investigated. The key gaps targeted by this project are summarized here in the order of importance. The main field of research is that of plasma-arc cutting. This is further broken down into the fields of empirical research of the PAC process, and modelling of the PAC phenomenology. The research was accomplished using a machine vision tool to acquire data; therefore, the development of such a tool is also reviewed in the literature.

1.2.1 Empirical research of the PAC process

The first section of the literature review considers the work people have done to gain an empirical understanding of the PAC process. This largely involves analysing the methods used to make measurements, and the measurements that were deemed important. This background gives a holistic view of the application of the PAC process in terms of what it can achieve, what aspects of the PAC process are limiting, and how the metrics are obtained.

The review of this section of the literature aimed to answer the following questions:

- What are the process parameters and quality measure of interest and how are they measured?
- Are there any shortcomings to the traditional approach of empirical studies when applied to PAC?

These questions are considered in the literature review and reveal the following unanswered questions.

- What is the relationship between kerf width, torch height, material thickness and cutting speed?
- What is the relationship between kerf angle, torch height, material thickness and cutting speed?
- How can the data acquisition process for kerf width measurement be improved?
- How can kerf angle be quantified?
- What is the impact of the assumption of kerf symmetry?

1.2.2 Modelling

The second section of the literature review looked at efforts to model the PAC process. A few researchers have proposed models for various aspects of the process and these are discussed in detail, commenting on the validity of assumptions made and assessing the scope of the current understanding. From this review the following questions were identified.

- What process leads to the profile of a kerf, and what shape does it take?
- What effect does radiation from the arc have on heat transferred to the plate?
- What are the properties of a plasma-arc in terms of the shape of the jet?

1.2.3 Vision

The third section of the literature reviews the use of machine vision to make measurements of the kerf and quality checking. Two questions were investigated.

- What is the typical structure of a machine vision implementation?
- Does a generalized approach to automatic visual inspection exist; and does it make use of numeric control (NC) code?

The literature review identifies the need for a method to perform automated measurement of parts based on the G-Code description of the part. It also provides typical machine vision architectures that will be investigated for potential application to answer the metrology literature gaps identified in the PAC section.

1.3 Scope

Considering the literature review and communications with Kerf Ltd. the following literature gaps are investigated by this research.

1. How much energy is imparted to the plate via radiation from the arc?
2. What is the shape of the front edge of the kerf and what mechanism causes this shape?
3. How do the process parameters of torch height, material thickness and feed rate affect the quality measures of kerf width and kerf angle?
4. How can empirical data for kerf width be collected more efficiently and more accurately?
5. How asymmetrical is the kerf and how can this be measured?

Various researchers have tried to describe the amount of radiation energy in the PAC process. Most of these agree that the energy is small, but none of them have set about measuring this contribution. This research aims to perform experimental work to obtain quantitative data on radiative heat transfer during PAC.

The shape of the leading profile has only been mentioned in passing in the literature. It has been

observed that the arc tends to tilt from vertical as the feed rate of the torch increases. Apart from this observation, the shape of the leading profile has not been investigated in the literature. This work examines the phenomenology of PAC and attempts to develop a cutting model to predict this shape.

Empirical investigations into PAC show that feed rate and torch height are influential factors in the cutting process. Material thickness is not commonly investigated despite its observed impact on the quality measures of kerf width and kerf angle. This research investigates the effect of feed rate, torch height and material thickness on kerf width and kerf angle.

There is little published work on the characteristics of the kerf width which is surprising since this is important industrially. The bulk of the cost of PAC arises from rework, and kerf width is an integral factor in how much rework is required. Reported measurement methods are time consuming, inaccurate and have low repeatability. This research aims to develop a method to acquire this data rapidly and accurately and present it in a clear manner.

Finally, throughout the literature, kerf asymmetry is discussed. However this has never been quantified or defined and many investigations still assume kerf symmetry, assuming the effect of asymmetry to be negligible. This work aims to obtain empirical data on kerf angle and use it to develop a method to measure the kerf asymmetry and to quantify its magnitude.

1.4 Challenges

Numerous challenges are involved in this research. Over the last fifty years automated, visual-inspection has grown rapidly. However, despite all the interest, no generalized automated, visual-inspection system has been developed. Such a system is complex due to the problems of view planning, occlusion and edge finding. This work develops such a system.

This automated, visual-inspection system can then be used to gather data on kerf width for varying torch height, feed rate, and material thickness. Developing an appropriate experimental methodology for this is a key challenge. It is important to modify the variables by a range that will allow a good amount of deviation in the measured response, without taking them too far out of typical operating zones, and without altering one predictor significantly more than the others. A further challenge of designing and gathering this data with automatic visual inspection is to allow validation of the results using a digital caliper.

The goal of quantifying kerf asymmetry is challenging because no specific method has been presented in the literature. As such, a method will need to be developed, and it will need to consider the pros and cons of other approaches. It should be easily replicable for future work in this area. The key challenge in measuring kerf angle is that the edges of the kerf are not linear, and they do not vary by the same amount. Further the kerf width on the top plane and the kerf width on the bottom plane will not necessarily be cantered on each other (they are generally offset) so this will need to be accounted for. This lack of cantering has again not been mentioned in the literature. A final challenge is that the kerf area is small, so a method will need to be developed to provide high quality data to better visualize the profile of a kerf.

The literature discusses heat transfer to the plate and suggests that radiation is negligible. This assumption has not been quantified, largely because it is challenging to estimate it with any reliability. The energy stream throughout the process is complex with energy coming in from the plasma-arc, and energy generated in the oxidation of the steel. Then energy is lost over the plate, in the plate and under the plate, and none of these are quantified exactly in the published work. Therefore, the challenge will be to devise an experiment where radiation is the dominant factor in heat transfer, and then the amount of energy transferred via this mechanism is measured.

The final contribution to the literature is a model to predict the shape of the front profile of the kerf. Understanding the morphology of the kerf and the phenomena that create it will lead to a better understanding of the process. However, this is a challenging task as very little data exists on the front profile due to the front face profile constantly being destroyed during cutting. The first challenge is to obtain information on the profile of the front face. The second challenge will

be relating key process parameters to this data and attempting to fit the model to the data.

1.5 Proposed Methodology

This work aims to develop an automated, visual-inspection method. A key element of modern fabrication is numeric control (NC) code. This code provides key information that can be utilized to obtain data, and assess the performance against a standard. A method will be developed that uses G-Code to provide information on where to collect necessary edge points. A G-Code parser can be developed to provide path planning for image acquisition. It can further be used to assist in edge detection in the image. These edge points can then be used to assess performance.

In order to develop an appropriate experimental plan, the literature will be consulted. This will provide an indication of the range over which parameters should be modified. The operating manual also gives suitable ranges for the operating parameters which will be considered. Finally; some preliminary experiments will be performed to validate the feasibility of the tests ability to provide relevant data.

The investigation into kerf asymmetry requires data on the shape of the kerf. The proposed method to obtain this data is to make use of the imaging system developed for the previous section. With this data, a standardized method to assess and present the effects of kerf asymmetry can be developed.

The final literature gap investigated in this research is the contribution of radiative heat transfer. The proposed method to acquire information on this is to generate an arc between an anode and cathode that does not conduct through the work piece. A sufficient gap will also be left to avoid interference from the annulus of the jet with the work piece. A microcontroller-based heat sensing system will be investigated, designed and evaluated to make measurements of the temperature of the work piece and quantify temperature change.

1.6 Outcomes

The outcomes of research work are:

- The development of a method for automated metrology for PAC.
- The development and validation of a model describing the slope of the leading edge of a kerf.
- Investigated and quantified the effects of radiative heat transfer during PAC.
- Performed a kinematic investigation for bevel capable PAC robotic heads.
- Investigated height control using stereopsis.
- Produced peer reviewed publications from this research.

Published research papers demonstrate the contribution of the work to the PAC literature. The first area of work, namely the application of machine vision to PAC, is published in (Flemmer, M; 2017a, Flemmer, M; 2017b). The research into modelling the PAC phenomenology will only be published after the thesis has been submitted.

A platform that acquires plasma-arc cutting data in real-time is developed through this research. This platform is able to provide large amounts of high quality data, which has been identified as a shortcoming of the literature. This platform uses machine vision to provide and process large amounts of data and has the capability to measure the kerf width. This platform could be used to improve PAC accuracy.

A method to automatically perform kerf width measurements based off G-Code is developed. This method provides the ability to measure the kerf width of any part by parsing its G-Code. This further provides the ability to assess the accuracy of the cut parts and tune the process parameters of the PAC machine to improve efficiency. It also could gather empirical data on freeform shaped parts. This deliverable is assessed by testing cuts that include free form cut paths and evaluating the ability of the method to find the edges and follow them, and then finally perform replicable measurements of the kerf width. These measurements are compared to

standard caliper measurements to validate the automatic kerf width measuring method.

A model that predicts the front profile of a kerf is developed. This considers the method of heat transfer and fluid flow and explains the morphology of the front face as various process parameters are changed. The model is validated in terms of its close prediction of measured data.

An experimental investigation into the effects of radiative heat transfer during PAC is undertaken. This is of value to the state of the literature because it is commonly assumed to have a negligible effect, but not validated. This deliverable requires developing an appropriate experiment and calculating the magnitude of the heat transfer.

A kinematic investigation of Kerf Ltd.'s novel bevel capable PAC head is conducted. This is of value to Kerf Ltd. and for new PAC head development. This deliverable is assessed by its ability to perform kinematic manipulations of the end effector. The design concept and structure is simulated in MATLAB®.

A feasibility investigation is conducted to assess the use of machine vision to maintain the height of the plasma torch to better than 0.25mm. This is of value for PAC quality control, and the developed test rig can investigate real time PAC height control. This deliverable involves fitting a model relating height to the scale factor of the image and then assessing the quality of the fit.

1.7 Thesis structure

The content of this thesis has been broken down into the following chapters.

Chapter 1 Introduction – Chapter 1 introduces the area of this research. It starts by giving a brief description of PAC, what it is and how it affects New Zealand and the world. The key areas investigated with respect to the literature and the requirements of Kerf Ltd. are then laid out. From this overview, the key gaps targeted from the literature review are summarized and broken down into the scope of the investigation and the challenges overcome. Finally, the deliverables of the thesis are stated.

Chapter 2 Literature Review – Chapter 2 covers the literature survey undertaken for this thesis. The literature review is comprehensive owing to the multi-field nature of the research undertaken. The literature review begins by examining the plasma-arc cutting research available in the literature, and breaking it down into empirical investigations and phenomenological investigations. Literature gaps are identified and discussed for these two main areas and lead to further review being undertaken on the field of applied machine vision.

Chapter 3 Materials and Methods - This chapter details the work done in setting up the experimental systems. This chapter explain how the experimental systems were set up to allow the results from subsequent chapters to be obtained. It also covers the work done for Kerf Ltd. on preliminary research development of 5-axis PAC control systems with competitive modern features. This chapter covers:

- Development of a quadrature decoder.
- A hysteresis investigation for the PAC gantry.

Chapter 4 Machine Vision for PAC – Chapter 4 covers all the work done in the field of performing PAC metrology with machine vision. This includes the design and development of a vision rig to mount the cameras on, and the algorithms involved to acquire and process the data. The vision chapter is broken down into four main sections which are:

- Development of a wide-view vision rig. This vision rig has 4 cameras mounted around the PAC torch. This provides opportunities for stereopsis as well as a wide field of view.
- Development of a close-view vision rig. This rig is developed to perform more precise measurements. It mounts 2 webcams in front of the torch with a much smaller field of view, but a much higher resolution. There is still potential for stereopsis with the 2 cameras. This vision rig is then applied in an empirical study to acquire data on kerf width.

- A height sensing investigation. Kerf Ltd. have suggested that a new approach to controlling the height of the torch could be very valuable. This section reports the results of the feasibility test performed with the close view vision rig.
- An empirical kerf angle and asymmetry investigation. The final section applies the close-view vision rig to a kerf angle empirical study. Slots are cut and examined and the profiles of the cut are shown. This provides data on the kerf angle response as well as investigating the assumption in the literature that the kerf is symmetrical.

Chapter 5 PAC Process Parameters and Modelling – Chapter 5 describes the research into understanding and modelling the PAC process. Specifically it aims to improve the understanding of heat transfer and material removal during cutting, and use this to explain the results profile shape. This chapter is broken down into:

- An analysis of the effect of radiant heat transfer from the plasma-arc.
- An analysis of the shape of the kerf on the left and right edges, and the leading edge.
- A model of the resulting kerf shapes.

Chapter 6 Kinematics and Control for Complex Cutting – Chapter 6 presents a kinematic derivation for a robotic head by Kerf Ltd. It couples this with kinematic derivations for two similar robotic heads that are already in the market for the purpose of validation and comparison. This work is a precursor to a novel feedback control algorithm that this chapter presents. This chapter has two main sections:

- Development of the kinematics for Kerf's novel torch-tilt system.
- An overview of the real-time feedback method.

Chapter 7 Conclusion – This final chapter summarizes the results of the previous chapters. It identifies the contributions made to the literature and evaluates the progress made with respect to the literature survey. It then reviews the deliverables and evaluates the results. Finally it discusses the direction of future work, both with respect to advancing the literature, and developing applicable technologies.

Chapter 8 Supporting Material – Appendices A-H contain supporting material that clarifies aspects of the work discussed in previous chapters. This includes specific data acquired from experiments and information on experimental runs.

2 Literature Review

Plasma-arc cutting (PAC) is a fabrication technology. It is viewed as a high throughput lower accuracy method when compared to laser and water jet cutting. The main areas of research in PAC include developing empirical relationships between process parameters and cut quality, making improvements to the power supply, and modelling. Much of the PAC research is industry driven and kept out of the literature (Ilii, Tanasa, & Munteanu, 2007; Keraita & Kim, 2007; Nemchinsky & Severance, 2006; Pipaş, Dindelegan, Pădurean, Ciupan, & Ciupan, 2014; Węglowski & Pfeifer, 2014).

This research aims to advance the understanding of PAC by providing a visual inspection method to acquire data on aspects of the PAC process. This data can then be used to provide a novel control methodology, data for further empirical research and more. As such the literature review covers three main areas.

1. Empirical research done in the field of PAC. This mostly concerns the relating of process parameters to various quality measures of PAC.
2. Theoretical research in the field of PAC. There is rather less of this, but it looks at the underlying phenomena behind PAC and attempts to model some of the aspects.
3. Computer vision applied to general metrology. This research aims to develop an industrial vision system that can be used to adjust process parameters to produce more accurate parts. Consequently, other metrology methods are reviewed.

Areas 1 and 2 are the primary research objectives of this project. However, the research into these areas aims to be applicable to area 3, so it is useful to be aware of this field.

2.1 Empirical relationship in PAC

Plasma-arc cutting (PAC) is a complicated process. A comprehensive knowledge of fluid dynamics, heat transfer, energy balances, circuitry and more is required to fully describe the process. This complexity also results in strong coupling effects between the process parameters (Lahri, Juriani, & Vaishya, 2016). Therefore, one approach to optimize the process is to use an empirical relationship where the parameters are adjusted systematically, and the cut features are observed. The resulting data can be used to develop relationships between the input and output parameters without a complete understanding of the underlying phenomena. Most studies into PAC, especially those sponsored by industry, use this approach.

2.1.1 Review Objective

The review of this part of the literature was undertaken in order to answer the following questions:

1. What are the process parameters and quality measures of interest in the literature, and how are these measured?
2. Are any process parameters or quality measures under-investigated in the literature, and if so, why?
3. What methods or tools are used to acquire the data?

The literature in this area can take a variety of forms. Some researchers purely aim to optimize a specific PAC set up for industry (Chen, Li, & Cox, 2009; Das, Kumar, Barman, & Sahoo, 2014; Paul, Babu, & Paul, 2014; Platov & Turygin, 2014). Others aim to investigate the response of a specific quality measure to a few PAC process parameters (R. C. Bidajwala & M. M. A. Trivedi, 2014; Ilii, Coteata, & Munteanu, 2010) . There is also research into the PAC phenomenology, which is validated or compared with relationships derived directly from the empirical data (R. Bini, B. Colosimo, A. Kutlu, & M. Monno, 2008a). Despite the variety of the approaches a few things are common to all the literature:

1. The range of applied testing.
2. The methods used to assess quality and the influential process parameters.

2.1.2 Range of applied testing

Optimization of the plasma cutting process parameters has been widely researched using a variety of materials, thicknesses, PAC machines and power supplies. Table 2.1 and Table 2.2 summarize the research and give an indication of the main areas of interest in terms of the frequency of the research in each area. It is apparent that the most common material investigated is mild steel, with a wide variation in plate thickness.

Of the 24 empirical studies reviewed, almost half investigated performance on mild steel, and a further third used stainless steel. The remaining 8 studies examined performance on titanium, aluminium and ceramics. There are two main reasons for this. Firstly, mild steel is a cheap material compared with most others and secondly it is a material that is commonly processed with PAC. The purpose of empirical studies is to provide useful information on operating parameters; ergo they tend to focus on materials of interest. Stainless steel is more expensive than mild steel, however, conventional methods of cutting it have low throughput and high tool wear, so thermal cutting is an attractive proposition.

Table 2.1: A summary of the scope of research in terms of material and thickness.
The first column under plate thickness represents research performed on material from 3mm up to 6mm, the second represents 6mm up to 9mm and so on.

Frequency of investigation of Material versus Thickness in empirical PAC studies										
	Plate Thickness (mm)									**Total**
Material	3 -	6 -	9 -	12 -	15 -	18 -	21 -	24 -	27 -	
Mild Steel	1	1	1	3	1	2		1	1	11
Stainless Steel	2	1	1	2		1			1	8
Other Steels			1						1	2
Titanium	1									1
Aluminium			1							1
Ceramics		1								1
Total	4	3	4	5	1	3	0	1	3	**24**

A wide range of machines have been used in the studies as summarized in Table 2.2. Most research uses a computer numerical control (CNC) gantry to drive a torch to a location and then a power supply from Burny, Hypertherm or a third party to do the plasma cutting. A very few studies use a hand-held torch set up, and there are no published studies using 5-axis CNC technology for the bevelling, or offsetting of bevelled cuts.

Table 2.2: A summary of the PAC systems used in the literature.
ND = no data.

PAC System		Power Supply	
Hypertherm	ND	Hypertherm	HT4000
	ND		HT2000
	ND		HD3070
	ND		PowerMax45
Kompact	KOMPACT3015	Hypertherm	ND
Yildirim	Plasma Jet 3015	Burny	ND
	Plasma Jet 3015	Hypertherm	ND
Kjellberg	ND	Kjellberg	HiFocus 360i neo
Kaltenback	KF2512	Hypertherm	HPR260
Silberin	Sharpline Bombay	Burny	Burny 10 LCD
ESAB	ND	ESAB	EPP-450

2.1.3 Quality assessment and influential process parameters

A wide range of measurements have been made in the interests of optimizing quality. There are significant interaction effects between the various process parameters, however due to the number of variables that can be adjusted, It is usually only feasible to adjust a few of these, and only useful to observe a few quality measures (Chen et al., 2009).

2.1.3.1 Quality Measures

The most commonly investigated quality measures are:

1. Surface roughness.
2. Unevenness.
3. Mass-removal rate.
4. Metallurgic effects.
5. Heat affected zone width.
6. Temperature.
7. Cutting accuracy.
8. Kerf angle.

Surface roughness (SR)

Surface roughness is the density of surface deviations from the average surface. It is typically measured with a surface roughness tool/profilometer. This is a very commonly researched quality measure in the literature and is important due to its effect on post processing. It is measured using a range of electrical stylus instruments and one of a variety of methods measuring surface roughness. (Ali, Prasad, Shankar, & Saw, 2016; R. C. Bidajwala & M. M. A. Trivedi, 2014; Das et al., 2014; Gariboldi & Previtali, 2005; Ilii et al., 2010; Salonitis & Vatousianos, 2012; Singh, 2012)

Unevenness (U)

Unevenness is defined as the maximum horizontal displacement along the kerf profile. This displacement is measured at 7 points along the thickness of the kerf as specified by ISO9013 Figure 2.1. This is typically measured using magnified photographs or a profilometer (Bini et al., 2008a; Chamarthi, Reddy, Elipey, & Reddy, 2013).

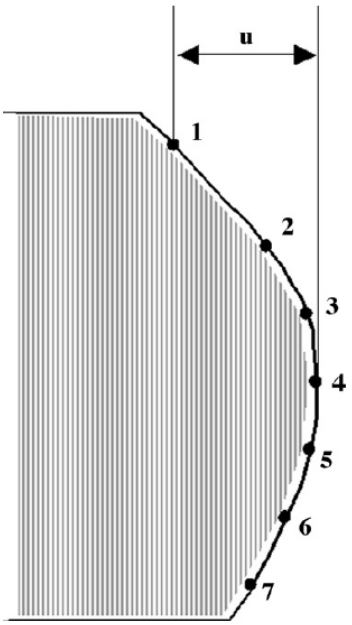

Figure 2.1 Point location for unevenness measurement for varying depth of the cut from the ISO9013 standard (ISO, 2017).

Mass-removal Rate (MRR)

The mass-removal rate is of interest because it is a direct representation of the throughput plasma cutting achieves. It can either be measured or estimated. MRR estimation is made by using approximations of the profile shape (often as a trapezoid with the material thickness as its height and the kerf width on the top and bottom of the plate as its width), the cut length, and the material density. MRR can be measured by measuring the mass of the plate before and after cutting, or by attempting to collect the material removed below and measuring that. It seems as though this metric should be normalized with material thickness, as a thicker material will have a wider average kerf width, however Das et al. (2014) were the only researchers to make any allowance for this. They observed MRR as the ratio of weight difference from cutting to the time taken (Das et al., 2014; Kavka et al., 2014; Singh, 2012; Wu, Hackett, Eickhoff, & Hanover, 1997).

Metallurgic effects

This investigation was only undertaken by Gullu and Atici (2006); however it seems to be of some importance for a comprehensive modelling of the PAC processes. It refers to the variation of the composition of the cut material due to PAC processing. In this study, the composition of pearlite and austenite was found to vary with cutting, and to affect other cut properties as conductivity of the metal was changed. Its examination depends on the property of interest. For example, the hardness can be assessed with a Bicker's hardness test, and microstructural changes can be assessed by etching the cut surfaces and then observing with high magnification microscopes (Gullu & Atici, 2006; Lazarevic & Lazarevic, 2017).

Heat affected zone width (HAZ)

HAZ is one of the most commonly researched quality measures in the literature. It has a metallurgical effect on the properties of the plate resulting in hardening and change in constitutional properties. This is most likely due to its effect on post processing. The HAZ measurement examines the distance from the kerf that the metal has been affected by the thermal cutting process. It is observed with the use of an etching material, such as Nital etchant, with magnification (Gariboldi & Previtali, 2005; Gullu & Atici, 2006; Lazarevic & Lazarevic, 2017; Salonitis & Vatousianos, 2012; Wu et al., 1997).

Tempera**ture**

Temperature distribution through the plate for the PAC process is not so much a measure of quality, but a measurement to aid in the development of the PAC phenomenology. It has however been investigated empirically in the literature and has close ties to other quality measures such as HAZ and metallurgic effects. In the literature the temperature is typically observed with either thermocouples, or thermal cameras. Thermal cameras are relatively expensive but can give a profile of the temperature variation across the plate. Thermocouples are relatively cheap, but only give temperature data for specific points (Ali et al., 2016; Peters, Bartlett, Lindsay, & Heberlein, 2008; Singh & Chattopadhyaya, 2014).

Cutting Accuracy

Cutting accuracy is relatively infrequently reported in the literature. Typically, it is only investigated for specific optimization problems. It is essentially a measurement of how well the kerf width conforms to expectations, and how well the gantry has accounted for this kerf width. It has been measured with digital calipers, steel tape and magnified photosets depending on the size of the part being assessed. Investigations of cutting accuracy at a high level of precision are limited to squares and rectangles in the literature, possibly due to difficulty in obtaining this measurement (Chen et al., 2009; Kechagias, Petousis, Vidakis, & Mastorakis, 2017; Paul et al., 2014).

Kerf Angle

Kerf angle, also known as bevel angle or conicity in the literature, is the angle the kerf edge is from perpendicular to the cut part. It can either be measured on the side of the cut that is of value, measured on both the cut piece and the remnant metal plate, or approximated. A profilometer or some form of magnification used with a caliper or ruler can be used to measure the angle accurately; alternatively, it can be estimated from measurements of kerf width at the top and bottom of the plate. This assumes the kerf is symmetrical, which is not the case. The method used depends on the accuracy required for the purpose (Chen et al., 2009; Dodun et al., 2016; Salonitis & Vatousianos, 2012).

2.1.3.2 Process Parameters

The literature also includes studies on a wide variety of PAC process parameters. These are investigated to determine their individual impact on quality measures, as well as to examine the effects of coupling process parameters. The process parameters that are most commonly investigated are:

1. Nozzle tip size.
2. Feed rate.
3. Arc voltage.
4. Arc current.
5. Gas pressure.
6. Cutting gas.
7. Torch height.
8. Material.
9. Thickness.

Due to the complexity of the PAC process, each of these parameters can affect the heat and potential transfer into the material, the fluid flow dynamics of the plasma and the chemical reactions that take place. These parameters are most commonly varied about the settings specified by the operator's PAC system manual.

Nozzle tip size (D)

Nozzle tip size affects the diameter of the plasma column; which, in turn, affects the location of the shock, and therefore the shape of the kerf. In the literature it is rarely chosen as the variable, because nozzle tips come in discrete diameters. It is typically varied at two or three levels between 0.1 – 4mm (Chen et al., 2009; Gullu & Atici, 2006; Xu, Fang, & Lu, 2002).

Feed rate (U)

The feed rate or cutting speed affects heat transfer into the material as well as the heat flow out of the material. It is the most commonly adjusted process parameter and is usually found to be the most significant factor. It is varied between 400mm/min for 12mm-thick, stainless steel and 11430mm/min for 1mm-thick, stainless steel (Bini et al., 2008a; Chamarthi et al., 2013; Chen et al., 2009; Dodun et al., 2016; Gariboldi & Previtali, 2005; Gullu & Atici, 2006; Ilii et al., 2010; Singh, 2012; Wu et al., 1997).

Arc voltage (V)

Arc voltage is investigated in several studies. It is directly related to the amount of electrical and heat energy going into the plate. It is most commonly investigated in relation to its effect on cutting accuracy. It is found to have a significant effect on intra-cut deviation (Bini et al., 2008a; Chen et al., 2009). It is closely coupled with torch height because many systems use voltage sensing to control the height of the torch, thereby also affecting the fluid flow dynamics. Conceptually, the gap between the plate and torch is proportional to resistance. Therefore, as the resistance goes up the arc voltage will need to increase to maintain the arc. The voltage has been varied from 100V to 149V for 15mm-thick, mild steel (Bini et al., 2008a; Chen et al., 2009; Singh & Chattopadhyaya, 2014).

Arc current (I)

Arc current is the predominant factor for supplying heat into the cut. It is one of the most commonly investigated parameters and found to significantly affect the kerf angle and mass-removal rate. Current is simpler to manipulate as altering the voltage can change the torch height on some machines. In the literature it is varied between 15A for 3.4mm-thick, mild steel and 340A for 25.4mm-thick, mild steel (Das et al., 2014; Dodun et al., 2016; Ilii et al., 2010; Peters et al., 2008; Platov & Turygin, 2014; Salonitis & Vatousianos, 2012; Singh, 2012; Wu et al., 1997).

Gas pressure (P)

The gas pressure affects the fluid dynamics of the plasma as the pressure the gas is supplied at, coupled with the pressure from thermal expansion, determines the plasma flow rate. Plasma flow rate acts to remove molten material, and the more momentum this has the larger the cut volume can be. This has been quite extensively researched, particularly in relation to its effect on surface roughness. Several models of the PAC process mention a thin molten metal layer between the plasma column and the solid metal. The width of this layer is proportional to the pressure of the gas (Nemchinsky & Severance, 2006). In the literature gas pressure is either altered directly or the plasma gas flow rate is adjusted. The two are related by the proportion of the gas that is used for shielding versus establishing the plasma column, and the nozzle diameter. The flow rate varies from 70 l/h for 12mm-thick steel to 2873 l/h for 15mm-thick, mild steel and the pressure varies from 45 psi to 101.5 psi for 15mm-thick, mild steel (Bini et al., 2008a; Chamarthi et al., 2013; Chen et al., 2009; Das et al., 2014; Salonitis & Vatousianos, 2012; Singh, 2012).

Cutting gas (G)

The cutting gas or primary gas can be oxygen (O_2), nitrogen (N_2), hydrogen (H_2), air, argon, or some combination. The primary reason this influences PAC is that oxidation can occur with oxygen and air, which affects the energy input. It also affects the fluid dynamics due to differing conductivities, densities and viscosities of the gas. This parameter is altered infrequently, largely due to the relatively small impact it has, and the effort it takes to swap the gas. Further, other parameters such as feed rate, nozzle diameter and plasma flow rate are significantly coupled (Gariboldi & Previtali, 2005; Gullu & Atici, 2006). A further variation of this parameter is to alter the gas used for the secondary gas. The cutting gasses investigated are N_2, a mix of 35%$H_2$65%Ar and O_2 and the shielding gas or secondary gas investigated are N_2 and a mix of 60%$N_2$40%O_2 (Bini et al., 2008a; Gariboldi & Previtali, 2005; Gullu & Atici, 2006; Lazarevic & Lazarevic, 2017).

Torch height (H)

Torch height is a relatively widely investigated parameter. It is easily adjusted and has been investigated for its effect on everything except unevenness and temperature distribution. Phenomenologically, it impacts the fluid dynamics of the process directly, but it is coupled with voltage. This is because as the standoff distance increases, the voltage must increase to maintain the arc. This causes more energy to be transferred to the plate. It is varied from 2 – 9.9mm and is found to significantly affect kerf angle, cut accuracy and surface roughness (Kechagias et al., 2017; Salonitis & Vatousianos, 2012; Singh, 2012).

Material (M)

The type of material cut affects almost all aspects of the cutting phenomena. Material's properties, such as electrical and thermal conductivity and melting point, have significant impacts on all the quality measures. Only a few papers have examined the difference in performance on different materials specifically: Ali et al. (2016) compared stainless steel and aluminium and looked at the variations in surface roughness and temperature profiles between the two; and Salonitis and Vatousianos (2012) compared the difference between stainless steel and mild steel for kerf angle, surface roughness and HAZ width. Otherwise research is done specifically on one material, although often variations in the composition of the metal are considered. Specifically, the composition is noted when the microstructure is suspected to be relevant, such as when HAZ or surface roughness are being investigated (Bini et al., 2008a; Chamarthi et al., 2013; Gariboldi & Previtali, 2005; Lazarevic & Lazarevic, 2017; Salonitis & Vatousianos, 2012; Xu et al., 2002).

Thickness (T)

The thickness of the material being cut affects how much heat needs to be put into the plate because the volume of material to melt increases with thickness. Additionally, the gas flow must remove more molten material. Thickness has been specifically investigated for its effect on the HAZ width for stainless steel between 10 and 30mm by Lazarevic and Lazarevic (2017) and found to significantly affect the surface roughness by Ilii et al. (2010) for 4 – 6mm-thick austenitic steel. Other studies have considered plate thicknesses ranging from 1mm to 80mm (Gullu & Atici, 2006; Wu et al., 1997).

2.1.3.3 Overview

Table 2.3 summarizes the published research. It shows the quality measures that are more frequently investigated (Surface roughness, HAZ width and the MRR) as well as the process parameters that are suspected to be most relevant to the process (feed rate, arc current and gas pressure).

Table 2.3: A summary of process parameters and quality measures investigated in the literature.
D = nozzle diameter, U = feed rate, V = voltage, I = current, P = plasma pressure, G = plasma gas, H = Torch Height, M = material, T = Thickness.

Overview of relationship investigation										
	Process Parameters									
Quality Parameters	D	U	V	I	P	G	H	M	T	Total
Surface roughness		5	1	4	4	1	3	1	1	20
Unevenness		2	2		2	1				7
Mass-removal Rate		2		3	2		2		1	10
Metallurgic effects	1	1				1			1	4
HAZ width	1	4		2	1	2	1		2	13
Temperature			1	2				1		4
Cutting accuracy	1	2	3	1			1			8
Kerf angle	1	3	1	3	1		1		1	11
Total	4	19	8	15	10	5	8	2	6	77

The commonly investigated quality measures reflect the areas that are most significant to industry. The HAZ width and surface roughness have a high impact on the amount of post processing required to finish a part, whilst MRR reflects the throughput of the process. Slight improvements in the optimizations of these have a large effect on the productivity of the process. The commonly investigated process parameters are those known to have significant effects on all process parameters. Feed rate, arc current and plasma gas pressure are almost always found to be the most dominant factor to explain variation in the empirical data. Less researched areas such as temperature distributions, metallurgic effects and unevenness are mostly of interest in attempting to understand the phenomenology of the PAC process (Bini et al., 2008a; Chamarthi et al., 2013; Dodun et al., 2016; Peters et al., 2008; Salonitis & Vatousianos, 2012).

Most of the process parameter settings across the research are specified in the PAC system operating manual. Research endeavours have been able to optimize these to improve the quality measure by as much as 50%, suggesting that there is room for improvement (Chamarthi et al., 2013; Chen et al., 2009; Das et al., 2014; Kechagias et al., 2017; Singh, 2012). There are some shortcomings of the research in this area. The optimized values are often detrimental to the lifetime of the consumables (decreased torch height, increased current, etc.) so potentially the recommended settings might incorporate a more holistic objective. Additionally, there have been some investigations that have identified certain parameters as very influential whilst neglecting to observe that the step size in the influential parameter is proportionally larger than that of other parameters (Chen et al., 2009; Dodun et al., 2016; Singh, 2012).

2.1.4 Modelling

The research in this field focuses on models that relate the quality measures of interest to the main process parameters. These models are fitted to the data obtained and can be used to identify optimization settings. To do so, the nature of relationship between the quality measure and the process parameter is inferred, and then constants are adjusted to tune the shape of the model to match the shape of the data. This is usually done numerically by minimizing the error between predicted values and data points (Bini et al., 2008a; Dodun et al., 2016). Not all of the empirical research has resulted in a model, typically these investigations stop at the best parameter combination found in the experiment and do not attempt to interpolate (Chen et al., 2009; Salonitis & Vatousianos, 2012).

Models available in the literature cover various quality measures. Bini et al. (2008a) and Chamarthi et al. (2013) modelled unevenness (u). Bini et al. predicted it as a response to arc voltage (V) and feed rate (f) (2.1) and Chamarthi et al. developed a surface response model in terms of arc voltage and plasma flow rate. Dodun et al. (2016) modelled kerf width with the assumption of kerf symmetry. They predicted kerf width in terms of its response to voltage (v), plasma pressure (g) and arc current (I) as

$$u = 83724 - 7.85f - 1105V + 0.0567f * V + 3.62V^2 \quad (2.1)$$

$$KW_s = 6.804v^{-0.704}g^{0.0495}I^{0.764} \quad (2.2)$$

$$KW_i = 0.163v^{-0.507}g^{0.456}I^{0.932} \quad (2.3)$$

Where KW_s is the kerf width on the top face (2.2) and KW_i is the kerf width on the bottom face (2.3). Dodun et al. (2016) also provided a model for kerf angle along with Salonitis and Vatousianos (2012). Dodun et al. (2016) modelled conicity (α_t) in terms of voltage (V), plasma pressure (g) and current (I) (2.4). Whilst Salonitis selected a model of the form (2.5) and regressed for the constants. This model made use of a lot of data and related the angle to current, feed rate, torch height, and plasma pressure, as well as the first order interactions (Salonitis & Vatousianos, 2012).

$$\alpha_t = 0.000414V^{1.090}g^{-0.389}I^{0.444} \quad (2.4)$$

$$\alpha_t = a_0 + a_1I + a_2f + a_3h + a_4g + a_5If + a_6Ih + a_7Ig + a_8fh + a_9fg + a_{10}hg \quad (2.5)$$

MRR has been thoroughly investigated in the literature. Singh (2012) provides a first order model (2.6), which relates the mass-removal rate to the plasma pressure, the arc current, the feed rate and the torch height. Wu et al. (1997) found a linear correlation between the power input, the product of arc current and arc voltage, and the *MRR*. Das et al. (2014) developed a model using arc current, torch height and plasma pressure for interpolation with a prediction accuracy of about 20%. This model is surprising because it does not take feed rate into account yet still predicts quite accurately.

$$MRR = 0.452 - 0.0205g + 0.000167I + 0.0000621f + 0.0194h \quad (2.6)$$

Salonitis and Vatousianos (2012), Singh (2012), and Das et al. (2014) investigated models for the surface roughness. Salonitis and Vatousianos used the same model structure, and regressed to match their surface roughness data. Singh modelled the surface roughness of mild steel with the relationship (2.7), relating surface roughness to plasma pressure, arc current, feed rate and torch height. Das et al. provide surface models relating surface roughness to torch height and plasma pressure, as well as surface roughness to torch height and arc current (2.8)

$$SR = 4.91 - 0.43g + 0.00897I + 0.00445f + 0.0183h \quad (2.7)$$

$$SR = a_0 + a_1I + a_2f + a_3h + a_4g + a_5If + a_6Ih + a_7Ig + a_8fh + a_9fg + a_{10}hg \quad (2.8)$$

Finally,Salonitis and Vatousianos (2012) and Wu et al. (1997) looked at models for the HAZ width. Salonitis and Vatousianos used an equation of the same form as before that related HAZ width to the arc current, feed rate, torch height and plasma pressure, and tuned the constants for the primary effects and interaction effects to match the data (2.9). Meanwhile Wu et al. identified a linear relationship between the HAZ width and feed rate.

$$HAZ = a_0 + a_1I + a_2f + a_3h + a_4g + a_5If + a_6Ih + a_7Ig + a_8fh + a_9fg + a_{10}hg \quad (2.9)$$

In general, the models in the literature are reasonable for interpolation on the data set they were applied to and are indicators of significant process parameters for a particular quality measure. Most predictions were accurate to within 25%, and some were accurate to less than 5% (Das et al., 2014; Salonitis & Vatousianos, 2012; Singh, 2012). These models are often presented in the literature as surface response plots and are useful tools for optimizing PAC performance.

One failing of the current approach in the literature is that models developed in one material do not seem to be valid for other materials. When Salonitis and Vatousianos (2012) attempted to use

their mild steel model for their stainless steel data the error was in the range of 20 – 60%. This is most likely a result of identifying some process parameters as more significant than they are, due to complex interaction effects. There does not appear to have been any effort made to combine existing empirical relationships for the same quality measure.

2.1.5 Gaps Identified

There is a large amount of literature over quite a broad range of process parameters and cut quality measurements, performed using various machines. However, no area has been covered exhaustively, and only a small amount of data exists on using torch height, feed rate and material thickness together, to predict bevelling and kerf width. Kerf width is a quality measure that has been neglected in the literature. One reason for the lack of investigation into kerf width is difficulty in measurement. The most studied area is surface roughness; which is easily measured in a rapid, automated process. Kerf width and bevelling studies are not particularly common in part because measuring them in a fast and reliable way is difficult.

In summary, three main gaps have been identified in the literature that this research can examine. Firstly, to develop a robust measurement method to acquire high quality kerf width and bevelling data rapidly and easily. Secondly, to acquire more data for the quality measures of kerf width and kerf angle. Thirdly, to develop a model to fit this empirical data and finally, to investigate the impact of the kerf symmetry assumption.

2.1.6 Relation between the literature and the work

The work in this project refers to various points of this literature review. The vision-based metrology method is intended as an alternative measurement technique that has not been utilized in the literature. It can offer similar measurements to those used for unevenness, MRR, temperature, cutting accuracy and kerf angle. Therefore, the results obtained will be compared to measurements that could be made using these techniques.

The modelling aspect of the project also makes use of some of the data presented in this section of the literature. Specifically, nozzle tip size, feed rate, arc current, gas pressure, torch height, and material thickness are all used to develop a first principle approach to estimation of the arc properties.

2.2 Modelling of the PAC process

The research into the field of PAC is varied and complex, as is the phenomena it attempts to describe. The understanding of the process has changed over the years and has been summarized in reviews and papers by Nemchinksy (Nemchinsky, 1994; Nemchinsky, 2017; Nemchinsky, 1998; Nemchinsky & Severance, 2006; Nemchinsky & Severance, 2009).

2.2.1 Review Objective

The review of this section of the literature aims to answer the following questions:

1. What process leads to the formation of the kerf profile, and how does it affect its shape?
2. How much energy is transferred to the cut via radiation?
3. What properties does a plasma jet have with regards to energy transfer and fluid dynamics?

These questions are relevant to developing a model for the kerf profile's formation. The literature presented is useful to understand the extent to which these questions have been explored in the literature, and to provide a detailed overview of the PAC phenomenology. It has been broken down into:

- An overview of the process.
- An analysis of structure and temperature of the arc.
- An analysis of the heat transfer to the metal.
- An assessment of the work on arc attachment.

- A review of current cutting models.

2.2.2 Overview

The PAC process was patented in 1955 by Gage and is described as a “Transferred Arc”. A plasma cutter consists of an anode that is incorporated in a cutting head Figure 2.2. The PAC process starts with a voltage being imposed between the cathode (1) and the torch nozzle (2). A gas (often air, oxygen, nitrogen or argon) flows through the plenum (3) and out of the nozzle (2). The electrostatic field causes the gas to become ionized and an electric arc is established between the cathode and the nozzle. The arc, after flowing out of the nozzle, is close to atmospheric pressure and accordingly is collision dominated (Jones & Fang, 1980). This means that the mean free path of the gas constituents is so short that collisions are frequent. This provides a high degree of self-mixing and therefore diffusion of quantities throughout the flow. Consequently, the gas can be viewed as being in a state of Local Thermodynamic Equilibrium (LTE) (Boselli et al., 2013; Cantoro et al., 2011; Ghorui, Heberlein, & Pfender, 2007; Jones & Fang, 1980; Kavka et al., 2013; Ramakrishnan, 1995).

Figure 2.2 Basic components of a PAC system (Girard et al., 2006).

The plasma permits the migration of ions and electrons, and this permits the arc to act as an Ohmic resistor, releasing a large amount of heat. Because the jet has a high transport velocity, ionic transport is low compared with electron transport. The pilot current is often administered in very short bursts. The plasma is carried through the nozzle and towards the work piece, a small distance (roughly 1 to 10mm) below the nozzle. The work piece is connected to the circuit and forms an anode in relation to the cathode. The arc transfers to the work piece and the electrical circuit adjusts to deliver the cutting current through the arc and into the work piece (Boselli et al., 2013; Cantoro et al., 2011; Ghorui et al., 2007; Jones & Fang, 1980; Kavka et al., 2013; Ramakrishnan, 1995).

The arc transfer process is extensively discussed in the literature but is not relevant to this work. It is relevant to the design and lifespan of the apparatus because of the stresses the nozzle and cathode suffer during this phase. Many torches have a helical gas path through the plenum so that the cold flow has angular momentum. This is known as “swirl” and improves rigidity of the plasma jet, but produces an unsymmetrical cut (Boselli et al., 2013; Cantoro et al., 2011; Ghorui et al., 2007; Jones & Fang, 1980; Kavka et al., 2013; Ramakrishnan, 1995).

Upon transfer, the arc begins heating the work piece and pierces through the cut piece once enough of the molten metal has been removed by the plasma jet. The plasma jet is then moved relative to the work piece, or vice versa, and a slot in the work piece is cut. Today this is often paired with CNC gantry control to precisely shape this cut.

From an industrial point of view the most interesting aspects of the PAC process are:

1. Erosion of the cathode and damage to the nozzle.
2. Cutting speed.
3. Kerf width.
4. Kerf angle
5. Dross formation.
6. Attachment of the arc to the work piece.
7. Surface quality of the kerf.

This research considers items 2 through 6 by developing a phenomenological model. The literature has provided models for some aspects of the process. Figure 2.3 shows depicts some of these aspects.

Figure 2.3 Some aspects of interest in a kerf (Colt, 2015).

2.2.3 Structure and Temperature of the arc

The morphology and temperature of the plasma-arc, after it leaves the nozzle, has been considered theoretically and experimentally many times (Boselli et al., 2013; Freton, Gonzalez, & Gleizes, 2003; Freton et al., 2001; Freton, Gonzalez, Ranarijaona, & Mougenot, 2012; Girard et al., 2006; Gonzalez, Lago, Freton, Masquere, & Franceries, 2005; Hlína, Šonský, & Gruber, 2017; Jones & Fang, 1980; Kavka et al., 2013; Kavka et al., 2014; Lago, Gonzalez, Freton, & Gleizes, 2004; Nemchinsky, 1998; Osterhouse, Lindsay, & Heberlein, 2013; Peters et al., 2008; Ramakrishnan, Gershenzon, Polivka, Kearney, & Rogozinski, 1997; Ramakrishnan, Shrinet, Polivka, Kearney, & Koltun, 2000; Teulet et al., 2006; Zhou et al., 2009). From this literature it is clear that the interaction between the arc and work piece (for a set gas and pressure) depends on cut speed, arc current/voltage, torch height and thickness of the work piece.

One method of examining the arc is to establish a stationary arc between a water-cooled, rotating disc and the nozzle. With this configuration, the exposed arc is conducting a small amount of heat into the rotating disc. Further, heat is being transferred into the surrounding air, as well as mass transfer from entrainment between the air and the plasma. In the literature this is referred to as “pumping” (Freton, Gonzalez, & Gleizes, 2000; Freton, Gonzalez, & Gleizes, 2003; Freton et al., 2001; Freton, Gonzalez, Peyret, & Gleizes, 2003; Freton et al., 2012; Girard et al., 2006; Gonzalez et al., 2005; Lago et al., 2004; Peters et al., 2008; Ramakrishnan et al., 1997; Zhou et al., 2009).

Radiation from an unconfined arc will be higher than that of a confined arc due to the temperature difference between the surroundings. The rate of energy transfer for radiation is given by the Stefan-Boltzmann equation:

$$\frac{Q}{Ar} = \varepsilon\sigma(T_h^4 - T_l^4) \tag{2.10}$$

Where ε is the emissivity of the surface; σ is the Stefan Boltzmann constant; Q is the power radiated in watts; Ar is the area radiating in m^2; T_h^4 is temperature in Kelvin of the radiating material; and T_l^4 is the temperature of the material being radiated to in Kelvin.

A typical plasma-arc can be 20,000K and the ambient temperature can be 293K for an unconfined jet and 1873K for the confined jet. The difference between the energy radiated for these cases is negligible and it can be assumed that measurements derived from unconfined arcs can be used for the modelling of a confined jet, provided radiation is the dominant mode of heat transfer.

Ramakrishnan et al. (1997) examined the portion of the jet between the nozzle and the work piece (a distance of 5mm). They presented arguments that, for the flow through the nozzle:

- The heated central portion expands and therefore accelerates as it passes along the nozzle. They cite (Jones & Fang, 1980).
- They present a dual layer theory where, because the hot central core has a low density, the bulk of the plasma flows in an annulus around this core. They propose that less than 10% of the mas flow is in the hot core.
- They suggest that the cooler annulus has a comparatively low conductivity, preventing the arc attaching to the nozzle. The cool layer heats as it travels along the jet and the 2 layers become entrained, increasing the conductivity until the arc can be conducted throughout the width of the jet.
- They cite Jones and Fang (1980) to propose that the Mach number for the core equals the Mach number of the surrounding flow. This statement is problematic. The local speed of sound is given by eq 2.11 (where c is the speed of sound in meters per second; γ is the specific ratio, the heat capacity to the specific volume, of a fluid, $\frac{C_p}{C_v}$; R is the ideal gas constant in $Jmol^{-1}K^{-1}$; and T is the temperature of the fluid in Kelvin). This and the measurements from Freton, Gonzalez, and Gleizes (2003), placing the core temperature around 25,000K, implies that the speed of sound is between 2 and 3 times faster in the core than the annulus. This would generate a large viscous force between the two and would result in a smooth cross-sectional velocity profile. Since the hot core contains only 10 percent of the mass flow, it would rapidly approach the speed of the annulus.
- They observed the presence of shocks. These indicate the flow at the nozzle's exit is under-expanded. According to Shapiro (1953), a short tube whose ratio of upstream pressure divided by the downstream pressure is greater than the critical ratio (1.89 for air) will have sonic velocity at the exit. If the exit pressure is greater than atmospheric pressure, the flow is termed "under-expanded". In this the large cross-section at the end of the tube is effectively a sharply divergent nozzle. Consequently, the velocity of the jet increases as for a deLaval nozzle. The pressure of the flow then undergoes either a normal or oblique shock to adjust to match the ambient pressure.

The phenomenology above was validated by Freton, Gonzalez, and Gleizes (2003). They modelled the flow of an oxygen jet using a Computational Fluid Dynamics (CFD) package (FLUENT) and modified their boundary conditions to agree with the experimentally observed flow. This indicates a shock just below the exit of the nozzle. Freton et al. present velocity and temperature fields for an unconfined jet. This shows the diameter of a plasma jet (5 bar plenum pressure, 1mm nozzle diameter) diverges from 1mm diameter at the nozzle to about 2mm

diameter 15mm away from the nozzle. Its central velocity varies from about 6000ms^{-1} just after the shock to about 5000ms^{-1} at 15mm from the nozzle. The central temperature at this point is estimated at 16,000K.

The speed of sound for air at 16,000K can be estimated by:

$$c = \sqrt{\gamma RT} \tag{2.11}$$

Substituting γ = 1.4, I = 8.314 Jmol^{-1}K, T = 16,000K

$$c = \sqrt{1.4 * \left(\frac{8314}{29}\right) * 16000} = 2{,}534\, ms^{-1} \tag{2.12}$$

Or for pure oxygen:

$$c = \sqrt{1.4 * \left(\frac{8314}{16}\right) * 16000} = 3{,}411\, ms^{-1} \tag{2.13}$$

This implies a supersonic flow of about Mach 2 at 15mm from the nozzle, conflicting with the conventional knowledge on fluid flow after a shock. Further, their figure describing the velocity field does not show any diminution in axial velocity as the flow traverses the standing shock (Figure 2.4).

Figure 2.4 Plots of experimental and modelled isotherms for the PAC process (Freton, Gonzalez, Peyret, et al., 2003).

Girard et al. (2006) used spectroscopic analysis coupled with photography to present temperature and composition for an oxygen plasma jet issuing from a 1mm nozzle diameter. The normal shock is photographed at about 1mm below the nozzle. They observe the expected diminution of axial

velocity to subsonic speed as the flow traverses the normal shock and a temperature change from 17,000K before the shock to 20,000K after the shock. This is consistent with conservation of energy as kinetic energy decreased and heat energy increased.

Freton et al. (2012) presented subsequent results with the FLUENT CFD software. They report qualitatively that their plasma jet diverges only slightly over 10mm axial length. The core temperature varies from 20,000K at the nozzle exit to 16,000K 10mm away. This agrees with other findings and validates this as a description of a free jet.

Bini et al. (2008a) and Peters et al. (2008) observed that the axisymmetric assumption is only valid for an ideal nozzle and cathode. Additionally, Boselli et al. (2013) and Hlína et al. (2017) used high speed imagery to observe fluctuations in the arc over a time scale of milliseconds. This suggests that the flow has coherent turbulent structures that can offset the centre of the arc by up to 500 microns. Industrially, when the consumables are no longer ideal, deflection should therefore be expected, reducing cutting accuracy.

Across the literature, a generic view of the free jet can be described as having a temperature of 20,000K at the nozzle and a temperature of around 16,000K 10mm downstream. The jet diameter approximately doubles over these 10mm, although due to difficulties in measurement the diameter is not precisely reported.

There is a wide range of variation in the velocity profiles presented in the literature. Zhou et al. (2009) found a velocity at the jet centre of 8,000ms^{-1} for a 20,000K oxygen jet. This implies Mach 2, which is impossible after a shock. This discrepancy is prevalent in the literature, particularly in ones that use CFD findings for velocity. Gonzalez et al. (2005) reports a velocity in the order of 100ms^{-1}. Nemchinsky (2017), in his survey did not report jet velocity, but in earlier papers assumed the velocities to derive Nusselt numbers and subsequently heat transfer (Nemchinsky, 1998; Nemchinsky & Severance, 2009). The presence of a normal shock has been repeatedly observed and photographed in the literature roughly 1mm from the nozzle (Figure 2.5).

Figure 2.5 Pictures of the location of shocks for varying cutting gas pressures (Colombo, Concetti, Ghedini, Dallavalle, & Vancini, 2009).

Consequently, the Mach number just below this shock will be less than 1. For air at 20,000K, this implies an upper limit of about 2,800ms^{-1}. This prediction is made more uncertain by the interactions between the jet and ambient air.

2.2.4 Heat transfer to the metal

Ramakrishnan (1995) and Jones and Fang (1980) provided a fundamental description of plasma-arcs. Ramakrishnan (1995) assumes that radiant heat transfer is small for plasma jets below 10,000K, however this is unsupported. Ramakrishnan et al. (2000) provided several hypotheses on heat transfer, namely:

1. Heat transfer to the work piece occurs primarily in the form of conduction/convection from the hot gas to the cool work piece.
2. Downstream of the nozzle, the entrainment of ambient air is small and the growth in diameter of the jet is also small. They do not however report the diameter of a jet.
3. Most of the electrical power required to produce the plasma-arc is lost to the surroundings (Ramakrishnan, 1995).
4. Approximately 70% of electrical power is converted into “thermal” power in the plasma jet (Jones & Fang, 1980).
5. 50% of the available power is transferred to the front cut face.
6. 90% of the gas flows in the outer annulus.

The contention that heat transfer occurs primarily from conduction/convection of the gas has not been examined. Conceptually, radiation from a 20,000K jet could be significant. The second contention is validated by several authors (Freton et al., 2012). The last hypothesis is plausible for the nozzle, but further along the jet there would be significant mass and momentum transfer. Freton et al. (2001) examines species concentration with respect to axial length and shows that significant mixing occurs between the zones. The two zone model becomes less valid as axial distance from the nozzle increases. Gonzalez et al. (2005) present a velocity profile for the jet leaving the model which indicates smooth variation in temperature and velocity. It therefore seems that the two-zone model has been superseded based on later CFD results.

Lago et al. (2004) suggests that slight deterioration of the cathode metal alters the plasma properties. CFD analysis was used to provide figures of the relative heat fluxes of different forms of energy. Girard et al. (2006) conducted spectroscopic analysis of an oxygen plasma jet, observing the emission spectra at specific wavelengths. Their data (Figure 2.6), for a 1mm nozzle, indicates that the local temperature variation with radial distance from the jet centre line becomes steadily flatter from 3mm downstream of the nozzle to 12mm downstream. The centre temperature declined from 18,000K at 3mm downstream to 15,600K at 12mm, but the temperature at 0.5mm from the centreline remains approximately constant at 12,500K.

Figure 2.6 Radial temperature profiles demonstrating the evolving distribution of temperatures at varying heights (Girard et al., 2006).

This demonstrates the progressive entrainment of ambient air. Girard et al. (2006) also measured a temperature increase through a normal shock about 1.5mm downstream from the nozzle. Significantly, they report that the centreline temperature variation for cutting compared to the rotating, water-cooled anode, are the same. However, they could only validate this for the first 2mm of the jet.

Teulet et al. (2006) suggest that 20% of the total jet energy is transferred to the plate (not the molten metal) at a cutting speed of 500mm/min and 40% at 1300mm/min. These were obtained

via temperature measurement of the plate. They also attempted to quantify the energy lost out of the bottom of the plate. They arrived at number of 57% for the slow cut and 1% for the faster cut. They offer no comment on whether energy input is via radiation or conduction/convection.

The only mention in the literature on the method of heat transfer, radiant versus conductive/convective, is by Nemchinsky and Severance (2009) and Nemchinsky (2017). They suggest that heat transfer occurs by conduction only on the front half of an ideal vertical plasma. This allows an approximation to calculate a Nusselt number for a parallel flow past a plate on the basis of the Dittus-Boelter approximation (McAdams, 1954). This approximation requires the assumption of gas velocity, however, the gas velocity varies with jet radius due to the pumping effect (Girard et al., 2006). Therefore, the speed of flow in proximity to the front cut surface is dependent on cut speed. Additionally, the front cut face is not usually vertical (Ramakrishnan et al., 2000). Therefore the calculations do not appear to be valid and the amount of radiant heat transfer is unknown. Ramakrishnan (1995) suggests that it is small.

Nemchinsky (2017) revisited the question of heat transfer. In doing so he cites Carslaw and Jaeger (1959) who compute the distribution of temperature in a plate for a moving line source. Experimental measurement of the computed temperature distribution was confirmed by Teulet et al. (2006). In the cutting model, they consider only heat transfer in the forward half circle and describe the phenomena as a sheet of molten metal falling down the cut surface, resisting heat flow. An energy balance is calculated and, from this, cutting speeds are estimated.

Conversely, work by Bemis and Settles (1998) shows that the kerf is wider than the plasma jet (Figure 2.7). This suggests that radiant heat transfer is not negligible. It is widely reported that the jet does not become more than twice of the diameter of the nozzle. Since in some of these images, the nozzle orifice is visible, it is clear that the jet does not impact the walls of the kerf. Therefore, under these conditions, heat is not being transferred by conduction/convection, or the temperature of the jet has dropped below what is observable.

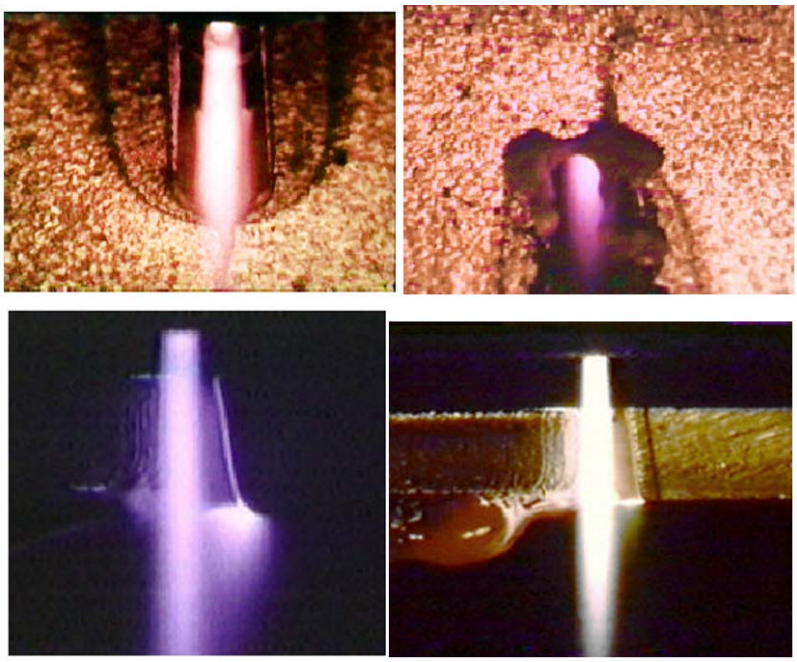

Figure 2.7 Examples of high speed imaging of the plasma-arc in various cutting conditions demonstrating a difference between observed kerf width and plasma jet width (Bemis & Settles, 1998).

2.2.5 Arc attachment

In the earlier descriptions of the plasma jet, at any instant, there is a well-defined path of electron flow. This path starts at the nozzle exit and ends at the attachment point on the anode. The attachment point appears to be a strongly radiating area because it is bright in photographs. In

several works, the location of this attachment point has been observed to change rapidly. This is presumably due to the arc following the preferred path of ionization and thus varying rapidly.

Teulet et al. (2006) suggested that the attachment point moves rapidly, often dwelling predominately at two different locations. At a slow cutting speed the attachment point is towards the bottom of the plate, but as cutting speed is increased, it moves upwards and then begins to oscillate between the two points. Eichler, Hussary, Siewert, and Schein (2014) stacked 6 insulated plates vertically to act as the anode. The current flowing through each plate was measured during cutting. The investigation showed that most of the current flowed through the top three plates. As cut speed was increased the current flow through the top plates was increased, validating Teulet et al. (2006). However, current always flowed through all the plates, implying the attachment point was jumping very rapidly, or there was another mechanism of electron drift. Ramakrishnan et al. (2000) and others have observed that the front cut face becomes inclined at higher cut speeds. This would cause the electrical path to the bottom of the plate to become longer and less electrically stable (Bemis & Settles, 1999).

Kavka et al. (2013) performed an experiment where 2 steel plates were positioned with an air gap between them. The plasma jet traversed this gap. For part of the traverse, only one plate was grounded, after that both were. When one plate was connected, only slight melting of the other plate occurred, but when both plates were grounded, both plates suffered melting. This occurrence was not explained. Teste, Leblanc, Rossignol, and Andlauer (2008) suggested, and it was reiterated by Nemchinsky (2017), that electrons bring their own kinetic and potential energy to the surface. This area of the literature needs development.

2.2.6 Cutting models

In order to cut, there must be sufficient heat transferred to the metal in order to melt the metal, and the molten metal must be removed. Nemchinsky (1998) suggested that the molten material would form a layer on the cut surface and would flow down under the influence of gravity and the shear force created by the jet. He suggested that this layer would be thin at the top and thicken as it moved further into the kerf. An energy and force balance were performed to create a cutting model. It was further noted that the liquid metal has a lower thermal conductivity than the solid, and that this would be a limiting factor of the cut. The thermal conductivity of solid steel is 50 Wm^{-1} whilst the conductivity of the molten material is 30 Wm^{-1}.

It was observed by Teulet et al. (2006) and Nemchinsky and Severance (2006) that the front cut face is angled so that the bottom of the kerf is closer to the jet than the top of the kerf, except at very slow cut speeds. This suggests that a sloped cut surface provides faster material removal due to the face deflecting the jet. This would cause turbulence in the jet stream, which was considered in the molten boundary layer model.

Ramakrishnan et al. (2000) presented data on the particle size distribution of the steel droplets blown through the kerf. It was found that at low cutting speeds, below the low speed dross limit, the droplets are about amm in diameter or larger. At high cutting speeds the distribution varies from 200 microns to less than 45 microns. This suggests that the shear over the molten layer from the jet is high. It also suggests that there are turbulent structures in the flow that create instability in the molten layer. This increase in surface area requires a large amount of energy.

Nemchinsky and Severance (2009) revisited the model in (Nemchinsky, 1994) and observe the slope of the front cut face. Heat transfer is again assumed to be by conduction and convection and thus a Nusselt number is estimated using the Dittus-Boelter correlation. However, the correlation is only valid for fluid flow parallel to a surface. Further investigation by Ramakrishnan et al. (2000) conflicted with the molten layer model. An experiment was performed where the plasma jet was extinguished, and the molten layer was allowed to solidify. This occurred rapidly due to the cut piece acting as a heat sink. The boundary layer was examined and found to have a uniform thickness, and to be less than 50 microns thick. Therefore, there is some uncertainty as to the validity of the boundary layer model, although it is the only model of PAC phenomenology that has been presented in the literature.

2.2.7 Gaps Identified

There is a substantial body of work into various aspects of the PAC phenomenology. The underlying principles of PAC are quite complex and thus there is a considerable amount of work that could be further developed. A common problem in this field is that making measurements with accuracy at extreme temperatures and in tight working environments is difficult. This results in substantial disagreements in estimations of operating parameters from paper to paper.

This research aims to address two gaps apparent in the literature, namely:

1. Is radiation a significant factor to the cutting process, and can we quantify it?
2. What is the shape of the front edge of the kerf, and what mechanism influences this?

2.2.8 Relation between the literature and the work

The literature presented from this section will be used to develop estimations for jet properties in the modelling section of the thesis. Where inconstancies have been presented in the literature, a compromise between the bodies of work will be used. As such the calculations presented are only an estimate of the situation, with the goal of verifying the assumption made in modelling the front face. Additionally, the method for examining an unconfined arc is modified and utilized in making measurements of the radiative heat transfer.

2.3 Vision Literature Review

The field of automated, visual-inspection (AVI) has been of great interest for more than 30 years. In that time, thousands of papers have been published considering everything from view planning to feature recognition for virtual machining from NC code. Researchers and reviewers of the field conclude that the potential for application is immense, and still a problem today (Anand, Raman, & Wysk, 1988; Dhumal, Patil, Dabhade, Papal, & Kulkarni, 2017; Kurada & Bradley, 1997; Newman & Jain, 1995; Savio, Chiffre, & Schmitt, 2007; Scott, Roth, & Rivest, 2003; Xu, Anwer, & Qiao, 2015).

This review considers six problems that are central to the implementation of AVI in this research project, namely:

1. What applications are AVI applied to?
2. What architecture should be employed?
3. How is the metrology assessed?
4. How accurate can the metrology be?
5. What complicates an AVI implementation?
6. What are the alternatives?

2.3.1 The application of automated, visual-inspection

Automated, visual-inspection, where the quality of parts is assessed, has been researched extensively for both 2D and 3D applications (Zhang, Singh, & Jagersand, 2015; Zhu, Mei, Yan, & Ke, 2014). Papers and reports on the subject include the addition of parts into the database of nesting programs for solution of stock cutting problems (Anand, McCord, Sharma, & Balachander, 1999). Jurkovic investigates visual inspection of degradation of a machining tool and evaluates the cause and extent of wear comparably to experienced machinists (Jurokovic, Korosec, & Kopac, 2005). Many researchers have considered the problem of view planning in manufacturing industries with the aim of optimizing the data gathering process (Chen, Li, & Kwok, 2011; Raffaeli, Mengoni, & Germani, 2013). External quality of fruits and vegetables has been inspected successfully using various implementations of visual inspection (Zhang et al., 2014). Inspection ranging from raw materials to complex assemblies in the aerospace, IC, automotive and food industries has all been researched (Newman & Jain, 1995; Ruz, Estevez, & Ramirez, 2009; Son, Park, & Lee, 2002; Zhang et al., 2014). Similarly, there is a broad field of recognition research, where a part is recognized by identified features (Chen et al., 2011; Newman & Jain, 1995).

Despite the abundant interest, researchers and reviewers agree that no generalized AVI system for manufactured/fabricated parts exists (Anand et al., 1988). Newman and Jain (1995) reported that estimates of the cost of poor quality in the manufacturing industries are approximately 20% of sales. Further, 10% of the labour costs for manufacturing industries are accredited to human visual inspection (Newman & Jain, 1995). The need for an inspection unit to examine conformity of manufactured parts against a standard is identified by Gao et al, Sebastian et al, and Chen et al (Chen et al., 2011; Momber, 2016; Newman & Jain, 1995; Tang, Tang, & Tay, 2016; Teti, 2015).

2.3.2 The automated, visual-inspection architecture

The standard architecture for an AVI implementation is to have a light source illuminating the object, and a charge-coupled device (CCD) in conjunction with a frame grabber or digitizer to transmit the image to a microcomputer or PC. In some applications a special light modulator (telecentric lens, filter, wavelength dispersion device, etc...) is included between the inspected object and the CCD (Chen et al., 2011; Jurokovic et al., 2005). A diagram of some of these components is shown in Figure 2.8. Depending on the application intended, different camera resolutions are used. For example Jurkovic uses a 768 x 493 pixel resolution for tool wear assessment whilst Anand uses a grey scale sensor with a 512x512 pixel resolution for re-engineering of leather garments (Anand et al., 1999; Jurokovic et al., 2005). Minetola uses a field of view of 6.7 x 9.0mm^2 to assess the impact of alignment between point clouds and object reference frames (Minetola, 2011).

Depending on the features of interest, computational power, and scale of application a variety of CCDs are used (Zhang et al., 2014). The simplest implementation uses a binary image to analyse the silhouette. Stereo vision is good for medium-to-small size object inspection and allows feature analysis (Scott et al., 2003). A range finder sensor is more appropriate for depth-intensive objects and larger scale applications in the automotive and aeronautics industries (Chen et al., 2011; Zhang et al., 2014). Triangulation-based range sensors are useful for analysing reflective surfaces and can achieve precision of less than 100 micrometres (Scott et al., 2003). These devices are moved around the object in one of two ways. A laser scanner can be coupled with a robotic arm to be moved to points of interest. Alternatively, a table can be used to rotate or move the object of interest in relation to the camera. The most common implementation involves the inspection of one part in a fixed position (Newman & Jain, 1995).

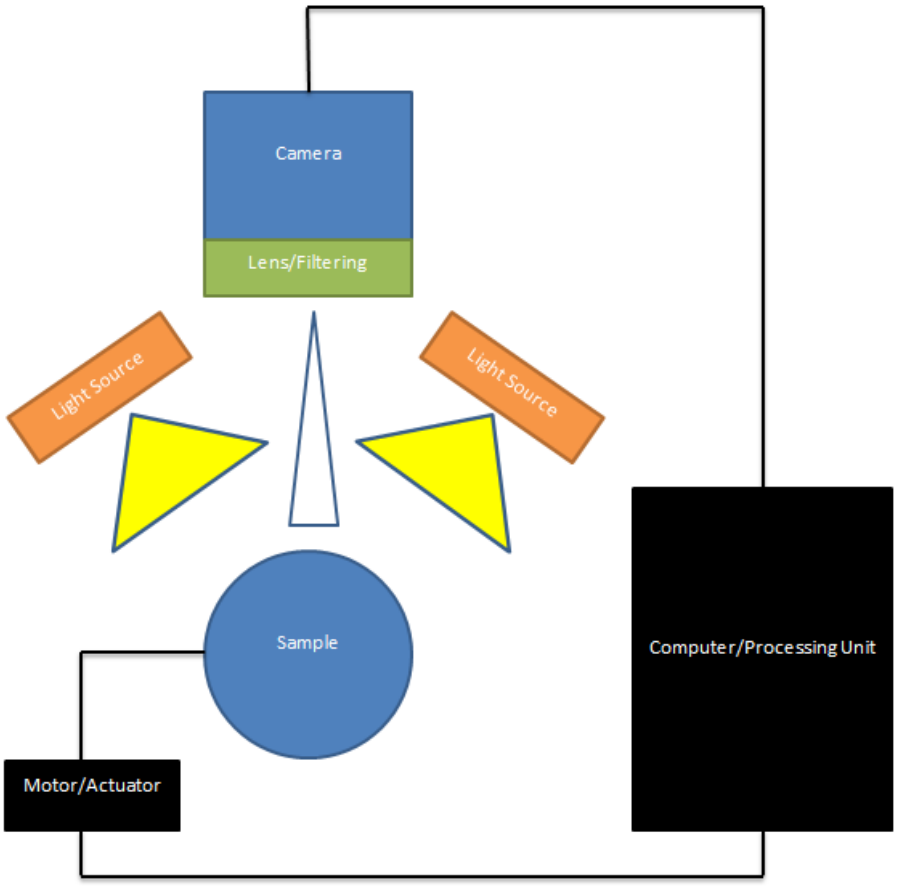

Figure 2.8 Typical components of an AVI system.

For this research project a standard CCD is envisioned. It will be attached to the robotic head of the plasma cutter and make use of the head movement to undertake sweep positioning to extend the object's point cloud. A standard PC will be sufficient to analyse the image as the part complexity is low, the movement speed is low, and the processing time available is large. This implementation is consistent with the architectures described in the literature (Chen et al., 2011; Jurokovic et al., 2005; Minetola, 2011; Zhang et al., 2014).

2.3.3 Metrology methodology

There are two main methods of analysing a part. The first is direct comparison, where points on the object are compared directly to a physical template. The second, and more commonly used, is indirect comparison, where the acquired points are related to a 3D geometrical mode (Savio et al., 2007). There has been significant research into reverse engineering (RE) CAD models from parts (Anand et al., 1999; Minetola, 2011; Savio et al., 2007). Xu et al have researched the derivation of CAD models from NC code (Xu, Anwer, & Mehdi-Souzani, 2015; Xu, Anwer, & Qiao, 2015).

The general process for 3D inspection is to analyse the CAD model and determine a suitable sensor path. The acquired images are registered and merged (or integrated) to remove redundant points (Raffaeli et al., 2013; Scott et al., 2003). Compensation for error positioning of the sensor is also accounted for here (Scott et al., 2003). A standard boundary walking algorithm can be used on the point cloud to generate the edges and the information can be used to describe a part as an appropriate CAD model, or as a set of points with distances and angles between them (Anand et al., 1999).

This project aims to parse the NC code used for fabrication to reconstruct a point cloud or CAD model using a similar approach to that used by Xu (Xu, Anwer, & Qiao, 2015). It will then reverse engineer the CAD model that corresponds to the scanned object as presented by Anand (Anand et al., 1999). The theoretical points from the ideal NC – CAD model can be compared with those scanned into the point cloud and an assessment of the part can be made. Newman suggests that this is how metrology should proceed in his review of the field (Newman & Jain, 1995).

2.3.4 Accuracy of the metrology

Depending on the application and scale of the process, the accuracy of measurements made range from centimetres for large applications (such as the automotive industry) down to micrometres (for analysis of ICs and other small components) (Newman & Jain, 1995; Zhang et al., 2014). The majority of applications are small scale however, and Jurokovic et al. (2005) describe a stereo vision camera with a resolution of 2.879 micrometres horizontally and 2.889 micrometres vertically (Jurokovic et al., 2005). Minetola uses 2 optical scanners in his demonstration of the importance of alignment. The first is an Advanced Topometric Sensory structured light scanner with an accuracy of 0.05mm for its working area of 200 x 160mm. the second is the triangulation laser scanner Vi-900 which has an accuracy of 0.08mm and a scan area of 111 x 84mm(Minetola, 2011). The required accuracy for this research project is only of the order of 0.1mm as that is the theoretical operating accuracy of a CNC plasma cutter.

2.3.5 Problems with automatic visual inspection

Despite the interest in the field, automatic visual inspection is still not a prevalent technology in the field of fabrication (Arpaia, De Matteis, & Inglese, 2015; Bas, Stoev, & Durakbasa, 2014). This is due to the complication of the endeavour. For 3D metrology as many as 70 images can be required to reconstruct the model (Chen et al., 2011).The acquisition of points occurs at the rate of about 50,000 points per second and takes between fifteen to sixty minutes for small to medium scale operations, and longer for larger ones (Chen et al., 2011; Minetola, 2011; Newman & Jain, 1995; Zhang et al., 2014). The time taken to process this amount of data can be longer still, and inaccuracies caused by noise, distortion, alignment errors and so on can make the problem even more complicated (Anand et al., 1999; Minetola, 2011; Newman & Jain, 1995).

As such, there are few companies that provide commercial AVI systems, and the systems that are provided are expensive and case specific (Newman & Jain, 1995). More general solutions have problems that unexpected obstacles can be in the sensor path, and that CAD models often do not match the NC code and the manufactured parts (Chen et al., 2011; Minetola, 2011; Newman & Jain, 1995). This project plans to take advantage of the large amount of time available to capture images and process the data, as well as working directly from the NC code to produce a cost efficient and generalized approach to fabrication metrology.

2.3.6 Alternative to visual inspection

Touch based CCM's already exist and are more accurate than 3D scanners with a precision of up to 1 micron (Minetola, 2011; Scott et al., 2003). Despite this, vision systems offer significant advantages such as: lack of contact, flexibility in application, rate of acquisition, and the inexpensive nature of the architecture (Savio et al., 2007). A successful inspection system needs to not bottleneck the fabrication process in order to be cost effective (Newman & Jain, 1995). X-ray computed tomography is a developing method that was originally used to detect defects within the part. It has been able to produce resolutions of better than a micrometre, but the technology is largely unquantified at this stage (Savio et al., 2007).

2.3.7 Gaps Identified

This review of the literature has highlighted the potential for a novel automated, visual-inspection system that makes use of NC code to assist with the problems of image rectification and path planning.

2.3.8 Work relevant in future chapters.

This research will make use of several of the concepts already expressed in the literature. The architecture of the vision rig will be very similar to the standard architecture expressed in the literature. Similar concepts to those of Anand et al. and Xu et al. are utilized (Anand et al., 1988; Xu, Anwer, & Qiao, 2015). It differs from these in practice because of the end goals of the endeavours. Anand et al. and Xu et al. aimed to reproduce NC code from a cut part, this project aims to assess the part against its NC code.

2.4 Literature Review Summary

The relevant fields of literature for this project are:

1. Plasma-arc cutting
2. The application of automated, visual-inspection

The plasma-arc cutting field has not seen a lot of research in recent years. It is mostly concerned with generating empirical data for performance under various conditions and improving performance by making slight improvements in the technology or maintaining performance and reducing costs for components. This field has potential for research into an underlying phenomenological model of the PAC process that can be used to predict empirical data and improve control. Additionally, many of the underlying principles presented in the research do not necessarily agree from paper to paper, or have yet to be quantified, such as the radiation contribution.

The field of automated, visual-inspection is also a thoroughly researched field, with the conclusion that there is still a need for the development of a generalized application. According to the literature there is great value in such a system. Current research in the field is split between reverse engineering of objects, metrology, sensor path planning, and novel sensor selection. There is potential for this project to advance the field by developing an automated, visual-inspection methodology.

This research project seeks to advance the fields of plasma-arc cutting, kinematics and control, and AVI in the following ways:

1. Investigation into the contribution of radiation to heat transfer in PAC.
2. Development of a phenomenological model for front profile shaping process.
3. An empirical investigation into the process parameters of torch height, material thickness and feed rate, with the quality measures of kerf width and kerf angle.
4. Development of an AVI methodology to facilitate the measurement of key process parameters and quality measures.
5. An investigation into the kerf asymmetry assumption.

3 Preliminary Investigations

This chapter covers investigative work performed to progress with the research. This material is intended to improve the reader's understanding of the methods undertaken and the tools used. It also allows the interested reader to replicate any elements of the work more easily. The research was undertaken on the plasma cutting performed by a PAC system provided by Kerf Ltd. to Massey University. This system was a ProCut (Figure 3.1). It used the Dynatorch XLS control software and the powers supply was a Hypertherm Powermax 45A system (Figure 3.2). This system had a 1m square gantry system and the torch was CNC controlled. It was capable of cutting steel up to 10mm-thick.

Figure 3.1 Massey University's PAC system.

Figure 3.2 The power supply used by Massey University's PAC System, Hypertherm Powermax 45.

Two areas of investigation were undertaken on this system. The first was a hysteresis investigation. It was necessary to be aware of the precision and accuracy of the system to avoid attributing error from the gantry system to the PAC process. The second area investigated was a method to determine the location of the torch on the gantry system. This information was not readily available from the Dynatorch software in a format that another program could utilize.

3.1 Hysteresis investigation

The methodology for a proposed vision system is to use the carriage of the plasma cutter to drive the cameras around to look at part edges. The edge finding aims to be accurate to 0.1mm, providing the hysteresis of the system is negligible. Accordingly, the first step is to investigate the amount of hysteresis in the carriage.

Hysteresis is when a system performs differently due to its past state. In this case, the carriage of the plasma bed might move with differing levels of accuracy based on previous movements. In mechanical systems a common cause of hysteresis is backlash. This backlash can occur in the numerous moving components due to deformation of the parts or imperfect coupling. For the carriage of a plasma system, the major source of backlash would arise from imperfect meshing

between the belt drive and its gears, and potentially in tension stored in the belt.

Figure 3.3(a) shows the hysteresis that arises from slight discrepancies in the meshing of the teeth of the gear and belt. As the gear changes direction there will be a small amount of lag as the gear rotates freely through this section, until it re-meshes on the opposite face of the teeth. Additionally, backlash can arise from the stretching of a belt (Figure 3.3(b)). This is easily observed when the belt is very slack, in the image below there is a tight side and a lose side. If the driver pulley continues rotating clockwise then the tight end will stay tight and there will ideally be a 1:1 movement ratio between the circumference of the pulley and the belt. However, if it starts rotating counter clockwise it will cause the loose side to tighten and the tight side to slacken, and whilst that occurs some movement less than 1:1 will occur depending on how much slack the system has in it.

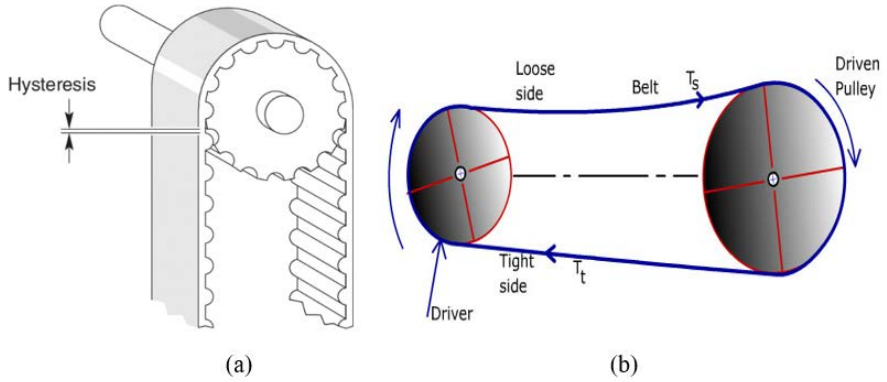

Figure 3.3 Hysteresis in (a) the meshing of the gear and belt (Newport, 2018) and (b) in the belt tension (NPTEL, 2013).

3.1.1 Experimental Plan

To test for the significance of the hysteresis an experimental plan was devised that used 2 methods of measurement in different scenarios. The first made use of the vision system that had already been implemented. The second used a digital gauge to measure small amounts of displacement.

In the first method, images of a horizontal and vertical cut were acquired (Figure 3.4). The images were acquired by cantering the camera above the measured slot. The carriage was then driven 300mm in an axes' positive direction, and 300mm in the negative direction to centre over the slot. It was then driven 300mm in the negative direction, and again, back over the slot. This was repeated 3 times, yielding 6 images; 3 of the slot when approaching from the negative direction, and 3 of the slot when approaching from the positive direction. The centres of these slots were measured, and the difference in measured location between the 2 directions recorded.

Figure 3.4 Vertical and horizontal slots used for vision-based, hysteresis measurement.

In the second method a surface gauge was used to measure the carriage displacement. The carriage was driven roughly 0.3mm into the gauge and zeroed at this position. The carriage was then

moved in 0.1mm increments into the gauge, recording the gauge readout at each position, this was done over 0.6mm. The carriage was then moved in 0.1mm increments away from the gauge, and the new readouts were recorded.

This was repeated twice at each position and positioned at 9 locations across the bed, With X at 0, 300, and 600mm, and Y at 5, 505, and 1005mm. These were all undertaken in one direction, where Y was driven negatively into the gauge and positively out of the gauge. The process was then repeated for each direction for X at 300mm, Y at 505mm.

A further test that was carried out was to investigate the relationship between the set movement length and the desired movement length. To do this, the carriage was moved in the positive direction to load the belt and mesh the gears. It was then moved approximately 1 meter in the same direction and the magnitude of the movement was measured. This was measured by placing the digital gauge at the desired end location and moving slowly into it.

3.1.2 Findings

The experimental data is included in Appendix A. The tests showed that initially the plasma cutter carriage had an average hysteresis of 0.154mm in the X- direction and 0.493mm in the Y-direction. Tightening the belts reduced this to 0.032mm in the X direction and 0.05mm in the Y-direction, i.e. a reduction of the hysteresis error by 79.2% and 89.9% in the X- and Y- directions respectively. This level of hysteresis error in the carriage position is acceptable in terms of the required accuracy of the edge-follower system. The slightly higher hysteresis in the Y-direction is attributed to there being more mass attached to movements in the Y-direction than the X-direction.

3.2 Quadrature decoder implementation

One of the main focusses of this research project is the development of a system that can automatically evaluate the PAC process. The camera rig to provide this will need to attach to the head of the PAC system. The field of vision will be somewhere in the order of 30 square centimetres. This provides a high level of resolution, making edge detection easier; however, it means that an image will only contain a small segment of the PAC bed. For the algorithm to make use of this it will need to know the location of the camera when the image was taken. With this information, multiple images can be rectified to evaluate performance over a larger area.

There were 2 options to acquire the position of the torch head and provide it to the image algorithms. Firstly, the PAC system's control software was developed by Dynatorch. Kerf has a working relationship with Dynatorch and could request that a modified version of the control software be provided. This software could stream the X, Y and Z position of the torch head to a serial port, and the algorithm could read these values. Further the control software could monitor a serial port for a command to move to a position, which would provide the image algorithm control to request a position to take an image from. This solution would have been ideal, however the lead time anticipated for Kerf to get in touch with Dynatorch, Dynatorch to implement the changes, for Dynatorch to return the software to Kerf and for Kerf to install the software on the PAC system at Massey was going to take roughly a year. This delay precluded this option, but in the future might be a great option.

The other option was to monitor the encoder lines to track incremental movements and calculate the resulting position. This option was appealing due to the relatively short time to implement. It also allowed resetting of the torch head's relative position without changing the position in the controller. A quadrature decoder could be achieved by purchasing some quadrature decoder ICs, designing a PCB to mount these and monitoring the outputs with a micro controller. The micro controller would keep track of relative changes made from a home position to track the absolute position of the torch head. However, it was decided that a quicker implementation would be to use the micro controller to directly monitor the encoder lines.

The requirements set for this implementation of a quadrature decoder were to be able to accurately count the number of encoder pulses and use this to track the position of the plasma cutting torch

head. Further, it needs to be able to communicate with the image algorithm platform via serial port. Finally, the implementation needed to be tidy and self-contained due to it being in a commonly used area.

3.2.1 Development

3.2.1.1 Materials/components

The materials used for the quadrature decoder implementation were:

1. Arduino Uno.
2. Shielded USB cable.
3. Sundries.

For this application, a micro controller with 6 digital input pins and a reasonably high clock speed was required. An Arduino Uno was selected as the microcontroller for the decoder implementation. It offered a suitable number of digital input pins and a clock cycle of 16MHz, yielding 200 clock cycles between encoder pulses, which was assumed to be sufficient. In addition to this, the Uno is inexpensive and was readily available.

Due to the high amount of noise produced by the arc, particularly on torch ignition, a shielded USB cable was chosen to protect the integrity of the serial output. Various sundries were also required. This included wires, connectors and spade terminals to connect the pins of the Arduino to the decoder lines. An aluminium case was constructed to contain the Arduino for the purposes of mounting and reducing noise it experiences.

3.2.1.2 Work Done

The concept of the quadrature decoder is to connect 6 digital input pins on the Arduino to the encoder lines from the PAC system. The Arduino will be mounted alongside the PAC's control box. The encoder line contains 4 wires, signal1, signal2, 5V and ground. Therefore one set of encoder wires will also have the ground and 5V lines piggybacked to supply power and a common ground as well.

The first step to implement the quadrature decoder was to probe the encoder lines to observe the signal size and frequency. This was to evaluate the feasibility of the proposed decoder implementation. An oscilloscope was connected to the 2 encoder lines on the Y axis, and the head was moved along the Y axis to observe the signal. Figure 3.5 shows the signals observed. The Y axis scale on the oscilloscope is in 2V increments showing that the signal is 5V for high and 0V for low. Figure 3.6 shows the head accelerating. The scale of the X axis is set at 25 microseconds, and it is observable that as the head accelerates, the oscillations have a period of roughly 50 microseconds. This corresponds to a change in state every 15 microseconds. Figure 3.6 shows how the 2 lines are out of synch, and therefore need to be sampled every 12.5 microseconds. The clock cycle of the Arduino Uno is $6.25*10^{-8}$ s, which leaves 200 clock cycles between encoder ticks.

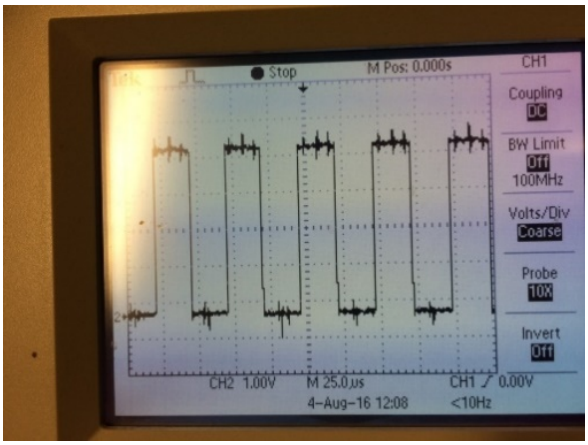

Figure 3.5 Oscilloscope readout showing the signal for an encoder line whilst travelling at a fast, constant speed.

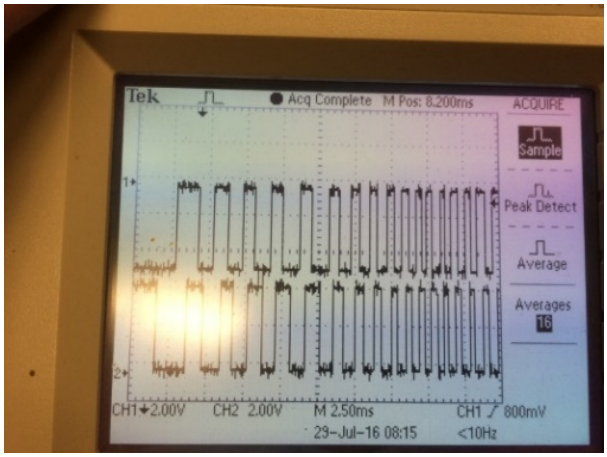

Figure 3.6 Oscilloscope readout showing the acceleration of the torch head and the corresponding signals on the 2 encoder lines.

With this feasibility test undertaken, wires were connected to the encoder lines and the ends were left to be able to be attached with a screw terminal to the appropriate pins on the Arduino. During the development of the system it was discovered that the ends of these wires needed to be grounded through a pull up resistor. If the ends were left to float, then noise would be read by the controller's decoder, and erratic movements ensued. This was performed by setting the Arduino's pins as inputs; enabling the pull up resistor, and then using the encoders 5V to power the Arduino whenever the PAC system was powered. Figure 3.7 shows the Arduino mounted in the PAC system's control box.

Initially the Arduino's 'digitalRead' command was going to be used to poll each pin separately on a loop every 12.5 microseconds. However, the time taken to perform a digital read transpired to be 4.4 microseconds. Therefore, for 6 pins, it would take 26.4 micro seconds. A different approach was used to poll the byte value of Port B, effectively reading all 6 pins at once. The time taken to perform this action was 5 microseconds, which was sufficient for the task.

A further complication that transpired was the time required for a serial output. This was in the order of 1,000 microseconds and therefore impossible to perform whilst also polling the encoder lines. To work around this, the code first polled the port, performed the logic transformation and then updated the counts of the 3 encoders. Then it checked how long it had been since they changed. If a second had elapsed, then the Arduino printed the current position of the 3 positions out to the serial port.

A final aspect of the code implemented was a check to make sure that counts were not being omitted. The logic behind a set of encoder signals is to use a grey scale, so that only one of the 2 lines may change between any encoder counts (I.e.-> 00 <-> 01 <-> 11 <-> 10<). The Arduino kept track of another variable that counted how many false steps were taken since the last time the position had been read and reported this value. This allowed evaluation of the accuracy of the decoder count. In addition to this, a reset command was also added, where if 'reset' was sent to the Arduino over the serial port, the encoder counts and dropped steps count were reset to zero.

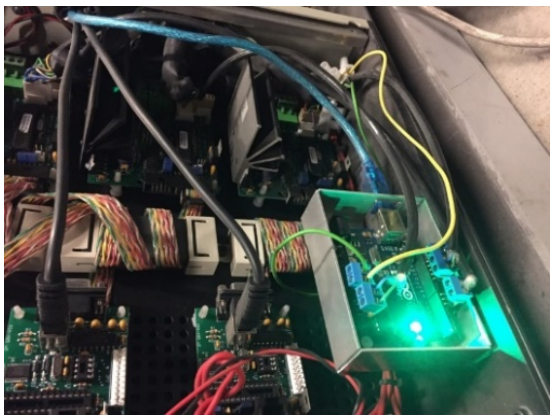

Figure 3.7 the Arduino mounted in its faraday cage with wires piggybacking off of the encoder lines and a shielded USB cable exiting the enclosure.

3.2.2 Results

This implementation of a quadrature decoder was sufficient to acquire the positional data needed for image taking. This encoder count was found to be accurate and repeatable for moderate speeds. The performance was assessed by comparing the position reported by the decoder, to the position reported by the control system. Further it was checked that false counts were not being taken. The positioning reported was accurate to 0.01mm, which was the accuracy that the control system reported.

The system was validated by its performance for 2 years, accurately reporting the position of the PAC head when the vision tools were being used. No detrimental effect on the PAC system was observed as a result, and the components are all still functioning properly at the end of the research. The vision measurements performed also confirm the accuracy of the system as rectification would be impossible without a system accurately reporting the position of the head.

Several limitations were found in this decoder system. Firstly, it was found that past a speed of approximately 2500mm/min encoder counts started to be dropped. This was compensated for by keeping movements below 2000mm/min. However, this needed to be considered for all future work using this system. Another limitation was the communication method used. Whilst it was acceptable for the development work to pause the camera as a means of communication to the Arduino to report the position, a real time implementation of a decoder would need to be able to report the position without the risk of missing encoder steps.

3.2.3 Future work

Future work in this area is unlikely to be undertaken as the implementation proved sufficient for the work performed. However, there is definite scope for improvement, and future work is likely to depend on knowing the position of the head in real time. Potential improvements to the system could be performed by using a faster processor, or a quadrature decoder IC, or even altering the Dynatorch system to output the position to a serial port. These possibilities were ignored for this project due to expense and lead time anticipated.

4 Machine Vision for PAC

This chapter details the work done in developing automated, visual-inspection (AVI) for PAC. The work described in this chapter is broken down into four sections:

1. Development of a vision rig with a wide field of vision to perform AVI of kerf width.
2. Development of a vision rig with a narrow field of vision to perform AVI of kerf width.
3. A feasibility study on height detection using the vision rig.
4. The empirical investigation of kerf angle with respect to torch height, material thickness and feed rate as process parameters using the vision rig.

Automated, visual-inspection offers many significant opportunities to PAC in industry. As discussed in the literature review, the majority of the time and expense associated with this fabrication method is the post processing and rework required. Post processing can be reduced by operating the PAC system as efficiently as possible, and AVI facilitates the assessment of errors and what parameters could be tuned to remedy these. Rework can also be avoided by the use of AVI. For example, a process run could be stopped if significant errors are detected, and again, provide valuable information on these errors.

Research into an AVI system also fills a gap identified in the literature review for such a system. There has been some use of NC code for path planning algorithms in metrology and attempts at reconstruction of NC code from parts. However, no work used NC code to path plan and measure manufactured parts.

A feasibility study for height detection using stereopsis from the developed vision rig is also presented. My sponsor, Kerf Ltd., expressed interest in the potential of this because of the shortcomings of voltage measurement to manage height.

The final piece of work, an investigation into kerf asymmetry, was undertaken because of a gap identified in the literature. This gap is the assumption of kerf symmetry reported in the literature. The presence of asymmetry in a kerf has been mentioned in the literature, but not quantified, and many works do not take it into account. This work provides an empirical investigation into the quality measures of kerf angle and kerf width, and then uses this data to examine the significance of kerf asymmetry.

The results of this work include the successful development of an AVI system for kerf width on a CNC PAC system. This system was validated on 5 test cuts of 5 parts with varying complexity and found to be capable of measuring to an accuracy of 0.1mm. In addition to this, a feasibility study of height detection using stereopsis from the close view vision rig was undertaken and found to be at least as accurate as the existing potential measuring systems. Finally, data on an empirical investigation is presented on the relationship between kerf angle, and the process parameters of torch height, feed rate and material thickness. The relationship is presented, and the impact of kerf asymmetry is assessed and found to be significant.

4.1 Vision rig: wide-view

One aim of this project was to use feedback from a sensor rig to optimize the process parameters of PAC in real time. Machine vision was chosen as a suitable sensor option for several reasons. Firstly, it could supply a large amount of data very quickly, a reasonable resolution picture of a kerf can have hundreds or thousands of data points. Secondly, the accuracy could be easily altered by changing the distance of the camera from the work. Finally, the literature has suggested that the application of machine vision is a useful possibility for improving the understanding of the process (Nemchinsky & Severance, 2006).

The first method investigated was to mount 4 cameras around the torch to inspect cut parts. Various output parameters, such as; kerf width and dross formation, could theoretically be observed. The PAC literature has models relating these output parameters to process parameters such as torch height, cut speed, and voltage set point that could be used to tune the process parameters to ideal values. Therefore, generalized inspection of plasma cut parts was investigated.

4.1.1 Design

The details of the design and calibration of the wide-view, vision rig are presented in Appendix B. A brief summary is presented here however. This vision rig mounts 4 inexpensive webcams at a height of about 390mm above the plasma bed around the plasma torch. This configuration provides the ability to use stereopsis, and acquire images for cutting in the X- direction and both Y directions for the gantry bed. Housings were designed for the cameras to protect them in the harsh environment. Figure 4.1 shows a Solidworks design of the test rig, and Figure 4.2 shows the actual assembly.

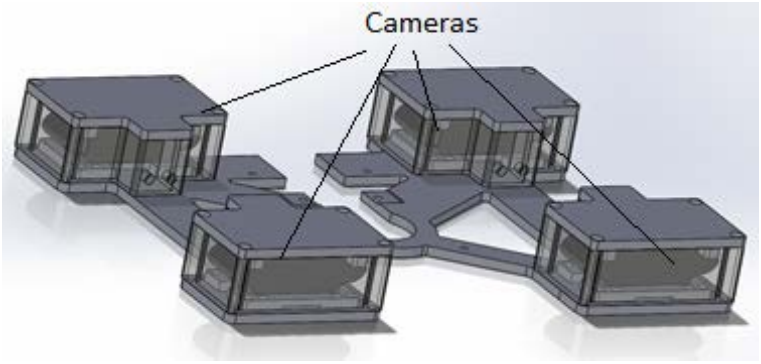

Figure 4.1 SolidWorks™ model of the wide-view vision showing the 4 cameras and their relative positions.

Figure 4.2 Image of the complete wide-view vision rig.

Calibration of the test rig was performed by taking images of a disc as the plasma head was moved in a grid pattern over it, at 5 different heights with 5mm offsets. The scaling parameters were estimated from measuring the known diameter of the fiducial disc, and the known offsets in the centre of the disk as the torch head was moved. Figure 4.3 shows an image of the disc captured from a camera and Figure 4.4 shows the grid pattern of the disc created by moving the torch. For a more detailed description of the calibration process please refer to Appendix B.

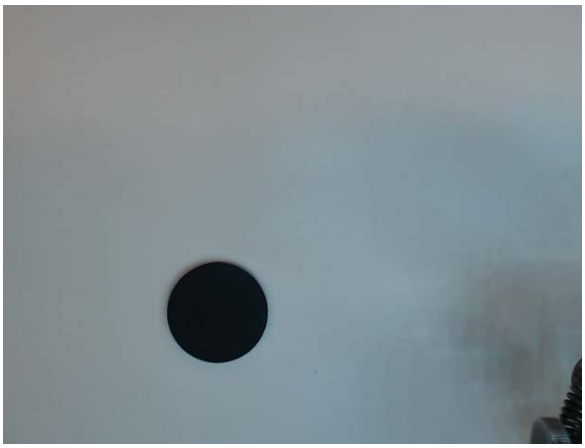

Figure 4.3 Example of an image being taken of the black disc on the white background.

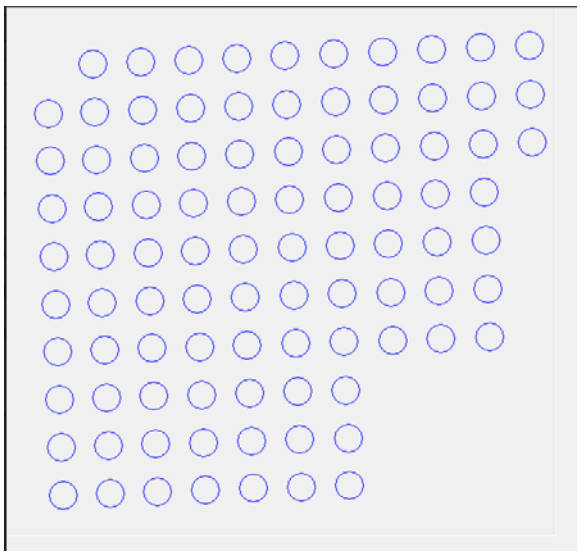

Figure 4.4 Image shows the disc centre moving in camera 1's reference frame as the torch head is moved in its grid pattern.

4.1.2 Results

After development of the calibration algorithm, the systems accuracy was assessed. The results from each of the stages of the algorithm are present below in Table 4.1. Regression 2 was the only step of the process that did not result in an error that exceeded the specification. This suggests that with the large amount of data obtained, the disc centres were quite accurately located, even if there was a large amount of deviation in the location of the edge points. The large error in regression 3 was investigated and found to be systematic as show in Figure 4.5. One possible source of such a systematic error would be fish eye distortion so a test was performed where a straight edge was placed at the edge of the camera frame. These are shown in Figure 4.6 and Figure 4.7 and there is evident systematic error in the edge points returned when fitted with a line. This suggests that fisheye distortion could be a significant factor. Overall the performance of this vision rig was accurate to slightly less than 2 pixels on overage, which is quite accurate, however not good enough.

Table 4.1 Regression results for the calibration method.

	Error						
	Cam1	Cam2	Cam3	Cam4	Average	Worst	Best
Regression 1	0.25	0.25	0.25	0.25	0.25	4	0.1
Regression 2	0.05	0.06	0.04	0.05	0.05	0.1	0.03
Regression 3	0.7	0.6	0.5	0.8	0.55	2	0.15

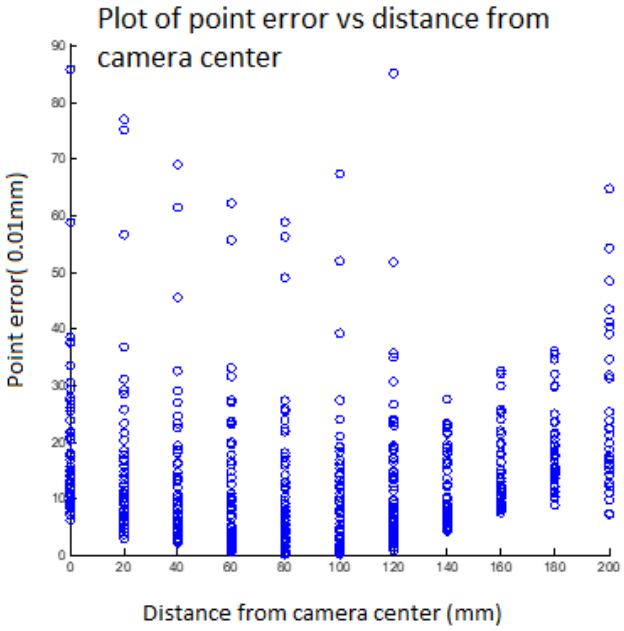

Figure 4.5 Plot showing relationship of point error with distance from the camera centre. The error, in hundredths of amm, varied significantly.

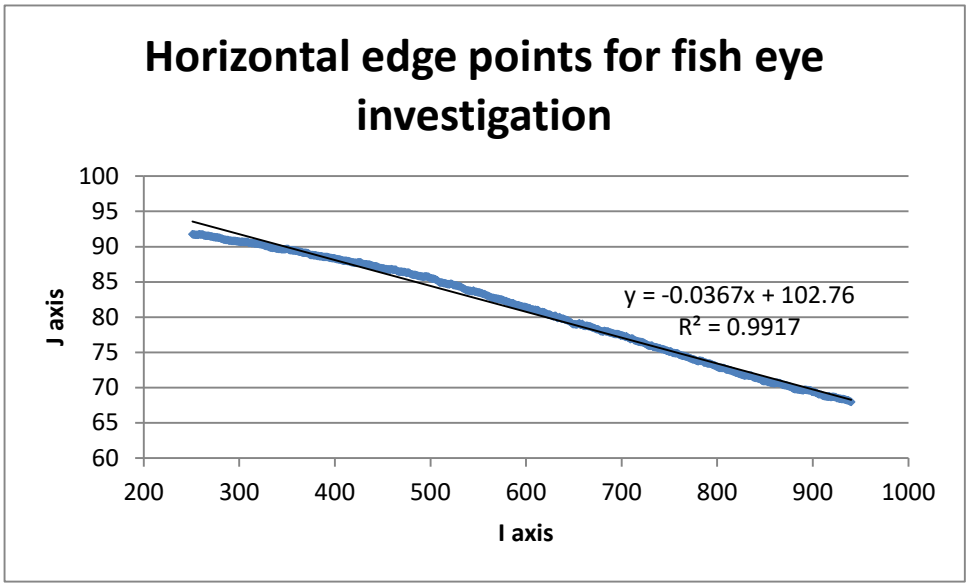

Figure 4.6 Edge points obtained for a straight edge at the top of the camera frame.

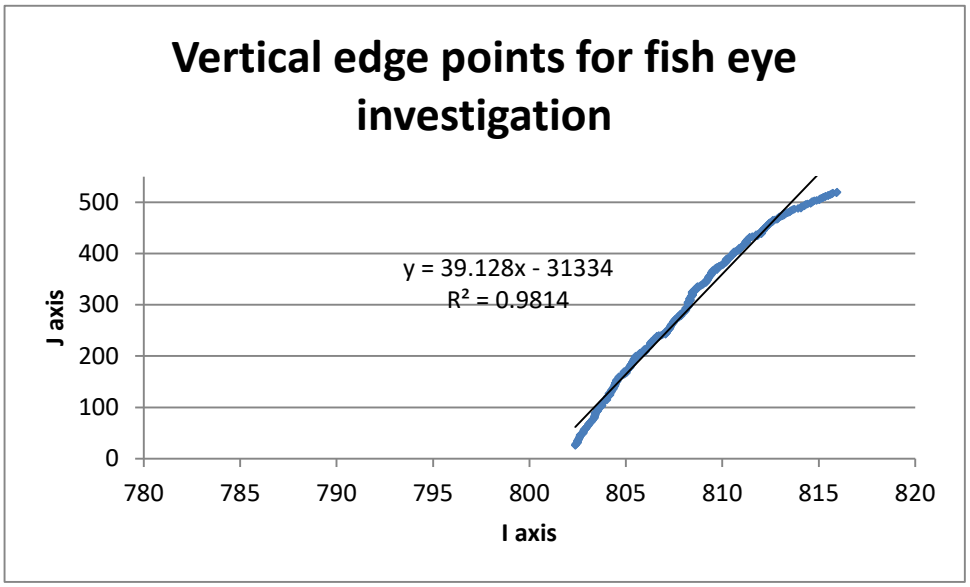

Figure 4.7 A plot of the edge points obtained for a straight edge at the left of the camera frame plotted over a line of best fit.

4.1.3 Conclusions and Recommendations

As explained in section 4.1.2, the general concept of the system provided an ability to acquire edge data and make measurements. However, this system was unable to meet the required accuracy. Several potential improvements were identified as part of the development of this 'wide-view' test rig. The key improvements were:

1. Fish eye compensation to reduce systematic error.
2. An increased resolution to aid with better edge finding accuracy.
3. Greater attention to the presence of bowing in the parts that caused some skew distortion of the image due to the camera being mounted not entirely parallel to the plasma bed.

It was decided to pursue an increased resolution by mounting the cameras approximately 195mm from the camera bed. This involved significant redesign of the mount and resulted in a separate close view rig being developed.

4.2 Vision rig: close view

4.2.1 Introduction

The close view chapter follows on from the requirements laid out in the wide-view vision chapter. The initial requirements for the wide-view chapter still stand. However, the wide-view system could not achieve the accuracy required so a new test rig was developed to help meet this. The key development for this rig was to bring the camera distance down to approximately 100mm from the cut surface. This effectively doubled the resolution, making the requirements on the edge detection less stringent. In the previous system the edge needed to be located to approximately a fifth of a pixel, whereas this arrangement requires only half a pixel.

4.2.1.1 Goals

The goal of this system is to be able to take any set of G-Code and assess the cut performance from this. The tasks for the "close-view" system can be broken down into:

- Perform generalized inspection of G-Code.
- Measure kerf width to an accuracy of 100 microns.
- Ensure that the measurements are repeatable.

- Design and build a detachable rig.
- Provide high quality data for empirical investigation of kerf width.
- Consider real-time implementation.

Generalized inspection of G-Code requires the development of an algorithm to parse a set of G-Code and to identify the parts within it. It then must be able to relate images taken in the real-world frame to the section of the part that they describe. Then it must evaluate the accuracy of the desired edge location compared with the actual edge location.

The result of the previous goal is to be able to get data that can be used to measure kerf width. Kerf width measurements need to conform to the requirements of industry and the research endeavours. Industrially, the top performance of PAC is accurate to 0.1mm, although most systems do not actually achieve this. Current research investigations into kerf width, cut accuracy and mass-removal rate use either a caliper or a profilometer to perform the measurement. Realistically caliper measurements of PAC parts are only accurate to about 0.1mm due to deviations in the surface and kerf angle. Caliper measurement also has low repeatability. A profilometer can yield very accurate measurements (the order of 1 micron). The close-view rig will not attempt to compete with this accuracy, because it is not possible with the components it uses. Instead it aims to provide more data with less effort and less expense.

The repeatability in kerf width measurement also needs to be accurate to 0.1mm. In summary, a goal of this research is to have a measurement method that is as accurate as the caliper alternative, but which is quicker and has much better repeatability.

The test rig needs to be conveniently attachable; it might need to be removed frequently due to the possibility of it interfering with specific bevelling cuts or configurations. It will also improve the component's life if they do not sit in the harsh environment when not in use. In addition to being conveniently attachable, the rig needs to be positioned at the same height and orientation; otherwise the calibration process would need to be repeated.

A further goal of the development of the algorithm is to provide high quality data for empirical investigation into kerf width as a function of the process parameters such as cut speed and material thickness. This empirical data will enhance the literature as well as validate the developed system.

Finally, future work for this system will likely include real-time implementation. Time constraints and a lack of components make this infeasible as a starting point; however, it has obvious value industrially. Therefore, the algorithm development needs to be readily adaptable to a real-time implementation.

4.2.1.2 Challenges

There are numerous challenges in achieving these goals. Some aspects of this system have been reported in the literature, however in general there is no automated way to do this type of cut quality assessment. Not all the challenges inherent in the task are worthy of note, however there are some key challenges worth mentioning.

G-Code parsing into parts requires identification of features versus part completion. There is little inherent difference between the two. They both start with a torch ignition code and end with a torch off code. Further acquiring a set of images that fully describe the periphery of the part is a commonly investigated problem in the literature.

A key challenge is meeting the 100-micron accuracy. This requires edge detection to sub-pixel accuracy with the cameras and mounting positioning required. Further, slight errors will be magnified when rectifying the edge points. An accurate calibration or tuning process will be required so that there is no error between pictures. More complexities in meeting this accuracy derive from finding the desired section of the edge despite noise in the material's surface, comparing the edge points to a set of G-Code and interpreting the comparison into a measure that is useful, i.e. kerf width and variation in kerf width.

A challenge that is closely entwined with the accuracy goal is making the accurate measurements repeatable. This challenge requires provision in both the algorithm and the test rig side of the tool. The algorithm needs to be robust to changing light and surface noise. This involves normalizing the input data in such a way as to not distort it and introduce errors. The test rig also needs to be designed so that it is robust and easy to mount in a repeatable way so that error is not introduced every time the rig is reattached to the torch. This is not a problem with academic merit but is still challenging none the less.

The goal of providing high quality data for the empirical investigation of kerf width has a key challenge of designing a test cut and experimental method that provides a good ratio of relevant data to irrelevant data. As such feasibility tests and research needed to be undertaken to identify an appropriate set of process parameters and operating conditions. Then the data needed to be presented in such a way that would make its interpretation intuitive. Throughout the literature this has been a bit of a short coming. Data is typically summarized and presented in tables, and the contribution to the empirical model is acquired from a Design of Experiment (DoE) software package.

A final challenge to be met during the development of this tool is to design it in such a way that it can easily be implemented as a real-time algorithm. This means designing the algorithm around the structure that data would be presented to it in real-time, as well as considering possible applications of the software so that significant rewrites would be unnecessary. While there will always need to be changes and improvements, minimizing the impact of these is challenging but important.

4.2.1.3 Expected deliverables

There are several expected deliverables from this endeavour. Firstly, a vision rig will be developed, tested and calibrated. It must provide mounts for 2 webcams onto the PAC torch allowing image acquisition in conjunction with the gantry. It must be easily attachable and detachable in a manner that will not undermine the accuracy and reproducibility of the system.

The next deliverable is the algorithm required to perform the analysis. This algorithm must have several capabilities. Firstly, to take a generic set of G-Code and interpret the commands to construct a set of parts and generate the edge coordinates describing the edges of these parts. Secondly to generate a position that the torch head needs to move to, to acquire an image that will allow the acquisition of desired edge points. Further, once it has this image, it must find the desired edge points in the image. The desired edge points are those that are covered by a suitable section of the G-Code, within a certain window. The edge points are for both the inside and outside edge of the cut. The algorithm must then rectify these edge points into a holistic description of the edge points of the part. Once this has been achieved the algorithm must compare the location of the cut edges with the G-Code generated edge point coordinates. This comparison then needs to be presented as cut accuracy around the edge of the part, as well as measures of the average kerf width and variation.

The final deliverables from this system are a set of data for kerf width and various process parameters. This data will be acquired over a test cut designed to examine various cutting scenarios. In the limit, it is envisioned that this data can be used to better predict kerf width with respect to process parameters. Further, the system can be developed later to allow real time assessment of cuts and provide feedback to tune the process parameters.

4.2.2 Test rig development

The details of the design and calibration of the close-view, test rig are presented in Appendix B for the interested reader. A brief summary of the process is included here. The close-view, test rig is shown in Figure 4.8. It provides mounting for 2 webcams approximately 100mm above the cut surface to all measurement requirements to be met. In addition it provided improved functionality for adding and removing it from the PAC machine.

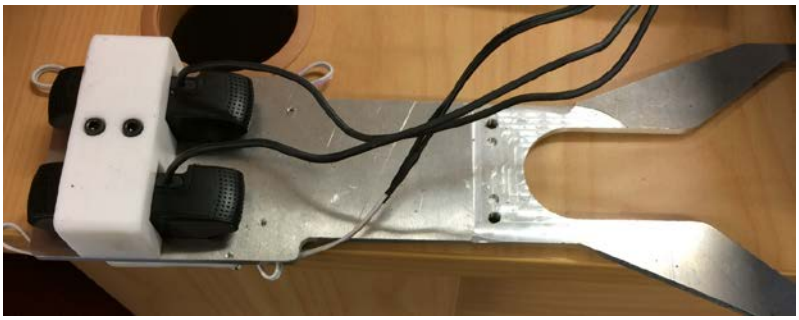

Figure 4.8 Completed assembly of the close-view vision rig, removed from the torch.

The calibration process for this test rig was simplified due to observations in the previous test rig's development. Complete details are presented in Appendix B for the interested reader. However, a rectangle with slots at known positions was used for the calibration process, this rectangle is shown in Figure 4.9. The calibration process used the locations of the slots to estimate the scaling factors and other calibration parameters.

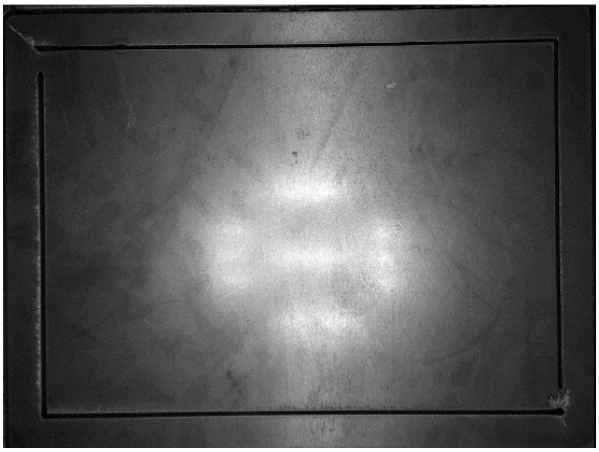

Figure 4.9 The fiducial calibration plate for the close-view vision rig.

Calibration results

Table 4.2 shows the values obtained through this process and used throughout this work. The values are all intuitively acceptable. I.e. the X and Y offset values are similar to what would be expected from the SolidWorks™ design and the camera rotation value is small and non-zero. They have also been validated through the rectification of the images taken. The fisheye correction has been neglected with minimal impact.

Table 4.2: The calibration parameters used for the close-view vision rig throughout the work.

Calibration Parameter	Symbol	Value
pixels per mm (X-direction)	$pmmx_0$	$4.70mm^{-1}$
pixels per mm (Y- direction)	pmy_0	$4.70mm^{-1}$
pixels per mm per mm height (X)	pmx_h	$0.03mm^{-1}$
pixels per mm per mm height (Y)	pmy_h	$0.03mm^{-1}$
X offset	s_x	194.17mm
Y offset	s_y	17.35mm
camera rotation	θ_c	-0.85^0

4.2.2.1 Test cut template

Overview

A test cut was designed to develop, assess and validate the metrology algorithm. Further, its evaluation should provide empirical data. It was designed with the following features:

1. Several straight edges for ease of measurement.
2. Spacious part allocation for ease of edge finding.
3. Cut in various orientations to the gantry system for investigation into systematic errors.
4. Curves of varying radii for investigation into relationship with kerf width.

Straight edges facilitate assessment of the algorithm accuracy. The quickest and easiest method to measure kerf width is to measure the dimensions of the cut parts and the dimensions of the left-over plate; and use that to estimate kerf width. Measurement of curves is relatively complex with a caliper, so accuracy can be assessed with straight edges and inferred to curves. Separating the parts on the plate will make it easier to detect edges as there will be a larger margin of error for where to look for the part's edge without encountering a different edge. Once the algorithm has been refined this problem can be dealt with, however for initial development it is unnecessary.

Various pieces of literature have ascribed systematic variation to the PAC process without identifying a reason. Further, communications with Kerf Ltd. have suggested that the torch height control (THC) can become inaccurate as the torch passes over the support slats of the bed. Therefore, cuts in perpendicular directions will assure that enough data is obtained to investigate cuts parallel to slats, perpendicular to slats, and in every direction. Finally, further communications with Kerf have suggested the kerf width could be affected by radius of curvature of the cut. The designed test cut template needs to facilitate this investigation.

Development

The first iteration of the test cut is shown in Figure 4.10. It was found that the 20mm wide parts were too thin, and the heat into the plate caused them to warp. Further, the long thin parts were no longer supported by the bed once removed from the frame, and thus could not be photographed without effort. It was also decided that the cut would waste less material and be easier to handle if it was kept within a 550 x 550mm square rather than 800 x 800mm.

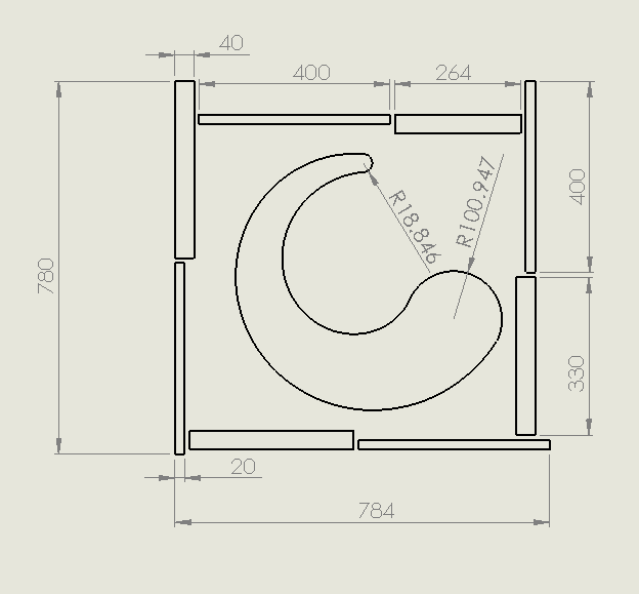

Figure 4.10 First iteration of test cut (dimensions in millimetres).

Final test cut template

The final design took these problems into account and is shown in Figure 4.11. The template has fillets on the corners of the rectangular cuts with varying radii from 1 – 24mm, and 2 Euler curves.

Aside from already mentioned improvements, this design also provided more radius data. The development, assessment and validation of the algorithm were completed using this template.

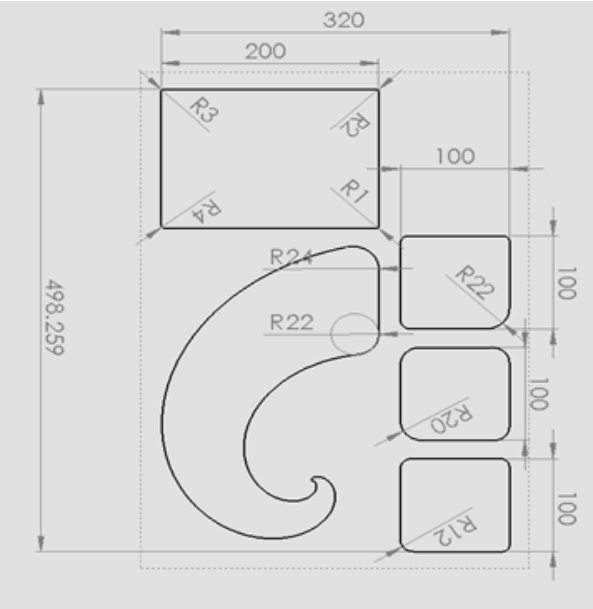

Figure 4.11 Final iteration of test cut (dimensions in millimetres).

4.2.3 Algorithm development

4.2.3.1 Algorithm concept

The goal of the algorithm is to be able to assess the accuracy of any 2D part. No good way of achieving this has been presented in the literature. However, it seems clear that the basis for comparison is the G-Code. The G-Code provides a set of edge points that the cut piece needs to match. To achieve this the G-Code is parsed and segmented into separate parts.

Once an ideal set of edge points was obtained, the algorithm needed an actual set of edge points to compare these to. Acquiring and matching these edge points is one of the largest problems that the literature deals with. The approach this algorithm employed was to use the ideal edge points, and the calibration data to predict the location of the edge in its field of vision. Initially, all edge points were obtained from their predicted location information, however this did not perform well at corners. It was then modified to use the predicted values to find the edge, but then to follow the edge once it had been located.

Once a set of images had been obtained, and a set of edge points located, sense had to be made of these. The approach chosen for this algorithm was to translate from the image reference frame back into the G-Code reference frame. This transformation could be reasonably accurately performed based off the calibration parameters. Therefore, a list of edge points that represented a part was generated from the images taken of that part. Initially it was left at that, however, the variation in point density was eventually removed so that an evenly spaced set of edge points was obtained.

The next goal was to compare the edge points acquired to the ideal set of edge points. However, these were still quite far away, so a further transformation was undertaken. This transformation shifted the edge coordinates in X and Y, as well as rotating them about a point to align it with the ideal edge points as closely as possible. This was accomplished using a least squares method simplex regression. The specifics of the regression changed many times, but eventually resulted in a fast, reproducible way to align the edge points appropriately.

Finally, the ideal edge points and actual edge points could be compared. The approach used was to iterate through observed edge points and calculate the minimum distance to the ideal edge points. This error could then be allocated to the part as a vector. This vector conceptually had a

magnitude of the size of the error, and a direction indicating whether it had been inside or outside of where it should be. Additionally, the average error could be used and reported, as well as variation around the edge for various parameters. This would provide various high-quality data for examining the kerf width.

4.2.3.2 Final algorithm

The final version of the algorithm was presented at the 2017 M2VIP conference (Flemmer, 2017b) and is presented below. Additionally, comments are made regarding the development process of the algorithm and potential improvements from this point.

1. The cutting instructions (G-Code) for the PAC system are first interpreted by the algorithm to generate an ideal set of edge points with a resolution of 0.1mm around the cut path (Figure 4.12). This path is then offset in both directions perpendicular to the cut path by half a kerf width, generating a first guess for the location of the cut edges.

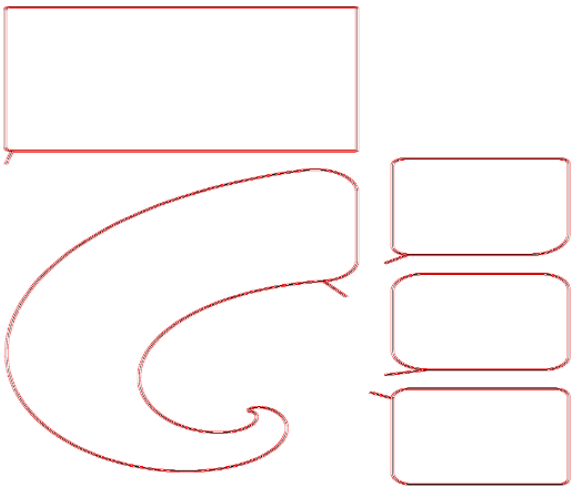

Figure 4.12 Ideal edge points obtained from parsing G-Code.

One unexpected short coming is that the cut path from the G-Code results in the traversal of the same points multiple times (i.e. redundancy). Two examples of this are firstly, on the lead in and lead out of a cut, much of the material in the lead out has already been removed. Secondly, as the torch corners, the path that has been offset inside will backtrack over itself. These pathing problems were solved iteratively. Firstly, problem locations were found in the middle path, i.e. sharp bends and the lead in/lead out indexes. For an inside corner, the overlap part of the cut was found by walking along the edge points forwards and backwards, until 2 points were found that were suitably close. The intermediate points were then replaced with this location. For an outside corner, edge points were generated so that the arc traversed was smooth and had enough points. The lead in and lead out were covered with a similar method, the overlap point was found, but this time the points of the lead in and lead out were also discarded as they do not result in information that describes the part.

2. A desired set of image locations is produced with the requirement that all edge points are observed, and that adjacent images overlap by approximately 50%. For this camera set up, images were taken every 10mm around the cut path (Figure 4.13). Theoretically this could be accomplished in real time, with the observation system tracking the position and taking an image when it is either: suitably close to a desired

location or observing new edge points. For this research the images were taken after the cut due to limitations in acquiring the position of the torch head in real time.

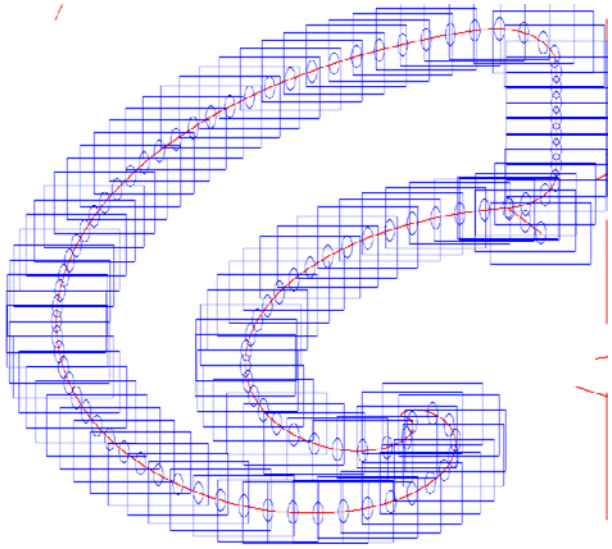

Figure 4.13 Example image showing image locations around a part.

During the development of the algorithm there were numerous problems resulting from not identifying the rotation parameter of the camera rig correctly. Some of the error associated from this was attributed to fisheye and skew distortion. Therefore, this small overlapping size was used. Conceptually there are other advantages to it, such as overlap between the 2 cameras for height sensing.

3. For each image, acquire the relevant edge points. A 200-pixel square window was selected in the centre of the image to acquire edge points from. The purpose of this was to limit the effect of lens fish eye distortion and skew distortion. The edge detection process is:

a) Firstly, edge point's locations are estimated by transforming the relevant ideal edge points from the G-Code reference frame into the image reference frame.

$$i_{estimated} = (x_n - x_t + x_c) * (pm_0 + pm_h * h) \quad (4.1)$$

$$j_{estimated} = (y_n - y_t + y_c) * (pm_0 + pm_h * h) \quad (4.2)$$

$i, j_{estimated}$ are the estimates for the location in the image. $x, y_{n,t,c}$ are the values of the n^{th} ideal edge point, location of the torch head for the image, and the camera offset respectively.

b) Next, 2 adjacent ideal edge points are used to calculate a traverse angle perpendicular to the cut direction. A set of grey levels is then obtained along a traverse line that intersects the theoretical cut edge at the calculated traverse angle. Each grey level is the average of 5 adjacent pixel values in a line perpendicular to the traverse angle and centred on the traverse line.

c) The resulting grey level profile (Figure 4.14) is then searched for the location of the first edge profile. The grey circles are a moving 5-point average of the original grey level profile (black circles). Both are used to locate the edge to filter against noise.

d) Ten points are found, and then the profile of the points is assessed to make sure they are consistent with an edge. If this is the case, then subsequent estimates of edge point locations are based on previous points, and the edge is followed until

it leaves the window. Once the edge points leave the window, the algorithm checks that enough data points have been returned. If either the initial 10 points were too varied, or not enough points were found before the edge could not be followed, then another 10 points are estimated from the G-Code and the process continues.

Figure 4.14 shows an example grey level profile. This profile is the average of 5 perpendicular points to the path that is constructed to be perpendicular to the edge. In the figure above the dark circles represent the grey level that is the average of the 5 perpendicular points, and the black circles represent the 5-point moving average. The grey levels have been normalized from 0 – 255. Figure 4.15 show an example of the resulting edge follower.

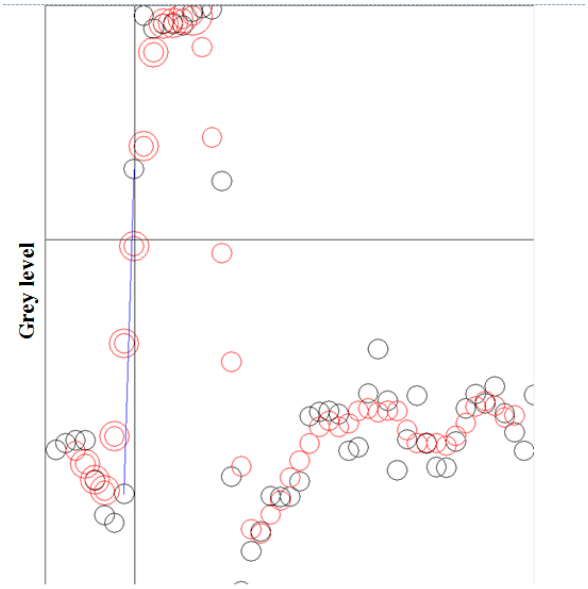

Figure 4.14: Example grey level profile.

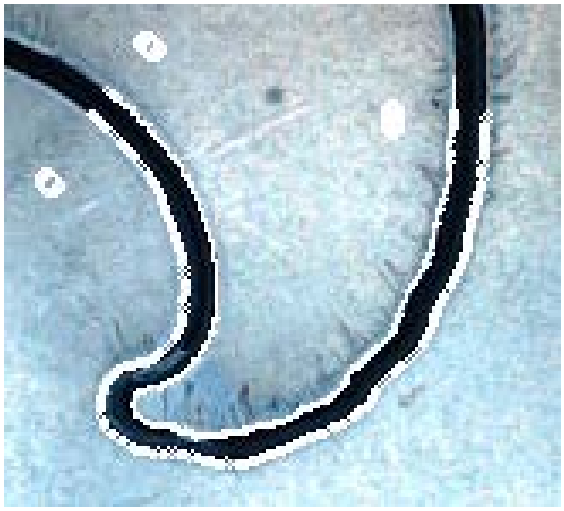

Figure 4.15 example of edge following showing inner and outer edges and start locations.

Initially, only the edge points on the inner cut piece were found. It was assumed that the cut would be symmetrical about the torch path. This assumption could reduce computational load and improve the calculation time. However, after testing and further development it was found that the performance and accuracy of the algorithm was significantly improved by accounting for both inner and outer edges.

4. The acquired edge points are next transformed into the G-Code's frame of reference from the image by:
   a) Firstly, rotating the acquired edge points about the centre of the image to account for camera rotation in the camera rig. Camera rotation for this rig was obtained during calibration (Table 4.2).
   b) Next the edge coordinates were scaled to convert from the pixel scale of the image frame to the mm scale of the G-Code frame. The scaling factor calculated for both axes (X and Y) is calculated by:

$$pixels\ per\ mm = pm_0 + \delta z * pmh \tag{4.3}$$

   Where pm_0 and pm_h were found during calibration and δz is the difference in Z height between the calibration height, and the image acquisition height.
   c) Then the edge coordinates are translated to account for the position of the plasma torch, and the X and Y offset of the camera in the rig. Again, these values were obtained during calibration.
5. Once all edge points have been acquired for a part, they are sorted so that the edge points are ordered, and redundant edge points are removed to maintain an even edge point density around the edge.

A full set of edge points is found for each image taken. Figure 4.13 (above) shows the image locations, and these image locations result in more points being found as the cut goes around a corner. Figure 4.17 shows 3 images' edge points and the overlap between them. The edge points are used to calculate the transformation required to align with the ideal edge coordinates. In order for the corners not to wind up with undue weighting, the edge point density is kept uniform around the edge by removing redundant edge points.

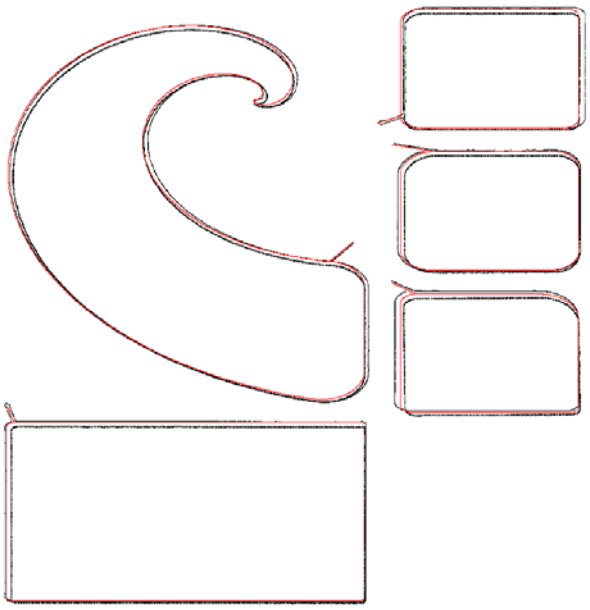

Figure 4.16: The edge points after transformation in black plotted over the centre location of the torch in red.

This is done by starting with the first edge point and finding the edge point closest to 0.2mm away, with an appropriate trajectory (i.e. not behind the path). Once a point is selected, nearby points are averaged with it. Finally, this point is stored, and the process is repeated from this new point. Some errors can arise due to following the path to a noisy point that happens to lie the right distance away. To compensate for this the algorithm can back track a few points if it gets stuck

and try again from a different starting point. It is also able to relax the angle threshold it must maintain to find new points if necessary.

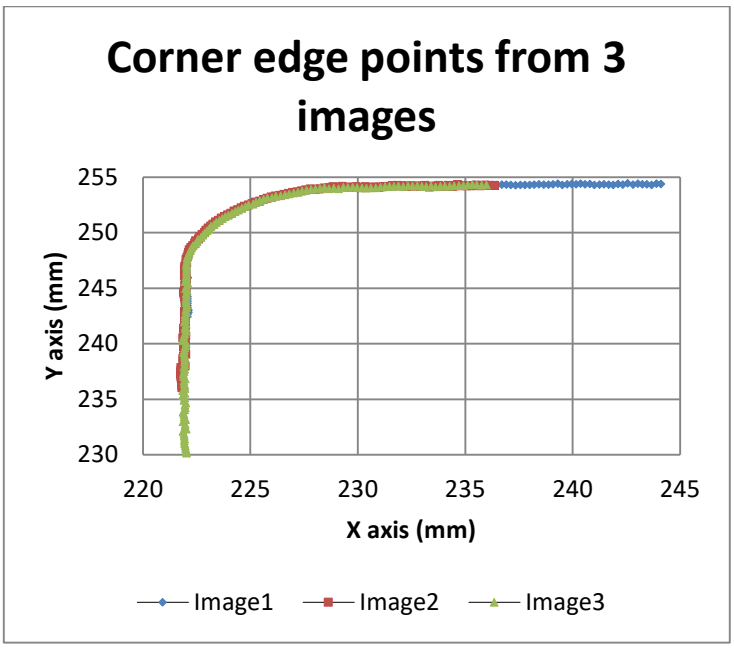

Figure 4.17 Edge points from 3 images demonstrating the image overlap around a corner.

6. Then a further transformation is applied to the edge points (Figure 4.18). This transformation accounts for movements of the cut piece after being severed from the metal. The points are rotated about the centre of the acquired edge points, and transformed in X and Y. The values for this transformation are estimated with a simplex regression. This minimizes the error function, calculated as the sum of squares of the distance between ideal edge points and acquired edge points.

The best transformation is calculated numerically, which leaves it susceptible to getting stuck in local minimum and not converging. However various steps are taken to minimize this possibility. Firstly, the step size of the regression is reset every hundred iterations to allow it to step over local minima. Secondly, the rough transformation performed from the calibration parameters in step 4 is used as a good start for the regression. Throughout the development the regression's objective function changed quite a lot. The two main options were setting the error for each point as the distance to the centre path, or the distance to the appropriate offset path. In the end it was decided to use the centre path, no advantage was found between the two, and using the centre path was the less computationally demanding of the two options.

At one point the kerf width was used as another variable to be regressed for. This over constrained the problem however, and the regression was able to achieve very low errors with infeasible kerf widths.

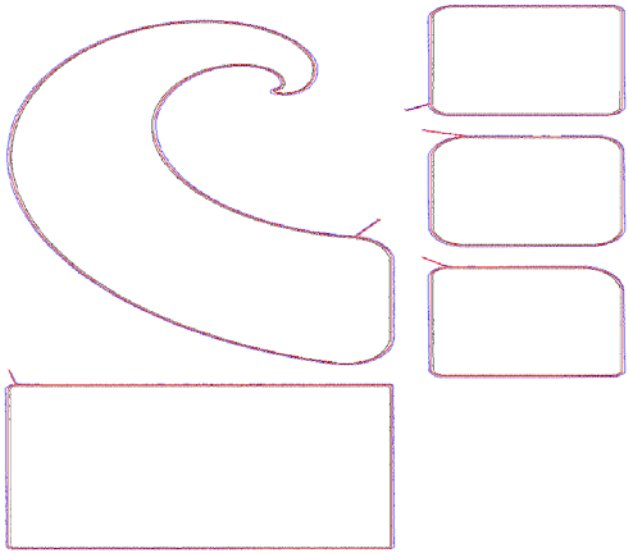

Figure 4.18 Edge points after transformation (blue) plotted over the path centre (red).

7. Finally, the kerf is calculated by finding the shortest distance between the inner edge points and a line between the closest outer edge points. The kerf width is calculated around the cut piece and the average is returned as the part's kerf width.

This calculation also changed a lot to reflect changes in the other stages. For example, when only the inside edge was found, the error was defined as twice the distance from the edge point to the torch path. However, on investigation of cut symmetry this was found to be less accurate than finding both edge points and then calculating the smallest perpendicular distance between the two.

4.2.4 Experimental plan

An experiment was designed with three objectives. Firstly, to test and validate the proposed algorithm. Secondly, to acquire data with which to develop an empirical model relating kerf width to cut speed and material thickness. Finally, it would validate this as a method for future empirical work, which is one of the gaps identified in the literature.

4.2.4.1 Equipment and materials

A CNC PAC system with a Hypertherm Powermax45 power supply was used for the experimental work. This PAC system uses a 3-axis gantry. The machine can either be operated with automatic torch height control (THC) where the voltage of the arc is maintained by raising and lowering the torch, or the torch height can be controlled manually. In this mode the torch is lowered until it contacts the plate, which is determined with a force sensor. It is then raised to the desired height and this is maintained. The advantage of THC is that the system can account for the gantry not being level, and for the plate being warped. However, there have been problems with the THC on this system so manual control was used.

The developed vision rig was mounted on the torch 103mm above the cut bed (Figure 4.19). Mild steel was selected as the material to cut. The reason for this is that it is cheap, easily available and the results would be comparable with those reported in the literature. Steel at thickness of 3 and 8mm was used for the test.

Figure 4.19 Image of the PAC system used for experimental work with the vision rig mounted.

4.2.4.2 Procedure

The experiment was performed twice on the 3mm-thick steel plate, at which point the procedure was evaluated and various changes were made. It was then performed once more on the 3mm plate, and twice on 8mm steel plate. The replication allowed observation to check that the changes to the algorithm and data collection process had not invalidated the data from the first 2 tests.

For each test, the plate was clamped to the bed. This removed plate warp as a factor and kept the cut frame stationary between cutting the parts and taking the images. The test cut was done, and then the head was moved with a set of G-Code to position the torch above the plate as outlined in the algorithm. Images were taken and stored, and the data analysis was performed with them. The cut parameters chosen were from the Dynatorch operating manual and are shown in Table 4.3. The 3mm-thick cuts all had a feed rate of 2800mm/min to assess the variation in the algorithm results. Theoretically the same cutting parameters for the same material and plate thickness should result in the same kerf width. Discrepancies in the surface of the plate however could cause some differences in the results obtained through the vision-based measurement system. Having 3 replicates of the 3mm thickness plate allows validation of the method and algorithm. Unfortunately, the PAC system malfunctioned on the fifth part of test 3, however the data already obtained was deemed sufficient for use as a replicate.

The settings for the 8mm-thick material were again taken from the manual as well as from some feasibility testing. They are set to the highest recommended cut speed and the lowest recommended cut speed. This allows observations of differing kerf widths. Further, there is potential that radius of curvature could affect the kerf width. This effect may be more pronounced at different cut speeds, so the cut speed variation investigates that.

Table 4.3: Cutting parameters used for the 5 test runs.

Trial #	Thickness	Cut Parameter	Setting
1 - 3	3mm	Cut Speed	2800mm/min
		Voltage	115V
		Current	45A
		Torch Height	3.8mm
4	8mm	Cut Speed	400mm/min
		Voltage	116V
		Current	45A
		Torch Height	3.8mm
5	8mm	Cut Speed	1000mm/min
		Voltage	116V
		Current	45A
		Torch Height	3.8mm

Data processing was undertaken in parallel with the experimental plan. This was to evaluate the appropriateness of the experimental plan. Overall the experimental plan was quite sound, but it relied on correctly calibrated parameters. The camera rotation parameter was not perfectly optimized at the start of the process, and Figure 4.20 below shows the systematic error introduced. It was not a large error, of the order of 0.1mm introduced over the length of the image window (20mm). However, tuning of this parameter reduced the systematic error by a further 0.05mm and removed the visual indication that systematic error was being introduced.

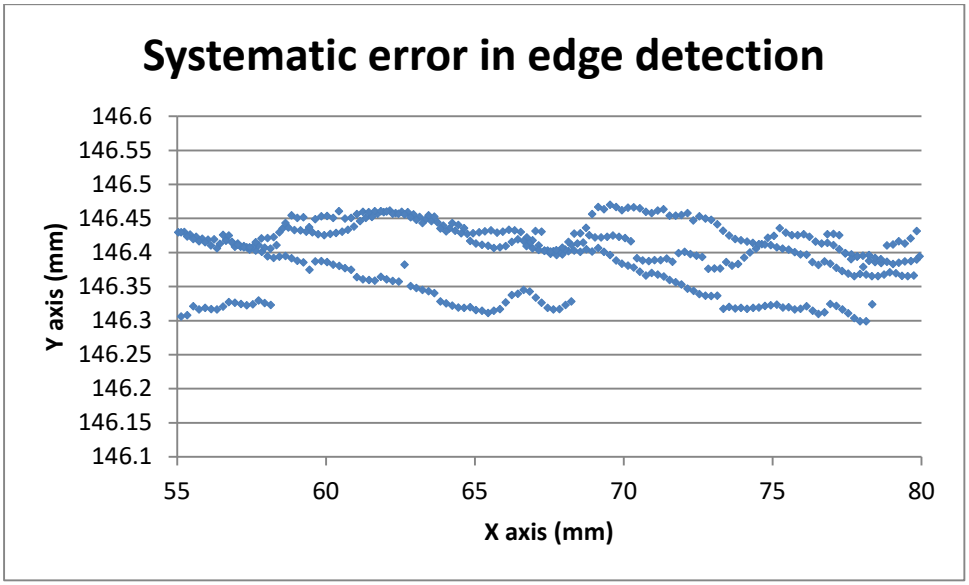

Figure 4.20 Segment of edge points along a straight edge demonstrating systematic error due to improperly calibrated camera rotation.

4.2.5 Results

4.2.5.1 Matched points

Figure 4.21(a) shows the edge points from test 1 part 2 after the algorithm has processed them. The ideal torch path is plotted in red and the transformed data points are shown on the inside

(black) and outside (blue) of this path. The edge points plotted are matched appropriately and demonstrate that the errors are too small to be perceived at this scale.

Figure 4.21(b) shows a magnified error plot for this part. The error is calculated as the deviation from the average kerf width, which is calculated for each edge point as described in the algorithm section. The error bars in red have been overlaid with the ideal torch path in black. The error bars are vectors where the magnitude is 50 times the difference of the instantaneous kerf width minus the sum of the regressed values for inner and outer kerf width. The direction of the vector is perpendicular to the torch path and inwards if the kerf width is greater than the average (i.e. the part is undercut) and outwards if the kerf width is less than the average (i.e. the part is overcut).The error bars have been magnified by a factor of 50mm in Figure 4.21(b) and the blue cross in the centre indicates the scale of 1mm in the X and Y directions.

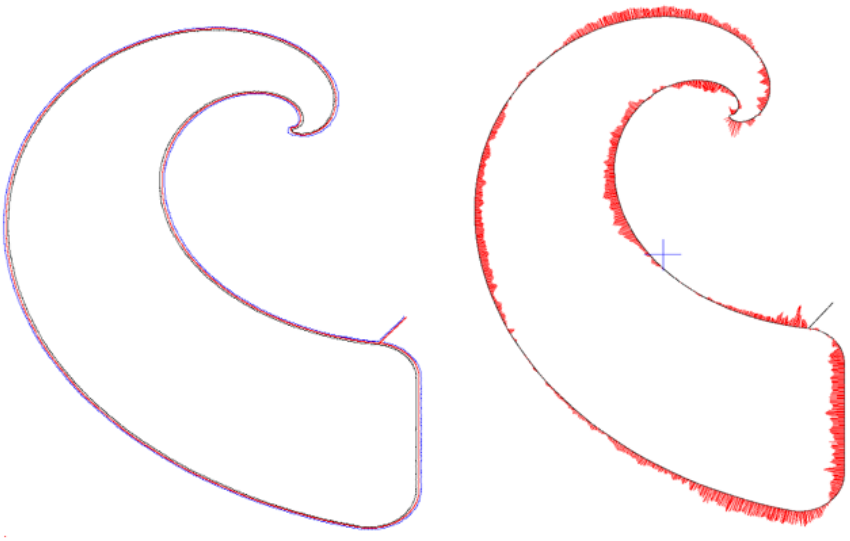

Figure 4.21 Presentation of error analysis from vision algorithm where (a) (left image) shows the ideal torch path as well as the inside and outside edge points sets in blue and black, and (b) (right image) shows the torch path in black with error bars in red overlaid. The blue cross in the centre of B represents a scale of 1mm in the X and Y directions for the error bars.

The error bars have also been smoothed with a 5-point moving average. Averaging seems appropriate for several reasons. Firstly, Figure 4.21 demonstrates that the averaged kerf width measurement reported is the average of thousands of individual measurements. Secondly, adjacent edge points are incapable of deviating drastically due to the process, so this increases the accuracy of any measurement.

4.2.5.2 Summary of algorithm results

A summary of the algorithm results for test cut 5 are presented in Table 4.4. Both the caliper measurement and the vision measurements of kerf width (KW) are shown for each part. The standard deviation of measurements from the average measured kerf width based on vision measurement is also reported. A more detailed set of results and the corresponding summary is presented in Appendix B. This includes error graphs for the parts in each of the tests as well as a table summarizing the kerf width measurements made.

Table 4.4: Example set of measurements using computer vision made on the 5 parts of test cut 5.

Test #	Part #	KW (Caliper) (mm)	KW (Vision) (mm)	σ (mm)
5	1	1.76	1.90	0.15
	2	1.82	1.73	0.22
	3	1.84	1.87	0.12
	4	1.67	1.80	0.21
	5	1.7	1.83	0.15

Table 4.5 shows a summary of the kerf width (KW) measurements made across all 5 tests. The kerf widths for the first fifteen parts are averaged together and presented as the KW for tests 1 – 3. Test 4 is the mean of the 5 parts kerf width measurements from test 4, and test 5 is the mean of the kerf width of the 5 parts that made up test 5. The kerf width measurements for the calipers were made by measuring inside the kerf for the second part of each test and measuring the widths and heights of parts 1 through 4 and the heights and widths of the corresponding off cuts. The range for both measurement methods is also presented and represents the largest measurement made minus the smallest measurement made over the applicable data set.

Table 4.5: Kerf width (KW) measurements and range of measurements for the KW measured using both methods, Caliper (Cal) and Vision (Vis) across all tests.

Test #	KW(C) (mm)	Range(C) (mm)	KW (Vis) (mm)	Range (Vis) (mm)
1-3	1.76	0.23	1.75	0.14
4	1.88	0.22	1.92	0.21
5	1.76	0.17	1.83	0.17

Table 4.6 shows a break-down of the 2 components of the kerf width measurements made for test 1. It also shows the kerf width resulting from assuming kerf symmetry and the kerf width when measured from both edges. Finally, it presents an average of the kerf width measurements made using both methods, demonstrating the difference between the two and the impact that has on measurement.

Table 4.6: Table showing cut asymmetry. Test Number (T#), Part Number (P#), Kerf Width assuming symmetry (KW1), New Kerf Width method (KW2), Inner measurement (Inner), Outer Measurement (Outer).

T#	P#	KW1 (mm)	KW2 (mm)	Inner (mm)	Outer (mm)
1	1	1.90	1.67	0.95	0.72
	2	2.03	1.96	1.01	0.94
	3	2.25	1.92	1.13	0.80
	4	1.98	1.88	0.99	0.89
	5	1.92	1.80	0.96	0.84
Average		**2.02**	**1.85**		

4.2.6 Discussion and conclusions

4.2.6.1 Evaluation of results

This algorithm and experimental process has produced a large amount of measurement data. During the development and execution, the process changed somewhat. Once all the data

processing was completed the data from tests 1 and 2 could be compared with test 3. Test 3 was a replicate of tests 1 and 2 and Table 4.7 confirms that the measurements show very little deviation.

Table 4.7: Validation test comparing replicates 1 and 2 with 3.

Test #	Part #	Kerf Width (mm)	Test #	Part #	Kerf Width (mm)
1,2	1	1.70	3	1	1.74
	2	1.84		2	1.72
	3	1.80		3	1.69
	4	1.79		4	1.70
	5	1.74			
	average	**1.77**			**1.71**
	range	**0.14**			

The results displayed in the previous section demonstrate many high-quality measurements for the kerf width. A key limitation for empirically deriving the interaction effects of the numerous process parameters of plasma cutting is the large amount of combinations that have an effect. Much of the literature presents at most 1 to 4 measurements of kerf width for a cut piece. This approach yields thousands of kerf measurements in a relatively short amount of time. The process parameters can be adjusted in the G-Code at little effort to human operators. This results in savings from reducing the material required for the test, reducing the time taken to perform the tests, increasing the reliability of the results and decreasing the time spent on data collection and processing.

An additional benefit is that the range of testing can be expanded. Figure 4.21 demonstrates error analysis of a free form part. This is the first time this has been presented in the literature. This allows investigation of the impact of cut profile on kerf width and radius of curvature. Preliminary investigation does not suggest a strong correlation in these areas, however this method provides the ability to investigate none the less, and at no additional cost. Table 4.5 (section 4.2.5.2) shows that the performance of the caliper and vision systems agree with each other to 0.1mm within the results returned for a test. Further the caliper measurements had a larger measurement range than the vision system had, which suggests that the caliper method is more subjective.

Table 4.5 shows that for all 5 tests the caliper and visions method agreed with each other. The averages of the 2 methods were within 0.07mm of each other which is well within the target accuracy. Further, the range of the caliper measurements was about 15% larger than the range of the vision method which again confirms the reliability of the vision method. The average kerf width for tests 4 and 5 has also increased over the kerf widths for tests 1 through 3, which is expected because as the thicknesses increases, more heat needs to go into the plate to remove it, which causes a wider kerf. Test 4 also has a wider kerf width than kerf 5 because of the slower feed rate. As feed rate decreases the amount of heat going into the plate increases, melting more material and resulting in a wider kerf width, which is again confirmed in these measurements.

The final summary, Table 4.6 shows why it is necessary to measure both sides of the kerf. The inner kerf width measured by the vision method is reliably 10 -15% bigger than the outer kerf width. This means that kerf width estimations purely from the inner half of the kerf would be between 20 and 30% too large. This observation confirms observations in the literature about kerf asymmetry. It is also a measure that traditional caliper measurement struggles to perform; which is another validation of the vision measurement method.

The magnified error plot allows examination for systematic error in cutting. Over the 5 tests that were completed, a few trends are evident. The machine seems to significantly undercut along the Y axis and over cut along the X axis. This occurred in 60% of the cut pieces. Another trend is that there is often a large error spike around the lead in point. In half of the cut parts the largest point of deviation was close to the lead in, often appearing as an undercut. In general, error along the vertical cuts tended to be less skewed than error along the horizontal cuts. Often the horizontal cuts would start as an undercut and become over cut or ideal over the length of the cut, whilst the error along the vertical cuts tended to be an overcut for the entire length.

The final trend in error is that the parts often have a similar error distribution. For example, part 4 in 80% of the tests has a large spike in over cut error at the lead in which trends to under-cut over the length of a side. Each side has this trend of over cut at the first end becoming more undercut at the far end traversing clockwise around the part. Meanwhile part 3 does not exhibit skewed cutting in any of the tests. Part 1 also has predominantly skewed error across all 5 tests. One goal of the research was to investigate the effect of radius of curvature on the magnitude of the error. No trend is evident in the part 2 measurements, which indicates that radius of curvature at different speeds and thicknesses do not influence the kerf width. The error at the tip of the curve is quite sporadic, but that has been attributed to jittering in the torch movement as opposed to kerf width.

4.2.6.2 Comparison to goals that were set

The results from this experiment show that all the goals set for the close view vision system were achieved.

- The measurements made using this method and traditional caliper measurements are within 0.1mm of each other.
- The range of measurements made using the vision method is smaller than the range of measurements made with the caliper.
- A substantial amount of high-quality data was returned as a result of this algorithm.
- The algorithm has been proven robust by application to multiple tests and test cuts.

The measurements made using this method and traditional caliper measurements agree to within 0.1mm for all cut pieces. This means that calipers offer no advantage in terms of accuracy. Further the range of measurements returned was slightly larger for the caliper (0.22mm) compared to the vision method (0.16mm). This is because the kerf surface is not smooth due to the presence of drag lines and has a varying kerf angle. Both factors make measurements using a caliper relatively subjective. The vision method makes measurements at the intersection of the top plane and kerf and does so with greater repeatability. This improvement results in higher quality data, and more confidence in conclusions drawn from such data.

The aim of this investigation was to develop a system that could produce a large amount of high-quality kerf width data that could be used for the investigation of the relationship between kerf width and cut speed and material thickness. This was also successfully completed. The system was able to provide kerf measurements at 0.2mm increments around the periphery of a cut piece. For the simple 100-millimeter square parts this resulted in approximately 2000 measurements, and rather more for parts 1 and 2. These measurements were taken for cut speeds of 400mm/min, 800mm/min and 2800mm/min, as well as at thicknesses of 3 and 8mm. Therefore, the efficacy of data acquisition has been proven superior to the caliper method with more data being acquired per test, and tests requiring less time and effort to complete.

Finally, the goal of providing a generalized solution has been met. Over the course of the development of the algorithm, it was applied to several different sets of G-Code, and 3 iterations of the test cut. The data acquisition process was demonstrated for all of these. This has included demonstration of the ability to identify separate parts in nested G-Code and acquire images to check the edges. These edges have included closely spaced parts, and sharp corners. Some testing has been done on examining features within a part. This was completed successfully for the simple

case of rectangles being cut out of a larger rectangle. However, this aspect could use further investigation to validate the ability to reliably identify features of a part and acquire the necessary images.

4.2.7 Conclusions

This work has developed a new tool that is useful for research into the PAC phenomenology as well as the field of metrology in general. The tool takes the form of 2 webcams on a test rig and an algorithm to process the data. The test rig attaches to the PAC torch and is sturdy and easy to mount in a replicable fashion. The algorithm parses G-Code to interpret parts and their ideal edge point locations. It requests pictures at locations that span the edge and analyses these to evaluate the kerf width around the periphery of the part. Both parts of the tool were completed successfully. A system block diagram of the hardware and software elements, and their interactions, is shown in Figure 4.22.

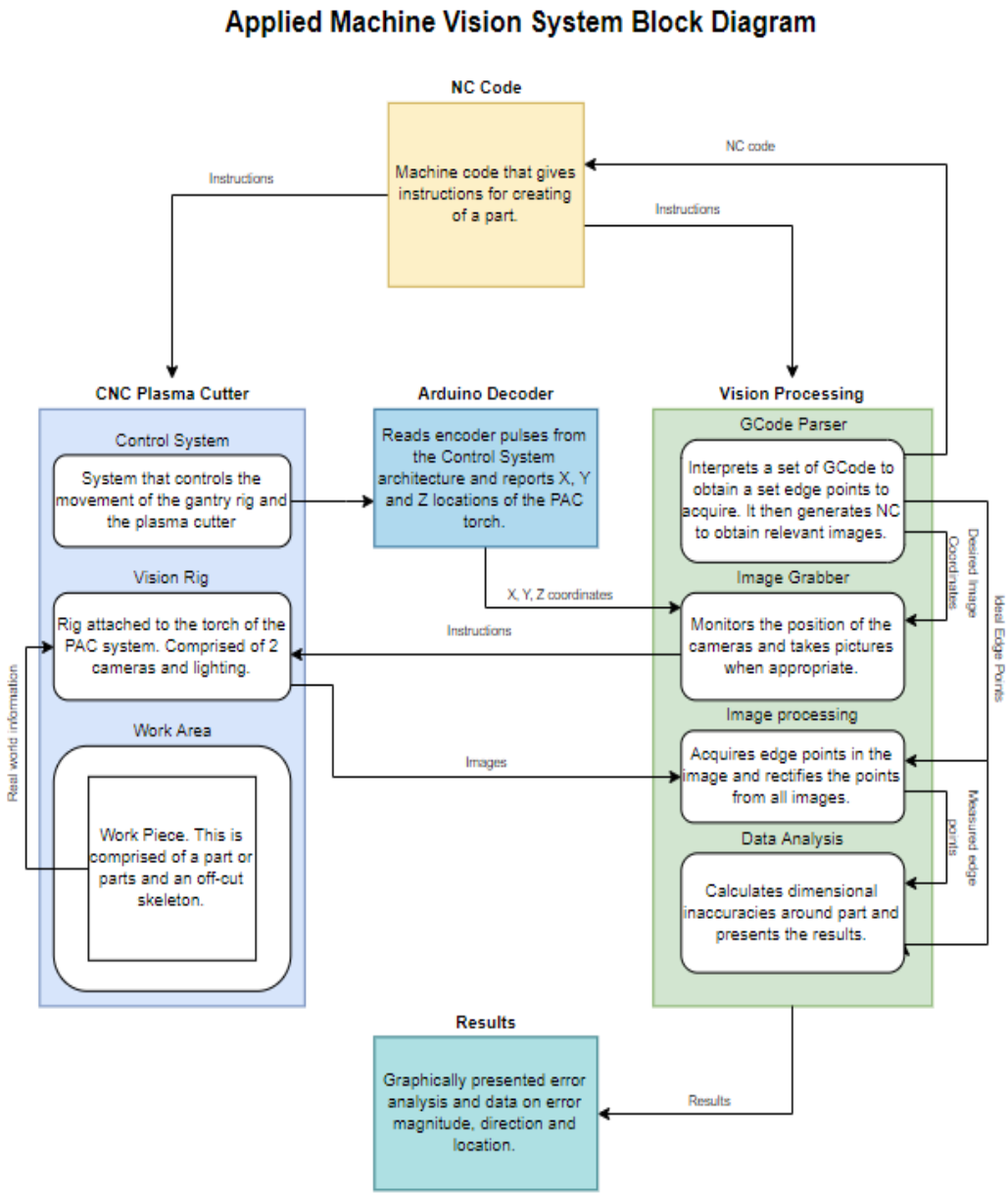

Figure 4.22: System block diagram of system configuration including hardware and software components, and their interactions.

The tool was validated on test cuts performed at feed rates of 400, 1000 and 2800mm/min and thicknesses of 3 and 8mm-thick mild steel plate. Five test cuts were performed in total. The research has provided empirical data relating cut speed and material thickness to kerf width, which varied between 1.67 and 2.02mm. The tool has been demonstrated to outperform caliper measurement in accuracy, repeatability, ease of use and amount of data provided.

The way this data is presented is unique and lends itself to a feedback implementation. Systematic errors were observed throughout the test cuts such as similar error profiles around the same parts in different tests. This method allows investigation into systematic errors present in the cutting process to identify their causes. One such systematic error investigated was the presence of error due to radius of curvature of the cut path. This was investigated by measuring cuts with varying radii of curvature. No correlation was observed between radius of curvature and the kerf width.

The largest deviation found across the 25 cut parts was approximately 0.3mm.

4.2.8 Recommendations, limitations and future work

The development of the close-view test rig has been completed with respect to the research. However, there are a few aspects that could be investigated in future work. Firstly, a real-time implementation of this algorithm could be industrially useful to the sponsoring company Kerf Ltd. Secondly, further empirical data would be obtained to further investigate the PAC process as well as future models predicting kerf width from process parameters.

4.2.8.1 Real time implementation

A real-time implementation of this algorithm is very achievable and of definite value. This was not accomplished during the research for a few reasons. Firstly, quadrature decoders were not available, and the time constraints of the project led to a work around solution being preferable. This solution was to use an Arduino to count the encoder pulses and report the position. Due to the processing requirements, the Arduino was only capable of reporting the position once movement stopped. This was sufficient for the development and investigation purposes but needs to be improved for a real-time implementation. Secondly, the control software for the PAC system was proprietary. This means that it was not able to be adjusted to communicate with the algorithm to request the torch head be moved to take images. Kerf Ltd. does have a working relationship with Dynatorch; however, the delay anticipated from adjusting the software precluded this option.

The benefits from a real time implementation are numerous. In the first instance, not needing a secondary operation to acquire images once the cutting is complete will save time and effort. Many of the image locations would be traversed during cutting operations and the images could be acquired then. Once a model relating the cut parameters to the kerf width is completed, or a model from the literature is selected, the results can be interpreted to tune the process parameters. Figure 4.23 illustrates how this task could be accomplished. This could make the PAC process, which is requires a skilled technician to operate efficiently, more user friendly and readily available to fabricators lacking the expertise. It can also provide real time tuning of the process parameters, which is only partially achievable by a skilled technician.

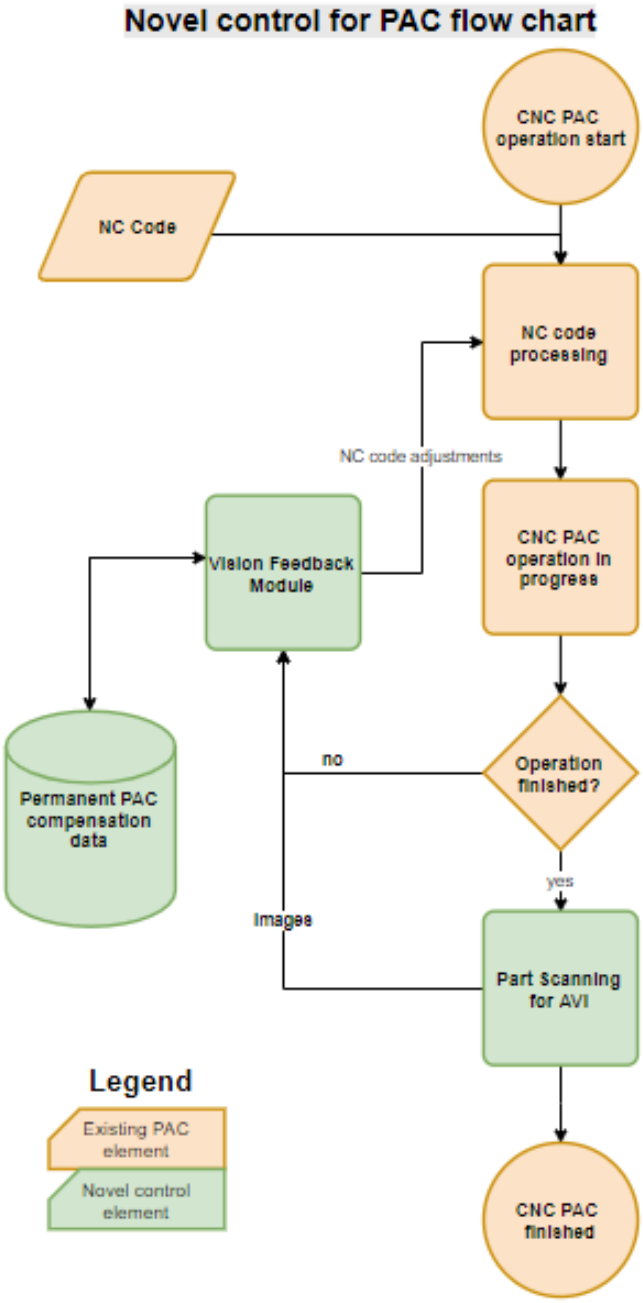

Figure 4.23 Flow chart depicting the potential for the algorithm to provide feedback and tune the PAC process.

Another application of real-time implementation is the capability for edge following. Currently there is large value in recycling offcuts of materials, either by fitting additional parts into an existing skeleton in an efficient way, or just to know the size of the wasted material to evaluate the efficiency of the nesting process. The edge detection algorithm developed in this research can easily be adjusted to be an edge following algorithm. With a real-time implementation the edge can be followed and G-Code can be constructed to produce such an offcut. This G-Code can then be used to evaluate the remaining material, or even reproduce the recycled skeleton, all of which is of value to Kerf Ltd. and other PAC system suppliers and users.

A final possibility lies in real-time implementation in conjunction with using the second camera for stereopsis. Torch height is known (both in the industry and in the literature) to be a very influential process parameter. Communications with Kerf Ltd. have suggested that the current

method of torch height control (sensing the arc voltage between the torch and the plate and raising and lowering the torch to maintain it at a set point) has shortcomings. This is because the slats of the gantry bed affect the voltage sensing and lead to inaccuracies. Height sensing using the stereopsis can be accurate to 0.1mm which is better than the 0.25mm reported by Kerf Ltd. for voltage sensing.

4.2.8.2 Further testing

The other avenue of future work is in research. The tool developed in this research has potential to advance the field of empirical research of PAC. This field is currently limited by the expense, in all forms, of data acquisition. Further testing can be done on various platforms to further investigate the process parameters of cut speed and material thickness on kerf width, as well as looking into voltage, torch height, arc current and many other factors that are known to impact the kerf formation. There is a common shortcoming in the literature that only a few parameters can be feasibly investigated, however the ease of implementation and the automation of process parameters can drastically increase the amount of interaction effects that can be investigated.

Investigation can also be done into using the second camera of the test rig. Initially, the aim was to use stereoscopic vision so that kerf angle could be calculated directly. This would again increase the amount of data obtained and would lead to large improvements in the empirical relations for kerf angle.

4.3 Feasibility study for height detection

4.3.1 Introduction

The investigation into height detection was identified as a potential area to investigate during the development of the vision rigs. It would have value in improvements over the height control offered by voltage height sensing and could lead to more appropriate process parameters being used consistently. Initially stereopsis was incorporated into the vision rig design to allow measurement of distance between observed points and the camera. This would improve real time control and allow an assessment of whether a part has rotated and left the XY plane (changed in height). This design aspect was therefore used for a feasibility study on height detection using stereopsis.

The concept of using stereopsis to calculate the height of the test rig is relatively straight forward. In the calibration stage of the close view test rig (section 0), a relationship for pixels per mm that accounted for variation in height was developed. This involved getting values for the initial pixels per mm at maximum height, and a relationship between change in height and change in pixels per mm ($ppmm_0, ppmm_h$). In order to use this to calculate height, the same point needs to be identified in both images. Then the pixel locations from the perspective of each camera frame, can be used to calculate the current scaling value of pm, and thus the height can be calculated.

The goals of this investigation are:

- To ascertain the feasibility of this method.
- To examine the accuracy of the method.

Theoretically this method just reverses the calibration process for determining the pixel per mm constants. However, this investigation aims to validate this process. Further it aims to quantify the precision of a vision-based method. The primary method for real time height detection used in the PAC industry currently uses voltage-based height sensing. Reportedly this performs to accuracies of about 0.25mm (Gray, 2014). Therefore, an estimation of the accuracy of the stereopsis-based height measurement is necessary to assess the practicability of this method.

The primary challenge anticipated in this method is identifying the same point in the 2 image spaces. Since the validity of this method depends on being able to compare the location of a point in 2 different camera frames, complications such as obfuscation of a point, and slightly different perspectives between the 2 frames could introduce some error and uncertainty. There is a further

challenge in comparing this method to the voltage sensing method. The voltage sensing method is probably less accurate but has a high sampling compared with a vision-based method. Therefore, it will be difficult to compare the two.

The anticipated deliverables from this investigation is firstly an analysis of the accuracy of the method and secondly an indication of the viability of the method. This will help direct the future work on PAC control and metrology testing.

4.3.2 Experimental design

An experiment was designed for this feasibility test that allowed the identification of the same point in two different frames of reference. The test rig developed in the 'close-view' section was reused for this experiment. For further information on the setup and calibration please refer to this section (section 4.2.2).

The location of this point precisely in both image frames is the primary challenge identified in this method. To simplify this as much as possible, a black piece of paper was placed on a white background with one visible in the images from both cameras. This gave two straight lines as the edge of the piece of paper, and an intersection point that was the corner. Figure 4.24 shows the piece of paper from both cameras' perspectives.

Thirty-three pairs of images were taken starting at a datum Z-position of 0mm (torch at maximum height). The first 14 consecutive image pairs were taken as the torch was lowered by 15mm from the datum. The next 19 consecutive image pairs were taken as the torch was raised to a Z-position of 4.32mm (4.32mm below the datum). This range of images provides a good range of height detection for the torch, as torch height for PAC typically varies between 2 and 10mm. It also provides a method to detect hysteresis in the process.

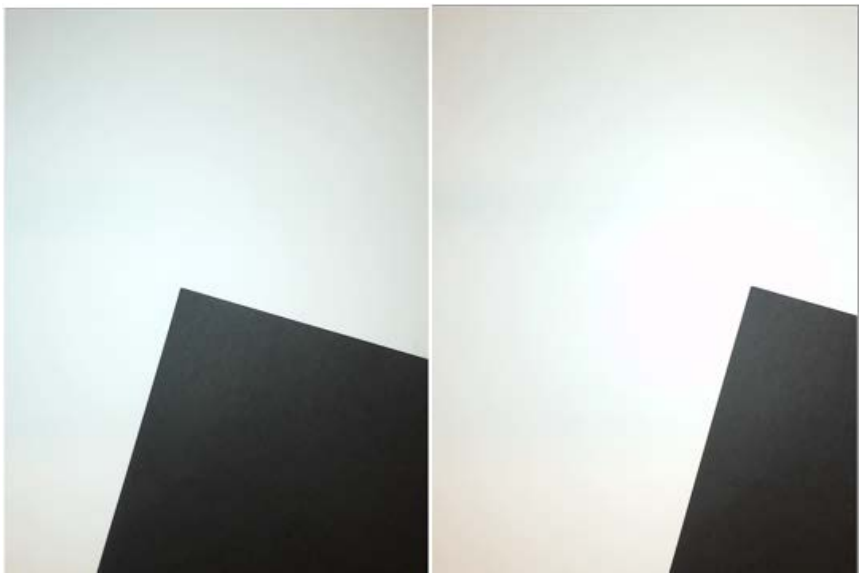

Figure 4.24 Sample image-pair showing images of black corner taken from camera 1 (left) and 2 (right).

The algorithm to calculate the height of the torch first identified the corner in each image. Figure 4.25 shows edge points being found in the image on both edges of the paper. A line of best fit is then placed through each set of data points, and the intersection of these lines is used as the common point. These points were found for each of the 33 image-pairs for varying torch height.

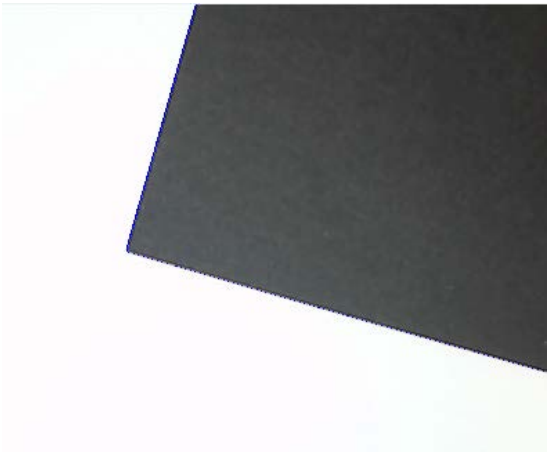

Figure 4.25 Edge points (blue dots) found on both edges of the black paper.

A relationship was derived between height and the pixel difference between the points identified in the two images. Conceptually, height is inversely proportional to the number of pixels between the point locations in the images. Further, the relationship between height and the scaling factor of pixels per mm was found to be linear. Therefore, the relationship can be expressed as

$$\frac{1}{h} = s(j_1 - j_2) + a \tag{4.4}$$

Or

$$h = \frac{s}{j_1 - j_2 + a} \tag{4.5}$$

Where *s* and *a* are the slope and intercept constants and have been set for convenience. j_1 and j_2 are the pixel location in the j-axis and *h* is the predicted height.

A simplex regression was then used to solve for the constants by minimizing the error function shown in equation 4.6. This calculated the sum of squares average for the 33 data points with the numerically solved constants (where subscripts 'm' and 'a' represent measured and actual).

$$regression\ error = \frac{\sqrt{\sum_i^{33}(h_m - h_a)^2}}{33} \tag{4.6}$$

4.3.3 Results

A full table of results is included in Appendix C. This includes the test number and the corresponding actual height, predicted height, location of the point in the j axis for camera 1, location of the point in the j axis for camera 2, the difference between the two locations, the error calculated as the difference between the predicted and actual height, and the error calculated as the square of the distance between predicted and actual height.

Figure 4.26 shows a plot of the actual height versus the difference between the locations of the point in the j axis for the two cameras. The data has been split into the data points taken for the torch descending, and for the torch ascending to show the effects of hysteresis on the results. Further, a line of best fit is included for both sets of data.

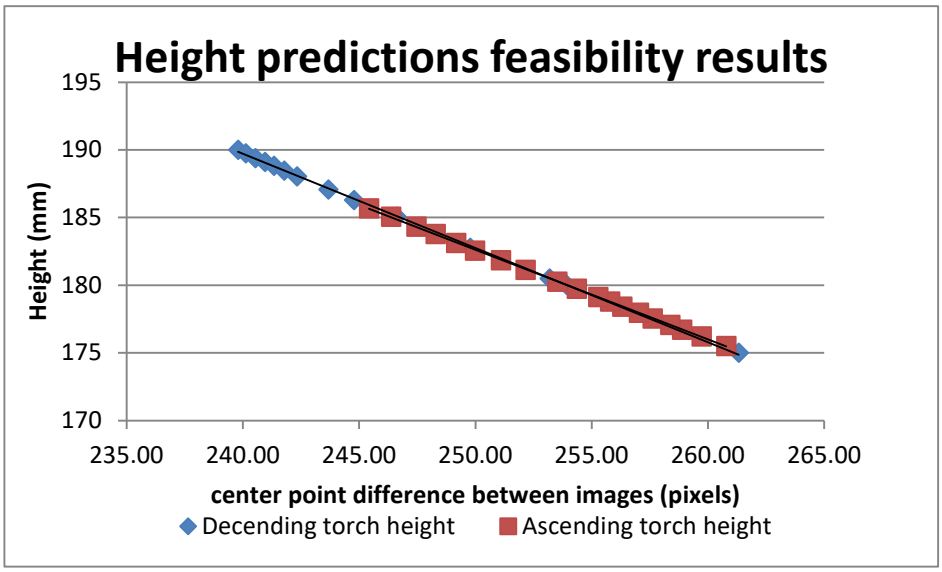

Figure 4.26 The results of the height detection feasibility investigation where the actual height in millimetres is plotted against the difference between the points in the two images in pixels.

Figure 4.27 presents a plot of the predicted height using equation 4.5 against the actual height the values used to make the prediction were measured at.

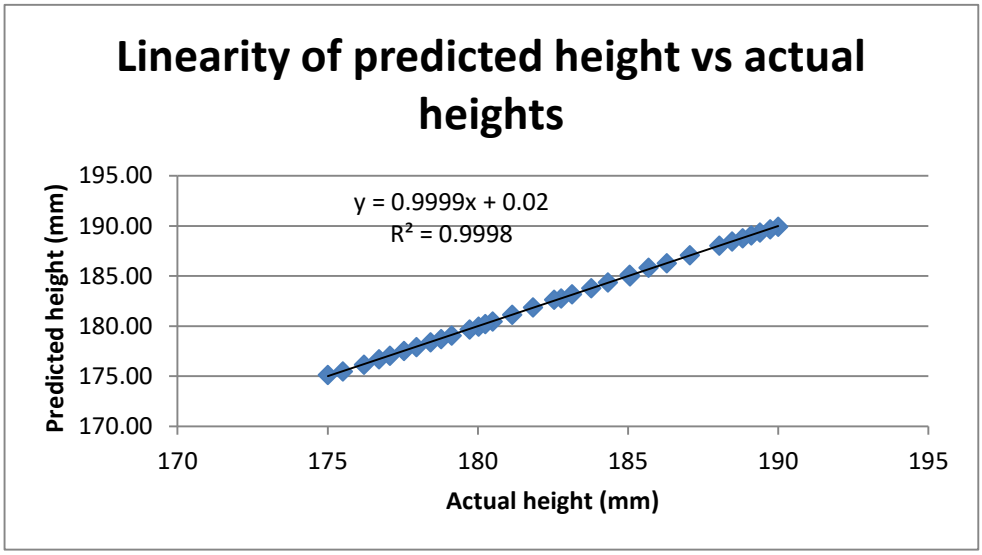

Figure 4.27 Plot of the predicted height in millimetres versus the actual height in millimetres.

4.3.4 Discussion

The relationship between the difference in pixels and the height was found to be linear. The best fit line for the data presented in Figure 4.27 had an R^2 value of greater than 0.99. The data was presented in descending and ascending groups to identify if hysteresis was a factor. A slight discrepancy was observed between the two sets of data; however, it appears to be small enough to be insignificant.

No trends are visible in the data range suggesting that there is no source of systematic error. The largest points of error were 0.15mm at a height of 175mm and 0.145 at a height of about 185mm. These error points are spaced over the range of the data. The average error for the 33 data points is 0.047mm, which is considerably more accurate than the voltage-based height sensing method (0.25mm).

The final plot of predicted height vs actual height is linear with a slope of almost 1, and an intercept of almost zero. The R^2 value for the data is 0.9998, which is very high and suggests that the predictions are not skewed over the data range. Whilst the stereopsis-based measurement of torch height is obviously accurate, it is based on a well-defined and artificially-created corner point in each image-pair. In reality there would be slight deviations in the location of a common point between the two images which would make this method less accurate. Another shortcoming is that the I-axis was disregarded. For the calculations shown here it could be neglected as the centre point was close to the centre of the I-axis in the image. However, in an application setting, this might not always be the case.

4.3.5 Conclusions

The goals set for this investigation were successfully met. The results show that a stereopsis-based method for estimating the height of the torch is a valid approach. A linear relationship was found between the deviation of the height of the torch, and the spacing between the common points in the two images. It was investigated for linearity over a 15-millimeter range of motion and at no point did the relationship appear to deviate from linear. This range was selected because it is slightly larger than a typical range of torch height positioning.

The method was found to be accurate at predicting torch height. A relationship was developed and used to predict the torch height based on the difference in location in the J-axes for the points in the two camera's frames of reference. The average accuracy was approximately 0.05mm, with the worst prediction having an error of 0.15mm. This is more accurate than the conventional voltage-based height sensing method (0.25mm).

4.3.6 Future work

There is large potential for future work in this area. The two main areas are investigations into:

- Height control of a PAC system based on stereoscopic vision.
- Metrology of a PAC system using stereoscopic vision.

Communications with Kerf Ltd. have highlighted height control as an important aspect of PAC; and this is supported in the literature. Current methods use voltage height sensing to account for deviations in the plate height. However, this is complicated due to voltage fluctuations across the gantry system due to support and grounding slats. Further, for 5 axis machining, the potential difference changes as the effective thickness of the material changes. Stereopsis based torch height detection can improve on these shortcomings. The next step in investigating this is to apply it to edge detection based off the G-Code to identify similar points between the two reference frames.

The second application is in metrology. Using stereopsis, the vision rig can perform 3D measurements. This can be useful in further empirical research as the top and bottom of the kerf can be identified, and the bevel angle can be estimated. It can also be used to improve the feedback provided by the system in the case of real time control.

4.4 Investigation of kerf angle

4.4.1 Introduction

The development of the AVI system for kerf width measurement identified the presence of kerf asymmetry and the necessity for a kerf angle investigation. This observation is also consistent with the literature. Therefore, the next part of the research aims to produce a model that predicts the shape of the kerf (kerf angle, kerf width) from feed rate, torch height, and material thickness. As such kerf angle was investigated empirically. Industrially kerf angle is of interest because it directly affects the amount of post processing required. The literature shows that there has been a lot of interest in kerf angle and that it is viewed as a complex phenomenon resulting from interactions between heat transfer and fluid dynamics. However, empirical literature on the kerf

angle is sparse, and the process has not been successfully modelled or described. With proper calibration of process parameters, PAC can perform to a class 2 level of accuracy according to the ISO standard on thermal cutting (ISO9013). However, this is rarely the case because of improper calibration arising from a lack of understanding of the process.

4.4.1.1 Goals

The goals of the kerf angle investigation are to:

- Develop an experiment to obtain empirical data relating kerf angle to the process parameters of torch height, cut speed and material thickness.
- Carry out the developed experiment and acquire a set of high-quality kerf angle data.
- Provide qualitative data for the asymmetry inherent in the PAC process.

This requires the development of a tool to obtain necessary measurements, and development of a test cut protocol that will provide a high ratio of accurate measurement data to time spent cutting. The close-view rig was used to obtain the measurements. This is because the development of the rig resulted in well-tuned edge finding algorithms, and a high level of proficiency with the tool. Therefore, the primary goal is to develop a test cut to use it.

Ideally this data will span multiple material thicknesses, cut speeds and torch heights. Further, this data should be presented in a way to promote an intuitive understanding of the relationship between the process parameters and kerf angle.

Kerf asymmetry has been observed in the literature but has yet to be quantified or explained. This investigation will provide both. This will provide value by providing a scale with which to view the effect of cut asymmetry on path planning and kerf modelling. Intuitively it is a process which is intertwined with the prediction of kerf angle, so both aspects will be investigated at the same time.

4.4.1.2 Challenges

This investigation has numerous challenges that need to be overcome. The primary challenge is to develop a process to investigate the phenomena as directly as possible. The more abstracted observations and measurements are the more potential for errors to become coupled with those observations. This principle has been applied to all the goals presented above.

The primary challenge in designing an experiment to obtain empirical data for kerf angle is the size of the kerf. A typical kerf width is about 1.8mm wide, which is too small to accurately investigate with calipers. Further, the kerf angle is of the order of 5 to 10 degrees, which means that it is mostly invisible when observed from more than 100mm away. Therefore, making observations within the cut slot is problematic. Another challenge is that there is variability in the kerf profile, so replicates are needed to differentiate between trends and anomalies. Finally, the kerf looks quite different in its steady state when compared with the kerf profile where the arc is extinguished, so this needs to be considered.

The primary concern in acquiring a valid set of empirical data from our developed experiment is that the range of variation of process parameters needs to be useful. Due diligence needs to be paid in selecting an appropriate range for the process parameters being investigated. This is a common shortcoming in the literature. For example, if an empirical study deviates all its process parameters except one by 10% and varies the last parameter by 100%, then the last parameter will seem to be the most significant. Therefore, this will be a consideration so that the data supplied will be an accurate representation of the importance of each parameter. Other challenges include keeping the test process consistent. This will be done by being aware of sources of potential variance and minimizing this variation.

The final challenge of this investigation is deciding how to approach the asymmetry investigation. Asymmetry of the kerf has not been examined in the literature, so a method of quantifying it needs to be developed. This method should be easily replicable in further investigations with various

measurement tools. This quantification should provide a way to normalize the data based on material thickness and other process parameters. Again, this has not been presented in the literature so there is no basis for comparison to evaluate the results obtained.

4.4.1.3 Deliverables

The deliverables from this experiment are:

- To develop a process to obtain empirical data relating kerf angle to torch height, cut speed and material thickness.
- To use the empirical data to develop a relationship between kerf angle and the varied process parameters.
- To develop a method to quantify cut and present kerf asymmetry.

The process of obtaining empirical data will use a range of important process parameters and an experimental plan to acquire a wide range of data to allow investigation of the PAC phenomenology. It will involve designing a test cut that will provide a large amount of the desired data as conveniently as possible. Finally, the process will be validated.

The empirical data will take the form of a set of coordinates describing the profile of both cut faces. Sets of data will be acquired for replicates of the same process parameters, as well as over a wide range of the relevant process parameters. Finally, these will be presented as a summary of the replicates as well as for the individual trials. This will validate the results by being intuitively correct, with a reasonable amount of deviation in the data and logical trends with respect to the variation of the process parameters.

The final deliverable will be development of a method for presenting kerf asymmetry, and a quantitative analysis of its magnitude and effect on the kerf shape. This will include comparison with published methods of derivation of the kerf angle when symmetry is assumed.

4.4.2 Experimental plan

An experimental plan was developed to provide the empirical data. The concept of the test is to cut multiple slots into small rectangular plates. The plates will have varying thicknesses, and the slots will be cut with varying torch heights and feed rates. The slots will then be examined with the vision rig to determine the profile of the kerf and the kerf angle. Two methods will be used to estimate kerf angle. The first will assume kerf symmetry and will look at the top and bottom faces. The second method will not make this assumption and will examine the slot end on. Ideally this process can meet the requirements of providing a large variety of high-quality data and allow empirical investigation into kerf angle and examination of the symmetry assumption.

4.4.2.1 Feasibility testing and development

A test piece template was designed to provide potential for gathering a large quantity of data. The template was designed with 9 slots cut into a 100-millimeter-wide, rectangular piece of mild steel. The slots were spaced 10mm apart. This spacing was deemed sufficient to avoid influence from the HAZ of the preceding slot. Figure 4.28 shows the test piece designed in SolidWorks™. It was then cut on the PAC system (Figure 3.1) to test the suitability of the test cut. Several factors were found to be a problem.

Figure 4.28 Test cut designed in Solidworks.

The first problem found was that the test piece deformed during cutting. This was due to the slots

going too far into the rectangle, leaving an insufficient amount of material to resist the thermal stresses from the process. The solution was to extend the width of the test piece. Initially the slots progressed 25mm into the 35mm wide plate. The width of the plate was extended to 40mm, leaving 15mm of uncut material. This was found to be sufficient to avoid distortion.

The next problem observed was that the kerf width varied significantly along its profile. This was expected at the lead in, where the arc pierces and is over a location for a significantly longer time. However, it was also found that the kerf width narrowed and rounded off as it approached the edge of the plate. The first attempted solution was changing the order of the cuts to do the slots first and then cut the outside edge of the test piece. This failed because the arc was not capable of spanning the kerf width gap. It was then decided to mill the ends of the slots down. Fivemm was found to be sufficient to reach a steady state section of the kerf intersection with the front face of the plate. Some finishing was performed with a linisher to remove small amounts of swarf from the edges.

The final problem was the dross formation. Due to the varying cut speeds, dross was adhering to the bottom surface, which would affect the quality of the edge detection. Therefore, all dross was removed from the top and bottom faces using a hammer and chisel.

Initial plan

Two methods of estimating the kerf width were chosen in this investigation. The first method assumed kerf symmetry and the second examined the slots end on.

The symmetrical-kerf method used an image of the top and the bottom of a test piece. The kerf width of the top and bottom were measured with the close-view vision test rig, and the angle was calculated from half the difference of these and the thickness as shown in equation 4.7.

$$\alpha_t = \operatorname{atan}\left(\frac{KW_t - KW_b}{2t}\right) \tag{4.7}$$

α_t is the kerf angle.
KW_t is the measured kerf width on the top face.
KW_b is the measured kerf width on the bottom face.
t is the thickness of the plate.

The slot-end method takes images of each slot cut into the test piece end on. The part is placed vertically in a vice fixed to the plasma bed and the camera is moved along the test piece, centred on each slot. Edge detection is then used to get the profiles for each side of the kerf, and from this kerf width is estimated. This method is comparatively time consuming, however it provides a very accurate measurement of the kerf angle and profile.

Initial results

Figure 4.29 shows the image processing for method the preliminary testing. Firstly, the top, left and right edges are located. This is done roughly for speed as it only needs to be located to within a few pixels. Once these values are known, they are used to predict the location of the first slot. A profile of 50 pixels is constructed and the slot edges are identified. The centre location of this slot is then used to produce an estimation of the centre of the next slot. This is repeated until all the slots have been identified. Edge detection is done starting roughly 15 pixels below the centre of mass of the piece, to avoid the initial piercing location, and proceeds for 50 pixels, to avoid the end of the piece. The slot data points are then used to get an average kerf width for the slot on the top and bottom face, as shown in Table 4.8. With this information the kerf angle is estimated, and Figure 4.30 shows the slot profiles obtained for the preliminary testing.

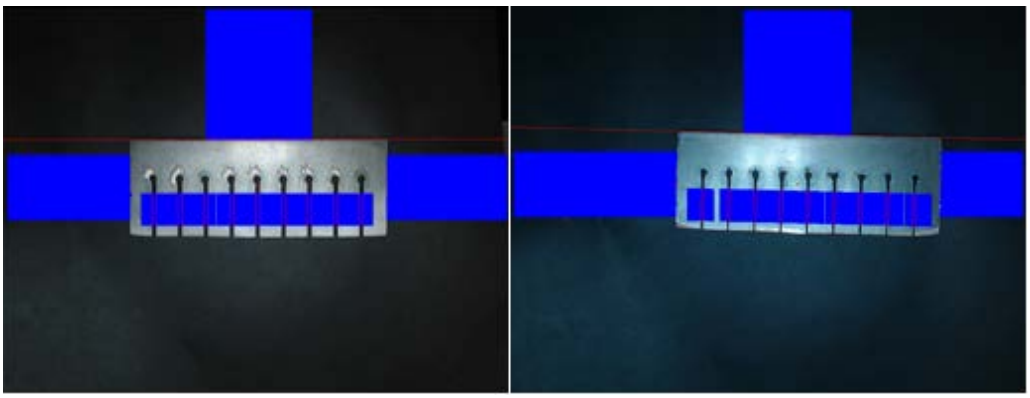

Figure 4.29 Kerf width measurement on the top and bottom faces of the test piece.

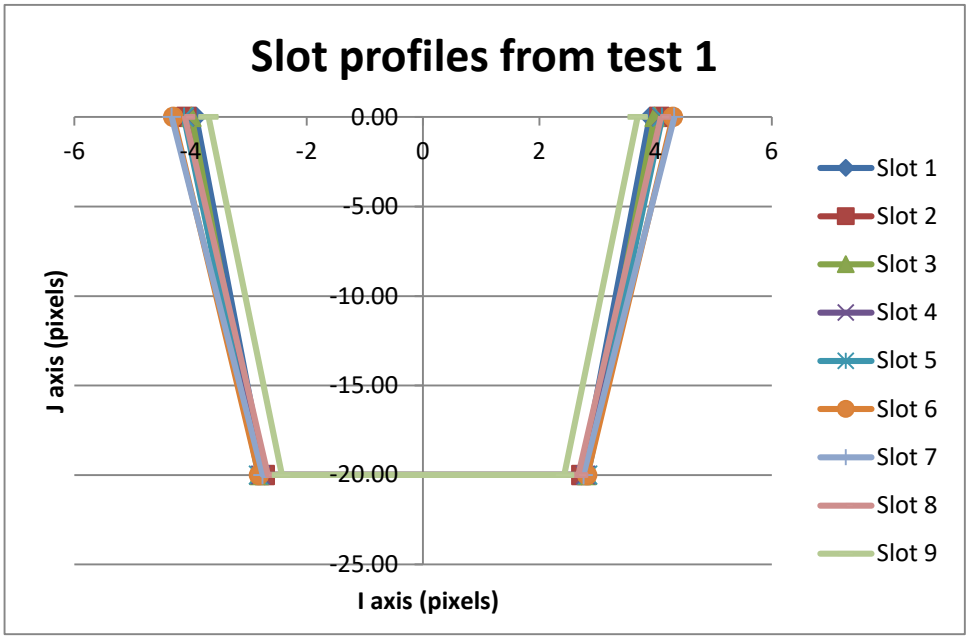

Figure 4.30 Slot profiles for the 9 slots of the preliminary test.

Table 4.8 and Table 4.9 summarize the results from the preliminary test. The difference in kerf widths for each slot is presented in Table 4.8. Table 4.9 averages the angle calculated for each slot using equation 4.7. The kerf angle returned is a reasonably low 5.26 degrees which is expected for this relatively thin plate (3mm) and matches observations from the literature. The standard deviation is low, showing a reasonable level of replicability using the same operating conditions. The pixels per mm (*pm*) value validates the result as it is what was expected. The very low standard deviation validates the carriage system, at least to the extent that the distance between slots was the same each time.

Table 4.8: Results from preliminary test to measure kerf angle, showing the kerf widths measured on the top and bottom faces.

Slot Analysis		
Top Width (pixels)	Bottom Width (pixels)	Top Location(pixels)
7.81	5.45	285.82
8.14	5.45	333.60
7.97	5.63	382.56
8.20	5.59	431.82
8.23	5.67	480.64
8.59	5.65	529.49
8.65	5.52	577.49
8.19	5.34	626.75
7.38	4.86	675.59

Table 4.9: Kerf angle results from preliminary test showing the kerf angle and pixel per mm measurement, as well as the standard deviation of both.

Averaged Results			
Mean Angle (degrees)	σ Angle (degrees)	*pm*	σ *pm*
5.26	0.49	4.87	0.05

Figure 4.31 shows the image processing for one slot of the slot-end method. Firstly, the top edge of the plate is found and a line of best fit is drawn through it (blue line). The worst fitting points are removed, and a new line is constructed to get a better estimation of the location and angle of the top face (red line). Next the left edge of the part is found (green) and used to estimate the location of the slot's centre. Grey level profiles are then constructed by traversing perpendicularly to the part (blue) and the edges are identified (red). The edge detection starts 3 pixels below the top face. It continues until the distance between the new kerf points and previous kerf points is too large. This indicates that the kerf is diverging rapidly, or that noisy points are present. The last few kerf points are omitted, resulting in approximately 20 kerf points being used for a plate of 3mm. This method also coincides nicely with the ISO 9013 standard on profile examination, where most parameters are calculated starting from 5% above and below the bottom and top faces. Figure 4.32 shows the edge points found without the processing information and Figure 4.33 shows the edge points for 9 slots with the same cut parameters overlaid on the same axes. This gives an indication of the variability of the process.

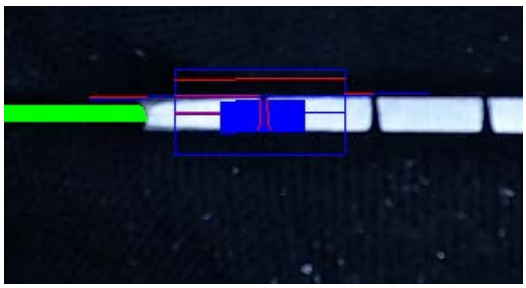

Figure 4.31 Edge detection for the slot-end method, showing the identification of the top face (blue and red lines), identification of the left edge (green lines) and the kerf scanning (blue lines with red dots for the edges).

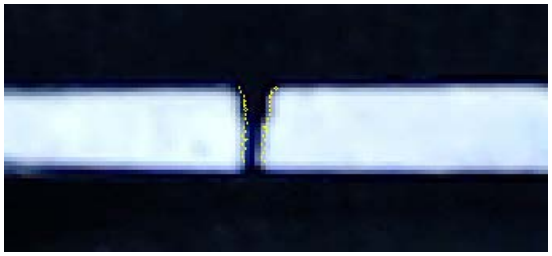

Figure 4.32 Kerf edges for the first slot in the preliminary testing.

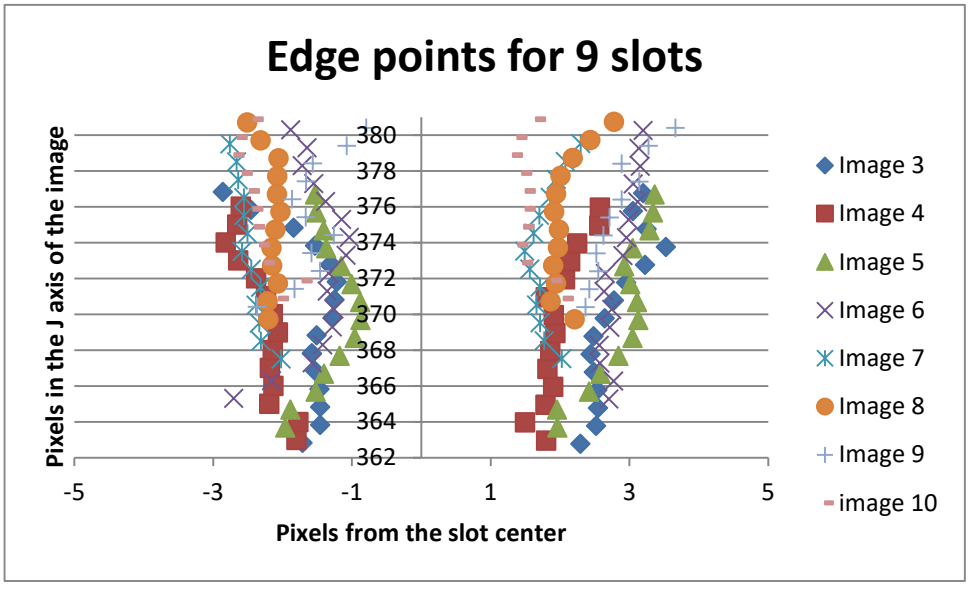

Figure 4.33 Edge points from the 9 slots of a preliminary test overlaid on the same axes showing the variation.

The kerf angle is then calculated for both faces by fitting a line through the edge points. Figure 4.34 shows the data from 9 slots in blue, and a parabola fit to the edge points of the kerf. This matches the profile of the kerf well, and there is little variation between the cuts. Figure 4.34 shows the preliminary test results for a 3mm and 8mm-thick test piece.

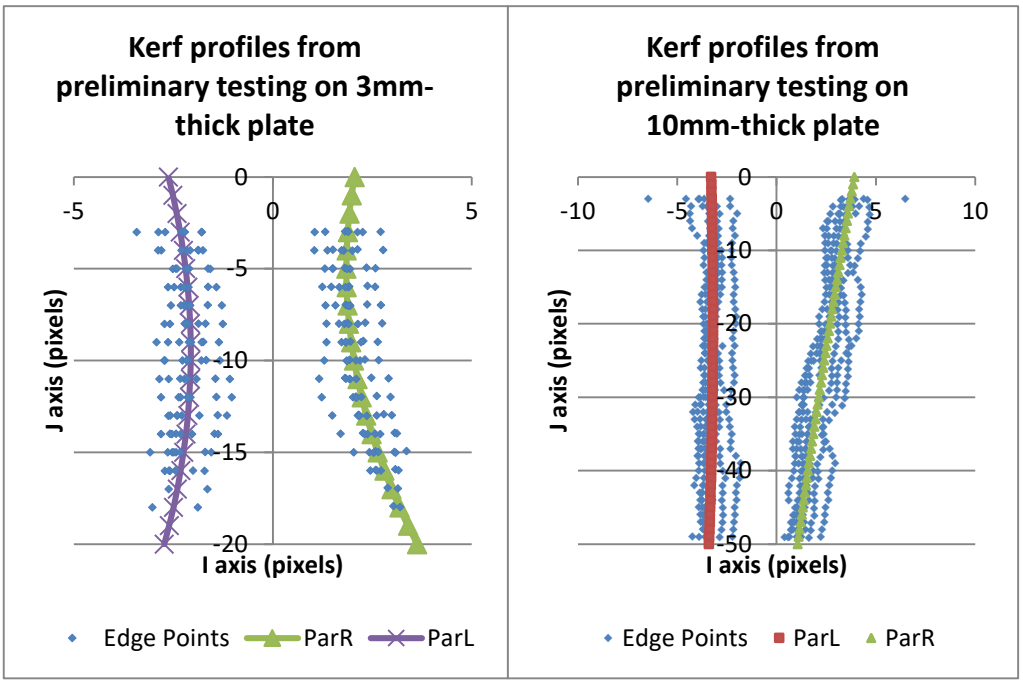

Figure 4.34 Examples of kerf profiles from two preliminary tests.

Recommendations and conclusions

The preliminary testing demonstrates the efficacy of the test piece template and validates the experimental method for obtaining the desired data. There is little variation in the measurements on the slot replicates, demonstrating the potential for these parameters to act as predictors, as well as validating the measurement technique. A few changes to the experimental and data collection process have been implemented because of the testing.

In symmetrical-kerf method, the primary source of spurious data was edge detection too close to the end of the slot. Therefore, the bottom edge of the part was also found and used to limit how close to the edge of the test piece data was collected. Otherwise the method performed well. In the slot-end method, the largest source of error and time consumption was poor alignment of the slot with the centre of the image, both horizontally and vertically. Two changes were made because of this; the slot centre estimation was based on previous slot locations, or the left edge in the case of the first slot. The grey level profile of the first horizontal edge found was used to determine whether it was a top or bottom edge in the case of plate thickness or vertical movement causing the bottom edge to be closer to the centre. Finally, the vice was fixed to the bed so that a more reliable positioning of the part was achieved.

4.4.2.2 Finalized plan

After preliminary testing and development, the final experimental plan was developed. It required three main stages:

- Test piece fabrication.
- The experimental run.
- The data acquisition and analysis algorithm.

Test Piece fabrication

A reliable method for test piece fabrication is important both for the validity of the testing and the convenience of the data acquisition. A process was designed and followed for all 35 test pieces. Firstly, the PAC parameters were set according to the experimental schedule and the part was cut out. The material the parts were cut from was clamped to the bed to remove buckling or warping of the plate as a source of variation (Figure 4.35).

Figure 4.35 Test material clamped to the gantry bed prior to machining.

After cooling, dross was removed with a hammer and chisel from the top and bottom faces. Figure 4.36 shows the part's faces with dross, and Figure 4.37 shows the part without dross. The part was then placed in a vice on top of a parallel on a knee mill. Approximately 5mm was then milled off the top of the plate with an 80mm diameter facing tool. This allowed multiple parts to be processed at once. The 5mm faced was performed in increments of 2mm with a final step size of 0.1mm to improve the finish and reduce the amount of rough material on the edge of the part. A linisher was then used to clean up the edges of the parts, removing most of the scraps of material. Finally, a thin file was used to remove the scraps on the inside of the slots, and then air blasted clean. Figure 4.38 shows the finished part.

Figure 4.36 Test piece 9, after fabrication with dross still attached to both faces. The left image is the bottom face, and the right image is the top face.

Figure 4.37 Test piece 9 after removal of dross. The left image is the bottom face and the right image is the top face.

Figure 4.38 Test piece 9 post processing ready for data acquisition.

The experimental run

Traditional experimental design methods, such as the Taguchi Method, were considered for formulating the experimental run. However, due to the complexity of the interaction effects in the PAC process, and the ease of experimentation and data processing, a full factorial run was undertaken, where every level was tested. Replication was also very easy due to the automated process, so 9 replicates were done at every level.

The 3 variables investigated were torch height, material thickness and feed rate. Preliminary testing suggested that material thickness would have the largest impact on kerf asymmetry, followed by torch height and feed rate. The relationships between the variables was also anticipated to be highly non-linear. Therefore, material thickness was investigated at 5 levels, torch height was investigated at 4 levels and feed rate was investigated at 3 levels.

An experimental run was developed that would provide a suitable range of variation for the process parameters. This range allows examination of the primary effects of the process parameters and the interaction effects. A summary of the experimental run is presented here; Appendix D contains a detailed listing of runs and process parameter settings. The process parameters varied were torch height, material thickness and feed rate. The experimental run was broken down into two sections. The first set varied the plate thickness and feed rate. Torch height was kept constant at 1.5mm. A middle value for feed rate was selected from the Dynatorch operating manual and feasibility testing. Upper and lower levels were then chosen to be about 16% above and below this value and then rounded to a convenient number. These 3 levels were then cut out of steel plate with varying thicknesses of 3, 4, 6, 8 and 10mm in a random order.

The second run varied torch height and thickness while keeping the feed rate constant at the middle value from the previous set. Torch heights of 3, 7 and 10mm were used to cut out the test piece from steel plates 3, 4, 6, 8 and 10mm-thick in a random order. In total, data from 35 tests was collected.

4.4.2.3 Data acquisition and analysis algorithm

The data acquisition took two stages. In the first stage, the test piece was placed on a flat surface on the PAC gantry with a black cloth behind it. An image was taken of the top and bottom surfaces. The test piece was roughly centred in the field of vision. This was repeated for all 35 test pieces and provided the data for the symmetrical-kerf method.

The second stage required a more complex data collection process. A vice was fixed to the PAC bed and aligned with its field of travel. A black cloth was placed over the vice and test pieces were placed so that their top face was against the top face of the vice and the slots ends were presented upwards towards the camera (Figure 4.39). The torch head was zeroed so that the centre of the camera was aligned with the centre of the first slot. G-Code to drive the camera to the centre of each slot and pause for image capturing was written, and the images were acquired in this way. This resulted in 9 images being taken for each of the 35 test pieces.

Figure 4.39 Data acquisition set up for the slot-end method showing the test piece's orientation in the vice, and the vice's orientation with the bed.

With the images acquired, the analysis algorithms then calculated kerf angle. The final implementation of the symmetrical-kerf method was quite similar to the preliminary testing. The first step was to identify the 4 edges of the test piece and the centre of gravity (Figure 4.40). The accuracy required for this step was only to a few pixels. These values are just indicators for where the next part of the algorithm should start looking for the slots.

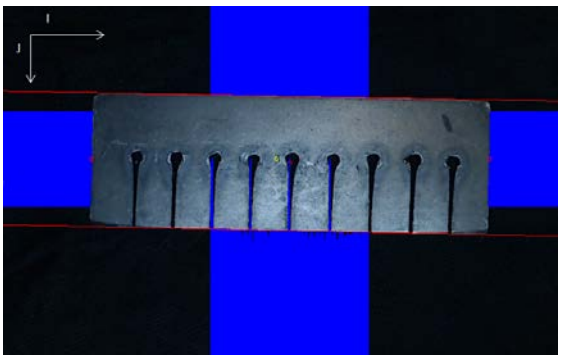

Figure 4.40 First step of the symmetrical-kerf method, identification of edges and centre of gravity of the test piece.

Next, for each slot a starting i and j value is predicted. These values are set to start sufficiently low in j so that the piercing location is avoided and located in the I-axis so that the slot is roughly 25 pixels away. A grey level profile is then scanned that is 50 pixels long, and the left and right edges of the kerf are identified. If the kerf edges are found to be too close to either end of the profile, subsequent profiles are shifted to attempt to centre the slot. This is repeated for 60 values of j, stopping when it gets close to the bottom of the part. This process and the identified kerf edges are shown in Figure 4.41.

Figure 4.41 The process of scanning a slot and identifying the kerf edge.

Once the edge points of the slot have been found, the slot width is calculated as the average of the distances between the 2 edge points located for a grey level profile. And the slot centre is calculated as the average of the mid-point between 2 edge points found in this manner. The estimate for the kerf centre is used to estimate the location of the subsequent slot and the process repeats. This is carried out for each of the 9 slots on the test piece and then repeated for the image of the bottom face of the test piece.

The result of this is 9 measurements for the slot widths on the top face, and 9 widths for the bottom face. Using these values 9 measurements for kerf angle were calculated using equation 4.7, and the average of these is presented as the kerf angle for this parameter setting. The variation between them is also recorded and presented.

The algorithm for the slot-end method begins with acquiring a picture of the first slot. A horizontal edge of the plate (either top or bottom) is found by fitting a line to 80 edge points. These edge points are found by taking vertical edge point profiles either side of the centre of the image, which is roughly centred on the slot. The edge points are offset from the centre by 20 pixels, to avoid

checking the area of the slot. Figure 4.42 shows the rough area of the slot in blue, and the estimated centre line of the part in red. The green vertical lines are the profiles being taken to find the edge points (blue), and the offset from the slot centre is visible. There are another 40 edge profiles mirrored over the slot.

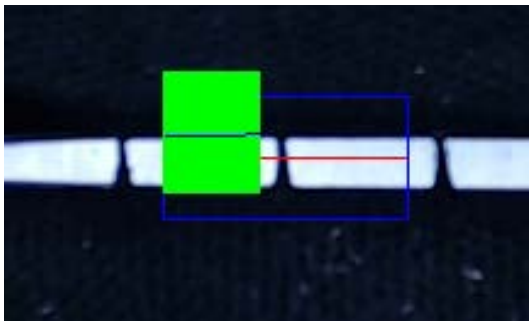

Figure 4.42 Location of the top edge of the test piece in the slot-end method.

A line is then fit through the edge points the worst fitting edge points discarded, and the line refitted. This line is shown in blue in Figure 4.43, and gives the location of the found edge of the plate, and its angle. Average grey levels, 10 pixels above and below the edge lines, are then calculated and used to decide if it is the top or bottom face of the test piece. If it is the top, then the algorithm proceeds. If it is the bottom face, then a new starting location is used, 15 pixels higher, and this process repeats until the top edge is found.

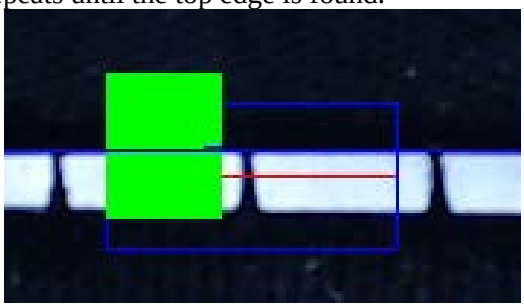

Figure 4.43 Identified top edge of the test piece for the slot-end method.

With this information the algorithm proceeds to find the edge points. If it is the first slot of the part, it begins by finding the left edge. It scans 15 pixels, starting from slightly below the identified top edge, and far to the left of the part. From this edge location the centre of the slot is approximated. If it is not the first slot, then the previous slot location is used to identify the succeeding slot. Grey level profiles are found at the same angle as the top face, centred on the slot location. These profiles start 3 pixels below the top face. The average grey level value of the pixel face is monitored, and when it drops low. This indicates that the algorithm has reached the bottom edge of the plate.

Edge points are found from these grey level profiles and are shown in Figure 4.44 in yellow. The last 3 edge points found prior to the loop finding the bottom of the plate are omitted due to the potential for discrepancies. These edge points are then transformed so that they are centred about the slot centre, and the top of the kerf is at zero in the J axis. This transformation allows the slots to be plotted on the same axis and compared. Finally, a line is fit to this data and the slope of the lines gives the kerf angle. A parabola is also fit to the edge points for the purposes of modelling the shape of the kerf.

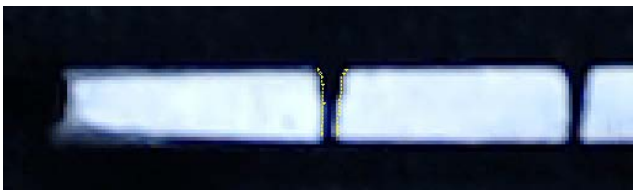

Figure 4.44 Edge points found for the first slot in the slot-end method.

4.4.3 Test Results

The results from the testing are presented in detail in Appendix E. For the symmetrical-kerf method this includes a measurement of average deviation between the bottom and top faces for each test, the standard deviation of the average deviation for the 9 slots of the test cut and an average kerf angle for the test piece. For the slot-end method this shows the parameters for the parabola fit to both sides of the test slot, and the kerf angle estimated using a line of best fit for each side of the kerf. A summary of the results is presented here.

4.4.3.1 Symmetrical-kerf method

A summary of the results obtained using the symmetrical-kerf method is presented in Table 4.10 and Table 4.11. Table 4.10 summarizes the responses in kerf angle as a result of variation in material thickness and the feed rate. Four kerf-angle measurements were made at the medium feed rate for each thickness. These 4 measurements were for variations in torch height, therefore the kerf angle presented for the medium feed rate is the average of these measurements. The range was identified as a useful measure of spread to reflect how influential a variation was on the kerf angle. Ranges for variations in material and variations in feed rate are shown.

Table 4.10: Summary of the kerf angles measured with the symmetrical-kerf method for variations in thickness and feed rate while keeping torch height constant. *t* = thickness, L = low level for feed rate, M = Medium level and H = high level.

Kerf Angle (degrees)				
***th* (mm)**	**Feed rate**			**Range (mm)**
	L	**M**	**H**	
3	5.5	8.0	6.0	**2.4**
4	4.7	7.9	4.6	**3.3**
6	1.5	5.0	2.6	**3.4**
8	0.1	2.7	1.1	**2.7**
10	0.1	2.6	1.5	**2.5**
Range	**5.5**	**5.4**	**4.9**	

Table 4.11 presents a summary of the kerf-angle measurements obtained for variations in torch height thickness and material thickness. Three measurements were obtained for test pieces at 1.5mm height for each thickness. Therefore, the values in this column are the average of these 3 measurements. The range of kerf angle due to variation in torch height and material thickness are also presented.

Table 4.11: Summary of the kerf angles measured with the symmetrical-kerf method for variations in torch height and thickness while keeping feed rate

constant

Summary Torch Height vs Thickness					
***th* (mm)**	**Torch Height (mm)**				**Range (mm)**
	1.5	**3**	**7**	**10**	
3	5.6	9.1	6.8	10.5	**4.9**
4	4.7	7.1	9.3	10.4	**5.7**
6	2.0	4.3	5.8	8.1	**6.1**
8	0.5	1.6	3.6	5.2	**4.7**
10	0.5	1.9	3.2	5.1	**4.6**
Range	**5.1**	**7.5**	**6.1**	**5.4**	

Figure 4.45 and Figure 4.46 show an example data set for test cut 20 using the symmetrical-kerf method. Figure 4.45 presents the profiles of the 9 slots obtained with the symmetrical-kerf method. They are overlaid and centred about the Z axis. Zero on the Z axis corresponds to the top of the plate. Figure 4.46presents the profile for the average of the 9 slots.

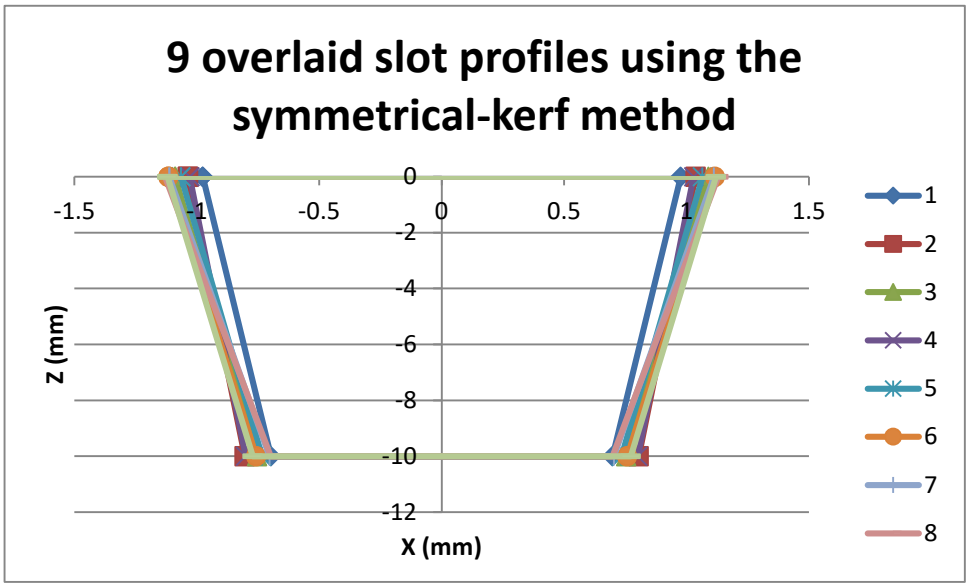

Figure 4.45 Nine slot profiles constructed using the symmetrical-kerf method for test cut 20.

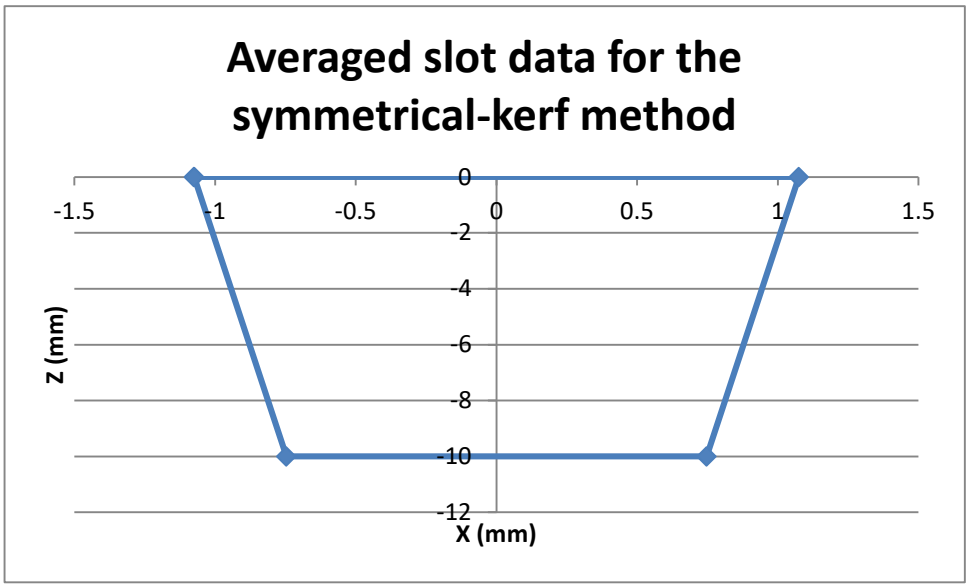

Figure 4.46 The average slot profile constructed using the symmetrical-kerf method for test cut 20.

4.4.3.2 Slot-end method

Table 4.12 shows a summary of the response of the left and right kerf angles to variations in the plate thickness and feed rate. Both sides of the kerf are presented individually as well as the range of variation for both data sets. These angles are calculated from the line of best fit through the data points. Four measurements were made on test pieces at the medium level of feed rate, so the data in that column is the average of the 4 measurements made for each thickness.

Table 4.12: Table showing summary of kerf angles with the slot-end method as thickness and feed rate are varied and torch height is kept constant. *t* = thickness, L = low level for feed rate, M = Medium level and H = high level.

Summary Feed Rate vs Thickness								
Left Angle (degrees)					Right Angle (degrees)			
t (mm)	Feed rate			Range (mm)	Feed rate			Range (mm)
	L	M	H		L	M	H	
3	5.4	9.3	11.1	**5.7**	0.5	3.6	-2.0	**5.6**
4	1.1	8.2	-9.0	**17.2**	0.7	4.9	6.4	**5.7**
6	-4.7	4.1	4.2	**9.0**	0.1	3.5	-0.9	**4.4**
8	-6.5	-0.3	-2.3	**6.2**	2.1	3.6	1.7	**1.9**
10	-1.1	-0.2	-2.5	**2.3**	-0.8	2.9	0.2	**3.6**
Range	**12.0**	**9.5**	**20.1**		**2.8**	**2.0**	**8.4**	

Table 4.13 presents the summary of the kerf-angle measurements made with the slot-end method as a response to variations in thickness and variations in torch height. Three measurements were made for test pieces cut with a torch height of 1.5mm. The data points in this column are the average of these 3 measurements for each thickness. The range of kerf angles corresponding to each variable's variation is also presented. Both sides of the kerf are presented individually.

Table 4.13: Table summarizing the kerf angle measured with the slot-end method as torch height and thickness are varied and feed rate is kept constant. *t* = thickness (mm).

Summary Torch Height vs Thickness					
Angle 1 (degrees)					
	Torch Height (mm)				
***t*(mm)**	**1.5mm**	**3mm**	**7mm**	**10mm**	**Range**
3	6.6	9.7	12.7	11.3	**6.1**
4	-2.0	6.2	10.6	14.1	**16.1**
6	0.7	3.5	8.3	11.6	**11.0**
8	-5.2	0.4	1.3	4.0	**9.2**
10	-2.5	-0.9	1.2	2.9	**5.3**
Range	**11.8**	**10.6**	**11.5**	**11.3**	
Angle 2					
	Torch Height (mm)				
t	**1.5**	**3**	**7**	**10**	**Range**
3	0.3	1.2	4.3	6.4	**6.1**
4	3.4	3.3	5.1	8.0	**4.7**
6	-0.2	3.8	4.4	5.7	**5.9**
8	2.0	1.8	3.1	3.7	**1.9**
10	0.2	2.9	3.3	4.2	**4.0**
Range	**3.6**	**2.6**	**2.0**	**4.3**	

Figure 4.47 presents an example set of raw data points for test cut 3. The raw data points are the profile points obtained from each slot on the test piece. The Z axis corresponds to the centre of the kerf at the top face of the material. A best fit line has been plotted through each side of the kerf. These are used to estimate the angle for each side of the kerf. A positive angle corresponds to a kerf side that approaches the Z axis, while a negative angle represents the kerf diverging from this axis. Additionally, a parabola has also been fit to each side of the kerf for investigation into the kerf shape.

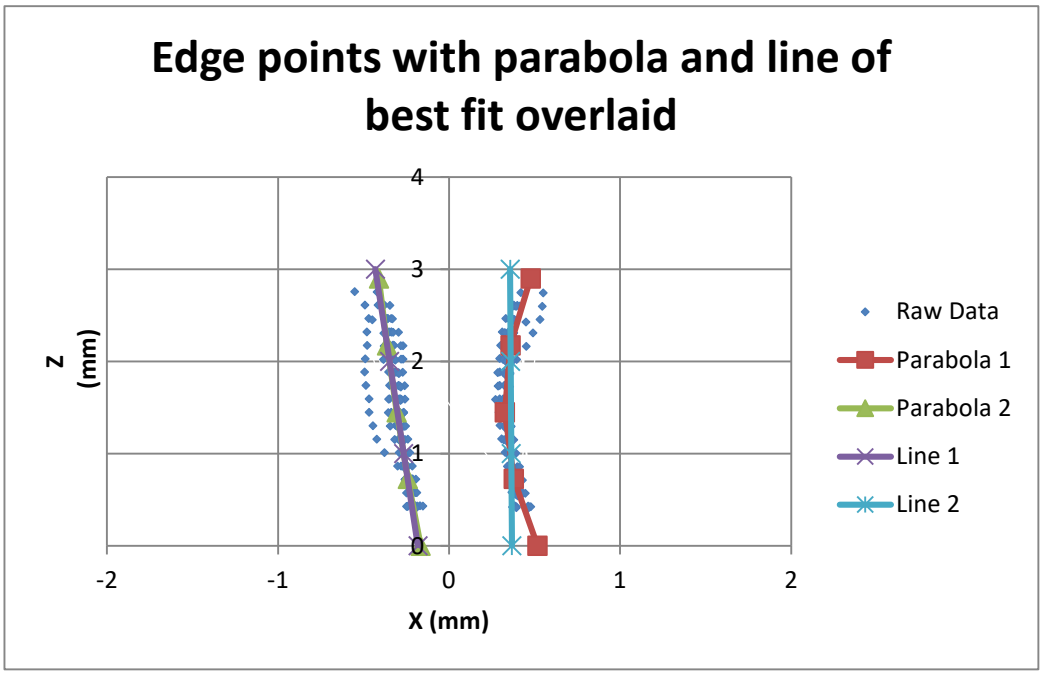

Figure 4.47 The slot profile constructed for test cut 3 using the slot-end method. The best fit line and best fit parabola are overlaid.

4.4.4 Conclusions and Discussion

This experimental protocol acquired a large amount of accurate measurement data. From this an empirical investigation into the relationship between kerf angle and the process parameters (torch height, feed rate and material thickness) is now possible. Further an investigation into the assumption of kerf symmetry allowed a quantification of the error this yields. For certain process parameters, the cut was found to be highly asymmetrical at times, dependent on the process parameters.

The goals set for this research were:

- To develop an experiment to obtain empirical data relating kerf angle to the process parameters of torch height, cut speed and material thickness.
- To carry out the developed experiment and acquire a set of accurate kerf angle data.
- To investigate the asymmetry inherent to the PAC process.

An experiment was successfully developed that obtained large amounts of accurate data relating kerf angle to torch height, cut speed and material thickness. This involved designing a test piece, an appropriate experimental plan and a data acquisition and analysis algorithm. The test piece provided the ability to easily vary the test parameters as well as produce replicates of the slot to examine the variability of the measurements. The experimental plan covered a wide range of process parameters. A typical experimental archetype reported in the literature is the factorial method. A 3-factor 3-level experiment requires 27 trials without any replicates. This method provided more detailed investigation into the effect of material thickness and into the variability of the measurement than has been reported thus far. The data acquisition and analysis methods were developed so that standard practices from the literature on surface roughness were used, as well as a method for examining the viability of the symmetrical-kerf method.

The experimental plan was implemented successfully and provided accurate measurement data in an efficient manner. This data was collected in 35 test cuts. Due diligence was exercised in reducing sources of variation in the process, and the variability of the measurements reflect this. The data summaries highlight trends for the kerf angle variation such as kerf angle increasing with torch height which agree with the findings in the literature ((Nemchinsky & Severance,

2009)). Using two methods to calculate the kerf angle allows investigation of the suitability of each.

Finally, the acquired data allowed the investigation of kerf asymmetry. As suspected, the kerf was very asymmetrical for some process parameter settings, and the two sides of the kerf were found to vary at different rates. The magnitude of the deviation from asymmetry is presented and found to be significant.

4.4.4.1 Symmetrical-kerf method

The first method of kerf-angle measurement (based on the average of the top and bottom kerf width measurement) proved useful and simple to implement. Most studies reported in the literature employ this measurement for kerf angle. It omits several aspects of the kerf profile that are important, such as differing angles on the two sides of the kerf, the offset between the location of the kerf on the top and bottom surfaces and the shape of the kerf in between the two faces. However, it does provide an indication of how the angle, and the mass-removal rate, varies with respect to profile parameters.

The results show that the primary factors that influence the kerf angle are torch height and material thickness (Table 4.12 and Table 4.13). The range in kerf angles for a constant material thickness and feed rate as the torch angle varied was between 4.6 and 6.1 degrees. Similarly, for varying material thickness, the kerf angle varied from 5.1 to 7.5 degrees. For varying feed rate, the kerf angle varies from 2.4 to 3.4 degrees, i.e., this has a relatively small effect. In general, the kerf angle was found to decrease as plate thickness increased. No trend was identified with feed rate, although the lowest angles were measured at the low and high levels of feed rate. Finally, as torch height increased, the kerf angle increased.

Measurements for the repeated cuts with the same process parameters indicate very little deviation between the slots. The average standard deviation was 0.08mm which is very accurate and is shown in Figure 4.47, where the edges of the kerf lie in close proximity to each other. This increases the confidence in the measurement results. However, a few shortcomings of this method have been identified. Firstly, the pixel accuracy was only about 0.2mm per pixel. Whilst sub pixel accuracy was achieved, as attested by the results, the difference between the top and bottom kerf widths was only of the order of 0.1mm in several cases. Therefore, a higher resolution would be preferable in making these measurements. The measurements made were checked with a caliper and found to be comparable. Secondly this method neglects several factors. One factor that could be addressed in future implementations is the incorrect assumption that the kerf width on the top face and the kerf width on the bottom face are centred at the same location.

4.4.4.2 Slot-end method

The second method of measurement (based on the profile of the cut viewed end on) was the preferred method of measurement for a few reasons. Firstly, it was visibly confirmed by the images taken. That is to say that profiles constructed and plotted in Excel were visibly similar to the kerfs produced. This increased confidence in the findings. This measurement method provided a way to measure kerf angle that was robust to rapid deviations in the kerf at the top and bottom faces, as well as providing data on the profile of the kerf inside the cut, which means that it achieved the set goals. Further, it allows evaluation of the symmetrical-kerf method's efficacy. This method is slower and more computationally intensive than the symmetrical-kerf method, but provides so much more data that the trade-off is worthwhile.

The data obtained with this method highlights several trends (Table 4.12 and Table 4.13). Firstly, the kerf-angle measurements were found to vary quite drastically. For varying plate thickness, the left kerf angle varied by up to 20.1 degrees and the right kerf angle varied by up to 8.4 degrees. Feed rate was found to have a moderate level of influence on kerf angle; the left kerf angle commonly varied by 10 degrees but could vary as much as 17.2 degrees. The right edge kerf angle ranged from 1.9 to 5.7 degrees as feed rate was varied. Finally, variation in torch height influenced the kerf angle by as much as 16.1 degrees on the left edge and 6.1 degrees on the right edge.

In general, kerf angle decreased as the plate thickness increased for both edges, and it increased with increase in the torch height for both edges. Again, no definite trend was identified between feed rate and kerf angle, but a smaller kerf angle was observed at the lowest and highest feed rates. There was quite a large difference between kerf angles measured for the right and left edges, which shows that the common assumption of kerf angle symmetry is not justified. In general, the right edge was more stable, and its kerf angle closer to zero than the corresponding left edge kerf-angle measurements.

Figure 4.47 shows the considerable variation in the shapes of the two edges. For this test piece the right edge is much less linear than the left edge. Measurements from this data set allow investigation into the effect of process parameters on the profile of the kerf as well as the kerf angle. The profiles of the slots for all the tests are included in Appendix E and show substantial variation with changing process parameters. The data points show that there is a reasonable level of conformity between slots cut with the same process parameters.

4.4.4.3 Comparison of two methods

The two methods used for kerf-angle measurements were both able to provide useful empirical data. The trends identified with both methods agreed with each other to a large extent and validate the experimental results. However, the slot-end method highlights the effect of several assumptions made by the symmetrical-kerf method.

The symmetrical-kerf method assumes that the kerf angle on both faces is the same. The slot-end method measures both angles separately and shows that in all cases the right edge was less affected by variation in the profile parameters than the left edge. This caused discrepancies of about 10 degrees between the methods in some cases. The symmetrical-kerf method also assumes that the kerf is perpendicular to the plane of the top/bottom face. Again, the slot-end method highlights that the cut can be skewed, further affecting the kerf-angle measurement.

Finally, the symmetrical-kerf method assumes a linear profile path between the top and bottom edges of the cut. The slot-end method shows that this path is in some cases linear but is also often curved. This significantly affects estimates of the kerf angle because the symmetrical-kerf method's angle measurement will be largely influenced by deviations that occur at the top and bottom of the plates, whilst the slot-end method is more robust to this. This led to very few negative kerf angles being recorded with the symmetrical-kerf method due to the rapid divergence at the lip of the kerfs, whilst the slot-end method could identify negative kerf angles.

The slot-end method's primary short coming is the additional processing steps that are needed. The symmetrical-kerf method is faster and easier to implement, whilst the slot-end method requires the end of the slot to be processed for better edge recognition and to expose the steady state section of the kerf. However, this trade off results in substantially more, and higher quality data.

4.4.5 Future work

Based on the results of this experiment future work in this area should include:

- Development of the symmetrical-kerf method.
- Revaluation of results obtained using the symmetrical-kerf method.
- Further empirical investigation.

During this investigation the effects of kerf asymmetry were found to be substantial. Therefore, development of the symmetrical-kerf method to estimate the asymmetry is necessary. This could be accomplished by measuring the centre location of the kerf on the top and bottom faces and evaluating the kerf angles as the angles between the right edges of the kerf and the left edges of the kerf. This would allow the symmetrical-kerf method to be used to investigate the profile parameters' effects on the kerf angles individually.

Due to the significance of kerf asymmetry on the kerf-angle measurement, the results obtained

with this method should be re-examined. Roughly half of the studies reported in the literature use this method due to its simplicity, however the results obtained will suffer from a high degree of inaccuracy and fail to take advantage of the ability to affect the edges of the kerf disparately. Investigating these research endeavours may explain discrepancies that exist and allow the work to be amended.

Finally, further empirical investigation should be pursued. In this study, torch height was not decoupled from arc voltage. Both process parameters should be investigated separately, not only for their effect on the kerf angles, but also for their effect on the kerf profiles. This research only investigated feed rate at 3 levels, over a range of about 35% of the recommended cut speed. Investigations beyond and within this range would complement the results of this work as feed rate is commonly found to be an influential process parameter in the literature.

4.5 Chapter Summary

This chapter has presented the work done in four areas:

1. Development of a vision rig with a “wide-view” to perform AVI of kerf width.
2. Development of a vision rig with a “close-view” to perform AVI of kerf width.
3. A feasibility study on height detection using the vision rig.
4. The empirical investigation of kerf angle with respect to torch height, material thickness and feed rate as process parameters using close-view, vision rig.

This work has provided contributions to the fields of machine vision and PAC in several ways. Firstly, 2 papers were published on the methodology and results of the AVI development and implementation for PAC. The AVI system developed was capable of measuring kerf width for a variety of parts to 0.1mm (Flemmer, 2017a; Flemmer, 2017b). The measurements were presented in such a way that systematic errors could be identified. This contribution helps to address the gap identified in the literature for such a system.

Additionally, the data of the empirical investigation into kerf angle and kerf width with respect to material thickness, torch height and feed rate provides data for future work to make use of. It also provides qualitative and quantitative information to help understand the phenomenology of PAC. This data was then used to investigate and quantify kerf asymmetry, addressing a second identified gap in the literature.

Aside from these, a feasibility study for height detection using stereopsis from the developed vision rig was undertaken. This study found that height could be measured at least as accurately as measurements made using traditional voltage differential options. Measurements were made to an accuracy of 0.15mm.

5 PAC Process Parameters and Modelling

This research has identified the potential for the use of machine vision to provide a novel, control algorithm PAC. The previous chapter developed a vision system to facilitate this control method, however accurate models of the PAC phenomenology are also required. This chapter aims to address several gaps in the literature on modelling the PAC phenomenology presented by the literature review. Specifically, it aims to:

1. Assess the consensus of the literature on plasma jet properties.
2. Investigate the assumption that the heat transfer due to radiation is insignificant in the total heat transfer during the PAC process. This has been assumed in multiple works but never quantified.
3. Present experimental work undertaken to gather data on the shape of the front edge of a kerf during steady state PAC.
4. Present a model to describe the shape of the front edge of a kerf during steady state PAC.

This chapter begins by collating and summarizing the data obtained in the literature review. This summarization assesses some of the works and presents them in a manner that facilitates use in future endeavours. It has the key challenge that these works were undertaken with plasma machines with different operating parameters. This work is of value because it improves the cohesiveness of the work presented in the literature for easier comparison.

With this summary complete, the chapter then investigates radiant heat transfer. This work draws from the literature by replicating and altering some of the testing methods presented by other researchers. The key challenge overcome in this section is designing an experiment to allow estimation of the radiative heat transfer effect. This value of this effort is that the assumption that radiation heat transfer is insignificant is made multiple times in the literature but has never been quantified.

Experimental work, performed to gather data on the leading edge of a kerf during steady state PAC, is then presented. The key challenge of this work was to design an experiment to best gather this data. The experimental plan is presented, and the data obtained is summarized.

Finally, this chapter presents the development of a relationship between the slope of the leading edge of the kerf with feed rate and material thickness. This work is valuable because it addresses a gap in the literature and improves understanding of the PAC process. The shape has been described anecdotally in the literature a few times, but no model has been put forth. A clearer understanding of the process that results in the shape of the leading edge of the kerf has been identified by Nemchinksy as a necessary research endeavour (Nemchinsky, 2017; Nemchinsky & Severance, 2006; Teulet et al., 2006).

5.1 Conceptualization of the PAC process

The work into conceptualization of the PAC process aims to develop data presented in the literature to a state that facilitates modelling of the kerf profile. The two areas analysed were:

- Characterization of the plasma-arc by normalizing key parameters.
- Investigation of the temperature profile of the cut piece near the arc.

5.1.1 Characterization of the plasma-arc

There have been several attempts in the literature to characterize the plasma-arc. Experimental data has been gathered that describes the variation of the temperature of the arc as it moves downstream and diverges radially. Several researchers have also attempted to fit models to this data to predict the temperature.

Conceptually, these temperature profiles can be normalized. Two possible characteristics that can account for variations between arcs in different set ups are the maximum temperature and the

nozzle diameter. To investigate this, data from several investigations (presented in the literature) was normalized by plotting temperature as the ratio of local temperature to maximum temperature observed, and normalizing radius, by plotting it as the ratio of local radius to nozzle diameter. Data on temperature profiles were obtained from work by Hsu, Etemadi, and Pfender (1983), Freton et al. (2000), Lago et al. (2004), Gleizes, Gonzalez, and Freton (2005), Pardo, González-Aguilar, Rodriguez-Yunta, and Calderón (1999) and Trelles, Chazelas, Vardelle, and Heberlein (2009). However, the works by Hsu et al. (1983); Lago et al. (2004) and Freton et al. (2000) were for unconfined arcs. Figure 5.1 shows an example of the data presented by these works:

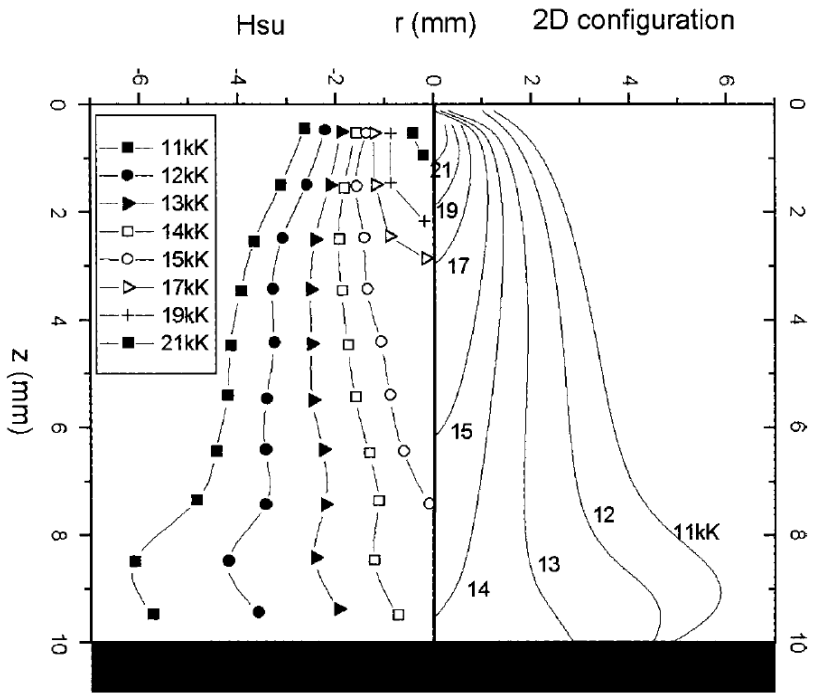

Figure 5.1 Example of data points for isotherms with respect to the distance from the nozzle (Z) and the radial displacement (r) (Hsu et al., 1983; Lago et al., 2004).

Figure 5.2 and Figure 5.3 show the results for normalized temperature of the arc and distance from the nozzle along the Z axis (Z). Temperature was normalized with respect to the maximum temperature achieved by the arc. Z was normalized with respect to the nozzle diameter. Figure 5.2 shows that there is a linear trend between these normalized values. Figure 5.3 shows the same normalized trend, but only for the data obtained from confined arcs.

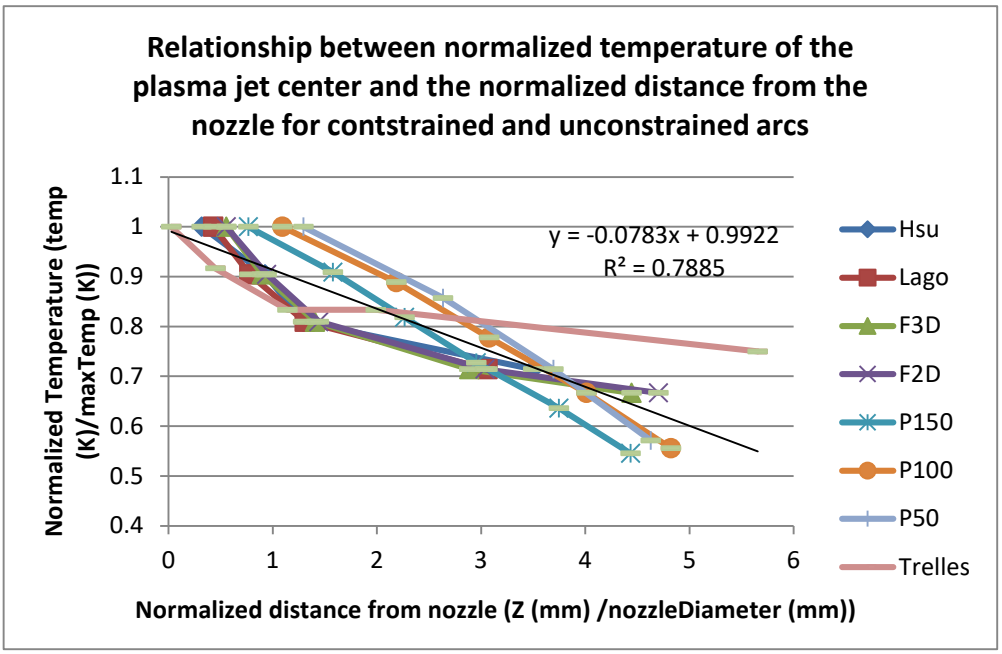

Figure 5.2 A plot of the relationship between temperature and nozzle diameter for several jets with temperature data.
In the legend: Hsu is data from Hsu et al. (1983); Lago is data from Lago et al. (2004); F3D is Freton's 3D model and F2D is Freton's 2D model from Freton et al. (2000); P150, P100, and P50 are data from 150A, 100A and 50A machines presented in Pardo et al. (1999); Trelles is data from Trelles et al. (2009).

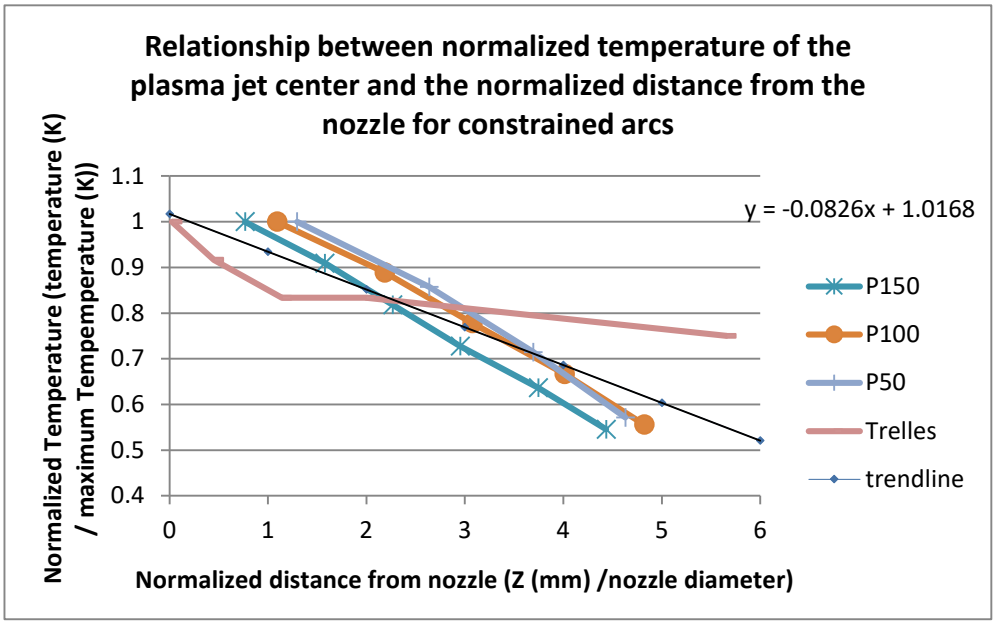

Figure 5.3 A plot of the relationship between temperature and nozzle diameter for constrained jets.
In the legend: P150, P100, and P50 are data from 150A, 100A and 50A machines presented in Pardo et al. (1999); Trelles is data from Trelles et al. (2009).

Figure 5.4 and Figure 5.5 show that the same normalized temperature plotted against a normalized radius (where the radius, or distance from the centre of the jet, is normalized with respect to the nozzle diameter). An approximation of this trend is linear as shown in these figures and represents

the data adequately. In Figure 5.4 the location of these data points is half a nozzle diameter from the nozzle, while in Figure 5.5 the location of these data points is 2 nozzle diameters away from the nozzle. These figures demonstrate the transition of the temperature gradient from very steep, to shallower (a slope of -1.29 and -1.08 respectively) as the jet moves further away from the nozzle. This transition is expected due to entrainment of the shielding gas with the plasma. Figure 5.2 - Figure 5.5 show that a linear approximation is valid for normalized data and allows prediction of these variables.

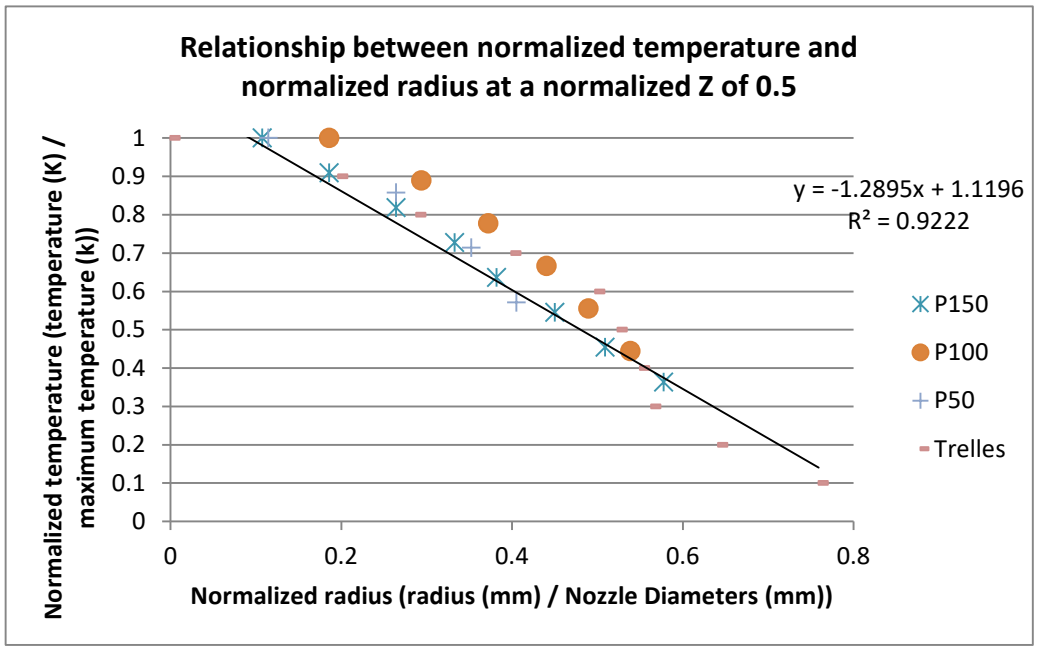

Figure 5.4 A plot of the relationship between temperature and normalized radius for a normalized Z of 2.
In the legend: P150, P100, and P50 are data from 150A, 100A and 50A machines presented in Pardo et al. (1999); Trelles is data from Trelles et al. (2009).

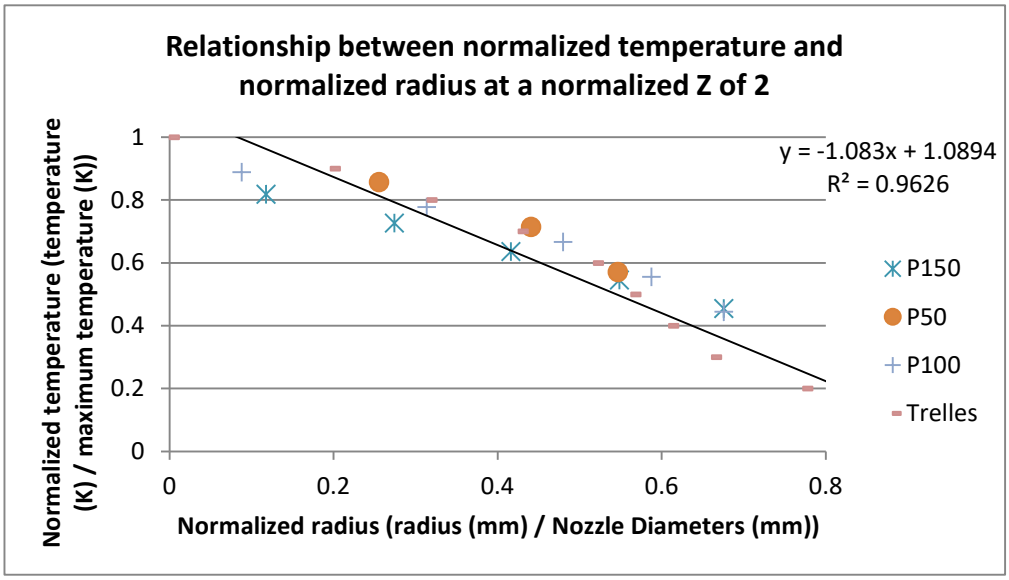

Figure 5.5 Plot of the relationship between temperature and normalized radius for a normalized Z of 2.
In the legend: P150, P100, and P50 are data from 150A, 100A and 50A machines presented in Pardo et al. (1999); Trelles is data from Trelles et al. (2009).

As a final step, the rate of change of normalized temperature with normalized radius for these data sets was plotted. This plot is shown in Figure 5.6 and Figure 5.7. They clearly show a trend

over the range of normalized depth (Z (mm) / Nozzle Diameter (mm)) from 0.5 to 4. This allows interpolation between data points to estimate temperature at any point in the plasma jet from the parameters of nozzle diameter and maximum temperature.

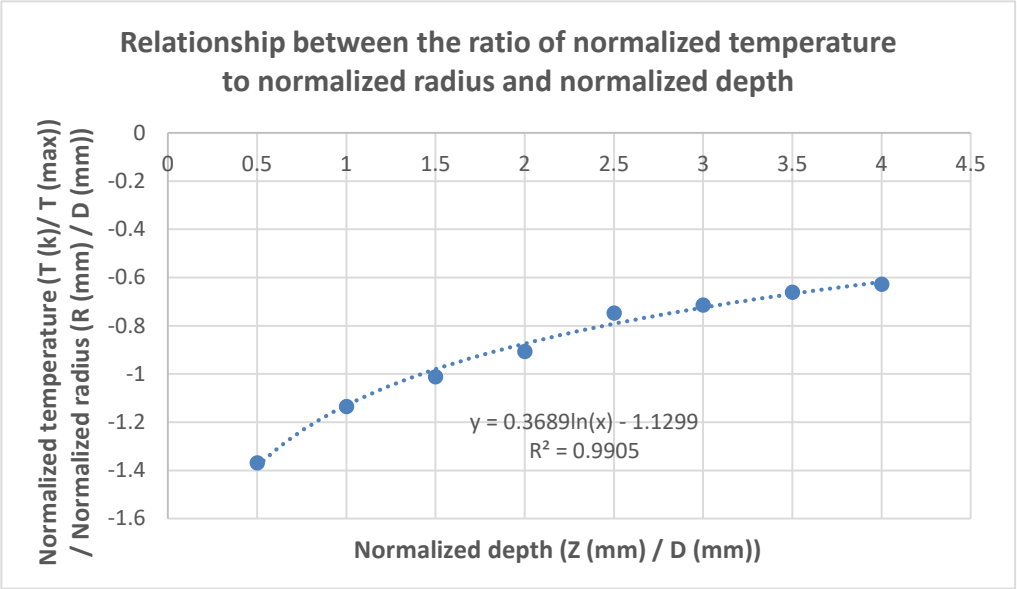

Figure 5.6 A plot of the rate of change of normalized temperature at r = 0mm for varying normalized depths.
T = temperature in Kelvin at a specific radius. Tmax is the maximum temperature of the plasma jet in Kelvin. R is the distance from the center of the jet in millimetres. D is the diameter of the nozzle in millimetres.

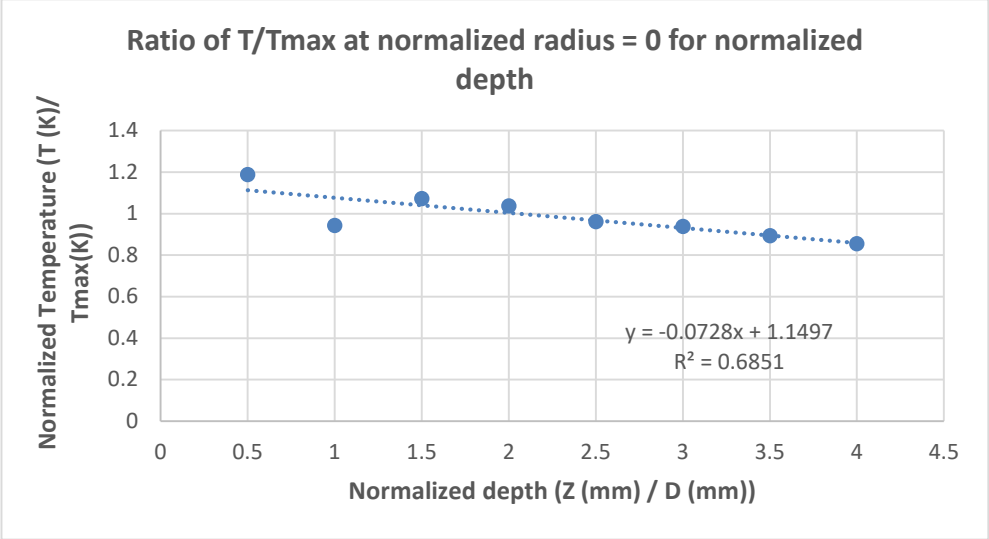

Figure 5.7 A plot of the rate of change of normalized temperature at r = 0mm for varying normalized depths.
T = temperature in Kelvin at a specific radius. Tmax is the maximum temperature of the plasma jet in Kelvin. R is the distance from the center of the jet in millimetres. D is the diameter of the nozzle in millimetres.

5.1.2 Temperature Profiles

Teulet derived a relationship for the temperature at a point, M, on the 2-dimensional plate, while the plasma torch advances steadily over the plate. The coordinate system is referred to the (moving) torch position and consequently, the temperature distribution does not change with time. The solution was originally derived by Carslaw and Jaeger (1959) and was adapted by

Nemchinsky (1997) to superimpose many line sources, distributed around the front semicircle of the cut face. Nemchinsky observed that these distributions were additive. Equation 5.1 is essentially the sum of linear heat sources distributed in a semi-circle on the front face of the arc.

$$T(M) = T_0 + \frac{Q_{HCL}}{\pi^2 \kappa_t th} * \int_0^{\frac{\pi}{2}} \exp\left(-\frac{\rho c_p v_t x_1(\theta)}{2\alpha_d}\right) * K_0\left(\frac{\rho c_p v_t r(\theta)}{2\alpha_d}\right) d\theta \qquad (5.1)$$

Where T is the temperature, Q_{HCL} is the power lost due to thermal conduction, κ_t is the thermal conductivity, th is the metal thickness, α_d is thermal diffusivity, ρ is the density, c_p is the specific heat capacity, v_t is the velocity of the torch head, x is the coordinate of the point of interest and r is the radius of the point of interest.

Equation 5.1 (Nemchinsky, 1997) simply says that the temperature at a point is equal to an initial temperature plus a scaling factor multiplied by the integral of the exponential of a term proportional to the distance along the X axis from the arc multiplied by a zeroth order Bessel function of a term that is proportional to the Cartesian distance between the point M and the coordinate of the arc edge as specified by the angle being varied in the integral. Interestingly, this integral is only taken over the range of 0 to π/2, or half a semi-circle. Teulet only plots the result of this equation for the range of 2 – 11mm on the Y-axis (Figure 5.8). When this equation is plotted over the range of -2mm to 10mm, (Figure 5.9) a lack of symmetry becomes apparent, so this relationship only seems appropriate for the range of Y values greater than +2mm.

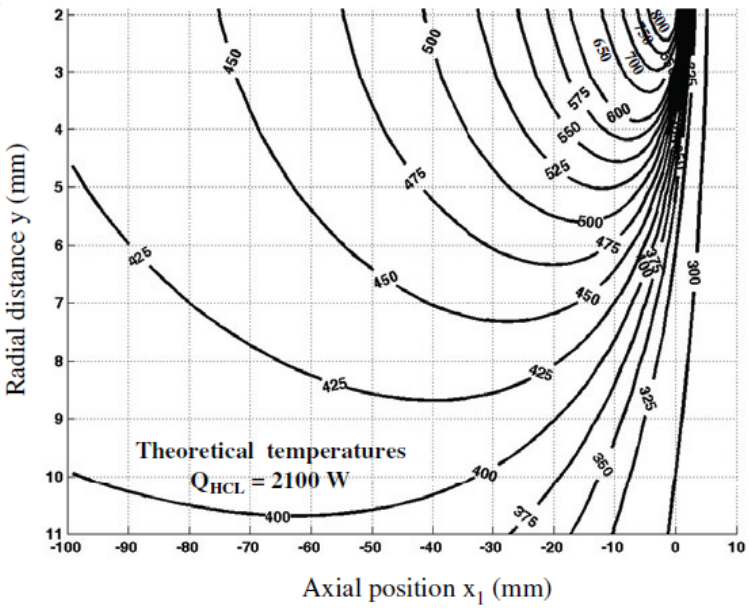

Figure 5.8 Plot of predicted temperature isotherms with respect to X and Y position from equations 5.1 (Teulet et al., 2006).

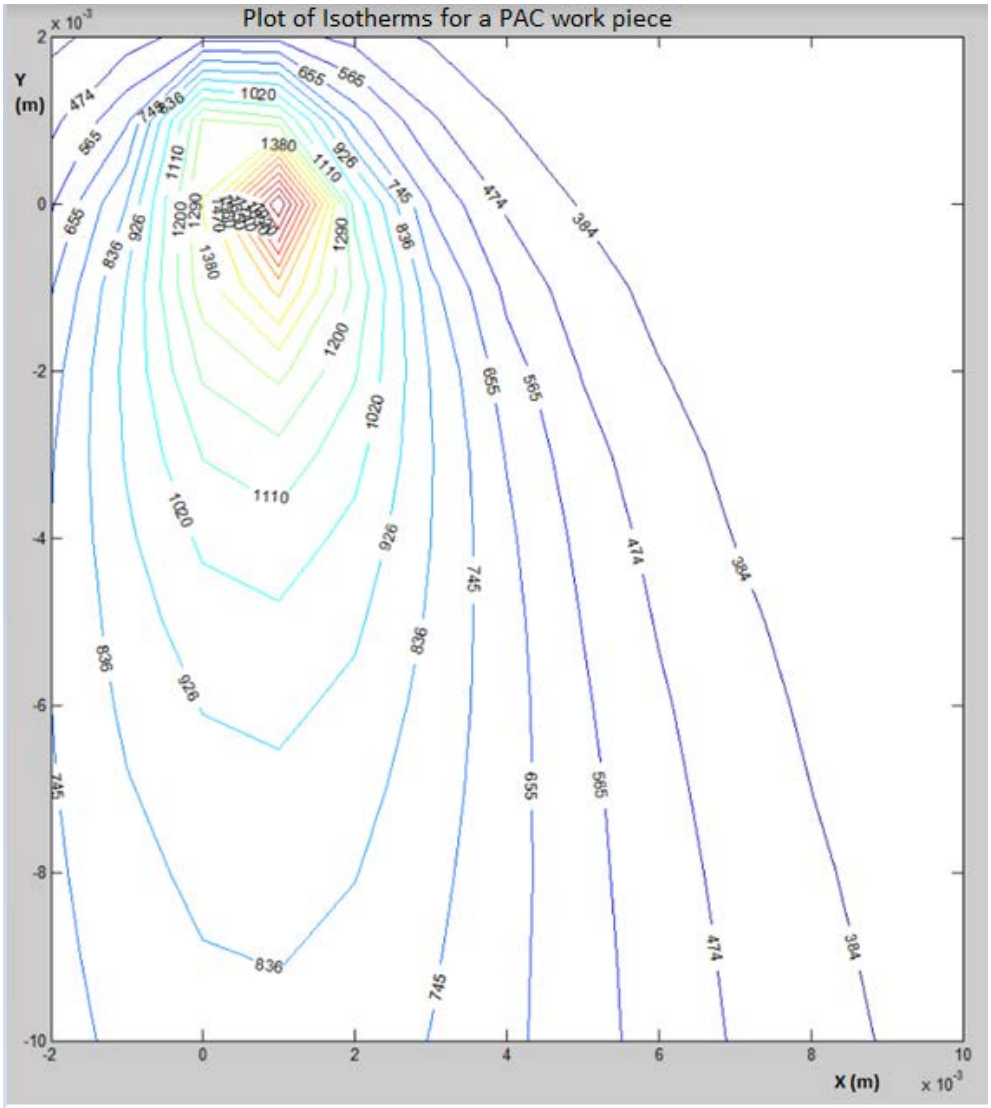

Figure 5.9 Plot of isotherms from equation 5.2 when plotted over the range -2 to 10mm for the Y-axis showing the asymmetry of the model.

Equation 5.1 from the literature was modified to reflect the logical assumption that symmetrical heating would occur on either side of the arc. The modified equation (equation 5.2) takes the integral over the range of -π/2 to π/2 and reduces the scaling factor to account for this larger summation of heat sources. There is still reasonable agreement, between the isotherms, over the range presented by Teulet. However, the profile over the whole region seems more realistic (Figure 5.10).

$$T(M) = T_0 + \frac{Q_{HCL}}{2\pi^2 \kappa_t h} * \int_{-\frac{\pi}{2}}^{\frac{\pi}{2}} \exp\left(-\frac{\rho c_p v_t x_1(\theta)}{2\alpha_d}\right) * K_0\left(\frac{\rho c_p v_t r(\theta)}{2\alpha_d}\right) d\theta \qquad (5.2)$$

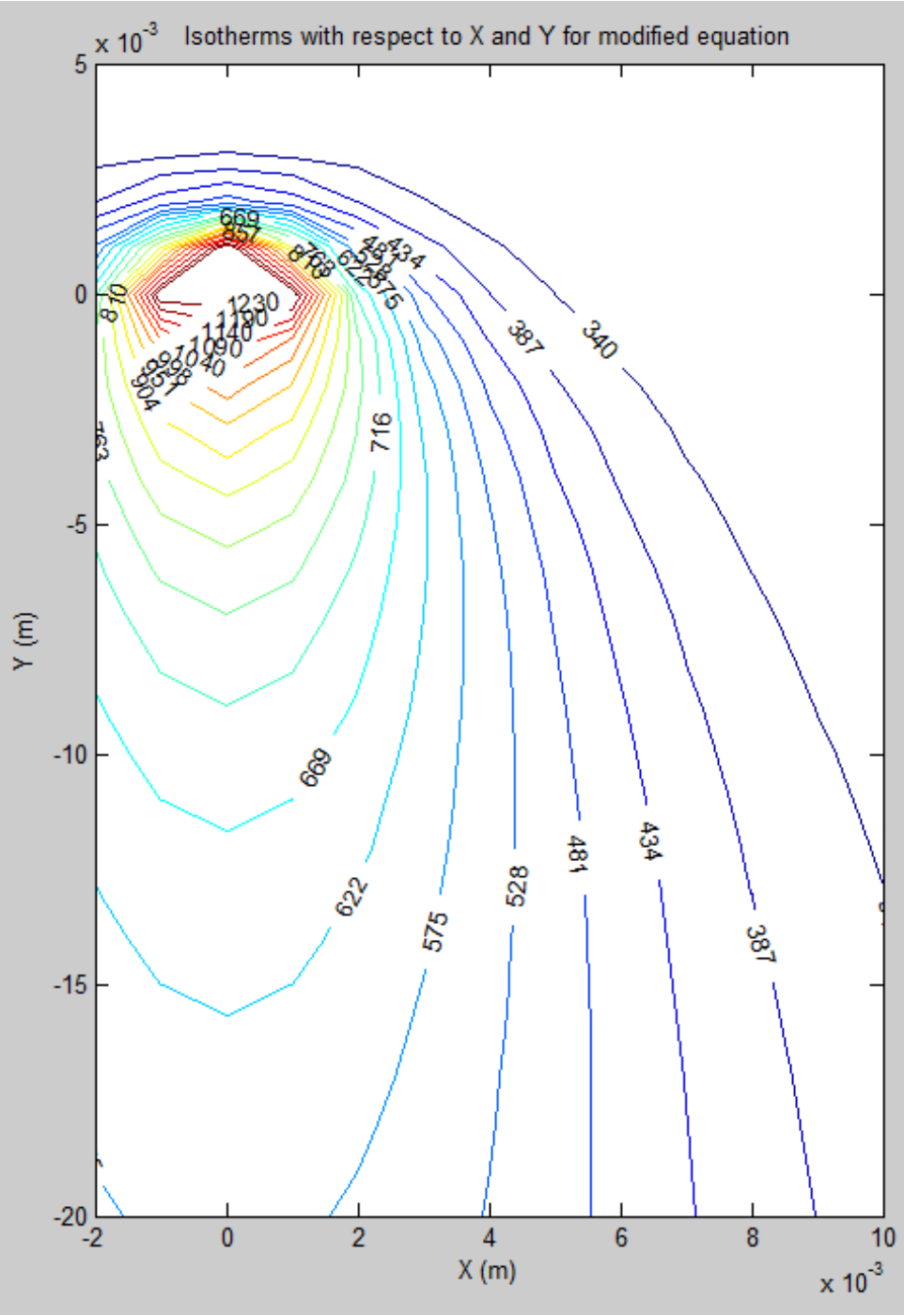

Figure 5.10 Plot of isotherms with respect to X and Y for the modified equation.

Accepting this modification, derivatives can be obtained for $\frac{\delta T}{\delta r}$ at each point around the front cut face semicircle and these can be used to predict the heat conduction away from the plasma and into the material. These derivatives reflect the temperature gradient with respect to radius at each point around the semicircle of the front cut face. Figure 5.11 presents a set of temperature derivatives at the edge of the arc.

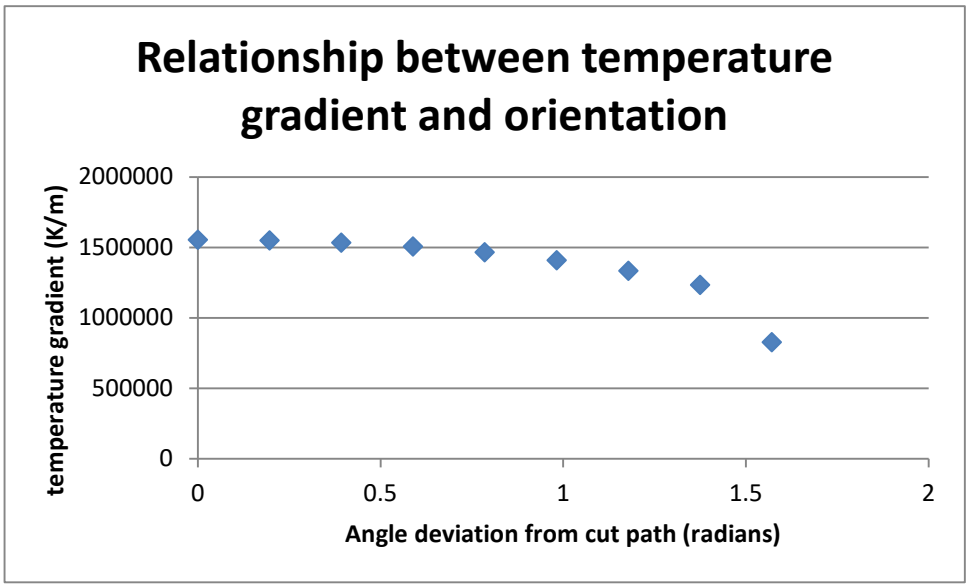

Figure 5.11 Plot of the relationship between the temperature gradient and the angle deviation from the cut path at the kerf edge for a 1mm radius kerf

Knowledge of this derivative, together with the coefficient of heat conduction for steel makes it possible to predict conductive heat transfer into the metal at each point.

5.2 Investigation into radiative heat transfer for PAC

Intuitively, it seems possible that the plasma would radiate significant heat and that this should be considered in a cutting model. The literature has modelled the process several times with varying results and conditions, but all researchers agree that radiation heat transfer is slight (Nemchinsky & Severance, 2009; Teulet et al., 2006). Naghizadeh-Kashani, Cressault, and Gleizes (2002) performed a careful analysis of the emission and absorption spectra, together with the effects of Bremsstrahlung. This is an extremely complex area of analysis and the authors believe that their results are probably accurate to 2 orders of magnitude. Given this indeterminate modern analysis, it seems that this effect should be experimentally determined, so an experiment was undertaken to quantify this heat source. The goal of the experiment was to minimize the amount of heat input to a plate from all other sources except radiative heat transfer. Achieving this would give a reasonable indication of the heat flux from radiation.

The concept of the experiment was to establish a free arc between a thermally conductive anode and the cathode. The anode would be water cooled so that the arc did not degrade it. Similar arrangements have been implemented in the literature; typically a rotating anode is used to distribute the heat (Freton et al., 2001). With an established arc in place, the radiation of the arc could be measured by positioning a plate around the arc and measuring the change in temperature profile of the plate with time. In order to reduce heat losses from the plate and reduce the risk of heat being transmitted to the plate from other sources, it was thermally lagged in all other directions. The temperature of the plate was measured with embedded resistance temperature detectors (RTD). This initial concept was developed to provide a functional experiment.

5.2.1 Materials and methods for evaluation of radiative heat transfer from the arc

The initial experimental plan is shown in Figure 5.12. A brass anode was chosen due to its high thermal conductivity. Channels were cut into the brass to allow water to be pumped through, cooling the material. A steel collar was positioned on top of the brass anode. The collar had thermal insulation provided above and below the plate, ideally restricting heat input to just the arc's radiation (Figure 5.13). The insulation material was a refractory paste.

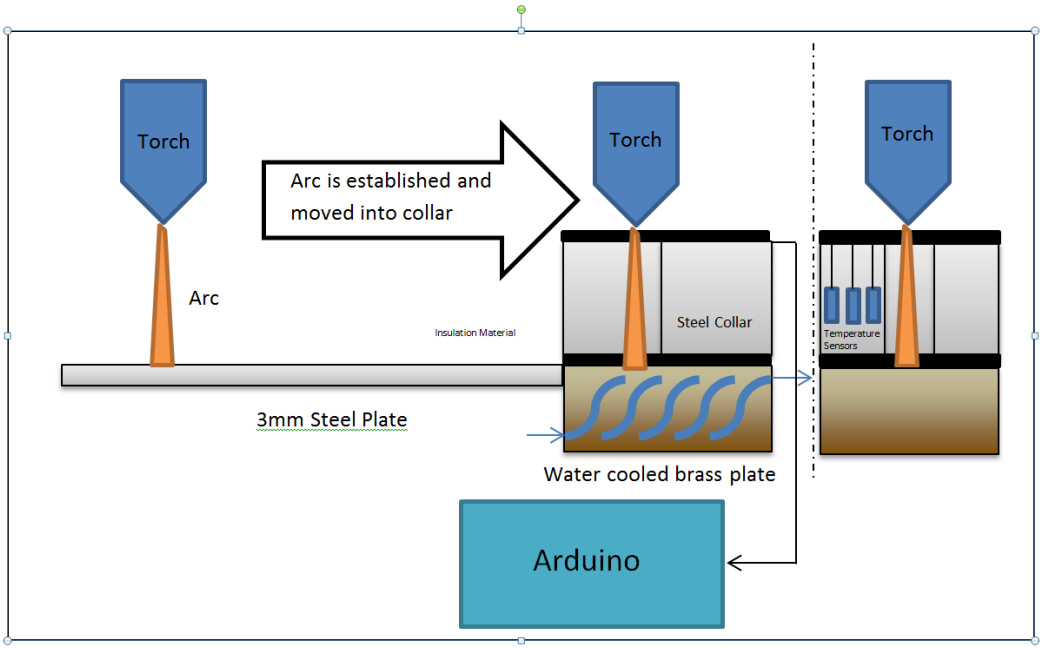

Figure 5.12 Diagram of the experiment to measure heat transferred by radiation.

Figure 5.13 Picture of the thermally lagged steel collar with embedded RTDs.

RTDs were positioned throughout the plate at various radii and angles. A circuit was designed to set them up as a voltage divider so that as their resistance varied with temperature, the voltage at a measured point would vary and allow the determination of the temperature. This measurement was performed with an Arduino Due. The Due streamed the voltage measurements every 10s to a serial port where it was logged on a laptop.

The experiment began with the steel collar at or close to ambient temperature. An arc was struck using a sacrificial steel plate and then moved into the centre of the collar. The arc was maintained at this station for 15s before being extinguished. The heat transferred to the plate was calculated from the data. Figure 5.14 illustrates the layout of the components.

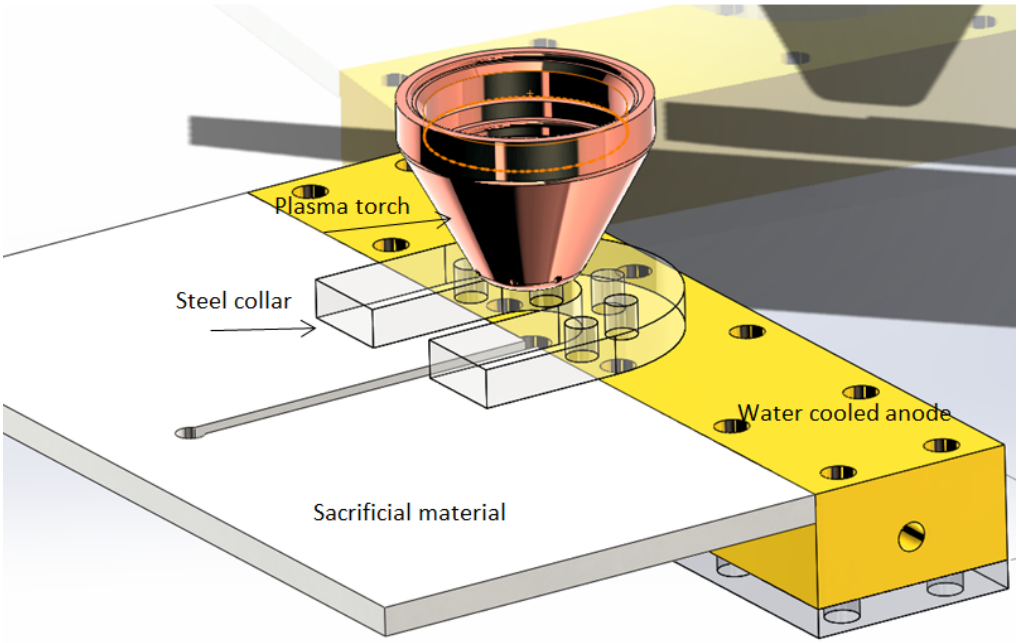

Figure 5.14 SolidWorks™ model of several components for the radiation experiment in relation to each other.

5.2.1.1 Water cooled anode.

The water-cooled anode designed for the test is shown in Figure 5.15. It was made from 12mm-thick brass. A 10mm slot (in Figure 5.14) was cut through the centre of the part. A small half cylinder of 2mm radius was excised to locate the plasma jet in its test position. This is where the arc was expected to attach and the primary location of heat transfer. Standard 1/8th inch BSP fittings were attached to either end of the pipe to allow a hose to be connected for the intake and exhaust. A 2mm-thick steel plate was bolted to the top of the anode to seal the channel. Finally, a paper gasket was placed between the brass and steel, sealing against water leaks.

Experimental work showed that for an arc length of 12mm, with a current of 45A, the arc voltage would be 190V. In the worst case, all this heat energy would need to be removed by the water. The input energy would be 45A * 190V = 8550W. Assuming that the water is heated from 20 degrees to 100 degrees then the mass flow rate required is given by equation 5.3. Testing of this design validated the capability of the water-cooled anode to maintain the arc without suffering damage.

$$\dot{m} = \frac{Q_{in}}{c_{p(water)} * \Delta T} \tag{5.3}$$

$$\dot{m} = \frac{8550\frac{J}{s}}{4.184\frac{J}{gC} * 80°C} = 26\frac{g}{s} \tag{5.4}$$

Where $\dot{m}$ is the mass flow rate, Q_{in} is the total energy in, $c_{p(water)}$ is the specific heat capacity of water, and ΔT is the temperature change.

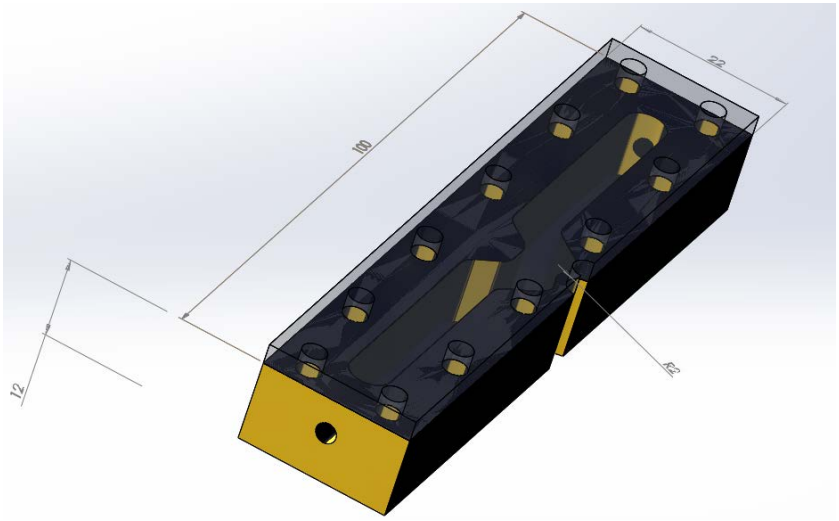

Figure 5.15 Solidworks model of water-cooled anode.

5.2.1.2 Steel Collar

The collar required appropriate thermal mass so that the plate would heat up sufficiently to view the heat transfer, but would not heat up too quickly. Figure 5.16 shows the initial concept for the collar. It housed the thermal sensors at varying radii and angles with replicates at a radius of 9mm to view the deviation between sensors. The location of the thermal sensors changed throughout development of the collar.

Figure 5.16 Initial design for steel collar. The RTDs are housed in the holes, which are located at varying radii.

Experimentation showed that the maximum arc length the PAC system could achieve was approximately 12mm. Therefore, the thickness of the piece was set at 6mm, which would allow a few millimetres of variation in the Z axis to investigate a relationship with height. After some development, this was reduced to 3mm. The radius of the outer circumference of the collar was set at 75mm as a size that comfortably fit on the anode and provided sufficient thermal mass. The diameter of the inner circle was set to 10mm. This distance gave the arc a wide berth, reducing the chance of the arc shorting to the collar, and then arcing from the collar to the anode. Holes were initially placed at radii of 7.5, 9 and 10.5mm from the centre with the replicates at 9mm.

5.2.1.3 Thermal Sensors

A PT100 was chosen for the thermal sensor. Since the temperature range of the test was not known, but had the potential to get quite hot, a sensor was selected that could go up to 600 degrees. The sensor dimensions were 1.6 x 1.2 x 0.8mm and had a response time of 2.5ms in air. The relationship between resistance and temperature was given by:

$$R(T) = R_0(1 + A_{RTD}T + B_{RTD}T^2) \quad (5.5)$$

Where R(T) is the resistance at a temperature, T, R_0 is the initial resistance, in this case 100Ω, and A and B are the linear and parabolic response which are $3.9083*10^{-3}$ and $-5.775*10^{-7}$ respectively (*600 C series Platinum sensor with wires for high temperatures*).

5.2.1.4 Voltage Divider Circuit

A simple voltage divider circuit was used to provide a signal that the micro controller could process. A 188Ω resistor was placed in series with the PT100, connecting voltage to ground. The Arduino then read the voltage between the 2 resistors and as the PT100's resistance varied, the voltage at the measured point varied, allowing the calculation of the temperature.

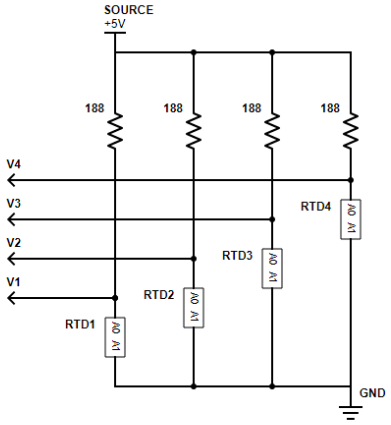

Figure 5.17 Schematic for voltage divider circuit.

5.2.1.5 Microcontroller

An Arduino Due was chosen as the microcontroller to collect the data with. The Arduino Due offered more than 6 analogue input pins with 10-bit resolution which would sample the 6 voltages to a reasonable accuracy. The Arduino Due was also readily available and easy to set up, so it seemed a suitable choice. The Arduino Due was programmed to read the voltage of each pin every 0.1s and stream these voltages to the serial port.

5.2.1.6 Refractory compound

Cemix Latite was chosen as the refractory compound. It provided a thermally resistive coating to the steel collar so that heat losses out of the collar could be assumed to be negligible. The thermal conductivity for this is $\lambda = 0.6\ W/mK$ whilst the thermal conductivity of steel is $\lambda = 46\ W/mK$ at a termpeature of 25 degrees. The Cemix Latite was also cheap and readily available.

5.2.1.7 Sacrificial plate

A sacrificial plate was required to strike the arc from. The arc was struck on the sacrificial plate at a length of 3.8mm and then moved into the steel collar. 3mm mild steel was used for the sacrificial plate.

5.2.2 Experimental plan

For several heights, the arc was struck and then it was moved to a stable position at the notch in the anode. Outputs from the sensors were logged. This procedure was repeated with the height of the test piece ranging from 0mm above the anode, to 5mm above the anode.

The heating imparted to the plate was relatively low. The temperature of the plate rose from just under 30 degrees to approximately 50 degrees over the 15 seconds of the test.

This implied that radiative heat transfer was slight. To assess the effect of the absorptivity of the steel surface, the face was coated with lamp black from a candle. This is reported in the literature to have a coefficient approaching unity. A polished steel surface could be expected to have about one twentieth of this value. The experiment was re-run with a coating of lampblack and no differences in before and after profiles were detected.

5.2.3 Temperature calculation

The temperature at the position of each of the sensor was calculated by measuring the voltage drop across each of the RTDs every 0.1s. This voltage could then be converted to a temperature by:

First, the voltage is converted to a resistance by:

$$res_{RTD} = \frac{188 * V_{RTD}}{5 - V_{RTD}} \tag{5.6}$$

Equation 5.5 is then rearranged to solve for temperature given a resistance. Since it is quadratic in nature, it is rearranged into standard form.

$$B_{RTD}T^2 + A_{RTD}T + \frac{res_0 - res(T)}{res_0} = 0 \tag{5.7}$$

Therefore:

$$A = B_{RTD};\ B = A_{RTD};\ C = \frac{res_0 - res(T)}{res_0} \tag{5.8}$$

And temperature for a given resistance can be calculated using the quadratic formula.

5.2.4 Results

For detailed data on the measurements made during each of the tests please refer to Appendix F. Appendix F contains plots of each of the measurements made from the 4 sensors every 0.1s for each of the test heights. Figure 5.18 presents the data from 4th test where the test piece is placed 4mm above the anode.

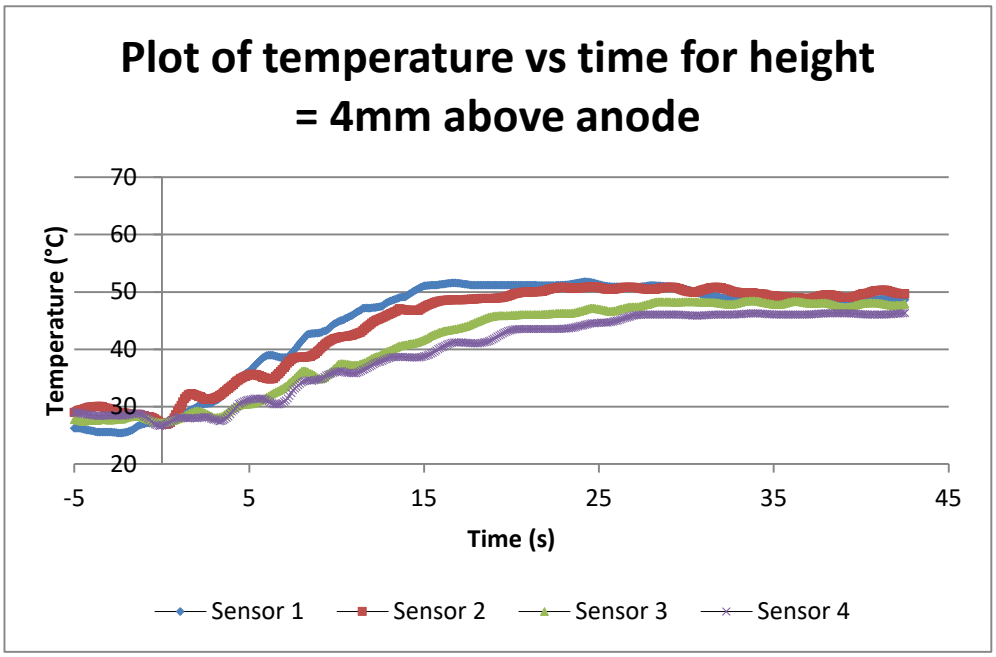

Figure 5.18 A plot of the temperature measured at each of 4 sensor positions over time during the radiant energy test with the test piece at a height of 4mm.

Figure 5.19 and Figure 5.20 present the summarized data from the 5 tests. Time = 0s has been set for where the arc was ignited. Approximately 5s before ignition is shown to demonstrate the

steady state of the temperature before ignition, and the final 10s of the plot shows the steady state of the temperature at the end of the test. Figure 5.19 shows the average start and end temperatures of the test piece over 40s for reach of the tests. The average temperature is just calculated as the mean of the 4 temperature measurements at any one time. One can observe that the temperature spread in Figure 5.18 is relatively small when the temperature arrives at steady state (within 5 degrees). Therefore, this is sufficient for the purpose of estimating the temperature of the plate in later calculations. Figure 5.20 presents the change in temperature from the start temperature for each of the tests. The calculations for heat transfer due to radiation use the total temperature change rather than temperature at a specific time, so this data is useful.

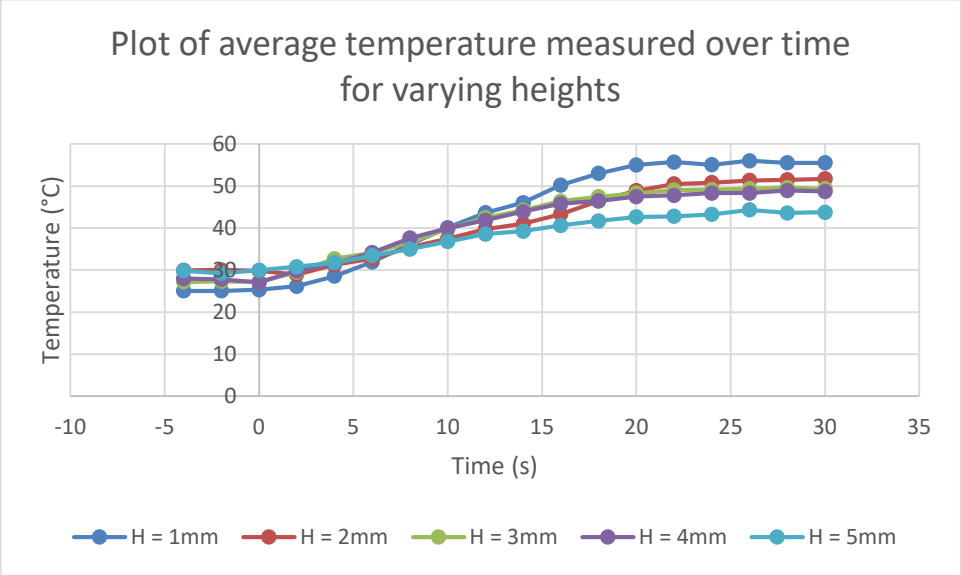

Figure 5.19 Plot of the average temperatures over time of the test piece at the 5 test heights

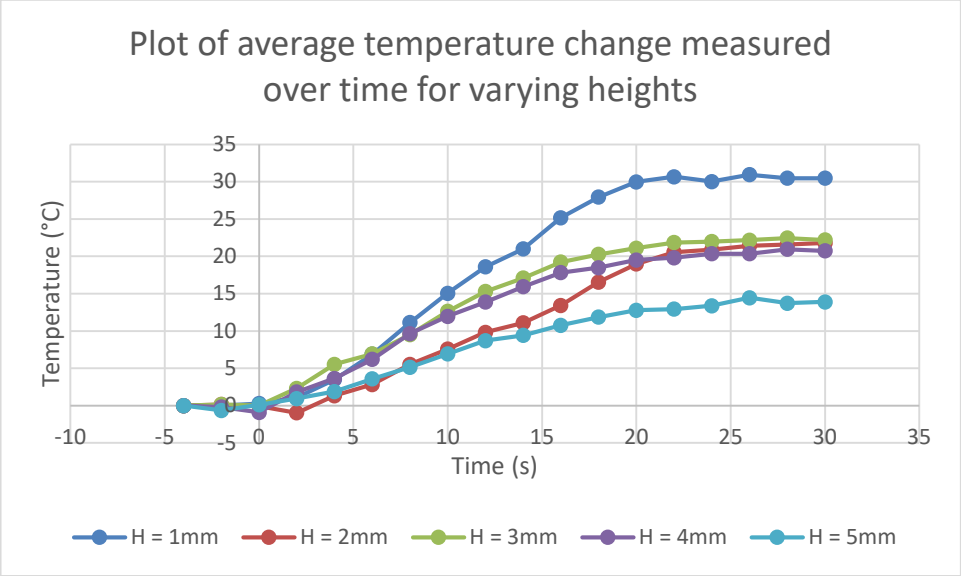

Figure 5.20 Plot of the average temperature change for each of the 5 test heights.

5.2.4.1 Calculation of energy input

The objective of this experiment was to measure the amount of energy put into the test piece via

radiation. This can be calculated as the amount of energy required to heat the test piece. The temperature measurement can be assumed to be accurate to 5 degrees, since that is the largest difference presented in the data for the plate at steady state. The largest temperature change observed in the experiment was 31 degrees for the first test, however this result seems too high as discussed in section 5.2.5, therefore a temperature change of 21 degrees (the median temperature change from the 5 tests) will be used. This is the temperature change reported by tests 2, 3 and 4. The specific heat of mild steel, c_p , is 502$\frac{J}{kgK}$. The mass of test piece was measured at 120 grams.

$$E = c_p * m * \Delta T \tag{5.9}$$

Substituting, we get:

$$E = 502 * 0.12 * 21 = 1{,}265.04\, Joules \tag{5.10}$$

$$E = 1300 \pm 300\, Joules$$

This energy was transferred over 15s, therefore

$$P_o = \frac{1265.04}{15} = 84.3\, W \tag{5.11}$$

$$P_o = 80 \pm 20\, W$$

The total amount of Power put into the plasma-arc is given by:

$$P_o = IV \tag{5.12}$$

Where the current, I, was 45A and the voltage, V, required to maintain an arc of 12mm is 180V. Therefore:

$$P_o = 45 * 180 = 8{,}100W \tag{5.13}$$

The ratio of the energy transferred by radiation can be given as:

$$Ratio = \frac{80}{8100} = 1.0 \pm 0.2\% \tag{5.14}$$

The amount of energy transferred by radiation follows Newton's Inverse Square Law, which states that:

$$\frac{I_1}{I_2} = \frac{r_2^2}{r_1^2} \tag{5.15}$$

Where I is the intensity of the radiation and D is the distance from the source. As laid out in Section 2.4 (from literature review) and Section 5.4.3 (further on in the modelling section) the diameter of the jet expands as it travels downstream. This expansion is rapid through the shock and then slows down significantly, arriving at somewhere between 2 and 3 times the nozzle diameter, directly after the shock. The amount expanded varies depending on gas and air properties. However, an estimate of a radius of 3mm, 6 nozzle diameters away from the nozzle seems realistic. This conforms to the size of the indent cut into the anode from sustaining this arc.

Therefore, we can estimate the ratio of the energy transferred at 5mm from the arc, compared to 3mm from the arc as:

$$\frac{I_1}{I_2} = \frac{5^2}{3^2} = 2.8 \tag{5.16}$$

Resulting in a total power transferred via radiation as:

$$1.5 * 2.8 = 2.8 \pm 0.6\% \tag{5.17}$$

5.2.5 Discussion

The results in section 1.2.4 show the measurements made, the summarized data for all the tests and the calculation of the energy transferred via radiation. A few points need to be made regarding the validity of the data, the trends apparent and the resulting energy calculation.

5.2.5.1 Experimental Results

Figure 5.18 shows an example of the temperature measurements made for one test. There is quite a bit of noise evident in the graph. This is most likely due to the large amount of current flowing near the sensors. A smoothing filter has been applied to the data to make the trend clearer, however any specific temperature measurement should be used with caution. Since the temperature change is calculated using the steady state temperature at the beginning and end of the test, this noise is not considered a problem for application the data is used for.

The data itself for the temperature change appears valid. The temperature measured at the smallest distance from the arc (sensor 1) heats up the most rapidly, and the sensor with the largest radial distance (sensor 4) heats up the slowest. All the sensors report the same temperature to within a few degrees of each other and the beginning and end of the test, once the energy has had time to dissipate through the test piece. These are expected trends and help to confirm the validity of the data.

There is a lag between finishing applying heat with the arc at 15s, and the plate reaching its maximum temperature. This lag is approximately 5 seconds and is most likely due to three factors. Firstly, it takes time for energy absorbed closer to the arc to be dissipated to the rest of the plate. Therefore, the 4 sensors have different rates of temperature increase, and since there is still 5mm of distance between the plate edge and the first sensor one would expect that to be reflected. Secondly, it will take time for the hot air where the arc is to decrease back to the temperature of the plate, so there will still be some energy being added to the plate after the arc is extinguished. Finally, the experimental methodology leaves some uncertainty as to when the arc was actually started, so there is potentially a few seconds of leeway in the position of time = 0s in the graphs.

Finally, there is an unexpected trend in the amount of temperature change experienced in each test. Section 2.2.3 of the literature review presents multiple works showing the decrease of temperature as the arc moves away from the nozzle. This would imply a reduced radiant heat transfer as the test piece moves away from the nozzle. However, the first test, where the test piece was located the farthest away from the arc had the most temperature change, and the temperature change decreased as the test piece was raised. This potentially implies that heat transfer was also occurring from the anode which was being heated to roughly 700 degrees. Therefore, this estimation of radiant heat temperature is probably too high, and it might be more realistic to use the temperature change for tests 3 – 5. In which case, the radiant heat transfer is between 0.5 – 1% in our experiment and between 1 – 3% in practice.

5.2.5.2 Energy calculation

This estimation of radiant heat transfer conforms to what is presented in the literature. Nemchinsky has suggested it is negligible in multiple works, and Lazarevic neglected to include it as a factor in his energy balance (Lazarevic, Manic, & Lazarevic, 2011; Nemchinsky, 2017; Nemchinsky & Severance, 2006). The interested reader is directed to the discussion of radiant heat transfer in the literature review (Section 2.2.4).

During the experimental setup, trial tests were conducted with lamp black applied to the absorption service to raise the absorptivity. The absorptivity of a black surface is close to 1 whilst the absorptivity of somewhat tarnished metal is between 0.3 and 0.9. A shiny metal surface's absorptivity is approximately 0.05. Since the absorption surface was produced by milling, the absorptivity would be expected to be between 0.3 and 0.05 (FLIR, 2017). The amount of radiation energy absorbed is directly proportional to the absorptivity of an object. However, no discernible difference was observed between the two experimental set ups, which also suggests that radiation is insignificant.

The estimation presented here has a large amount of uncertainty. The key factors that influence this are the estimation of the arc width for the scaling factor between this experiment and practical

application, and the uncertainty in the temperature measurements. The observation that the observed energy transferred decreased as the test piece was raised suggests that another form of energy transfer is still evident. Therefore, the amount of energy transferred via radiation could be significantly lower than the 3% calculated here.

5.2.6 Conclusions and Recommendations

The conclusion is drawn that the heat transfer by radiation is low. Due to its accordance with the assumptions in the literature, and the presence of expected trends in the data, this estimation seems appropriate. Further work can be done to try to improve this estimation. This work could take the form of redesigning the experiment to further reduce the possibility of other heat transfer methods or using more accurate equipment for temperature measurement. However, this value represents a quantification of the amount of energy transferred by radiation, which answers the question that has been presented in the literature.

5.3 Investigation of kerf profiles

The final experimental effort was to determine the shape of the front end of the cut. This was accomplished by performing PAC slot cuts and examining the cross sections of the cuts. Two experiments were designed to obtain this information. The first experiment attempted to get the profile of the kerf along the centre-line of the cut. The second obtained data to model the profile of the front face of the cut.

5.3.1 Experiment 1: Centreline profiles

The goal of the first experiment was to determine by experiment the shape of the profile of the kerf at the leading edge along the centre of the kerf. This information was of value because the shape of the profile changes with process parameters, but most directly with feed rate. Conceptually feed rate directly affects the rate of heat transfer to a section of the kerf, by altering how long the section is exposed. It is observed in the literature and experimentally that the plasma-arc deflects as the feed rate is increased and approaches vertical as the feed rate is lowered. This change in arc orientation is bound to influence the heat transfer to the metal. This phenomenon has not been quantified or explained in the literature. Therefore, this experiment attempts to quantify it.

Observing the front profile of the kerf is a challenging endeavour. Whilst cutting, the plasma-arc frustrates attempts to view the front face. Further the kerf is small and making measurements inside it is difficult and intricate. Finally, as process parameters are varied, the kerf angles change on the left and right side of the cut, thus changing the axis of the cut.

5.3.1.1 Experimental Plan

An experiment was designed that could overcome these challenges and acquire the information. A series of slots was cut into a steel work piece. The arc pierced the plate and proceeded for approximately 50mm to ensure steady state. At approximately 50mm, the arc was switched off and the torch continued to move. This ensured that the arc did not dwell at the end of the cut and that the cooling jet, that continued to run after cutting completes, did not affect the shape of the profile.

This experiment aimed to assess the relationship that feed rate and material thickness had on the slope of the leading edge of the kerf. Traditional Design of Experiments (DOE) methods, such as the Taguchi Method, were considered for selecting an efficient number of experiments, however due to the exploratory nature of the experiment and the complexity of some of the interaction effects, all combinations of the parameters were tested.

Feed rate was identified as the most significant variable effecting the slope, and the relationship was presumed to be best explained through a high order relationship. Five levels were chosen to investigate this relationship. Material thickness was suspected to have a 2^{nd} order relationship with the slope angle, therefore 3 levels were tested. Due to the difficulty of replicating

experiments and the goal of the experiment being to identify trends, no replication of runs was undertaken.

Slots were cut out at 5 different feed rates. These feed rates were selected to vary evenly over a range from just above the lower boundary for the dross free zone to just below the upper boundary of the dross free zone. These feed rates were selected using the recommended operating conditions from the Hypertherm Powermax 45 operation manual, and by experiment. Material thickness was also varied. Thicknesses of 6, 8 and 10mm were chosen as they would provide a sufficient length to observe the change in profile of the kerf. Figure 5.21 shows an example of the test cut modelled in SolidWorks™.

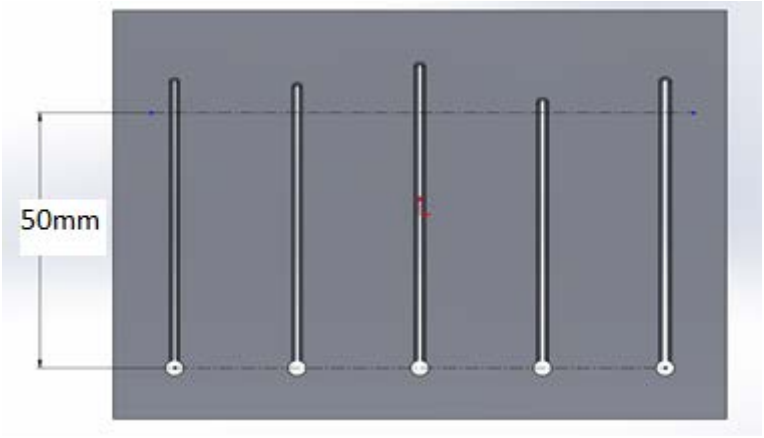

Figure 5.21 An example of the first stage of the experimental cut, drawn in SolidWorks™

Once the test piece slots were cut (Figure 5.21), the slots were sectioned. A combination of band saw, and angle grinder were used to cut the plate a few millimetres away from the centre axis of the top face of the cut. This provided a set of pieces that had a section of the slot cut into them (Figure 5.22). A caliper was then used to estimate the difference in kerf width between the top of the slot and the bottom of the slot, and from this the kerf angle of the slot for the remaining face. A vice capable of being rotated was then used to adjust the test piece so that the central axis of the cut was parallel with a horizontal plane. A face mill was then used to face the slot down to the centre point of the slot. This was repeated for all the test pieces.

Figure 5.22 An example of a sectioned slot, drawn in SolidWorks™

The result of these operations was an exposed section of the kerf profile along the axis of the cut. These edges were photographed, and edge data was obtained. This data demonstrated the trends observed in the arc from the perspective of the kerf. Figure 5.23 demonstrates one such edge. For more detailed information on the process parameters for these experiments please refer to Appendix G.

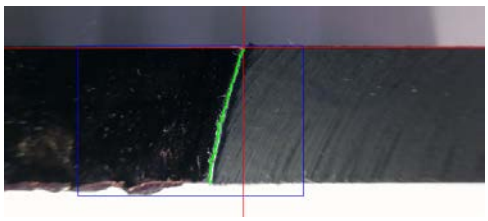

Figure 5.23 Example image of the exposed section for the kerf profile on the cut axis.

5.3.1.2 Results

Table 5.1 shows the summary of the test results. For each of the fifteen trials the corresponding process parameters are shown. From the data points obtained for that process parameter combination, a corresponding graph is presented in Appendix G. A parabola was then fitted to the data points. The parabola was set to intercept the origin, therefore only the A and B parabola parameters were non-zero. These parameters are also shown in the test results.

Table 5.1: Summary of results for Experiment 1 (T# = Test Number).

Profile Experiment 1: Test Results					
	Process Parameters			Parabola Constants	
T#	Thickness (mm)	Feed rate (mm/min)	Height (mm)	A	B
1	6	2000	1.5	-0.07	2.05
2	6	1800	1.5	-1.09	1.29
3	6	1600	1.5	-0.39	2.95
4	6	1400	1.5	-0.41	1.69
5	6	1200	1.5	-0.90	1.50
6	8	1200	1.5	0.10	2.98
7	8	1100	1.5	-0.36	2.22
8	8	1000	1.5	-0.36	2.33
9	8	900	1.5	-0.59	2.39
10	8	800	1.5	-0.33	2.88
11	10	800	1.5	-0.84	2.47
12	10	725	1.5	-0.15	3.93
13	10	650	1.5	-1.52	1.33
14	10	575	1.5	-0.66	3.49
15	10	500	1.5	-0.32	3.33

Figure 5.24 shows an example set of data points acquired, and the parabola that was fit to the curve. The data points are smoothed with a 5-point moving average. This is to compensate for the large level of noise in some of the images.

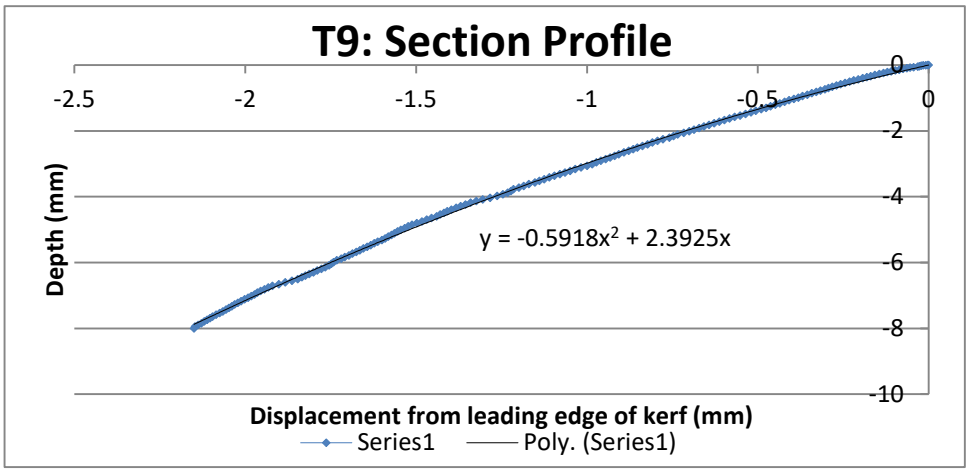

Figure 5.24 Data points found for test 9 in experiment 1 with a fit parabola.

5.3.1.3 Discussion

The experimental method and results show the process and corresponding measurements made for this experiment. However, a few observations need to be made to evaluate the usefulness and potential error in these results. These are:

- Discussion on the validity of the edge points.
- Discussion on the results obtained and their validity.
- Summary of the trends observed.

The first concern of this experiment is to judge the accuracy of the edge points. There are two main sources of error. The first comes from machining the test pieces to expose the section. There will be error in how accurately the midpoint of the profile was found, and how accurate the angle was. While effort was made to align this properly, the cut height would only have been accurate to about 0.1mm and the angle was calculated assuming a kerf symmetry (that has been shown to be invalid). This calculation was visually checked before cutting. The angle error is estimated to be about 2 degrees, which could have introduced an error of up to 0.2mm over a 6mm deep kerf. The second source of error comes from finding the edge points on the kerf with the image analysis. There was substantial noise over the kerf profile due to shiny bits of metal from the PAC process and the subsequent machining. In some cases, this resulted in a shiny swath of metal down the length of the kerf, which caused erroneous edge point detection. Averaging of the data points mitigated this error source.

The second concern for these experiment results is the validity of fitting a parabola to the test results. In some cases, the profile of the section seemed to resemble a parabola over its entire length, such as Figure 5.24. However, in some cases, the profile seems more suited to being modelled with a parabola describing the top of the profile, and a parabola describing the bottom of the profile (Figure 5.25). Conceptually, a concave up parabola seems like the most likely shape of a kerf profile due to the methods of heat transfer. However, the top of the kerf in all cases seems to be more appropriately modelled with a concave down parabola.

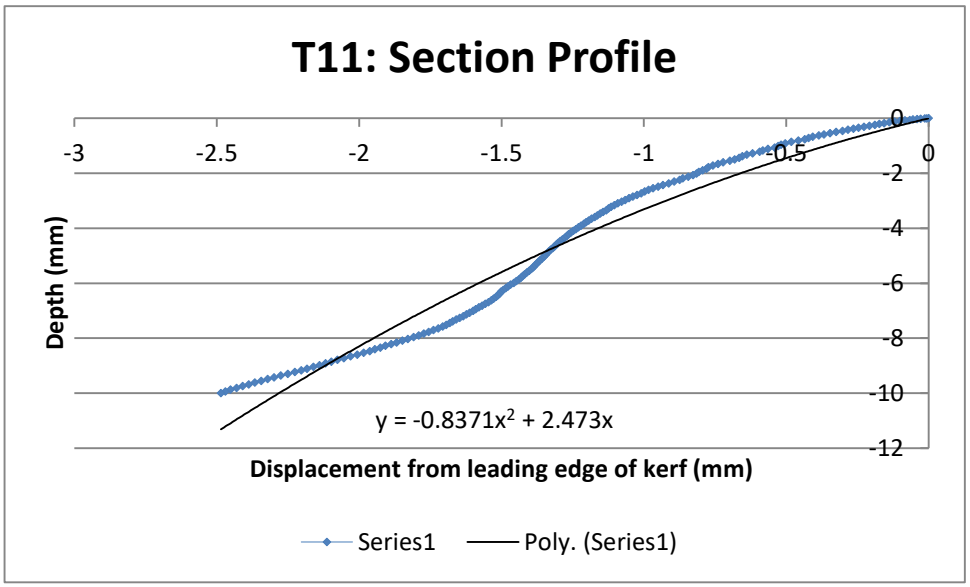

Figure 5.25 Example of a kerf profile better suited to two parabolas.

The final observation from this experiment is the analysis of trends from the data. The parabolas fit to the data do not appear to have a trend; however, this could be due to obfuscation from the regions of the profile. In general, it can be observed that kerf angle increases at higher feed rates for each thickness. Further the amount of bend in the shape also seems to increase. As the feed rate is lowered for each thickness; the kerf angle moves back towards the vertical. This trend is consistent with what has been observed in the literature.

5.3.1.4 Conclusions

This experiment successfully provided data on the front profile of the kerf during PAC and is the first method presented in the literature for acquisition of this data. The data can be used to better understand the phenomenology of heat transfer for the kerf formation process. Future work could focus on examining the profiles in sections and improving the experimental method to increase confidence in the accuracy of the profile obtained.

5.3.2 Experiment 2: Front face profiles

Observations from the literature and experimental work show that the shape of the front of the kerf is roughly a semi-circle. The goal of the second experiment was to quantify the deviation of this profile as it progressed down through the plate. This would provide a level of quantification for the literature as the deflection of the arc has only been described anecdotally, and not in relation to the front profile of the kerf. This may potentially provide insights into the cutting process of the kerf formation process.

The primary challenge in this endeavour was acquiring edge point data at various section of the kerf. No method for acquiring this information exists in the literature on plasma cutting although this is potentially due to no experimental process existing to acquire the leading profile of a kerf. Conventional measures were challenging due to the shape and size of the kerf and would not provide the level of accuracy required.

5.3.2.1 Experimental Plan

An experimental plan was devised to acquire this data. As in the preceding experiment, slots were cut into test pieces and the arc was terminated once it had reached steady state, whilst the torch continued moving. Test pieces were cut for 3 different feed rates, a low level, a medium level and a high level, and at two different material thicknesses, 6mm and 10mm. For a detailed list of profile parameters used for the cutting of the slot, please refer to Appendix G.

Once the 6 test pieces had been acquired, photographs were taken of the top and bottom faces of

each. After these photographs were taken, 2mm was faced off each test piece over the end of the kerf, providing a section view at a different depth. Photographs were taken of the end of the kerf and this process was then repeated. This resulted in 4 profiles of the front end of the kerf being photographed for the 6mm-thick test pieces at depths of 0, 2, 4 and 6mm; and 6 profiles being collected for the 10mm test pieces as depths of 0, 2, 4, 6, 8 and 10mm. Edge detection was then used on these photographs to acquire sets of edge data for each depth. Figure 5.26 and Figure 5.27 shows one such set of photographs, and Figure 5.28 shows the edge points found for one example picture.

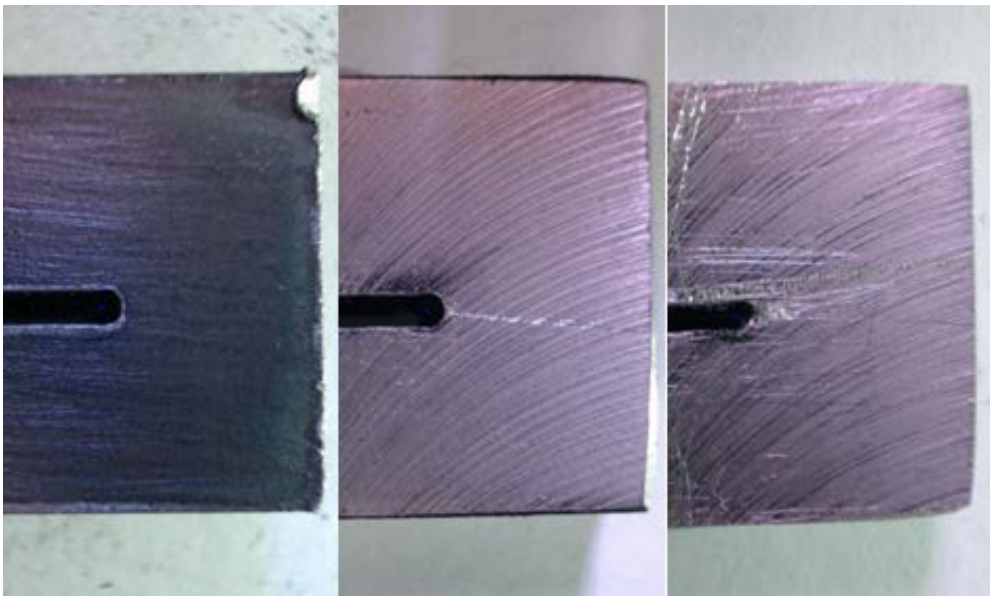

Figure 5.26 Example of profile pictures. 10mm-thick test piece sections at depths of 0, 2 and 4mm.

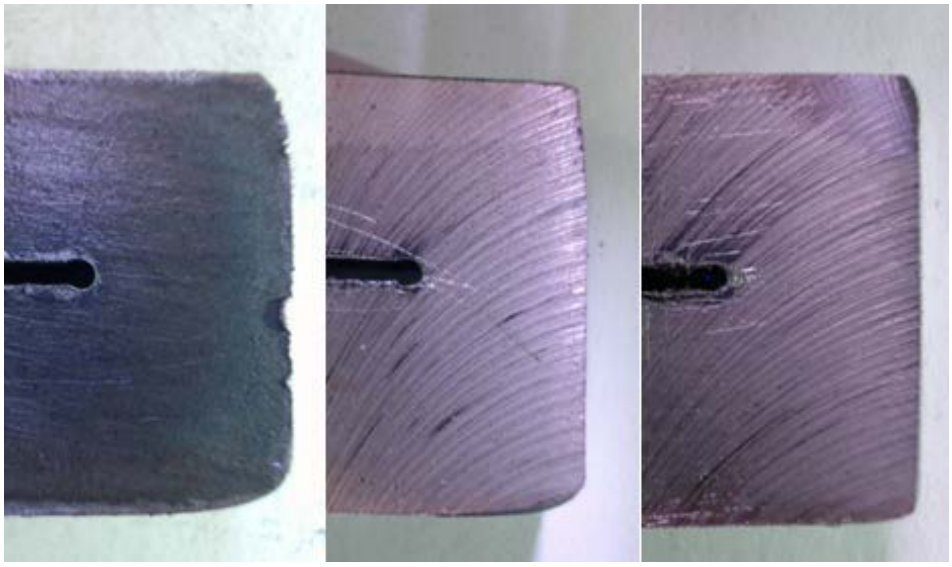

Figure 5.27 Example of profile pictures. 10mm-thick test piece sections at depths of 6, 8 and 10mm.

Figure 5.28 Edge points found for an example test piece.

Each test piece had multiple sets of edge points that described the shape of the end of the kerf. 10mm-thick test pieces had 6 profiles and 6mm-thick test piece had 4 profiles. These profiles were adjusted to move them to a common point of reference. Specifically, images were taken of both sides of the plate to decrease the amount of time taken machining and photographing the test pieces. To compensate for this, the images taken of the reverse side are mirrored. The centre of the arc is located for each image, shown in Figure 5.28 as a blue point. The edge profiles are also scaled in relation to the centre of the arc. This is because as the location of the part changed in relation to the camera, the size of the slot changed in the image. The scaling factor is calculated by using the number of pixels between the top and bottom side of the piece and dividing that by the known width for each part. Finally, a 5-point moving average was used to smooth the radius of the cut part. Due to imperfections in the processing, some test piece profiles have edge point noise from shiny sections of metal. This averaging reduces the weighting of the noisy points. The variation of the cut surface, with its machining marks was not a serious disadvantage in the metrology because the background to the cut section was completely dark and therefore an adequate contrast was obtained on the edge.

5.3.2.2 Experiment 2 Results

The results from Experiment 2 are summarized in Table 5.2. Table 5.2 shows the parameters used, the resulting measurements taken and the order of data acquisition for the experiment. All tests were performed with a torch height of 1.5mm. The results presented here demonstrate the type of data obtained and what one such set of profiles for this data looks like. For information on the results for all the tests please refer to Appendix G.

Table 5.2: Summary of results for Profile experiment 2.

Profile experiment 2: Test results									
Test piece	Test	Image #	Feed rate (mm/min)	Thickness (mm)	Offset (mm)	Height (mm)	Width (mm)	Pm	KW (mm)
1	1	1	650	10	0	10	18.69	18.62	1.48
1	2	3	650	10	2.17	7.83	18.82	16.50	1.46
1	3	5	650	10	4.22	5.78	18.95	16.68	1.27
1	4	6	650	10	4.18	4.18	19.05	16.72	1.13
1	5	4	650	10	1.95	1.95	19.19	16.56	1.17
1	6	2	650	10	0	0	19.31	18.80	1.24
2	7	7	550	10	0	10	18.69	18.79	1.84
2	8	9	550	10	2.21	7.79	18.82	16.39	1.39
2	9	11	550	10	3.9	6.1	18.91	16.43	0.85
2	10	12	550	10	3.78	3.78	19.04	16.50	1.57
2	11	10	550	10	2.12	2.12	19.14	16.63	1.25
2	12	8	550	10	0	0	19.26	18.78	1.35
3	13	13	450	10	0	10	18.50	19.05	1.52
3	14	15	450	10	2.02	7.98	18.53	16.64	1.56
3	15	17	450	10	4.05	5.95	18.56	16.55	1.32
3	16	18	450	10	3.86	3.86	18.60	16.53	1.19
3	17	16	450	10	2.53	2.53	18.62	16.60	1.15
3	18	14	450	10	0	0	18.66	18.99	1.30
4	19	19	2000	6	0	6	18.12	15.34	2.15
4	20	21	2000	6	1.9	4.1	18.34	15.63	1.26
4	21	22	2000	6	1.97	1.97	18.60	15.61	1.64
4	22	20	2000	6	0	0	18.83	15.69	1.62
5	23	23	1600	6	0	6	18.37	15.24	2.40
5	24	25	1600	6	1.83	4.17	18.48	15.80	1.74
5	25	26	1600	6	1.92	1.92	18.61	15.59	1.70
5	26	24	1600	6	0	0	18.72	15.70	1.63
6	27	27	1200	6	0	6	18.11	15.44	2.53
6	28	29	1200	6	1.77	4.23	18.30	16.04	1.75
6	29	30	1200	6	1.89	1.89	18.56	15.77	1.55
6	30	28	1200	6	0	0	18.77	15.28	2.02

The profiles obtained from the data for test piece 5 are shown in Figure 5.29-Figure 5.31. The first 3 figures show a 3D scatter plot of the data points obtained plotted using MATLAB®. These figures are plotted with various elevations and azimuths that demonstrate salient information. Figure 5.32 shows a plot from above produced with Microsoft Excel.

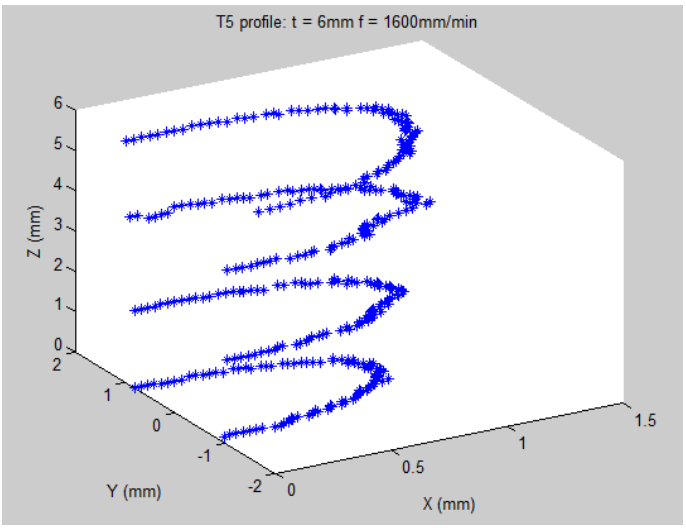

Figure 5.29 3D plot of data points for test piece 5 with azimuth at 30 degrees and elevation at 30 degrees.

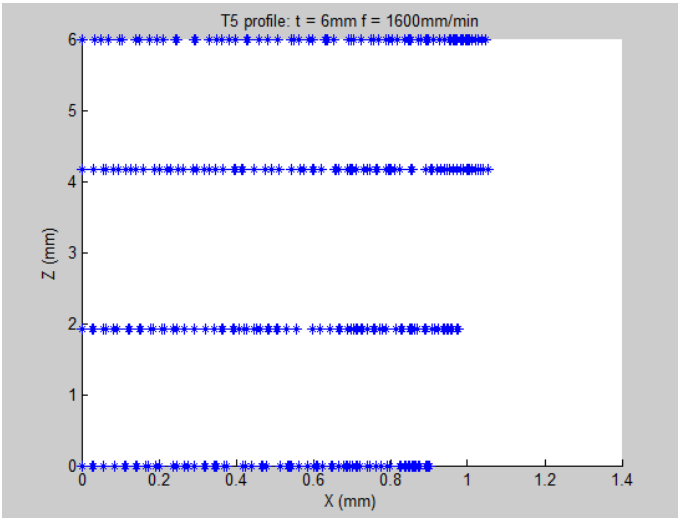

Figure 5.30 3D plot of data points for test piece 5 with azimuth at 0 degrees and elevation at 0 degrees.

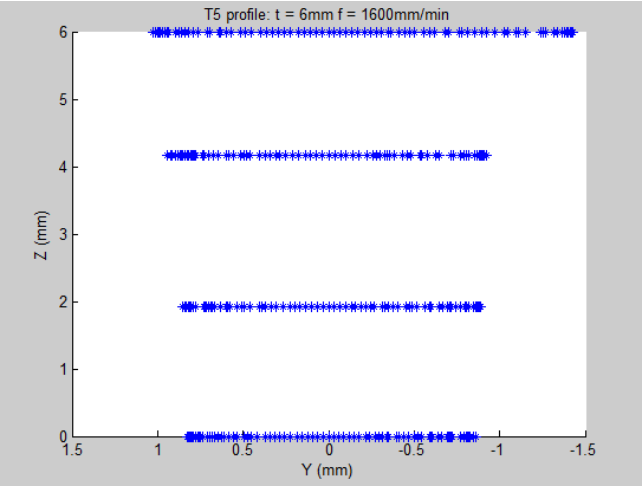

Figure 5.31 3D plot of data points for test piece 5 with azimuth at 90 degrees and elevation at 0 degrees.

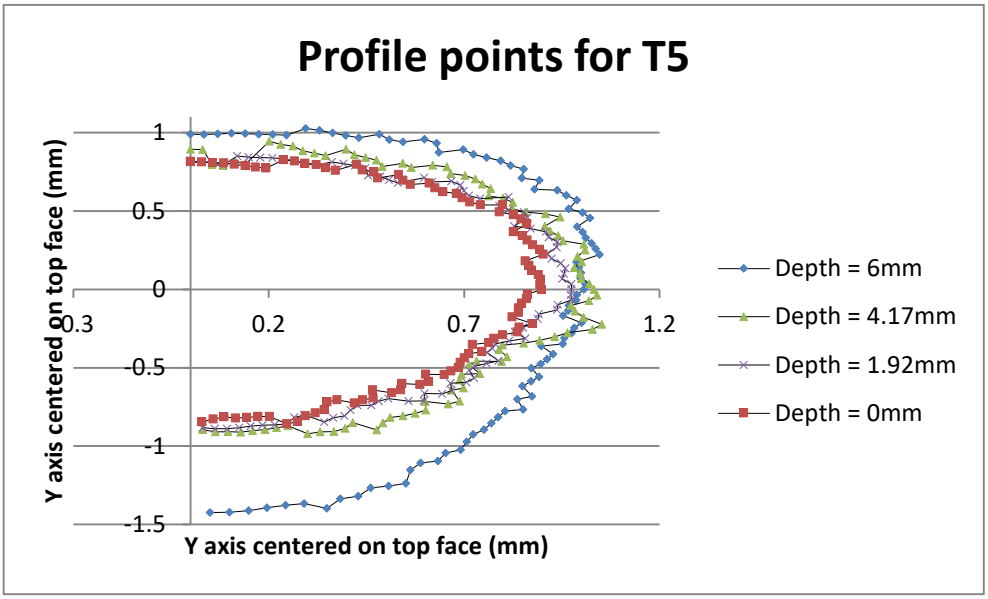

Figure 5.32 Plot of data points for test piece 5 showing the separate depths of data point acquisition.

5.3.2.3 Discussion

Figure 5.29-Figure 5.32 demonstrate a typical set of data obtained. These figures allow the comparison between the variation in kerf width and the variation in the profile of the leading edge of the kerf for various process parameters. It can be observed that the profile of the kerf is not completely smooth over its entire depth through the plate. This is most likely due to compositional deviations in the material and complex interaction effects between the flow of dross out of the kerf and the remaining metal. Some of this deviation is likely due to the method of data acquisition and processing. This could be at either the machining state, where the kerf is somewhat affected by the facing operations, or the data acquisition where noise in the image leads to spurious edge points. However, the deformation in the bottom half of the kerf, towards the leading edge of the kerf appears in the majority of the test results so this is likely to be from mechanics of the kerf formation process.

Various trends are observable from Table 5.2 and the plots shown in Appendix G. Namely, average kerf width for each test piece seems to increase as the feed rate is decreased. This conforms with known behaviour and provides some validation for the data. The overall angle of

the leading edge of the kerf seems to increase as feed rate increases, which confirms the results obtained in experiment 1, and suppositions in the literature.

The data obtained has a potential source of error from the method used to overlay the different sets of data. This was performed as accurately as possible by measuring the centre point of the arc in each of the images and transforming the plots with the pixel scaling factors to place them in a relative reference frame. However, small errors in this would dramatically affect the perceived shape of the profile, so this data is best used to observe trends.

5.3.2.4 Conclusion

This experiment successfully obtained data relating the changing process parameters to the kerf width and to the shape of the leading edge of the cut. It transformed the data points obtained into profiles that confirmed the results of the previous experiment, and the expectations of the literature. The data obtained could be improved by developing a more robust method for the overlay of the various depths, or by using a profilometer to collect the data. However, the method used was sufficient for the goal of observing the relationship between the shape of the leading face of the kerf, and varying process parameters.

5.4 Model development

From observations made in the preceding experimental work and throughout the literature, a model can be developed that predicts the morphology of the front profile and explains it as a result of heat transfer from the plasma-arc. To produce this model, it is necessary to identify the assumed interactions and characteristics of the jet and work piece. The cutting process can be broken down into four key areas, which are:

1. The annulus is sheared off the plasma-arc.
2. Heat transfer to the work piece.
3. Jet structure above the kerf.
4. Temperature gradient inside the kerf.

5.4.1 Structure of the Jet as it leaves the nozzle

A two-zone model describing the plasma jet has been presented in a number of papers (Ramakrishnan & Rogozinski, 1997). It suggests that as gas flows through the nozzle, it heats up and dissociates, becoming a plasma, which is the core. A cooler annulus surrounds this core and is the shielding gas. The central core acts as a conductive pathway between the cathode and work piece and suffers Ohmic heating. This structure is supported by the observation that in normal operating conditions the arc does not attach to the nozzle, due to insulation provided by the cool, non-conducting, annulus. Ramakrishnan calculates that because the central plasma is so hot it has a very low density. Therefore, only about 10% of the mas flow occurs in this central region.

Measurements and modelling of the distribution of temperature and velocity in the jet have been presented in the literature. These suggest that there is, initially, a sharp radial discontinuity in velocity and temperature (Figure 5.33). Further, as the jet proceeds, this discontinuity diminishes due to entrainment between the 2 zones. Over travel of approximately 10 nozzle diameters it has been considerably smoothed (Freton et al., 2001).

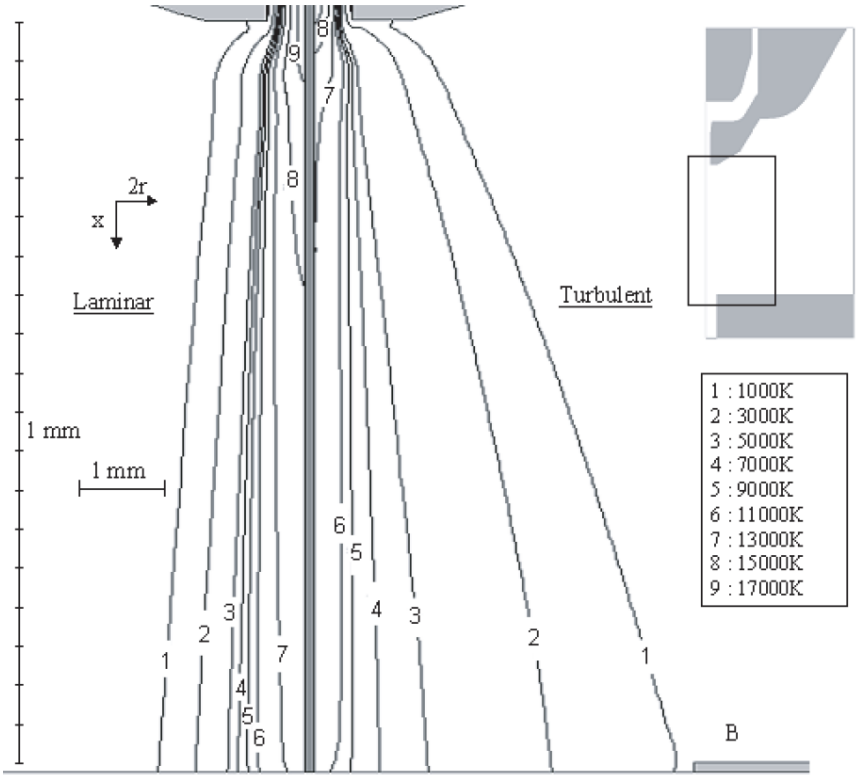

Figure 5.33 Diagram demonstrating radial discontinuity close to the nozzle (T = 13 - 17 000K). Dimishing discontinuity as the jet progresses in the X direction (T = 1 - 11 000K) (Freton et al., 2001).

It is predicted and is in fact observed that a normal shock is present in the central flow at a distance of approximately 1 nozzle diameter downstream of the nozzle (Girard et al., 2006).This occurs because compressible flow in the duct, if it has sufficient driving pressure, will choke to a speed of Mach 1 at the outlet of the duct (Shapiro, 1953). Under these conditions, if the pressure after the outlet and before the shock is higher than atmospheric pressure, the jet will be classified as "under expanded" and will continue to accelerate and expand as it moves into a regime of atmospheric pressure. Because it is in the supersonic flow region, the pressure will continue to decrease as it expands, and the flow accelerates until it passes through a normal shock. By passing through this shock, it slows down and recovers pressure to match atmospheric pressure. The classical 1-dimensional analysis (Shapiro, 1953) yields the equations:

$$M_y^2 = \frac{\frac{2}{\gamma-1}+M_x^2}{\frac{2\gamma}{\gamma-1}M_x^2-1} \tag{5.18}$$

Where M_x is the Mach number just before the shock, M_y is the Mach number just after the shock. γ is the specific heat ratio, given by:

$$\gamma = \frac{C_p}{C_v} = 1.4 \text{ for air} \tag{5.19}$$

The static pressure ratio across the shock is:

$$\frac{P_y}{P_x} = \frac{2\gamma}{\gamma+1}M_x^2 - \frac{\gamma-1}{\gamma+1} \tag{5.20}$$

And the ratio of area between the current area, *A*, at Mach Number, *M*, and the area after the shock, *A** is given by:

$$\frac{Ar}{Ar^*} = \frac{1}{M}\left(\frac{\frac{\gamma+1}{2}}{1+\frac{\gamma-1}{2}M^2}\right)^{\left(\frac{\gamma-1}{2-2\gamma}\right)} \tag{5.21}$$

The relation between reservoir pressure and the Mach number is:

$$P_x = \frac{P_0}{\left[1+M_x^2\frac{\gamma-1}{2}\right]^{\frac{\gamma}{\gamma-1}}} \tag{5.22}$$

These equations can be used to calculate the Mach number after the shock, M_y. For the current experimental apparatus, the reservoir pressure, P_0, was 445.83 kPa. The pressure after the shock is atmospheric pressure, P_y = 101,325 Pa. Substituting these values into equation 5.10 gives M_x = 3.257 and M_y = 0.4616.

This analysis assumes isentropic flow, which is an approximation. This approximation is valid for the cool annulus, which makes up 90% of the mass flow (Gonzalez et al., 2005). Gonzalez et al., (2002) argued that the plasma stream and the annulus have the same Mach number. If we assume the post shock temperature, is 20,000K, then the jet velocity can be calculated by equation 5.23.

$$v = M_y\sqrt{\frac{\gamma RT}{M}} \tag{5.23}$$

Where R, the ideal gas constant, = 8.314Jmol^{-1}K^{-1}; T = 20,000K; M, the molar mass of air, is 29 gmol^{-1}; γ and M_y were previously calculated as 1.4 and 0.4616 respectively.

This gives v as 1307.8 m/s. By comparison, Zhou et al. (2009) used CFD to compute a velocity of 8,000ms^{-1} and Gonzalez et al. reports a value of 100ms^{-1} (Gonzalez et al., 2002). The assumptions made in computing the velocity of the jet at 1307.8ms^{-1} don't justify an error range of more than 800% and 1307.8ms^{-1} is a more realistic estimate than the figures provided by Zhou and Gonzales. This is because a speed of 8000ms^{-1} implies greater than Mach 3 speed, which isn't possible after the shock.

Typically, the distance between the nozzle and the work piece is less than 2 nozzle diameters; it can be assumed that the structure of the jet has not degraded much when it strikes the plate. Because the jet is under-expanded, it needs to expand to a Mach number of 3.257 in order for the pressure after the shock wave to be atmospheric. Equation 5.24 can be used to determine the diameter of the jet after this expansion and before the shock.

$$\frac{Ar}{Ar^*} = \frac{1}{M}\left(\left(\frac{2}{\gamma+1}\right)\left(1+\frac{\gamma-1}{2}M^2\right)\right)^{\frac{\gamma+1}{2(\gamma-1)}} \tag{5.24}$$

Where Ar^* is the area at the nozzle exit, and A is the area just before the shock. Substituting γ = 1.4 and M = 3.257 we calculate that Ar/Ar^* = 5.4047. Further, this area ratio can be used to calculate the radius of the jet at the shock, r, with r^*, the radius of the nozzle, by:

$$r = \sqrt{\frac{Ar}{Ar^*}}r \tag{5.25}$$

Substituting r^* as 0.5mm from our experimental equipment, and the ratio calculated above, then the radius at the shock is approximately 1.16mm. Teulet's analysis indicates that jet diverges very slowly after the shock (doubling in diameter over 12 nozzle diameters)(Teulet et al., 2006). Therefore, it may be assumed that this is approximately the diameter of the jet when it meets the plate. Figure 5.34 shows a diagram of the jet expansion.

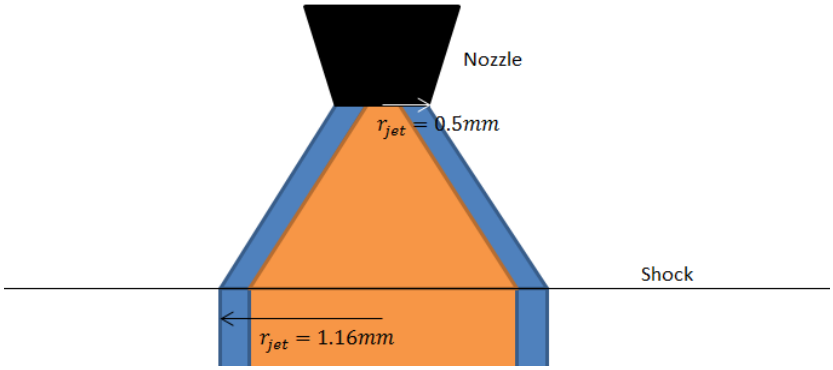

Figure 5.34 Diagram showing the jet expanding to meet the shock.

5.4.2 Heat transfer from the jet to the work piece

Ramakrishnan and Rogozinski (1997) state that the heat transfer from the jet by radiation is slight. In order to calculate the amount of heat transferred via radiation, complex calculations considering the spectral radiation of nuclei and electrons must be considered with the effects of bremsstrahlung. Naghizadeh-Kashani et al. (2002) developed a radiation coefficient on theoretical grounds. However, they stated that the error in such a calculation was in the order of 2 orders of magnitude. Accordingly, the experimental work in section 5.2 was undertaken to quantify the radiative transport, and this transport is shown to be insignificant.

Jones and Fang (1980) state that the heat transfer is exclusively by conduction of heat from the plasma jet. The experimental work in section 5.2 confirms this. With this assumption he proposes a model for the heat flux, *H*, (equation 5.26) which relates the thermal conductivity of the jet, k_{jet}, (without any contribution by shear fields and associated mass transfer), T_{jet}, the absolute temperature of the jet, *r*, the radius of the jet, and *Nu*, the Nusselt number describing the flow of the jet.

$$H = \left(\frac{k_{jet}T_{jet}}{r}\right) * Nu \tag{5.26}$$

Nemchinsky (1997) calculates the Nusselt number, from the Reynold's number (*Re*) and Prandtl Number (*Pr*) by using the Dittus-Boelter correlation:

$$Nu = 0.023Re^{0.8}Pr^{0.4} \tag{5.27}$$

By substituting this approximation, Nemchinksy estimates heat transfer to be given by:

$$Q = 0.0023\pi r\left(\frac{k_{jet}T_{jet}}{r}\right)\left(\frac{\rho^{0.8}v^{0.8}r^{0.8}}{\mu^{0.8}}\right)\left(\frac{c_p^{0.4}\mu^{0.4}}{k_{jet}^{0.4}}\right) * \delta z \tag{5.28}$$

$$Q = \frac{0.0023\pi T_{jet}k_{jet}^{0.6}\rho^{0.8}v^{0.8}r^{0.8}c_p^{0.4}}{\mu^{0.4}} * \delta z \tag{5.29}$$

Where ρ is the density of the jet, v is the velocity of the jet, μ is the viscosity of the jet, c_p is the specific heat of the jet and δz is the thickness of the plate under consideration.

This relationship requires knowledge of the jet velocity and the temperature of the jet. The literature presented demonstrates that there is a large amount of uncertainty in any estimation of the jet velocity. The temperature of the jet at any point is also difficult to estimate reliably. The Dittus-Boelter approximates the Nusselt number for fully developed pipe flow. A pipe flow can be considered developed approximately 60 nozzle diameters downstream of the nozzle (Shapiro, 1953).The use of this approximation in a scenario that's not pipe flow, and that takes place in less than 10 nozzle diameters is a large potential source of error.

Despite these approximations, it is the most careful estimation of heat transfer available. In this work, it is considered that the exponents in the Nemchinsky equation cannot be relied upon and, accordingly a simplified relation is suggested. This will be validated against experimental data in

section 5.4. The model presented in this work (equations 5.30 and 5.31) has a similar form to that of Nemchinsky.

$$\frac{Q}{Ar} = h.T_{jet} \tag{5.30}$$

Where h, the heat transfer coefficient is given by:

$$h = \frac{k_{jet}\rho V^n c_p}{\mu} \tag{5.31}$$

5.4.3 Structure of the jet in the kerf

Figure 5.35 shows the top surface of a cut. The front face of the cut is approximately circular with a diameter of 2.3mm. Section 5.4.3 established and justified the assumption that the two-zone structure of the jet is valid at the top of the work piece. The annulus is relatively cool, less than the melting point of the brass nozzle; therefore, it is incapable of melting the steel. Consequently, in front of the jet, it must collide with the plate and be shorn off and spread over the top surface of the plate as shown in Figure 5.36.

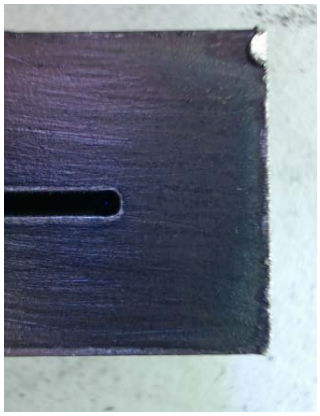

Figure 5.35 Top surface of a cut.

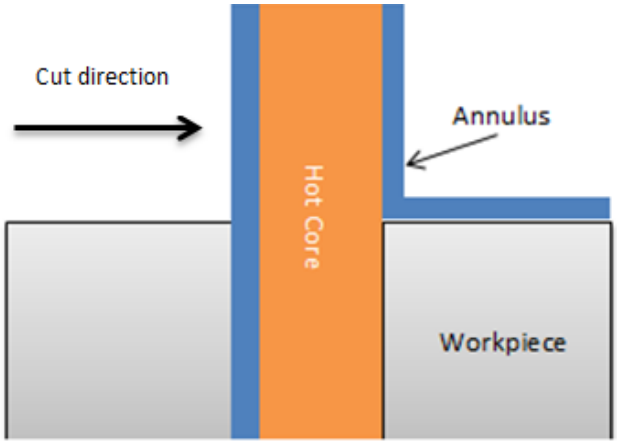

Figure 5.36 Diagram showing the interaction between the work piece and the plasma jet.

Behind the jet, some of the cool annular flow can flow into the kerf; but on the sides of the cut, it will spread out over the top surface of the plate. Ramakrishnan suggested that approximately 10% of the total mass flow is in the central hot plasma. The plasma core has a temperature of about 20,000K and the annulus temperature is about 300-400K. Jones and Fang stated that the Mach numbers of both flows are identical (Jones & Fang, 1980).This Mach number was calculated in section 5.4.2 (M_y = 0.4616). With this information, it is possible to estimate the diameter of the central jet.

From Ramakrishnan et al. (1997):

$$\frac{\dot{m}_c}{\dot{m}_a} = \frac{\rho_c v_c A r_c}{\rho_a v_a A r_a} = \frac{1}{9} \tag{5.32}$$

Where $\dot{m}$ is the mass flow rate, ρ is the density, v is the velocity of the jet and Ar is the area of the jet. The subscript 'a' refers to the annulus' value of the parameter and 'c' refers to the centre jet's value of the parameter.

Let the radius of the central stream be r_p and the outer radius of the annulus is r_{jet} = 1.15mm – calculated above. Then the velocity at the centre can be calculated by:

$$v_c = M_y c \tag{5.33}$$

Where M_y is the Mach number after the shock and 'c' is the speed of sound. This velocity was calculated at 1307.8ms^{-1} in section 5.4.2. Since the pressure of the jet after the shock is known to be atmospheric, and because the streamlines of the jet are straight (Teulet observes that the jet diverges very little) it follows that the static pressure in the jet is the same as the static pressure across the (straight) streamlines. Thus, we are sure that the static pressure in the jet is atmospheric and it is possible to compute ρ_c from the perfect gas law, which is known to be accurate at high temperatures

$$P c_v = nRT \tag{5.34}$$

Where v is the specific volume. Rearranging and converting to density:

$$\frac{1}{\rho} = \frac{1000RT}{MP} \tag{5.35}$$

Where n is the number of moles, R is the ideal gas constant, T is the temperature in degrees K, c_v is the specific volume of the gas and P is the pressure of the gas. Substituting values of P = 101,325 Pa; M = 29 gmol^{-1}; T = 20,000K; R = 8.314 Jmol^{-1}K^{-1}. This gives density of the centre = 0.017672 kgm^{-3}.and density of the annulus = 1.18 kgm^{-3}. Using the postulate of Jones and Fang (1980), the Mach number in the annulus is 0.4616 and therefore the velocity is 160.2ms^{-1}.

Rearranging equation 5.32 gives:

$$\frac{1}{9} = \frac{\rho_c \pi r_c^2 v_c}{\rho_a \pi \left(r_{jet}^2 - r_c^2\right) v_a} \tag{5.36}$$

The velocity of the annulus can also be calculated by:

$$v_a = M_y c \tag{5.37}$$

Where the speed of sound, 'c', can be calculated from eq 5.25 by substituting γ=1.4 and T = 300:

$$c = \sqrt{\frac{\gamma RT}{M}} \tag{5.38}$$

$$c = \sqrt{\frac{1.4*8.314*300*1000}{29}}$$

Substituting into equation 5.37 with M_y = 0.4616 and c, the velocity of the annulus is:

$$v_a = M_y c = 160.2\ ms^{-1} \tag{5.39}$$

Substituting ρ_a = 1.18, ρ_c = 0.017672, v_c = 1307.8ms^{-1}, v_a = 160.2ms^{-1}, and r_{jet}= 1.16; $r_a$can be calculated as 69% of the radius of the after the shock, or 0.8mm. This seems like a realistic value based on the observations in the literature. This value assumes a strict two-zone model when in fact there would be some smoothing between the discontinuous regions of the two-stream model. Consequently, the radius of the jet that is at a temperature higher than the melting point of steel could be slightly larger than this value. The values calculated in this section are summarized and presented in Figure 5.37.

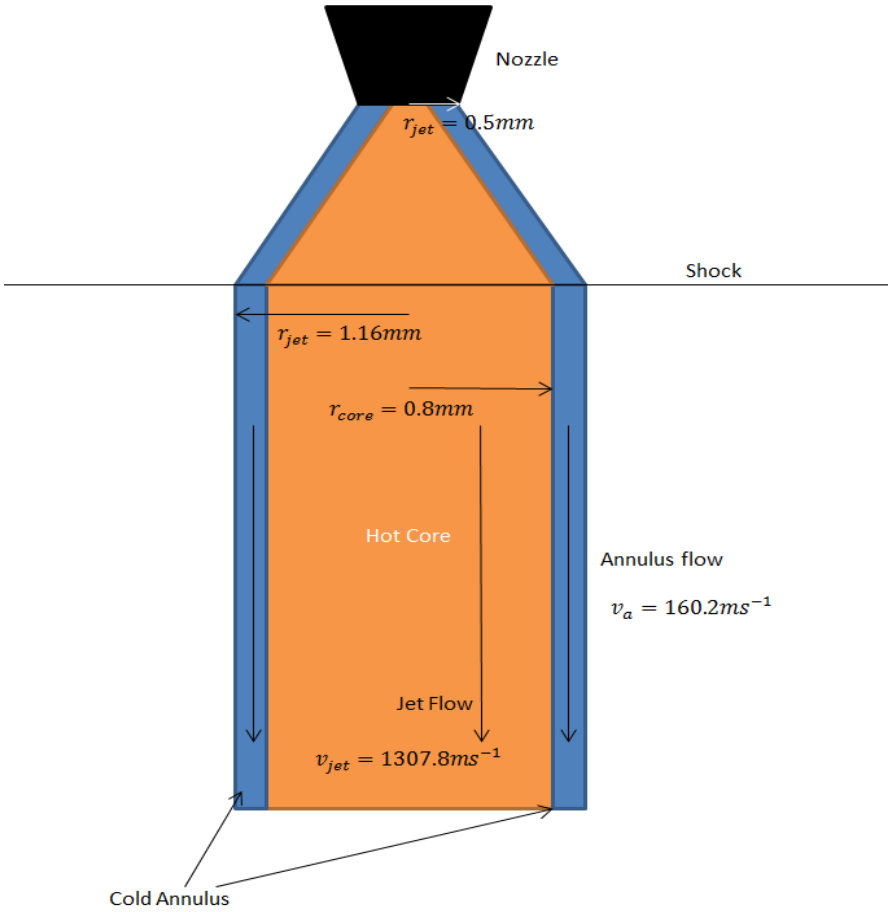

Figure 5.37 diagram showing radius and velocity of the core and annulus of the jet.

5.4.4 Temperature of the Jet

The next aspect of the process is to conceptualize how the temperature of the jet changes as it flows through the kerf. From studies of free jets, the temperature is known to decay in a measured way, primarily because of entrainment of the jet medium with the surrounding atmosphere. For the jet to transform the incoming cool air into plasma, consider heating is required in the nozzle. Specifically, the specific heat at constant pressure, C_p, spikes up to 300 $kJkmol^{-1}K^{-1}$ during dissociation of the gas (Figure 5.38)

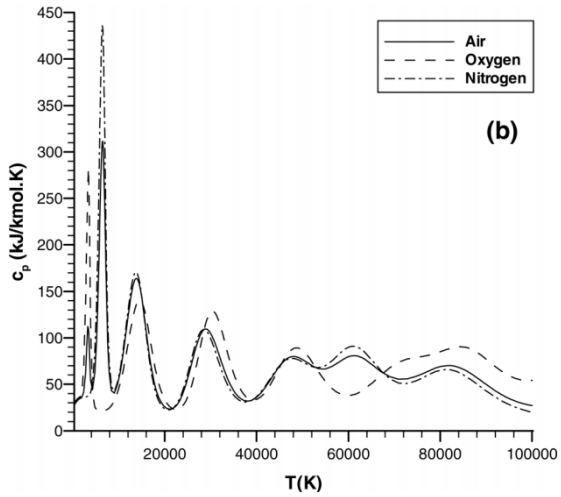

Figure 5.38 Plot of the specific heat capacity versus temperature for air (Eisazadeh-Far, Metghalchi, & Keck, 2011).

It has been observed that the jet retains the character of plasma until it has passed out of the bottom of the cut and consequently Ohmic heating continues throughout the depth of the cut. Eichler et al. (2014) observed from careful experimental measurements that the current through the jet decreased steadily over its length. They showed this by measuring the current through the arc attachment points at each level. For free jets, where the current through the jet is constant because they attach only at their ends, normalizing the radius with respect to nozzle radius; and normalizing the axial distance of the jet with respect to the nozzle radius is appropriate. Figures of the relationship between normalized temperature and normalized radius for normalized depths ranging from 0 to 5 are presented in Appendix H.

The distribution of temperatures varies as the jet progresses downstream of the nozzle. The temperature is maximized at the axis of the jet and decreases as the distance from the axis increases. This rate of decrease is sharp close to the nozzle and becomes smoother as it gets further away from the nozzle. This is consistent with the notion that this is mixing between the hot central portion and the cooler annulus, and between the annulus and the ambient air.

A small amount of pumping occurs over the traversal of 1 nozzle diameter past the shock. The work piece is typically placed approximately this far from the nozzle, so it can be assumed that there is some small spreading of the profile before it interacts with the cut plate.

The temperature profile of the jet can then be assumed to vary predictably as it moves through the plate and a functional form for the decay will be developed, to be validated by later comparison with experiment. As the jet moves through the plate in steady state cutting, it must remove all the material in front of it. This material can be viewed as small increments of δz high. These sections must have the same length in the direction of the cut because the cut progresses at a constant rate. Therefore, the heat lost can be assumed to be linear with the depth through the plate, and consequently the temperature of the jet can be approximated by the linear relationship:

$$T = T_0 \left(1 - a * \frac{th}{th_{plate}}\right) \tag{5.40}$$

Where a is the factor describing the linear relationship, T_0 is the initial temperature above the plate, th is the distance from the top of the plate to the point of interest, and th_{plate} is the overall thickness of the plate.

5.4.5 Cutting model of the front cut face

In section 5.3 a set of experiments was described. These experiments gathered data on the front profile of the kerf for several plate thicknesses and at several feed rates. From this data, a set of curves was obtained describing the shape of this profile. In these experiments, the power was cut

to the torch while it was cutting. The gas flow was terminated shortly after. Ramakrishnan presented similar profiles and reports tests to show that the thickness of the melt film is about 50 microns thick. Therefore, the profiles obtained in Table 5.2 are a representation of the cut face during the steady state operation of the cut for various values of the process parameters.

The assumptions and calculations in the previous sections of this chapter are reasonable, but unverified. A model was developed to predict the shape of these measured profiles using the developed phenomenological model and validate the assumptions. This would then constitute the first cutting model with predictive capability. This model makes the following assumptions:

1. The melt film is very rapidly scoured from the cut face by the high-speed jet. The melt surface can be thought of as waves on the ocean that are getting the tops knocked off by high speed gusts of wind. This view is supported by the fact that the jet flow is known to be turbulent (Shapiro, 1953). Accordingly, the surface of the melt film will not be smooth, but it is scoured away by the gas flow and the residue is very thin (less than 50 microns).
2. Each small layer of the plate of height δz must be removed at the same rate as the jet advances. i.e. for a cut profile where the top of the plate the front is vertical, and at the bottom of the plate where the leading edge might be at 45º. For the jet to advance by a small amount, every layer of the plate must be cut by that same small amount. Whilst the angle of the face can vary and influence the transfer of heat, the volume must be the same or the cut would not proceed at a steady state and the arc would eventually break.
3. In accordance with assumption 2, the amount of heat going into each layer of the plate must be the same.
4. The cut face can be approximated by a polynomial and can be assumed to be smooth. Therefore, the angle of the front cut face at each z within the plate can be calculated.
5. The angle of the profile as Z increases changes for fast cuts of thick plate. This offers greater surface area for heat transfer when the jet might be cooler

The final form of the model (equation 5.41), fitted to the profile data, made use of two observations. Firstly, the amount of energy transferred from the arc to the work piece is proportional to the deflection angle of the face. This was originally suggested by Nemchinksy et al. and follows from the Reynold's Analogy. Secondly, the amount of energy required to advance by a unit of cut speed (f) is inversely proportional to the thickness of the material. This is an obvious statement, as the thicker the work piece is, the more material needs to be removed. Both parameters have been left as a first order interaction. It seems quite likely that the relationship with thickness could be presented as th^n, due to the multitude of aspects thickness impacts (length of drag experience by expunged material, volume of material present to conduct heat away, etc.). However, without a larger data set, such a model would risk being over fit.

$$\theta_{surface} = a\frac{f}{th} + b \tag{5.41}$$

This model provides a reasonably good fit for the data points collected from the 15 tests described in section 5.3. Figure 5.39 shows the measured deflection angles (blue) plotted against the predicted deflection angle (red), as well as a line of best fit representing the relationship between deflection angle and feed rate. The model was fit using a simplex regression and a was estimated at 4.155 and b was estimated at 1.044.

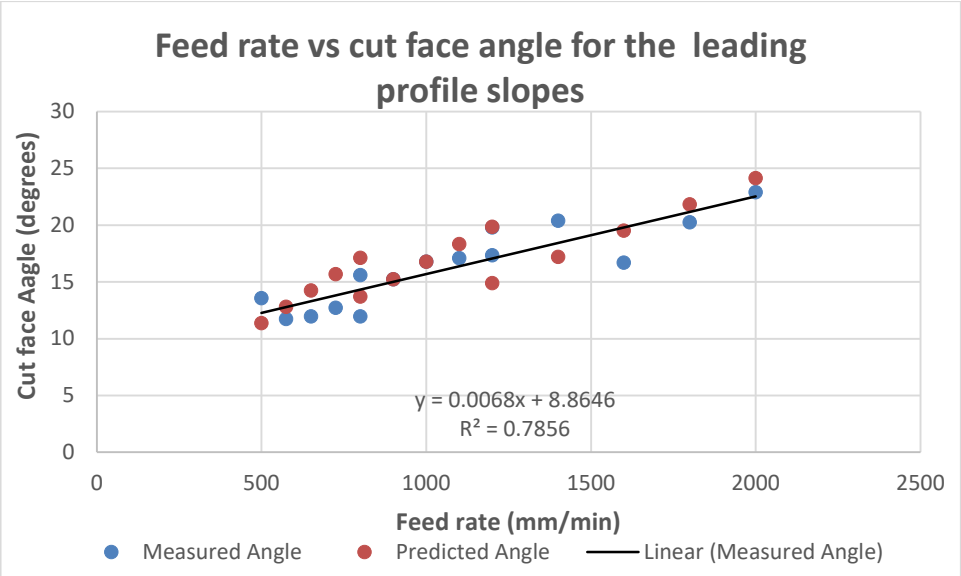

Figure 5.39: plot of measured and predicted deflection angles against feed rate.

From the Reynolds' Analogy, that heat transfer is related to momentum transfer, we might suggest:

$$\frac{Q}{Ar} \propto \frac{\delta}{\delta t} momentum \tag{5.42}$$

Since:

$$Q = hAr\Delta T \tag{5.43}$$

And:

$$Q = (mc_{psteel}\Delta t + mL_{steel}) \tag{5.44}$$

Where $m, c_{psteel}, \Delta t, L_{steel}$, are the mass of the steel melted, the specific heat capacity of steel, the change in temperature, and the latent heat of melting for steel respectively.

Substituting equation (5.41) we can form the relationship:

$$\Gamma\left(a\frac{f}{th} + b\right) = \rho_{steel} f (c_{psteel}\Delta T + L_{steel}) \tag{5.45}$$

Where Γ is a proportionality factor.

5.4.6 Simple model of cutting speed

The model presented in section 5.4.5 attempts to incorporate complex interactions and, for its validation, would require a very large dataset, over a larger range of cutting conditions than is possible with the current equipment. However, by examination of the images for the front cut face (section 5.3 and Appendix G), a simple observation is possible.

It is known that the jet expands only slightly from the top to the bottom of the plate. Material can only be removed from the front cut face if the jet impinges on it. The horizontal distance from the top (front) edge of the cut face to the bottom (trailing) edge is never much larger than the width of the jet core diameter and this changes only slightly over a vertical distance of 10mm below the nozzle. In fact, the cut face offset only varies in length from 1.6mm to 3.1mm over this change in Z (3mm to 10mm).

It follows therefore that the slope of the cut face is less oblique for thin plates – 1.6mm horizontal offset over a depth of 3mm, as compared with a thick plate which has a 3mm offset over a depth of 10mm. It is also intuitively clear that thin plates are cut faster than thick plates. We may therefore expect that the steeper is the angle of the cut face, the slower is the cut. If, therefore, we plot this cut face angle versus cut speed, we might see a clear relationship, as shown in Figure 5.39.

This clear linear relationship represents a distinct advance in the understanding of PAC cutting. Apparently, a greater cut face angle provides better heat transfer and therefore faster cutting. We might suggest that the greater angle provides more area for heat transfer. We might also invoke Reynolds' Analogy that heat transfer is related to mass and momentum transfer and as the fluid sees a greater deflection, there is more turbulence. This would imply greater heat transfer but also that the front cut face sees a continuously refreshed flow stream. Consequently, the fluid material in contact with the cut face will be hotter as it is moved in from the hotter free stream into the boundary layer.

5.4.7 Discussion

There are several key things to observe in work laid out in this section. Firstly, the estimates presented throughout the modelling section incorporate a large amount of uncertainty. There is a large amount of disagreement between values calculated in the literature, for example; estimations of the jet velocity ranging from 100 – 8000ms^{-1} (Gonzalez et al., 2005; Zhou et al., 2009). Further these estimations of parameters used in relationships are only estimations as they depend on many factors, most of which are not known accurately.

Secondly, despite the uncertainties, this work has arrived as several estimations of process parameters, which are summarized in Table 5.3. These represent a large amount of comparison between methods of estimation presented in the literature and are therefore of value. The values of the estimation all have reasonable agreement with values presented in the literature and values observed in practice (where practicable).

Table 5.3 parameters estimated or developed in section 5.

Calculated jet Parameters			
Parameter	**Value**	**Unit**	**Eq. Number**
Jet radius after expansion	1.16	mm	5.18-5.25
Heat transfer coefficient	$h = \frac{k_{jet}\rho V^n c_p}{\mu}$	$\frac{W}{m^2K}$	5.26-5.31
Relationship between annulus velocity and radius, and core velocity and radius.	$1/9 = \frac{\rho_c \pi r_c^2 v_c}{\rho_a \pi (r_{jet}^2 - r_c^2) v_a}$	-	5.32- 5.38
Velocity of annulus	160.2	ms^{-1}	5.39
Core radius after expansion	0.8	mm	5.36
Velocity of core	1307.8	ms^{-1}	5.33
Relationship between feed rate over thickness and deflection angle	$\theta_{surface} = \gamma f/t + b$	°	5.41

Finally, the model presented, relating deflection angle to feed rate and material thickness, provides a good fit to the data obtained for the profile slops. It can be useful in evaluating other methods of heat transfer estimation due to Reynolds analogy and to improve the understanding of the cutting process. This represents the first model in the literature describing this feature. This accuracy of the model is only as good as the data that it was fitted to. As mention in section 5.3, gathering data on these features is quite complex and prone to error. As such, this model is only an estimate of the relationship.

5.4.8 Conclusions and future work

This section has presented a model relating deflection angle to the process parameters feed rate and material thickness. Deflection angle is a key parameter in understanding the PAC process and has not been specifically addressed in the literature, so this represents a significant contribution. During the development of the model, the concepts presented in the literature were contrasted and compared. This provides a holistic view of the current state of understanding, which was used to calculate various process parameters and validate them.

There is potential for further work in this area. Specifically, application of this model to other data sets would be valuable. This is a challenge because there is a scarcity of data available on these features. So, the first step would be designing and implementing an experiment to provide this data. The data this model was calculated with was also quite limited. The machine used to perform the tests was limited to 10mm-thick steel. Conversely, as the test piece became thinner, the reliability of the deflection angle measurement decreased. The model could also be further developed with access to a larger set of data, for example the nature of the relationship between deflection angle and material thickness could be investigated.

5.5 Chapter Summary

An accurate model of the PAC process, and the ability to relate this between PAC systems is necessary in order to implement a novel control methodology that incorporates feedback to tune PAC process parameters. This chapter presents work on improving the modelling of PAC. The results of the work presented in this chapter include:

1. A summary of the conceptual presentation of the PAC process in the literature and a novel normalization application to standardise the data.
2. An investigation and quantification of the contribution of radiation to heat transfer for the PAC process.
3. An empirical investigation into the profile of the kerf's leading edge for various profile parameters.
4. Estimations of the characteristics of the plasma jet from first principals, that agree with the literature.
5. Development of a model, from first principals, relating the shape of the kerf profile during steady state operation to the process parameters feed rate and material thickness.

The research has overcome multiple challenges, namely:

1. Collation of a complex field of literature. This field presents many similar concepts of energy and momentum conservation that result in disparate calculations. Assessment of the works and normalization of the data was a significant challenge.
2. Designing an experiment that would allow the minimization of the conductive and convective heat transfer methods and allow suitable estimation of the resulting radiative contribution. Then relating this operation set up back to a practical application.
3. Designing and undertaking experimental work that allowed the collection of data on the shape of the front kerf profile during steady state operation.
4. Identifying the aspects of the acquired data that could be related to process parameters and developing these into a suitable model.

In overcoming these challenges, this chapter presents significant and original contributions to the literature. A normalization of the data on temperature distribution around the plasma jet was presented and shown to be valid. Modifications to a long standing equation, commonly used in the literature were suggested. Experimental work was presented that enabled the quantification of energy transfer via radiation at an upper limit of 3%. The experimental method is also a contribution in and of itself as it is a simple method that can be easily replicated and represents

an improvement on similar methods presented in the literature.

The experimental work presented to gather data on the shape of the leading edge of the kerf is another contribution. This represents the first data presented of this nature in the literature and is a simple and easily replicated process. This can facilitate the collection of more data and the improvement of the understanding of the PAC process. Finally, a model relating the shape of the leading edge of the kerf was presented. It related the shape to the process parameters of material thickness and feed rate. The model was a good fit and demonstrates the relationship well. This is the first model describing this feature in the literature.

6 Kinematics and Control for Complex Cutting

This chapter focuses on the control system work done for Kerf Ltd. At the beginning of the project, the scope was to develop a bevel capable plasma cutter for Kerf. As the project progressed, the scope of the project shifted from control of a robotic end effector towards the idea of a novel control methodology using machine vision to provide feedback for a PAC system. Whilst incomplete, a substantial amount of work was done for the development of a control system for a 5-axis plasma cutter. This work can be broken down into:

- Development of the kinematics of the end effector.
- Proposal of a novel feedback control algorithm.

The kinematics derivation provides value to Kerf Ltd. It allows them to implement a control algorithm for their robotic manipulator. In addition to this it can be used in future work on the implementation of the proposed feedback control algorithm. An accurate model of the kinematics of a robotic system is crucial to providing a control algorithm, and this derivation provides that for Kerf Ltd. There is also value in a novel feedback control algorithm that can make use of the work done in developing a machine vision rig in Chapter 4, the modelling work presented in Chapter 5 and the kinematics this chapter presents. Such a control method would be very innovative and could make the PAC technology more efficient and accessible.

6.1 Kinematics

A kinematic analysis of 3 robotic heads was undertaken. The 3 heads chosen were the AKS RoboKut, the Koike Arronson 3D-LT, and the Kerf heat. This analysis was undertaken on Kerf Ltd.'s behalf and facilitates development of new bevel capable PAC heads. It has potential to be used in future work implementing control to this system. Three heads were analysed to allow comparison with existing solutions. The analysis is presented by:

1. Simplifying the heads into joint linkage diagrams.
2. Selecting appropriate Denavit-Hartenberg (DH) coordinate frames and identifying the parameters relating these frames.
3. Solving for the homogenous transform matrices.
4. Comparing the analysis to previous work.
5. Developing the relationship for the Jacobian and dynamics of the Kerf head.

These heads have been selected because they are both popular solutions in industry and exhibit mechanical and kinematic approaches. The AKS RoboKut is a kinematic style of machine. The torch focal point changes position for deviations in the 2 actuated joints. The kinematic solution requires compensation in the X, Y and Z axes for deviations in torch angle, but the head is often lighter. The Kerf head and the Koike Arronson 3D-LT are both mechanical solutions. They are simpler to control, which is an advantage when retrofitting.

6.1.1 Joint linkage diagrams

A joint linkage diagram simplifies a mechanism to its joints and the links that connect them. This simplification makes the DH parameterization more intuitive. Figure 6.1 shows the heads of interest and the corresponding joint linkage diagram. The dashed lines indicate the actuation axis of the joints.

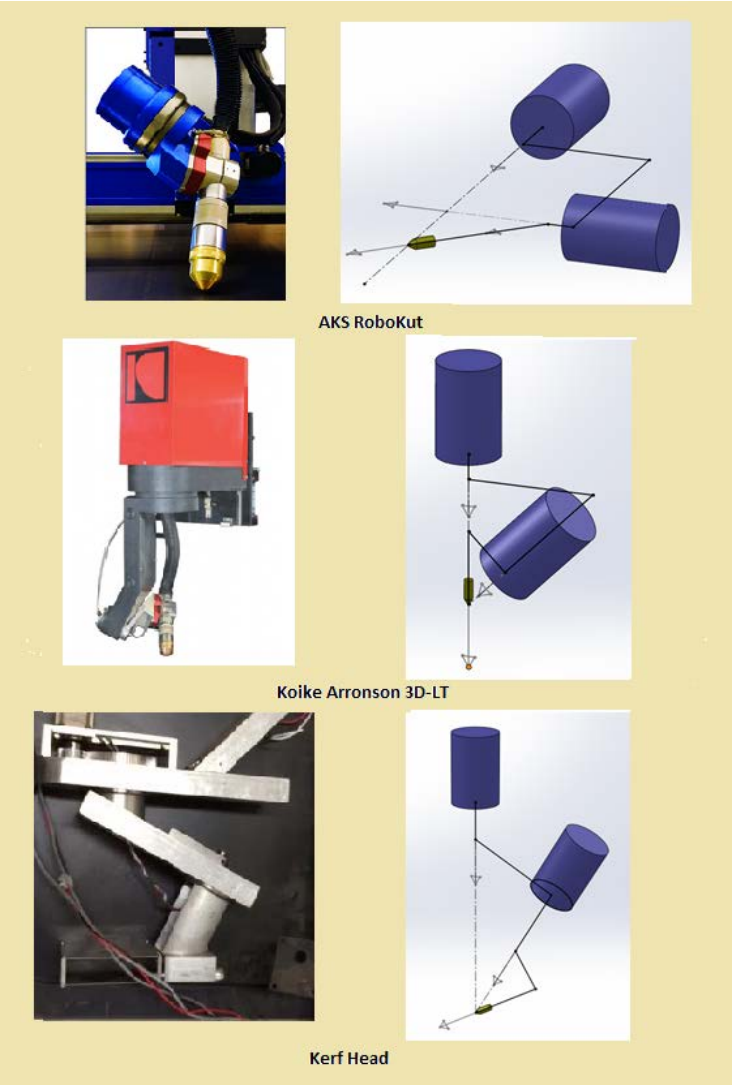

Figure 6.1 Bevel head mechanisms with corresponding joint linkage diagrams (AKS, 2014; Koike, 2014).

Figure 6.1 shows the difference between the kinematic and mechanical style of head. The Z axes for the joints of the RoboKut do not all intersect on one point. The Z axes of the joints for the 3D-LT and the Kerf head intersect at the focus point of the tip. The Kerf mechanism and that of the 3D-LT are similar but differ in the angle between the links.

6.1.2 Homogenous Transform Matrices Derivation

The homogenous transformation matrix is a relationship between a perspective frame and an original frame. Its notation is:

$$A^{new\ Frame}_{Original\ Frame}$$

Where A is a 4x4 matrix that is comprised of a rotational component, a translational component and space filler. The rotational component is a 3x3 matrix in the top left that gives the orientation of the X, Y, and Z vectors in the new frame, with respect to the original frame. The translational component is a 3x1 matrix in the top right that gives the coordinates of the new frame's origin in the original frame. Finally, there is a 1x4 matrix at the bottom that facilitates multiplication of the matrices so that they retain the same format. This matrix is [0, 0, 0, 1].

The Koike Arronson 3D-LT and Kerf head had the same non-zero DH parameters. Consequently, the transform matrices for the two mechanisms are the same prior to substitution. The AKS

RoboKut transform matrix and the Koike Arronson/Kerf matrix are both presented.

6.1.3 AKS RoboKut transformation matrix

The first transformation matrix is the result of the multiplication of the homogenous rotation matrix of the rotation about the Z axis (θ_1^*), by the transform matrix for the length of the joint along the Z axis (d_1) and finally by the rotation matrix for the angle between the joints about the X axis (α_1):

$$A_1^0 = \begin{bmatrix} cos\theta_1 & -sin\theta_1 cos\alpha_1 & sin\theta_1 \sin\alpha_1 & 0 \\ sin\theta_1 & cos\theta_1 cos\alpha_1 & -cos\theta_1 sin\alpha_1 & 0 \\ 0 & sin\alpha_1 & cos\alpha_1 & d_1 \\ 0 & 0 & 0 & 1 \end{bmatrix} \quad (6.1)$$

The second transformation matrix has the same set of parameters, therefore:

$$A_2^1 = \begin{bmatrix} cos\theta_2 & -sin\theta_2 cos\alpha_2 & sin\theta_2 \sin\alpha_2 & 0 \\ sin\theta_2 & cos\theta_2 cos\alpha_2 & -cos\theta_2 sin\alpha_2 & 0 \\ 0 & sin\alpha_2 & cos\alpha_2 & d_2 \\ 0 & 0 & 0 & 1 \end{bmatrix} \quad (6.2)$$

The final Transformation matrix contains only d_3 and is very simply:

$$A_3^2 = \begin{bmatrix} 1 & 0 & 0 & 0 \\ 0 & 1 & 0 & 0 \\ 0 & 0 & 1 & d_3 \\ 0 & 0 & 0 & 1 \end{bmatrix} \quad (6.3)$$

Combining these transforms yields a relationship between the position of the end effector and the original reference frame of:

$$A_2^0 = A_1^0 A_2^1 A_3^2$$
$$= \begin{bmatrix} c\theta_{12} - s\theta_{12}c\alpha_1 & s\theta_1 s\alpha_{12} - s\theta_1 c\alpha_{12} c\theta_2 - s\theta_2 c\theta_1 c\alpha_2 & c\theta_1 s\theta_2 s\alpha_2 + s\theta_1 c\theta_2 c\alpha_{12} + s\theta_1 s\alpha_1 c\alpha_2 & s\theta_1 s\alpha_1 d_2 \\ s\theta_1 c\theta_2 + c\theta_1 s\theta_2 c\alpha_1 & -s\theta_{12} c\alpha_2 + c\theta_{12} c\alpha_{12} - c\theta_1 s\alpha_{12} & s\theta_{12} s\alpha_2 - c\theta_{12} c\alpha_{12} - c\theta_1 s\alpha_1 c\alpha_2 & -c\theta_1 s\alpha_1 d_2 \\ s\theta_2 s\alpha_1 & c\theta_2 s\alpha_1 c\alpha_2 + c\alpha_1 s\alpha_2 & -c\theta_2 s\alpha_1 c\alpha_2 + c\alpha_{12} & c_{\alpha_1} d_2 + d_1 \\ 0 & 0 & 0 & 1 \end{bmatrix}$$

(6.4)

6.1.4 Denavit-Hartenberg Parameterization

Denavit-Hartenberg (DH) parameterization is the academic and industry standard for forward kinematics(Craig, 2005). There is a Modified DH Parameterization technique, which has slight differences and is designed to be slightly more intuitive, but the original method is still preferred (Lee, 1982) The process of parameterization is first to affix reference frames to the links, and then to identify the parameters that relate the frames to each other (Craig, 2005).

The process of attaching reference to links according to Craig is (Craig, 2005):

1. Identify the joint axes.
2. Identify the shortest line between two neighbouring joint axes.
3. Assign the Z axis for a joint to be the joint axis.
4. Assign the X axis to be parallel to the shortest line. If the joint axes intersect, then X should be perpendicular to both.
5. Use the right-hand rule for cross products to select the Y axis.

The DH parameters presented by Craig are (Craig, 2005):

1. a_i - the distance from $\hat{Z}_\iota$ to $\hat{Z}_{\ i+1}$ measured along $\hat{X}_i$
2. α_i - the angle from $\hat{Z}_\iota$ to $\hat{Z}_{\ i+1}$ measured about $\hat{X}_i$
3. d_i - the distance from $\hat{X}_{i-1}$ to $\hat{X}_i$ measured along $\hat{Z}_i$
4. θ_i - the angle from $\hat{X}_{i-1}$ to $\hat{X}_i$ measured about $\hat{Z}_i$

It is worth noting that there are multiple solutions to most kinematic linkages, depending on the selection of the positive and negative direction of the axes. However, a general rule is to select directions that cause most parameters to be zero. Further, it is appropriate to add additional reference frames if it makes the conceptualization simpler. The reference frame selection and resulting parameters are shown for the AKS RoboKut, the Koike LT-3D, and the Kerf Design.

6.1.4.1 AKS RoboKut DH Parameterization

The first reference frame (frame 0) can be arbitrarily selected. In this case it has been attached to the first joint, with the Z_0 axis (blue) aligned with the joint axis. The X_0 axis (red) is vertical for convenience of picking the α parameters. Y_0 (green) completes the frame in accordance with the right-hand rule for cross products.

The second reference frame's (frame 1) origin is coincident with the joint axis for the second joint. It translates the frame along the Z_0 axis and rotates it about the X_0 axis. It is identified as frame 1 in Figure 6.2. The third reference frame (frame 2) has been translated along the Z_1 axis and rotated about the X_1 axis as well. Frame 2's origin is coincident with the 2nd joint axis still and has been used to simplify the translation between frames 1 and 3 by breaking it into 2 steps. The fourth frame (frame 3) is translated along Z_2 and the origin is coincident with the tip of the torch.

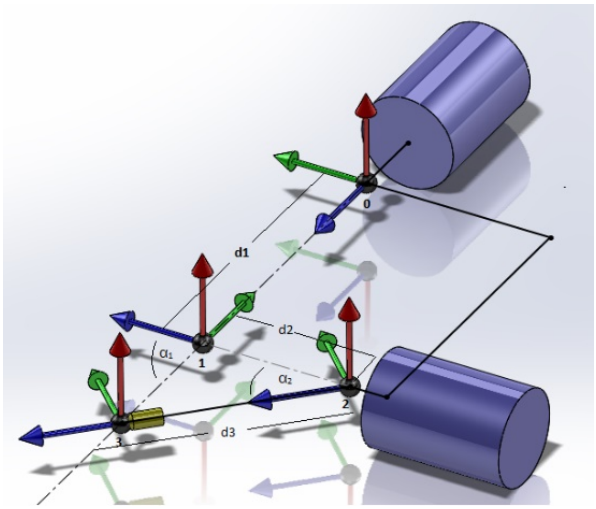

Figure 6.2 AKS RoboKut reference frames and DH parameters (Z - blue, X - red, Y - green).

The DH parameters for the first link are θ_1^*, d_1 and α_1. θ_1^* is the rotational displacement made by joint 1. The asterisk denotes that is an actuated parameter. d_1 is the distance along the Z_0 axis between the 0th (black) origin and the 1st origin (black). α_1 is the rotation about X_0 from Z_0 to Z_1. The direction of this rotation is negative in this diagram in accordance with the right-hand screw rule.

The DH parameters for the second link are θ_2^*, d_2 and α_2. θ_2^* is the rotational displacement of the second joint, and is the actuated parameter. d_2 is the distance between origin 1 and origin 2 along the Z_1 axis. α_2 is the rotation about X_1 between Z_1 and Z_2. In this case the rotation is positive in direction.

The DH parameter for the third link is just d_3. The only non-zero parameter is the translation along Z_2 between origin 2 and origin 3. $a_{1\text{-}3}$ are all zero for this mechanism, as the origins were all picked within a frame orthogonal to the X axes for simplification of calculation. The parameters are presented in Table 6.1.

Table 6.1: AKS RoboKut DH Parameters.

DH Parameters				
Link	θ	a	d	α
1	$\boldsymbol{\theta_1^*}$	0	d_1	α_1
2	$\boldsymbol{\theta_2^*}$	0	d_2	α_2
3	0	0	d_3	0

6.1.4.2 Koike LT-3D DH Parameterization

Figure 6.3 shows the allocation of the reference frames and the non-zero DH parameters. The first reference frame (frame 0) for the Koike LT-3D was selected at an arbitrary point near the first joint and coincident with the joint axis. Z_0 (blue) is aligned with the first joint axis. X_0 is orthogonal to the link to make the α parameters easy to visualize. Y_0 completes the vector cross product.

The second and third reference frames (frame 1 and frame 2) are coincident with the torch, and the intersection of the first and second joint axes. This sets the a_1, a_2, and d_2 values to 0, and simplifies the kinematic relationship. Z_1 is in the direction of the second joint angle and is the result of a linear translation along Z_0 and a rotation about X_0. Z_2 is in line with the end effector (torch) and reference frame 2 is translated from frame 1 by rotating about X_1.

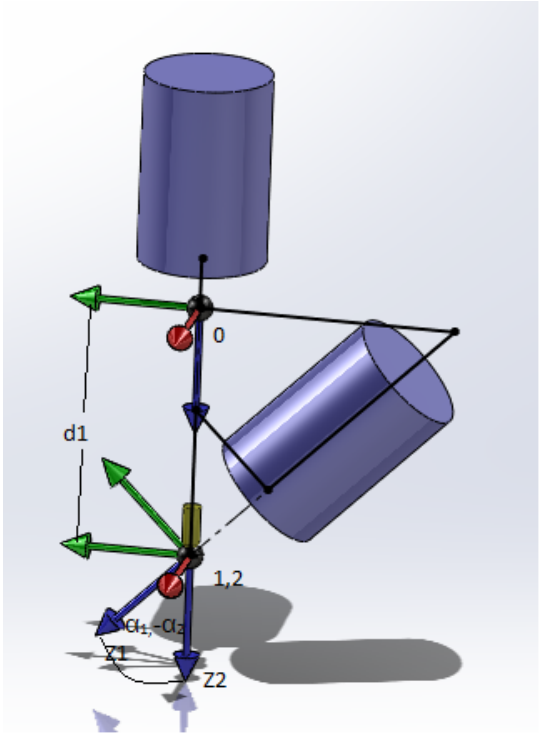

Figure 6.3 Koike 3D-LT reference frames and DH parameters (Z- blue, X - red, Y - green).

Link 1 has the DH parameters θ_1, d_1 and α_1. θ_1^* is the rotational displacement of joint 1, and is the actuated parameter. d_1 is the linear translation of origin 0 to origin 1 along the Z_0 axis. α_1 is the rotation about X_0 to from Z_0 to Z_1. Its direction is negative. Link 2 has only θ_2 and α_2 as non-zero parameters. θ_2^* is the rotational displacement of joint 2 and is an actuated parameter. α_2 is the rotation of frame 1, about X_1 to get to frame 2. Its direction is positive. These parameters are shown in Table 6.2.

Table 6.2: Koike Arronson 3D-LT DH Parameters.

DH Parameters				
Link	θ	a	d	α
1	$\boldsymbol{\theta_1^*}$	0	d_1	α_1
2	$\boldsymbol{\theta_2^*}$	0	0	$-\alpha_2$

6.1.4.3 Kerf Ltd. Head DH Parameterization

The Kerf Ltd. head is similar to the Koike Arronson 3D-LT and is also a mechanical linkage type. Therefore, the reference frame assignment and parameterization are similar to Koike's. Frame 0 is located with its origin coincident to the first joint's joint axis. Z_0 (blue) is directed along this joint axis. X_0 (red) has been chosen so that frame rotations are about this axis, making visualization of this parameter easy. Y_0 completes the right-hand rule for cross products.

Frame1 and Frame 2 are coincident with the end effector and have been rotated about X_0 and X_1. These rotations are aligned with the orientation of joint 2 and the orientation of the end effector. Figure 6.4 shows the coordinate frames and the non-zero DH parameters.

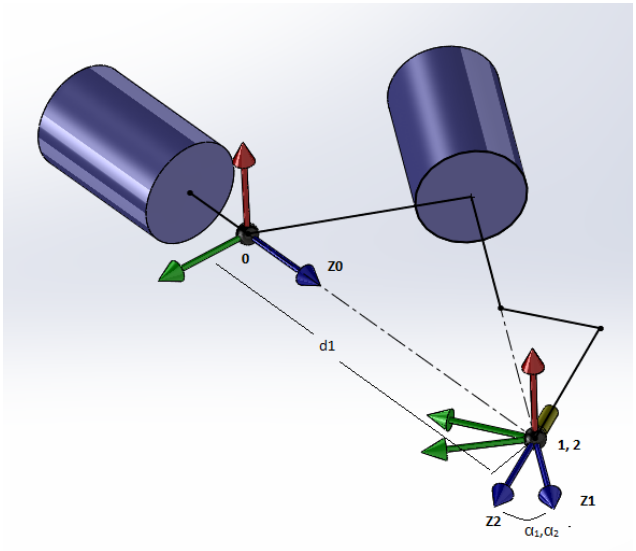

Figure 6.4 Kerf head reference frames and DH parameters (Z - blue, X - red, Y - green)

The first link of this mechanism has the parameters of θ_1^*, d_1 and α_1. Like Koike's mechanism, d_1 move frame 1 along Z_0 to have its origin coincident with the intersection of the two joint axes. α_1 is the rotation about X_0 that aligns Z_2 with the joint axis of the second joint. The rotational displacement of the first joint is θ_1^*. The second link of the mechanism rotationally displaces the end effector frame (frame 2) by θ_2^*. α_2 is the rotation about X_1 that aligns Z_2 with the end effector. These values are shown in Table 6.3.

Table 6.3: Kerf head DH Parameters.

DH Parameters				
Link	θ	*a*	*d*	*α*
1	$\boldsymbol{\theta_1^*}$	0	d_1	α_1
2	$\boldsymbol{\theta_2^*}$	0	0	α_2

The DH parameters for the AKS RoboKut, the Koike LT-RD and the Kerf head have been derived and justified logically. They fulfil the conventions of the DH parameterization. They are verified again by relating the end effector and reference frame locations with the joint variables.

6.1.5 Koike Arronson and Kerf transformation matrix

The first set of parameters for these machines is the same as that of the AKS machine, due to the similarities between the mechanisms:

$$A_1^0 = \begin{bmatrix} cos\theta_1 & -sin\theta_1 cos\alpha_1 & sin\theta_1 \sin\alpha_1 & 0 \\ sin\theta_1 & cos\theta_1 cos\alpha_1 & -cos\theta_1 sin\alpha_1 & 0 \\ 0 & sin\alpha_1 & cos\alpha_1 & d_1 \\ 0 & 0 & 0 & 1 \end{bmatrix} \tag{6.5}$$

The 2nd link's parameters are slightly different, lacking d_2.

$$A_2^1 = \begin{bmatrix} cos\theta_2 & -cos\alpha_2 sin\theta_2 & sin\theta_2 sin\alpha_2 & 0 \\ sin\theta_2 & cos\theta_2 cos\alpha_2 & -cos\theta_2 sin\alpha_2 & 0 \\ 0 & sin\alpha_2 & cos\alpha_2 & 0 \\ 0 & 0 & 0 & 1 \end{bmatrix} \tag{6.6}$$

This gives the transformation relating the end effector position to the starting reference frame:

$$A_2^0 = A_1^0 A_2^1$$
$$= \begin{bmatrix} c\theta_{12} - s\theta_{12} c\alpha_1 & s\theta_1 s\alpha_{12} - s\theta_1 c\alpha_{12} c\theta_2 - s\theta_2 c\theta_1 c\alpha_2 & c\theta_1 s\theta_2 s\alpha_2 + s\theta_1 c\theta_2 c\alpha_{12} + s\theta_1 s\alpha_1 c\alpha_2 & 0 \\ s\theta_1 c\theta_2 + c\theta_1 s\theta_2 c\alpha_1 & -s\theta_{12} c\alpha_2 + c\theta_{12} c\alpha_{12} - c\theta_1 s\alpha_{12} & s\theta_{12} s\alpha_2 - c\theta_{12} c\alpha_{12} - c\theta_1 s\alpha_1 c\alpha_2 & 0 \\ s\theta_2 s\alpha_1 & c\theta_2 s\alpha_1 c\alpha_2 + c\alpha_1 s\alpha_2 & -c\theta_2 s\alpha_1 c\alpha_2 + c\alpha_{12} & d_1 \\ 0 & 0 & 0 & 1 \end{bmatrix}$$

(6.7)

The homogenous transformation matrices are useful for several reasons. The solution of these yields the inverse kinematics. The dynamics of the mechanism can also be derived from these. Additionally, the effect of the joint variables on the end effector can be expressed visually. This validates the mechanisms can achieve the required orientations.

6.1.6 Previous work on the Kerf Ltd. head

Whilst DH parameterization is the preferred method of kinematic analysis, geometrical methods are also possible for simple mechanisms. A previous student of Massey University used a geometrical projection method for the Kerf Ltd. head (Etherington, 2014). By projecting the lengths of the two arms into previous reference frames, he was able to arrive at a relationship between the projected length and the angle of the end effector. Figure 6.5 shows the geometrical projections for the Kerf Ltd. mechanism by Etherington.

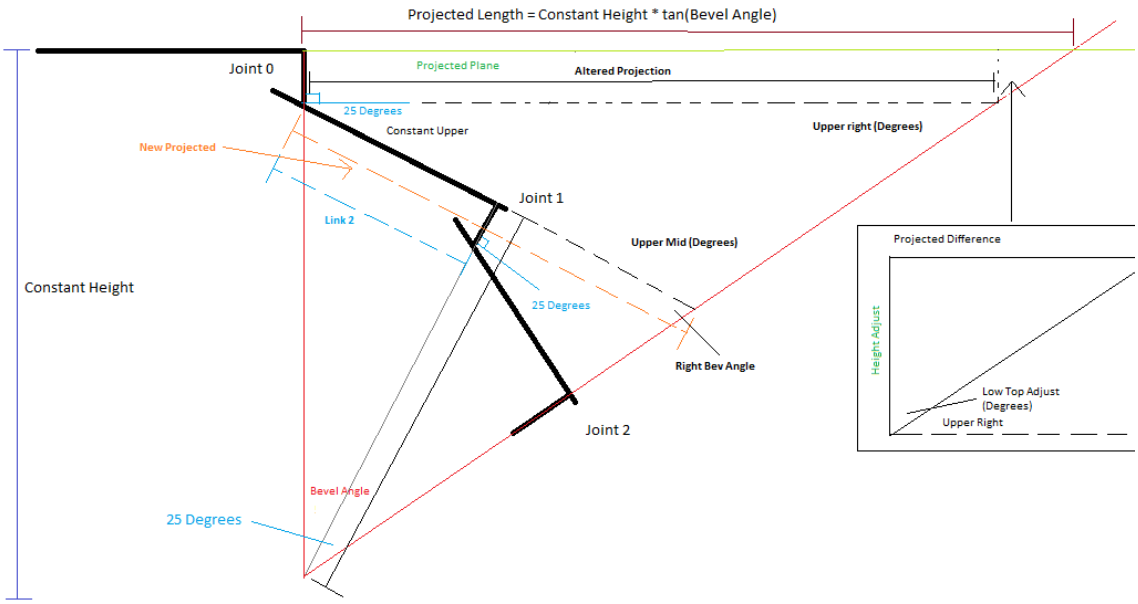

Figure 6.5 Kerf Ltd. head with geometrical projection method (Etherington, 2014) used with permission.

As the arm is bent, the projected length shortens. This is shown in Figure 6.6. The relationship between the projected length and the end effector angle derived is given by (Etherington, 2014):

$$Projected\ length = sqrt(\left(Constant\ Height * Tan(A)\right)^2 + (Constant\ Height * Tan(B)^2) \quad (6.8)$$

This method has approximation errors however, and a completed DH parameterization is more desirable.

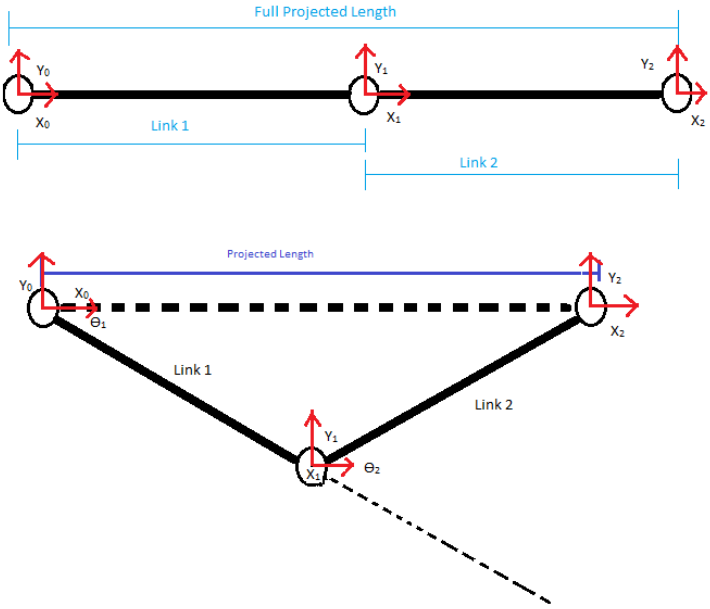

Figure 6.6 Linkage planar projection when not at 50^0(Etherington, 2014) used with permission.

6.1.7 Kerf Ltd. head dynamics

The dynamics for the kerf head were also derived. These are useful for assessing performance of the arm and selecting appropriate motors and gearing. The first step in the dynamics is the calculation of the Jacobian.

6.1.7.1 The Jacobian for the Kerf Ltd. head

The velocity Jacobian is essentially a linear mapping between the relation of angular displacement of the joints with time, and the linear and angular velocity of the end effector (Craig, 2005). The Jacobian can be calculated by taking the derivative of the transformation matrix.

$$\begin{matrix} v_e \\ \omega_e \end{matrix} = J(\theta_1, \theta_2) \times \begin{matrix} \dot{\theta}_1 \\ \dot{\theta}_2 \end{matrix} \tag{6.9}$$

Where:

$$J(\theta_1, \theta_2) = \begin{bmatrix} z_{i-1} \times (O_n - O_{i-1}) \\ z_{i-1} \end{bmatrix} \tag{6.10}$$

For a 2 joint system there are 2 columns in the Jacobian:

$$J(\theta_1, \theta_2) = \begin{bmatrix} z_0 \times (O_n - O_0) & z_1 \times (O_n - O_1) \\ z_0 & z_1 \end{bmatrix} \tag{6.11}$$

Where:

$$O_n = \begin{bmatrix} 0 \\ 0 \\ d_1 \end{bmatrix}, O_1 = \begin{bmatrix} 0 \\ 0 \\ d_1 \end{bmatrix}, O_2 = \begin{bmatrix} 0 \\ 0 \\ d_1 \end{bmatrix}, z_0 = \begin{bmatrix} 0 \\ 0 \\ 1 \end{bmatrix}, z_1 = \begin{bmatrix} s\theta_1 s\alpha_1 \\ -c\theta_1 s\alpha_1 \\ c\alpha_1 \end{bmatrix}$$

Thus:

$$J(\theta_1, \theta_2) = \begin{bmatrix} 0 & 0 \\ 0 & 0 \\ 0 & 0 \\ 0 & s\theta_1 s\alpha_1 \\ 0 & -c\theta_1 s\alpha_1 \\ 1 & c\alpha_1 \end{bmatrix} \tag{6.12}$$

This result is intuitive because for a mechanical style linkage there is no linear velocity imparted by the two joints. The first joint's rotational velocity is the same as the end effector's and the second joint's angular velocity is related to the end effector's by $\alpha_1$and θ_1.

This result can be condensed into the form:

$$\omega = \begin{bmatrix} 0 & s\theta_1 s\alpha_1 \\ 0 & -c\theta_1 s\alpha_1 \\ 1 & c\alpha_1 \end{bmatrix} \begin{bmatrix} \dot{\theta}_1 \\ \dot{\theta}_2 \end{bmatrix} \tag{6.13}$$

6.1.7.2 Static Force

The static force requirements of the joints were also calculated for the Kerf Ltd. head. From (Craig, 2005), the forces and torques can be calculated using:

$${}^i f_i = {}^i_{i+1}R\, {}^{i+1} f_{i+1} \tag{6.14}$$

$${}^i n_i = {}^i_{i+1}R\, {}^{i+1} n_{i+1} + {}^i P_{i+1} \times {}^i f_i \tag{6.15}$$

$$\tau_i = {}^i n_i^T\, {}^i \hat{Z}_i \tag{6.16}$$

Where f_i is the force on the i^{th} link, ${}^i_{i+1}R$ is the rotation matrix between two links, P is a point vector between two points, n is the torque exerted on a link by another link, τ_i is the joint torque and $\hat{Z}$ is the directional vector of the joint.

Since none of the joints are prismatic, there is only a reaction torque for the joints. The method for determining the force Jacobian involves applying a force and torque to the end effector, and then determining the resultant forces to maintain static equilibria, working backwards towards the zero frame. The force and torque applied are given by:

$$^2f = \begin{bmatrix} f_x \\ f_y \\ f_z \end{bmatrix}, ^2n = \begin{bmatrix} n_x \\ n_y \\ n_z \end{bmatrix} \tag{6.17}$$

$$^1f_1 = {}_2^1R\,^2f_2 = \begin{bmatrix} c_2f_x - s_2c\alpha_2f_y + s_2s\alpha_2f_z \\ s_2f_x + c_2c\alpha_2f_y - c_2s\alpha_2f_z \\ s\alpha_2f_y + c\alpha_2f_z \end{bmatrix} \tag{6.18}$$

The torque for first link is then:

$$^1n_1 = {}_2^1R\,^2n_2 + {}^1P_2\,^1f_1 \tag{6.19}$$

In this case:

$$^1P_2 = d_2\,^2\hat{X}_2 = 0 \tag{6.20}$$

Thus:

$$^1n_1 = \begin{bmatrix} c_2n_x - s_2c\alpha_2n_y + s_2s\alpha_2n_z \\ s_2n_x + c_2c\alpha_2n_y - c_2s\alpha_2n_z \\ s\alpha_2n_y + c\alpha_2n_z \end{bmatrix} \tag{6.21}$$

In the zero frame:

$$^0f_0 = {}_1^0R\,^1f_1 = \begin{bmatrix} (c_1c_2 - s_1c\alpha_1s_2)f_x + (s_1s\alpha_1s\alpha_2 - s_2c_1c\alpha_2 - s_1c\alpha_1c_2c\alpha_2)f_y + (c_1s_2s\alpha_2 + s_1c\alpha_1c_2s\alpha_2 - s_1s\alpha_1c\alpha_2)f_z \\ (s_1c_2 + c_1c\alpha_1s_2)f_x + (c_1c\alpha_1c_2c\alpha_2 - s_1s_2c\alpha_2 - c_1s\alpha_1s\alpha_2)f_y + (s_1s_2s\alpha_2 - c_1c\alpha_1c_2s\alpha_2 - c_1s\alpha_1c\alpha_2)f_z \\ s\alpha_1s_2f_x + (s\alpha_1c_2c\alpha_2 + c\alpha_1s\alpha_2)f_y + (c_1c\alpha_2 - s\alpha_1c_2s\alpha_2)f_z \end{bmatrix} \tag{6.22}$$

And the torque for the zero frame is then:

$$^0n_0 = {}_1^0R\,^1n_1 + {}^0P_1 \times {}^0f_0 \tag{6.23}$$

Where:

$$^0P_1 \times {}^0f_0 = \begin{matrix} -d_1\,^0f_{0(x)} \\ d_1\,^0f_{0(y)} \\ 0 \end{matrix} \tag{6.24}$$

$$^0n_0 = \begin{bmatrix} (c_1c_2 - s_1c\alpha_1s_2)(n_x - d_1f_x) + (s_1s\alpha_1s\alpha_2 - s_2c_1c\alpha_2 - s_1c\alpha_1c_2c\alpha_2)(n_y - d_1f_y) + (c_1s_2s\alpha_2 + s_1c\alpha_1c_2s\alpha_2 - s_1s\alpha_1c\alpha_2)(n_z - d_1f_z) \\ (s_1c_2 + c_1c\alpha_1s_2)(n_x + d_1f_x) + (c_1c\alpha_1c_2c\alpha_2 - s_1s_2c\alpha_2 - c_1s\alpha_1s\alpha_2)(n_y + d_1f_y) + (s_1s_2s\alpha_2 - c_1c\alpha_1c_2s\alpha_2 - c_1s\alpha_1c\alpha_2)(n_z + d_1f_z) \\ s\alpha_1s_2f_x + (s\alpha_1c_2c\alpha_2 + c\alpha_1s\alpha_2)f_y + (c_1c\alpha_2 - s\alpha_1c_2s\alpha_2)f_z \end{bmatrix} \tag{6.25}$$

With the torques and forces supplied by the joints for each link to maintain static equilibrium calculated. The torques the joints will supply is:

$$\tau_0 = \begin{bmatrix} 0 \\ 0 \\ s\alpha_1s_2n_x + (s\alpha_1c_2c\alpha_2 + c\alpha_1s\alpha_2)n_y + (c_1c\alpha_2 - s\alpha_1c_2s\alpha_2)n_z \end{bmatrix} \tag{6.26}$$

$$\tau_1 = \begin{bmatrix} 0 \\ 0 \\ s\alpha_2n_y + c\alpha_2n_z \end{bmatrix}$$

Or:

$$\tau = \begin{bmatrix} s\alpha_1s_2 & s\alpha_1c_2c\alpha_2 + c\alpha_1s\alpha_2 & c_1c\alpha_2 - s\alpha_1c_2s\alpha_2 \\ 0 & s\alpha_2 & c\alpha_2 \end{bmatrix} \begin{bmatrix} n_x \\ n_y \\ n_z \end{bmatrix} \tag{6.27}$$

This set of dynamics gives a relationship between time and displacement. As such it provides insights into the selection of motors, gearing and material dimension to suit the needs of applications. It also provides a means of implementing computed torque control.

6.1.8 MATLAB® envelope simulations

The forward kinematics was modelled using MATLAB®. Modelling of the kinematics provides a visual representation of the response of the mechanism, which validates the model. It also confirms the viability of the Kerf Ltd. head. Further, with an accurate and reliable model, the inverse kinematics can be modelled as well. The goals for the modelling are:

1. Demonstrate what happens for each linkage movement
2. Demonstrate the location and orientation of the tip for all orientations of all joints.

6.1.8.1 AKS RoboKut

The linkage of interest for the AKS RoboKut is the 2nd link. The first link rotates the arm around its axis, and when vertical causes no change. The second link causes a considerable change in angle of the torch/ end effector as shown in Figure 6.7.

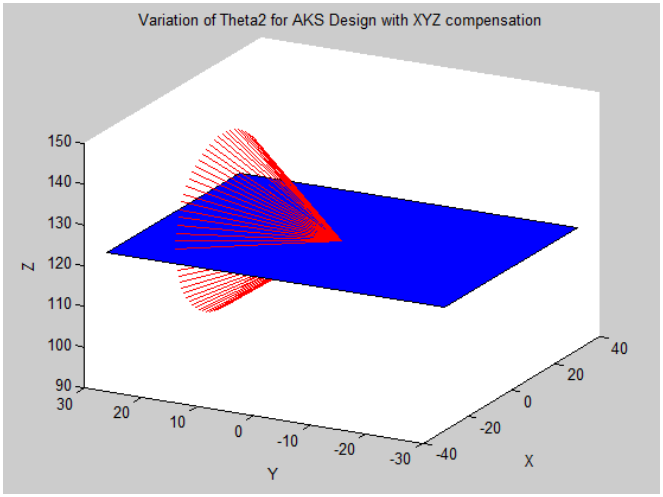

Figure 6.7 AKS RoboKut variation of joint 2.

Figure 6.7 shows a few important aspects of the AKS model. Firstly, a full rotation of joint 2 causes the torch angle to vary through a right-angled cone. Secondly, at this orientation of joint 1, not all combinations will be physically viable without collision with the environment. Thirdly, this cone could only be formed by compensating for the X, Y, and Z shift that the mechanism introduces as the bevel angle changes. This translation is because of the kinematic nature of the mechanism, and a control implementation will need to account for this shift as has been done here.

As the first joint angle is rotated for each full rotation of the second joint angle, Figure 6.8 shows that a sphere of bevel angles is possible. In other words, this mechanism can meet any required angle. The model has been adjusted to keep the bevel angles coincident with the point 0, 0, 120. The real-world application will be limited to about 45^0 of bevel rotation due to the nature of the arc.

6.1.8.2 Koike Arronson 3D-LT

The next mechanism modelled is Koike Arronson's 3D-LT bevel head cutter. Intuitively if joint 2 is rotated, then a right-angled cone is created by the orientations of the torch as seen in Figure 6.9. At the one extreme, the end effector is fully vertical; at the other it is fully horizontal. The orientation changes between 0 and 90 degrees with the Z axis when joint 2 is rotated through 180º. The orientation also changes with respect to the X and Y axis, but joint 1 can be used to

adjust for this.

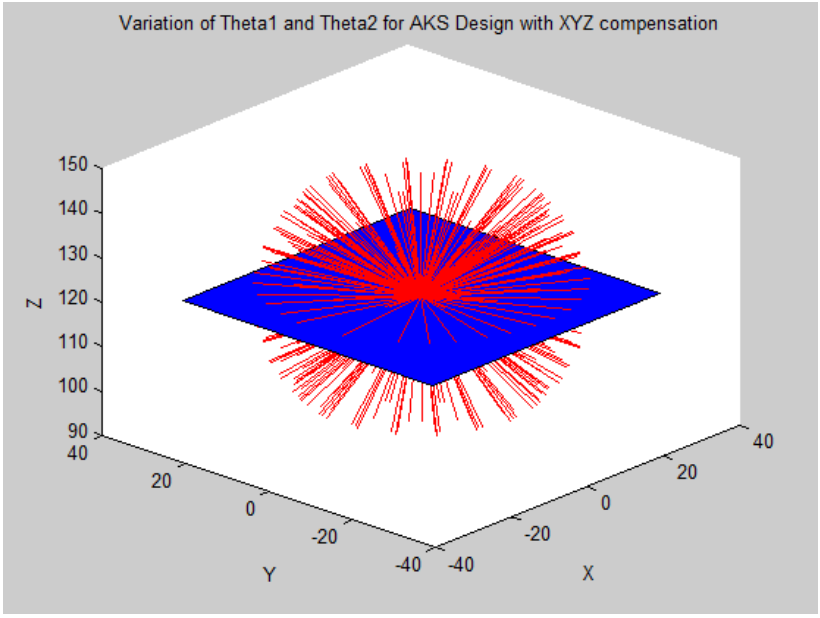

Figure 6.8 AKS RoboKut variation of joints 1 and 2.

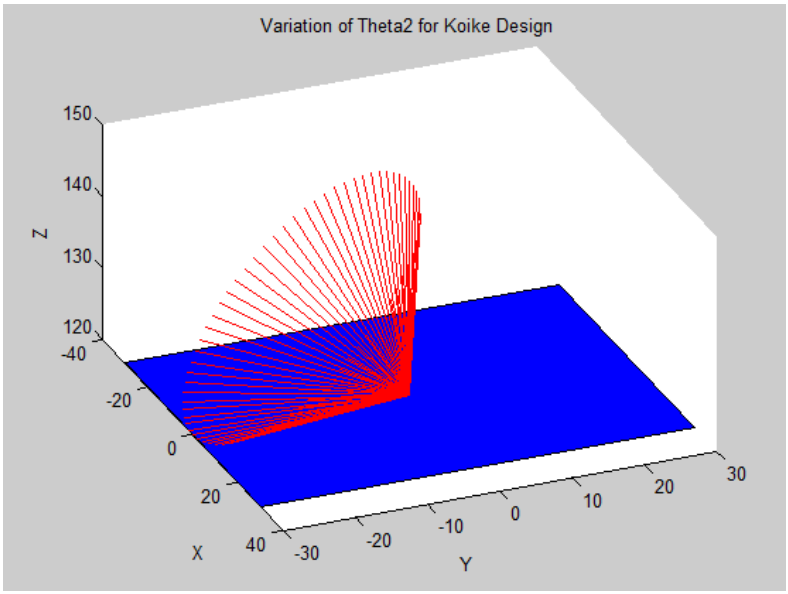

Figure 6.9 Adjustments of joint 2 of the Koike Arronson 3D-LT Bevel Head Cutter.

Rotating the set of orientations, visible in Figure 6.9, through 360 degrees results in a hemisphere of torch angles. This is observable in Figure 6.10. This validates the model of the 3D-LT machine since intuitively and observably it produces this envelope.

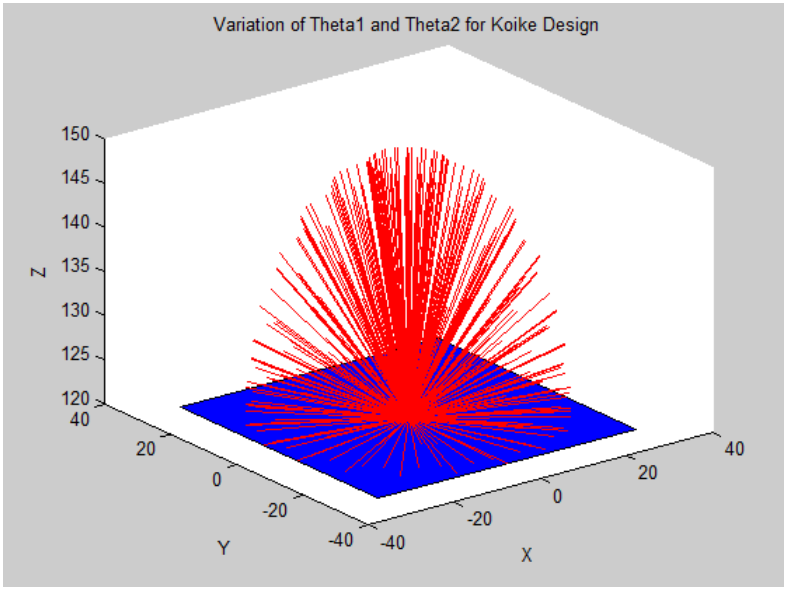

Figure 6.10 Adjustments of joints 1 and 2 of the Koike Arronson 3D-LT Bevel Head Cutter.

6.1.8.3 Kerf Ltd. head

The final model constructed was for Kerf Ltd.'s head. As mentioned, the transformation matrices are the same as those for Koike Arronson's design, however the alpha parameter for both joints are different. Because of this, a slightly different profile is observable in Figure 6.11. As joint 2 is rotated a cone with a smaller angle is observed. This is 60° or double α_2.

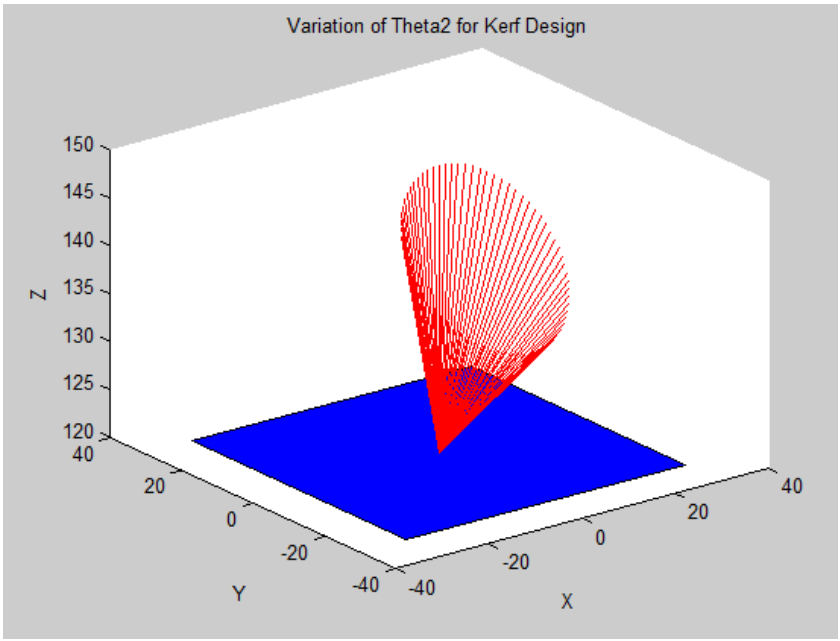

Figure 6.11 Orientation of end effector for varying angles of joint 2 modelled in MATLAB® .

Performing this rotation of joint 2 at varying angles for joint 1 results in a similar envelope to that of Koike Arronson's. However, since the angle of 0^0 to 30^0 is not attainable by rotating joint 2, it is a slightly smaller envelope. This is observable in Figure 6.12.

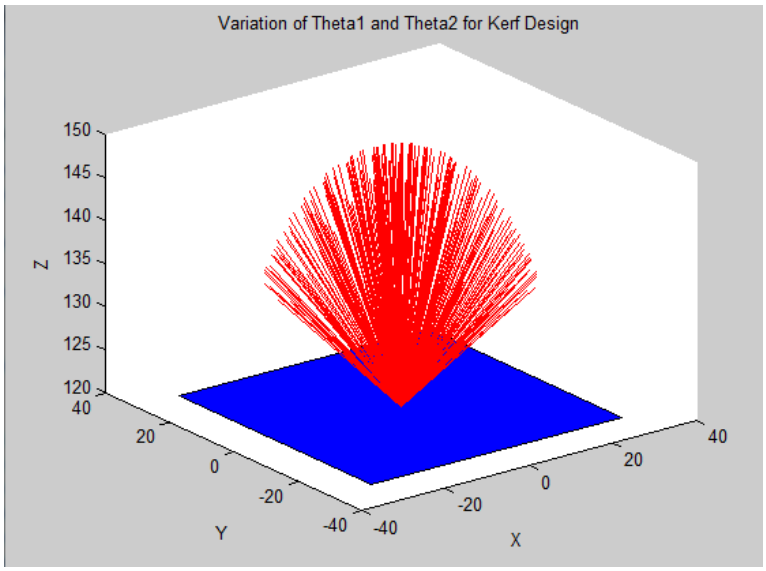

Figure 6.12 Orientation resulting from variation of joints 1 and 2 for the Kerf Ltd. machine.

6.1.9 Comparison and summary

The 3 machines modelled all confirm that the DH parameterization is correct, and the resulting homogenous transformations are all adequate at describing the change in the reference frame introduced by the rotation of joint axes. Further, as seen by the development of the Kerf Ltd. head parameters from the Koike parameters, they are quite generalizable, and several of the other available solutions could be modelled by adjusting the DH parameters.

It is worth noting is that the observable envelopes, whilst logical, do not coincide with the values quoted by the companies. This limitation arises for a few reasons. Firstly, at some orientations, parts of the arm that are not coincident with the reference frame might collide with the work piece, reducing the effective orientation that is achievable, as shown in Figure 6.12. Secondly, bevelling at such extreme angles is not particularly attractive as it can cause the metal thickness to become much larger. Finally, complications with wire routing can be problematic.

Thus, all these machines effectively have the same operable envelope despite the theoretical possibility of the mechanical assemblies. All these assemblies are capable of meeting industry standards as proven by the presence of two of them in industry.

This analysis provides a complete DH Parameterization and kinematic solution for Kerf Ltd.'s proposed head design. Future work can be undertaken to implement the control of this head and produce a bevel capable plasma system. It can then be used to implement the novel control methodology.

6.2 Feedback control proposal

A potential novel control methodology using real time feedback of the PAC performance to tune the process parameters and adjust the G-Code has been identified as one with significant potential. The work presented so far represents movement toward such a system. This work would follow on from the development of the kinematics of the robotic system presented in section 6.1, the implementation of an AVI methodology, and modelling of the PAC process.

The feedback method could take the form of an iterative learning control algorithm to calibrate a PAC control system (Figure 6.13). Currently, PAC systems require a large amount of experience from the operator, even systems with CNC control (Gray, 2014; Keraita & Kim, 2007; *Plasma*

Processes of Cutting and Welding, 1976). The PID parameters need to be set correctly for each machine and adjusted to achieve desired performance. The correct settings for kerf width and material speeds are also adjusted until satisfactory performance is achieved. (Aloke, Girish, Scrutton, & Molian, 1997; R. C. Bidajwala & M. A. Trivedi, 2014; R. Bini, B. M. Colosimo, A. E. Kutlu, & M. Monno, 2008b; Etherington, 2014; Ferent-Pipas, Dindelegan, Padurean, Ciupan, & Ciupan, 2014; Gariboldi & Previtali, 2005). For example, Massey's PAC system's cut accuracy has increased from more than 1mm error to about 0.5mm after having the machine for several months. There are numerous papers published that explore operating parameters for various materials (R. C. Bidajwala & M. A. Trivedi, 2014; Bini et al., 2008b; Ferent-Pipas et al., 2014; Gariboldi & Previtali, 2005). This model can make use of data acquired from a feedback unit assessing the PAC performance.

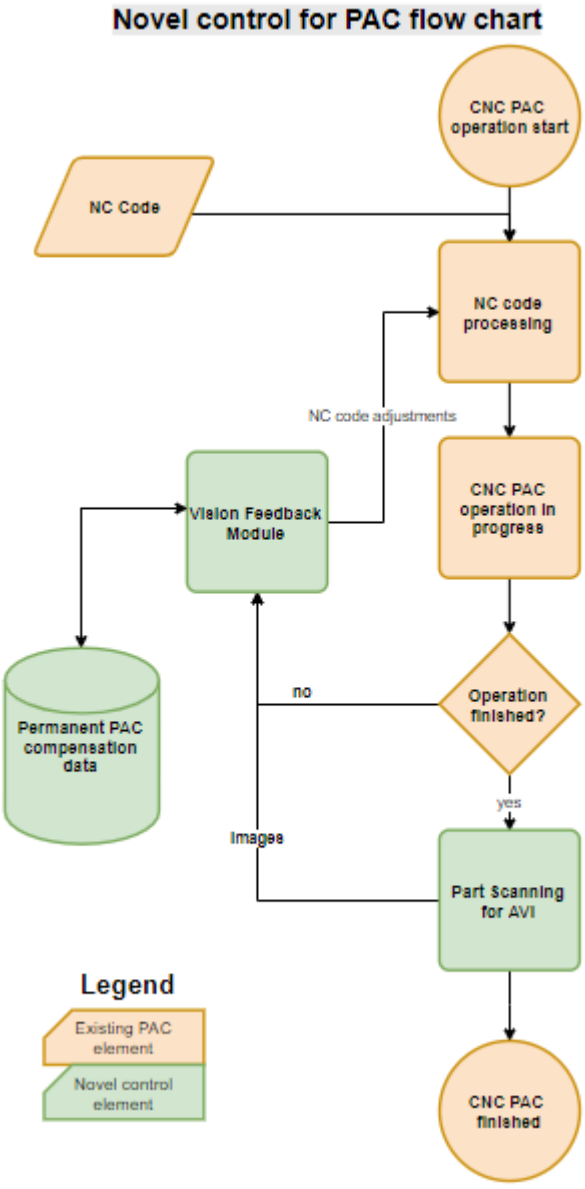

Figure 6.13 Functional block diagram of proposed feedback control structure.

The functional block diagram (Figure 6.13) highlights two opportunities to provide feedback and tune the process. The first is during the cutting process, during and between the cutting of parts, the feedback can provide information on the deviation from the desired position/ part dimensions. This feedback can then be assessed to determine the best course of correction. If it is a constant

dimensional issue, for example consistently overcutting in one axis and undercutting in another axis, then the NC code could be adjusted. In this example, dimensions in the X axis could be altered to reflect this overcut. This would require a G-Code parser to interpret the current commands. It would then modify these commands to account for measured errors. Alternatively, if the machine is consistently over cutting in all axes, then process parameters could be adjusted to increase/decrease kerf width. Tuning of the PAC system would need to consider the kinematics of the positioning system of the torch head, as well as the process parameters of PAC.

The second opportunity is to assess the cut after its completion and draw inferences about performance based on cutting parameters. For example, if most parts were more undercut than normal, and the material thickness had been changed, then new set points could be implemented for the process parameters to tune this aspect. Alternatively, if no process parameters had changed and a significant decrease in accuracy was observed, then a warning could be issued to check the machine's consumables. With a memory of performance, the system could optimize itself over time.

6.3 Chapter Summary

This chapter highlights work done on the kinematics and control of PAC. It began by developing a set of kinematics for Kerf's proposed head and comparing it to existing models. The kinematics was developed using the DH parameterization method, and this was applied to two other industrial models. Relationships for the dynamics of the Kerf head were developed and the work space was simulated in MATLAB®. This set of work provides Kerf Ltd. with a foundation for developing control of their mechanism. It also provides an example of kinematics derivation for a 3 DoF robotic manipulator to the literature.

A feedback control method is also proposed. This method has an iterative learning control algorithm that would use feedback to improve the systems performance over time. A functional block diagram of the standard control method for a PAC system is outlined, and opportunities to incorporate feedback to improve performance are suggested.

7 Conclusion

This research considered the potential for implementation of a novel feedback control methodology for PAC. In order to advance this concept, several gaps in the literature on plasma-arc cutting are addressed, namely:

1. How much energy is imparted to the plate via radiation from the arc?
2. What is the shape of the front edge of the kerf and what mechanism causes this shape?
3. How do the process parameters of torch height, material thickness and feed rate affect the quality measures of kerf width and kerf angle?
4. How can empirical data for kerf width be collected more efficiently and more accurately?
5. How asymmetrical is the kerf and how can this be measured?

The specific objectives met by this research are:

1. An informative research thesis was written.
2. Two peer reviewed research papers were produced.
3. A PAC vision test rig was developed and implemented.
4. A method for automated, visual-inspection was developed and validated.
5. A model predicting the slope of the leading edge of the kerf was produced and validated.
6. An empirical relationship between kerf width and kerf angle with feed rate, torch height and material thickness was produced, and experimental data obtained.
7. Experimental data on, and a quantitative analysis of kerf asymmetry were performed.
8. A kinematic investigation of a bevel capable PAC head was conducted, and a novel control methodology was proposed.
9. An investigation into height control using stereopsis was conducted.
10. An experimental study on the effects of radiative heat transfer for PAC was completed, and the transfer was quantified.

The development of a vision test rig that mounts 2 inexpensive webcams to the torch of a PAC system is presented. This test rig facilitates measurement of kerf width around an objects periphery and compares this to the part's G-Code to assess the accuracy of the cut. The measurements have an accuracy of approximately 0.1mm, which is the level of accuracy of a high-end PAC system. The algorithm is validated on test cuts of mild steel at different thicknesses. This validation provides empirical data to the literature for measurements of kerf width for varying feed rate and material thickness. The algorithm is easily replicable and provides an efficient method for the acquisition of more empirical data on kerf width in future work. Experimental work to quantify kerf asymmetry using the vision test rig is then presented.

An investigation into the phenomenology of the PAC process was conducted and is presented along with a model predicting the shape of the kerf front profile. This investigation extends existing studies in the literature and presents a method to characterize the parameters of a plasma jet with respect to the maximum temperature of the jet, and the nozzle diameter. It also examines models of the temperature distributions in a plate of metal being cut by PAC. A modified model is presented which better reflects the symmetry of the temperature distribution and is then used to estimate conductive heat transfer. Experimental work is then presented that quantifies the radiative heat transfer to a cut piece and shows it to be insignificant (less than 3% of the total power transfer). Further experimental work focused on qualitative data for the shape of the kerf front profile. From this work, a first order, simple cutting model is presented that predicts the slope of the leading edge of the kerf using material thickness and feed rate.

7.1 Machine vision for plasma-arc cutting

The research into the field of applied machine vision, specifically for PAC, was successful. It begins by describing the development of a vision rig that performs measurements to an accuracy of 0.1mm using inexpensive webcams and attaching to the torch of a PAC system (Figure 7.1). The design considerations are justified, and the means of manufacturing are explained. The calibration procedure is then discussed in depth and the calibration parameters and their resulting

values are presented in Table 7.1. The calibration enables measurements to be made to an accuracy of 0.1mm using sub pixel techniques.

Figure 7.1: Image of the PAC system used for experimental work with the vision rig mounted.

Table 7.1: The calibration parameters used for the close-view vision rig throughout the work.

Calibration Parameter	Symbol	Value
pixels per mm (X direction)	$ppmmx_0$	4.70mm^{-1}
pixels per mm (Y direction)	$ppmmy_0$	4.70mm^{-1}
pixels per mm per mm height (X)	pmx_h	0.03mm^{-1}
pixels per mm per mm height (Y)	pmy_h	0.03mm^{-1}
X offset	s_x	194.17mm
Y offset	s_y	17.35mm
camera rotation	θ_c	-0.85^0

An algorithm to acquire and process edge point information using the vision rig is also developed. This algorithm uses a part's G-Code to plan a path to acquire data points that describe the edge of the part. These edge points are then compared to the part's G-Code to assess the cut accuracy and measure kerf width. The results from the data analysis by the algorithm are presented graphically and numerically. The graphical representation allows visualization of the kerf width and assessment for systematic error and the numerical measurements provide quantitative data on the size of the error. These measurements have an accuracy reaching 0.1mm and are validated by comparison with measurements made using a digital caliper. The accuracy achieved meets the goal set for this tool.

The results from these investigations are peer reviewed and published in (Flemmer, 2017a; Flemmer, 2017b). This demonstrates a substantial contribution to the literature. The objectives for this research are all successfully met.

7.2 Modelling of PAC

The research into modelling of the PAC process, specifically the modelling of the shape of the front profile of a kerf was successful, and has developed work done by Nemchinsky, Teulet and Ramakrishnan. The current understanding of the PAC phenomenology in the literature was examined. The characterization of plasma jets and the temperature distribution in a theoretical cut piece are examined. Data from the literature is used to characterize plasma jets, allowing comparison between existing studies. Data on the temperature of the plasma jet, with respect to its distance from nozzle and its displacement in the X and Y-axes is normalized and presented. Two observations are made. Firstly, that linear interpolation for the temperature of a plasma jet

at its core is appropriate, provided that the temperature is normalized with respect to the maximum temperature of the jet, and that the distance from the nozzle is normalized with respect to the nozzle diameter. Secondly, that the temperature profile with respect to radius for the data presented in the literature is again linear when normalizing temperature with respect to maximum temperature and radius with respect to nozzle diameter. This linear relationship varies with distance from the nozzle.

Two pieces of experimental work are presented, an investigation into heat transfer via radiation from a plasma-arc and an investigation into the shape of the leading edge of a kerf during steady state cutting. The investigation into heat transfer via radiation successfully quantified the effect of radiation. Experimental work is presented where heat transfer via conduction and convection are effectively negated, leaving radiative heat transfer as the only source. The heat transfer is then measured with a tool designed for this purpose and the temperature profiles are presented. Heat transfer via radiation is estimated to be less than 3% of the input power. This experiment confirms that heat transfer via radiation is negligible, validating the literature. The second piece of experimental work measured the shape of the front profile of a kerf during steady state process, over a range of material thicknesses and feed rates. This experimental work provides a better understanding of the PAC process.

A model relating PAC process parameters to the steady state shape of a kerf which is developed and validated. A 2-dimensional approximation is presented that quantifies the heat transferred from the plasma-arc as a function of jet viscosity, thermal conductivity, jet velocity, jet temperature and the angle of the jet. This heat transfer is then related to the energy required to remove a volume of material from the plate, allowing calculation of the feed rate. The key observation made is that heat transfer over the depth of the cut must be constant to maintain a constant feed rate during steady state operation. The 2-dimensional approximation is unable to be fit to the data set acquired in the preceding experimental work. However, a simplified model is successfully fit to the data.

7.3 Kinematics and control methodology

The kinematics for Kerf Ltd.'s bevel capable robotic head for PAC is presented. Additionally, a novel control methodology for this robotic head is proposed. Kerf Ltd. have developed a robotic head to allow tilting of a PAC torch and 5-axis cutting. The DH-parameterization of the robotic head is presented along with the relationships for the dynamics, and a simulation of the envelope of the head using MATLAB®. This work validates the feasibility of the system and allow implementation of control to the robotic head. A novel control methodology that incorporates the developed AVI system is proposed for Kerf Ltd.'s robotic head. This methodology can improve the accessibility of the PAC technology.

7.4 Other work

Work is presented on the assessment and development of Massey's PAC system for the research, and the work done on kinematics and control for Kerf Ltd.'s robotic head for bevel capable PAC. This work has a wide application within the industry. A feasibility study on a vision-based torch height control method is also presented. The accuracy of the height detection is less than 0.15mm, which validates the feasibility of the approach.

An investigation into hysteresis of the Massey PAC rig, and the development of a quadrature decoder implementation to provide position data for the vision test rig is presented. The hysteresis investigation used two methods to quantify the hysteresis in the X and Y axes of the PAC system. The first method made use of a digital gauge to measure the displacement of the torch head as the head was moved a small distance in one direction, and then a small direction in the opposite direction.

The second method used the vision rig to measure the displacement over a larger range of motion for opposing directions. Both methods show that hysteresis was significant and prompted calibration of the machine to provide a more accurate gantry system. A quadrature decoder

implementation is presented. It details the steps to provide position information to the data acquisition algorithm. This is essential for performing rectification of tiled images, which allows the vision algorithm to assess the cut accuracy.

7.5 Concluding remarks

In summary, the research has made the following contributions to the field of plasma-arc cutting (PAC). Firstly, an accurate vision-based metrology system has been developed that allows rapid acquisition of cut edge points and thus, accurate measurements of kerf. This system was published in the International Journal of Mechanical and Production Engineering and presented at the 2017 Mechatronics and Machine Vision in Practice (M2VIP) conference. Secondly, a model describing the cut surface angle of the leading edge of the kerf during PAC has been developed, a simple model comparing cut face angle, feed rate and material thickness was elucidated verified for a range of test cuts with varying steel plate thickness and feed rate. It also addressed quantitatively the effect of radiative heat transfer during PAC and the significance of kerf asymmetry. Finally, the research has made two contributions that are of practical importance to the funding company, Kerf Ltd. and to the wider industry. These are a kinematic investigation of a bevel-capable PAC head and an investigation into height control using stereopsis.

8 Supporting material

8.1 Publications

This research produced the following publications:

1. Flemmer, M. T., Liqiong. (2017a). Accurate Metrology for Plasma-arc Cutters. *International Journal of Mechanical and Production Engineering, 5*(9), 47-51.
2. Flemmer, M. T., Liqiong. (2017b). *Computer Vision for Automatic Accurate Plasma-arc Cutting Measurement.* Paper presented at the Mechatronics and Machine Vision in Practice (M2VIP), 2017 24th International Conference on, Auckland, New Zealand.

8.2 List of References

600 C series Platinum sensor with wires for high temperatures. Retrieved from: http://docs-asia.electrocomponents.com/webdocs/14ec/0900766b814ec831.pdf

AKS. (2014). "Robo-kut" 5-axis plasma bevel head. *Products.* Retrieved March 3 2016 from http://www.faheyinc.com/product/robo-kut-5-axis-plasma-bevel-head/

Ali, S., Prasad, D. K., Shankar, S., & Saw, K. (2016, 20/03/2016). *Experimental investigation of temperature distribution and surface roughness for cutting aluminium-19000 and stainless steel 304 using plasma arc cutting.* Paper presented at the 4th International conference on Recent Innovations in Science Engineering and Management, New Delhi.

Aloke, R., Girish, V., Scrutton, R. F., & Molian, P. A. (1997). A model for prediction of dimensional tolerances of laser cut holes in mild steel then plates. *International Journal of Machine Tools & Manufacture, 37*(8), 1069-1078.

Anand, S., McCord, C., Sharma, R., & Balachander, T. (1999). An integrated machine vision based system for solving the nonconvex cutting stock problem using genetic algorithms. *Journal of Manufacturing Systems, 18*(6), 396.

Anand, S., Raman, S., & Wysk, R. (1988). Vision assisted NC milling path generation. *Journal of Manufacturing Systems, 7*(3), 233-240.

Arpaia, P., De Matteis, E., & Inglese, V. (2015). Software for measurement automation: a review of the state of the art. *Measurement, 66*, 11-23.

Bas, G., Stoev, L., & Durakbasa, N. M. (2014). *Assesment of the production quality in machining by integrating a system of high precision measurement.* Paper presented at the DAAAM International Symposium on intelligent manufacturing and automation, Vienna.

Bemis, B. L., & Settles, G. S. (1998). *Visualization of liquid metal, arc, and jet interactions in plasma cutting of steel sheet.* Paper presented at the 8th international symposium on flow visualization (Sorrento, Italy.

Bemis, B. L., & Settles, G. S. (1999). Ultraviolet imaging of the anode attachment in transferred-arc plasma cutting. *IEEE transactions on plasma science, 27*(1), 44-45.

Bidajwala, R. C., & Trivedi, M. A. (2014). Parametric Optimization On SS 304L Using Plasma Arc Cutting - A review. *International Journal for Innovative Research in Science and Technology, 1*(7), 147-149.

Bidajwala, R. C., & Trivedi, M. M. A. (2014). Parametric optimization on ss 304l using plasma arc cutting-a review. *technology, 152*, 156.

Bini, R., Colosimo, B., Kutlu, A., & Monno, M. (2008a). Experimental study of the features of the kerf generated by a 200A high tolerance plasma arc cutting system. *Journal of materials processing technology, 196*(1), 345-355.

Bini, R., Colosimo, B. M., Kutlu, A. E., & Monno, M. (2008b). Experimental study of the features of the kerf generated by a 200A high tolerance plasma arc cutting system. *Journal of materials processing technology, 196*(1-3), 345-355.

Boselli, M., Colombo, V., Ghedini, E., Gherardi, M., Rotundo, F., & Sanibondi, P. (2013). High-speed imaging investigation of transient phenomena impacting plasma arc cutting process optimization. *Journal of Physics D: Applied Physics, 46*(22), 224010.

Cantoro, G., Colombo, V., Concetti, A., Ghedini, E., Sanibondi, P., Zinzani, F., . . . Vancini, M. (2011). *Plasma arc cutting technology: simulation and experiments.* Paper presented at the Journal of Physics: Conference Series.

Carslaw, H., & Jaeger, J. C. (1959). Conduction of heat in solids, 510 pp., clarendon. In: Oxford, UK.

Chamarthi, S., Reddy, N. S., Elipey, M. K., & Reddy, D. R. (2013). Investigation analysis of plasma arc cutting parameters on the unevenness surface of hardox-400 material. *Procedia Engineering, 64*, 854-861.

Chen, J. C., Li, Y., & Cox, R. A. (2009). Taguchi-based six sigma approach to optimize plasma cutting process: An industrial case study. *The International Journal of Advanced Manufacturing Technology, 41*(7), 760-769.

Chen, S., Li, Y., & Kwok, N. M. (2011). Active vision in robotic systems; A survey of recent developments. *the international journal of robotics research, 30*(11), 1343-1377.

Colombo, V., Concetti, A., Ghedini, E., Dallavalle, S., & Vancini, M. (2009). High-speed imaging in plasma arc cutting: a review and new developments. *Plasma Sources Science and Technology, 18*(2), 023001.

Colt, J. (2015). Troubleshooting CNC plasma cutting, Part 2. *Practical welding today.* Retrieved 26/02 2019 from https://www.thefabricator.com/article/cuttingweldprep/troubleshooting-cnc-plasma-cutting-part-ii

Craig, J. J. (2005). *Introduction to Robotics: mechanics and control*. Upper Saddle River: Pearson Prentice Hall.

Das, M. K., Kumar, K., Barman, T. K., & Sahoo, P. (2014). Optimization of process parameters in plasma arc cutting of EN 31 steel based on MRR and multiple roughness characteristics using grey relational analysis. *Procedia Materials Science, 5*, 1550-1559.

Dhumal, M. R. R., Patil, M. H. H., Dabhade, M. A. R., Papal, M. H. M., & Kulkarni, M. N. K. (2017). A review of pipe inspecting robot and its applications.

Dodun, O., Bangu, S. I., Slătineanu, L., Vasile, M., Beşliu, I., & Coteaţă, M. (2016). *Kerf generation during the plasma cutting process.* Paper presented at the AIP Conference Proceedings.

Eichler, S., Hussary, N., Siewert, E., & Schein, J. (2014). *Investigation of the anode attachment process in plasma arc cutting.* Paper presented at the Journal of Physics: Conference Series.

Eisazadeh-Far, K., Metghalchi, H., & Keck, J. C. (2011). Thermodynamic properties of ionized gases at high temperatures. *Journal of Energy Resources Technology, 133*(2), 022201.

Etherington, D. (2014). *Robotic head for CNC machine*. Palmerston North: Massey University

Ferent-Pipas, S., Dindelegan, M., Padurean, B., Ciupan, E., & Ciupan, C. (2014, March). Cost Calculator for Water jet, laser and plasma machining. *Applied Mathemematics and Mechanics,* 73-76.

Flemmer, M. T., Liqiong. (2017a). Accurate metrology for plasma arc cutters. *International Journal of Mechanical and Production Engineering, 5*(9), 47-51.

Flemmer, M. T., Liqiong. (2017b). *Computer vision for automatic accurate plasma arc cutting measurement.* Paper presented at the Mechatronics and Machine Vision in Practice (M2VIP), 2017 24th International Conference on, Auckland, New Zealand.

FLIR. (2017). Use low-cost material to increase target emissivity. Retrieved 20/10 2017

Freton, P., Gonzalez, J., & Gleizes, A. (2000). Comparison between a two-and a three-dimensional arc plasma configuration. *Journal of Physics D: Applied Physics, 33*(19), 2442.

Freton, P., Gonzalez, J., & Gleizes, A. (2003). *Temperature measurements in a shock wave created by a cutting plasma torch*. TOULOUSE-3 UNIV (FRANCE).

Freton, P., Gonzalez, J., Gleizes, A., Peyret, F. C., Caillibotte, G., & Delzenne, M. (2001). Numerical and experimental study of a plasma cutting torch. *Journal of Physics D: Applied Physics, 35*(2), 115.

Freton, P., Gonzalez, J., Peyret, F. C., & Gleizes, A. (2003). Complementary experimental and theoretical approaches to the determination of the plasma characteristics in a cutting plasma torch. *Journal of Physics D: Applied Physics, 36*(11), 1269.

Freton, P., Gonzalez, J., Ranarijaona, Z., & Mougenot, J. (2012). Energy equation formulations for two-temperature modelling of 'thermal'plasmas. *Journal of Physics D: Applied Physics, 45*(46), 465206.

Gage, R. M. (1957). Arc torch and process. In: Google Patents.

Gariboldi, E., & Previtali, B. (2005). High tolerance plasma arc cutting of commercially pure titanium. *Journal of materials processing technology, 160*(1), 77-89.

Ghorui, S., Heberlein, J., & Pfender, E. (2007). Non-equilibrium modelling of an oxygen-plasma cutting torch. *Journal of Physics D: Applied Physics, 40*(7), 1966.

Girard, L., Teulet, P., Razafinimanana, M., Gleizes, A., Camy-Peyret, F., Baillot, E., & Richard, F. (2006). Experimental study of an oxygen plasma cutting torch: I. Spectroscopic analysis of the plasma jet. *Journal of Physics D: Applied Physics, 39*(8), 1543.

Gleizes, A., Gonzalez, J.-J., & Freton, P. (2005). Thermal plasma modelling. *Journal of Physics D: Applied Physics, 38*(9), R153.

Gonzalez, J., Freton, P., & Gleizes, A. (2002). Comparisons between two-and three-dimensional models: gas injection and arc attachment. *Journal of Physics D: Applied Physics, 35*(24), 3181.

Gonzalez, J., Lago, F., Freton, P., Masquere, M., & Franceries, X. (2005). Numerical modelling of an electric arc and its interaction with the anode: part II. The three-dimensional model—influence of external forces on the arc column. *Journal of Physics D: Applied Physics, 38*(2), 306.

Gray, G. (2014). CEO Kerf. In.

Gullu, A., & Atici, U. (2006). Investigation of the effects of plasma arc parameters on the structure variation of AISI 304 and St 52 steels. *Materials & design, 27*(10), 1157-1162.

Hlína, J., Šonský, J., & Gruber, J. (2017). Tomographic measurements of temperature fluctuations in an air plasma cutting torch. *Plasma Chemistry and Plasma Processing, 37*(3), 689-699.

Hsu, K., Etemadi, K., & Pfender, E. (1983). Study of the free-burning high-intensity argon arc. *Journal of applied physics, 54*(3), 1293-1301.

Ilii, S.-M., Coteata, M., & Munteanu, A. (2010). Experimental results concerning the variation of surface roughness parameter (Ra) at plasma arc cutting of a stainless steel workpiece. *International Journal of Modern Manufacturing Technologies, II/1*, 31-36.

Ilii, S. M., Tanasa, R., & Munteanu, A. (2007). A statistic evolution of plasma beam machining interest. In: Nonconventional Technologies Review.

ISO, B. (2017). 9013: 2017 Thermal cutting. *Classification of thermal cuts. Geometrical product specification and quality tolerances*.

Jones, G., & Fang, M. (1980). The physics of high-power arcs. *Reports on progress in physics, 43*(12), 1415.

Jurokovic, J., Korosec, M., & Kopac, J. (2005). New approach in tool wear measuring technique using CCD vision system. *International Journal of Machine Tools & Manufacture, 45*(4), 1023-1030.

Kavka, T., Chumak, O., Šonský, J., Heinrich, M., Stehrer, T., & Pauser, H. (2013). Experimental study of anode processes in plasma arc cutting. *Journal of Physics D: Applied Physics, 46*(6), 065202.

Kavka, T., Tossen, S., Maslani, A., Konrad, M., Pauser, H., & Stehrer, T. (2014). *Experimental investigation of energy balance in plasma arc cutting process.* Paper presented at the Journal of Physics: Conference Series.

Kechagias, J., Petousis, M., Vidakis, N., & Mastorakis, N. (2017). *Plasma arc cutting dimensional accuracy optimization employing the parameter design approach.* Paper presented at the ITM Web of Conferences.

Keraita, J. N., & Kim, K.-H. (2007). PC-based low-cost CNC automation of plasma profile cutting of pipes. *ARPN Journal of engineering and applied sciences, 2*(5), 1-6.

Koike. (2014). Plasma chamfering head 3D-LT. Retrieved March 3 2016 from http://www.directindustry.com/prod/koike/product-19388-1458525.html

Kurada, S., & Bradley, C. (1997). A review of machine vision sensors for tool condition monitoring. *Computers in industry, 34*(1), 55-72.

Lago, F., Gonzalez, J., Freton, P., & Gleizes, A. (2004). A numerical modelling of an electric arc and its interaction with the anode: Part I. The two-dimensional model. *Journal of Physics D: Applied Physics, 37*(6), 883.

Lahri, V., Juriani, A., & Vaishya, A. L. (2016). Plate cutting error in fabrication shop & their remedial measure with industrial case study. *International Journal of Scientific & Engineering Research, 7*(3).

Lazarevic, A., & Lazarevic, D. (2017). Investigations of material hardness and structural changes in the heat-affected zone during plasma cutting. *Welding in the World, 61*(6), 1069-1075.

Lazarevic, A., Manic, M., & Lazarevic, D. (2011). *Energy balance of the plasma arc cutting process.* Paper presented at the Proceedings on 34th International Conference on Production Engineering, Serbia Google Scholar.

Lee, C. S. G. (1982, Dec). Robot arm, kinematics, dynamics and control. *Computer,* 62-80.

McAdams, W. H. (1954). *Heat transmision 3rd edition* (3 ed.). NY: McGraw Hill Publishing Company.

Minetola, P. (2011). The importance of a correct alignment in contactless inspection of additive manufactured parts. *International journal of precision engineering and manufacturing, 13*(2), 211-218.

Momber, A. (2016). Image processing as a tool for high-pressure water jet coating removal assessment. *The International Journal of Advanced Manufacturing Technology, 87*(1-4), 571-578.

Naghizadeh-Kashani, Y., Cressault, Y., & Gleizes, A. (2002). Net emission coefficient of air

thermal plasmas. *Journal of Physics D: Applied Physics, 35*(22), 2925.

Nemchinsky, V. (1994). *Liquid metal movement during plasma arc cutting*. American Welding Society, Miami, FL (United States).

Nemchinsky, V. (2017). Heat transfer in plasma arc cutting.

Nemchinsky, V. A. (1997). Dross formation and heat transfer during plasma arc cutting. *Journal of Physics D: Applied Physics, 30*(18), 2566.

Nemchinsky, V. A. (1998). Plasma flow in a nozzle during plasma arc cutting. *Journal of Physics D: Applied Physics, 31*(21), 3102.

Nemchinsky, V. A., & Severance, W. (2006). What we know and what we do not know about plasma arc cutting. *Journal of Physics D: Applied Physics, 39*(22), R423.

Nemchinsky, V. A., & Severance, W. (2009). Plasma arc cutting: speed and cut quality. *Journal of Physics D: Applied Physics, 42*(19), 195204.

Newman, T. S., & Jain, A. K. (1995). A survey of automated visual inspection. *Computer vision and image understanding, 61*(2), 231-262.

Newport. (2018). Technical note: Stage components considerations. Retrieved November 10 2017 from https://www.newport.com/n/stage-components-considerations

NPTEL. (2013). Positions of slack and tight sides of belt. *Machine Elements and Drives.* Retrieved November 10 2017 from http://nptel.ac.in/courses/116102012/8

Olsson, D. M., & Nelson, L. S. (1975). The Nelder-Mead simplex procedure for function minimization. *Technometrics, 17*(1), 45-51.

Osterhouse, D., Lindsay, J., & Heberlein, J. (2013). Using arc voltage to locate the anode attachment in plasma arc cutting. *Journal of Physics D: Applied Physics, 46*(22), 224013.

Pardo, C., González-Aguilar, J., Rodriguez-Yunta, A., & Calderón, M. (1999). Spectroscopic analysis of an air plasma cutting torch. *Journal of Physics D: Applied Physics, 32*(17), 2181.

Paul, E., Babu, D. E., & Paul, B. (2014). Design of an accuracy control system in ship building industry. *International Journal of Emerging Technology and Advanced Engineering, 4*(6), 6.

Peters, J., Bartlett, B., Lindsay, J., & Heberlein, J. (2008). Relating spectroscopic measurements in a plasma cutting torch to cutting performance. *Plasma Chemistry and Plasma Processing, 28*(3), 331-352.

Pipaş, S. F., Dindelegan, M., Pădurean, B., Ciupan, E., & Ciupan, C. (2014). Cost calculator for water jet, laser and plasma machining. *ACTA TECHNICA NAPOCENSIS-Series: APPLIED MATHEMATICS, MECHANICS, and ENGINEERING, 57*(1).

Plasma Processes of Cutting and Welding. (1976). Florence: bethlehem Steel Corporation.

Platov, S., & Turygin, Y. (2014). *Railtruck robotic spring end process operating system.* Paper presented at the Robotics in Alpe-Adria-Danube Region (RAAD), 2014 23rd International Conference on.

Raffaeli, R., Mengoni, M., & Germani, M. (2013). Context dependent automatic view planning: the inspection of mechanical components. *Computer-Aided Design and applications, 10*(1), 111-127.

Ramakrishnan, S. (1995). Technological challenges in thermal plasma production. *Australian Journal of Physics, 48*(3), 377-402.

Ramakrishnan, S., Gershenzon, M., Polivka, F., Kearney, T. N., & Rogozinski, M. W. (1997).

Plasma generation for the plasma cutting process. *IEEE transactions on plasma science, 25*(5), 937-946.

Ramakrishnan, S., & Rogozinski, M. (1997). Properties of electric arc plasma for metal cutting. *Journal of Physics D: Applied Physics, 30*(4), 636.

Ramakrishnan, S., Shrinet, V., Polivka, F., Kearney, T., & Koltun, P. (2000). Influence of gas composition on plasma arc cutting of mild steel. *Journal of Physics D: Applied Physics, 33*(18), 2288.

Ruz, G. A., Estevez, P. A., & Ramirez, P. A. (2009). Automated visual inspection system for wood defect classification using computational intelligence techniques. *International Journal of Systems Science, 40*(2), 163-172.

Salonitis, K., & Vatousianos, S. (2012). Experimental investigation of the plasma arc cutting process. *Procedia CIRP, 3*, 287-292.

Savio, E., Chiffre, L., De, & Schmitt, R. (2007). Metrology of freeform shaped parts. *CIRP Annal - Manufacturing Technology, 56*(2), 810-835.

Scott, W., Roth, G., & Rivest, J. F. (2003). View planning for automated 3D object reconstruction and inspection. *ACM computing surveys, 35*(1), 63-96.

Shapiro, A. H. (1953). *The dynamics and thermodynamics of compressible fluid flow* (Vol. 1): John Wiley & Sons.

Singh, D., & Chattopadhyaya, S. (2014). Temperature measurement in plasma cutting through infra red imaging and comparison with FEM. *Manufacturing and Industrial Engineering, 13*(3-4).

Singh, V. (2012). *Analysis of process parameters of plasma arc cutting using design of experiment.*

Son, S., Park, H., & Lee, K. H. (2002). Automated laser scanning system for reverse engineering and inspection. *International Journal of Machine Tools and Manufacture, 42*(8), 889-897.

Tang, C. H., Tang, H., & Tay, P. K. (2016). Low cost digital close range photogrammetric measurement of an as-built anchor handling tug hull. *Ocean Engineering, 119*, 67-74.

Teste, P., Leblanc, T., Rossignol, J., & Andlauer, R. (2008). Contribution to the assessment of the power balance at the electrodes of an electric arc in air. *Plasma Sources Science and Technology, 17*(3), 035001.

Teti, R. (2015). Advanced IT methods of signal processing and decision making for zero defect manufacturing in machining. *Procedia CIRP, 28*, 3-15.

Teulet, P., Girard, L., Razafinimanana, M., Gleizes, A., Bertrand, P., Camy-Peyret, F., . . . Richard, F. (2006). Experimental study of an oxygen plasma cutting torch: II. Arc–material interaction, energy transfer and anode attachment. *Journal of Physics D: Applied Physics, 39*(8), 1557.

Trelles, J., Chazelas, C., Vardelle, A., & Heberlein, J. (2009). Arc plasma torch modeling. *Journal of Thermal Spray Technology, 18*(5-6), 728.

Węglowski, M. S., & Pfeifer, T. (2014). Influence of cutting technology on properties of the cut edges. *Advances in Manufacturing Science and Technology, 38*(2), 63--73.

Wu, Y., Hackett, C. M., Eickhoff, S. T., & Hanover, N. (1997). *The effects of plasma arc cutting on mild steel.* Paper presented at the Proceedings of the FabTech International Technical Conference.

Xu, S., Anwer, N., & Mehdi-Souzani, C. (2015). *Machining feature recognition from in-process model of NC simulation.* Paper presented at the Computer-Aided Design and

applications, London.

Xu, S., Anwer, N., & Qiao, L. (2015). *Feature recognition for virtual machining.* Paper presented at the Proceedings of the 21st international conference on industrial engineering and engineering management 2014, Zhuhai.

Xu, W., Fang, J., & Lu, Y. (2002). Study on ceramic cutting by plasma arc. *Journal of materials processing technology, 129*(1), 152-156.

Zhang, B., Huang, W., Li, J., Zhao, C., Fan, S., Wu, J., & Liu, C. (2014). Principles, developments and applications of computer vision for external quality inspection of fruits and vegetables: A review. *Food Research International, 62*, 326-343.

Zhang, X., Singh, A., & Jagersand, M. (2015). *RKLT: 8 DOF real-time robust video tracking combing coarse RANSAC features and accurate fast template registration.* Paper presented at the Computer and Robot Vision (CRV), 2015 12th Conference on.

Zhou, Q., Yin, H., Li, H., Xu, X., Liu, F., Guo, S., . . . Xu, P. (2009). The effect of plasma-gas swirl flow on a highly constricted plasma cutting arc. *Journal of Physics D: Applied Physics, 42*(9), 095208.

Zhu, W., Mei, B., Yan, G., & Ke, Y. (2014). Measurement error analysis and accuracy enhancement of 2D vision system for robotic drilling. *Robotics and Computer-Integrated Manufacturing, 30*(2), 160-171.

8.3 Appendix A: Hysteresis Measurement

8.3.1 A.1 Vision Method Hysteresis Measurement (Method 1)

The data acquired using the vision method (Method 1) is shown in the tables below. The initial measurement (repeated 3 times) in Table 8.1 shows a significant amount of hysteresis in both axes. Table 8.2 and Table 8.3 show the effect of adjusting the X- and Y-direction belts respectively.

Table 8.1 Initial hysteresis of the carriage.

X					
	Distance (Pixels)				
	1	2	3	Average	Range
dir 1	425.369	425.369	425.254	425.331	0.115
dir 2	425.967	425.982	425.983	425.977	0.016
			pixels	0.647	
			mm	0.154	
Y					
	Distance (Pixels)				
	1	2	3	Average	Range
dir 1	380.674	380.629	380.702	380.668	0.073
dir 2	382.840	382.800	382.873	382.838	0.073
			pixels	2.169	
			mm	0.493	

Table 8.2 Effect of tightening the X-axis belt.

X					
	Distance (Pixels)				
	1	2	3	Average	Range
dir 1	459.849	459.847	459.828	459.841	0.021
dir 2	459.737	459.705	459.684	459.709	0.053
			pixels	0.133	
			mm	0.032	
Y					
	Distance (Pixels)				
	1	2	3	Average	Range
dir 1	365.477	365.523	365.492	365.497	0.046
dir 2	364.658	364.486	364.348	364.497	0.310
			pixels	1.000	
			mm	0.227	

Table 8.3 Effect of tightening the Y-axis belt.

X					
	Distance (Pixels)				
	1	2	3	Average	Range
dir 1	459.876	459.874	459.856	459.869	0.020
dir 2	459.764	459.731	459.708	459.734	0.056
			pixels	0.134	
			mm	0.032	
Y					
	Distance (Pixels)				
	1	2	3	Average	Range
dir 1	365.598	365.642	365.671	365.637	0.073
dir 2	364.907	364.891	364.914	364.904	0.023
			pixels	0.733	
			mm	0.167	

8.3.1.1 Findings

The tests showed that initially the plasma cutter carriage had an average hysteresis of 0.154mm

in the X-direction and 0.493mm in the Y-direction. Tightening the belts reduced this to 0.032 in the X-direction and 0.167 in the Y-direction, i.e. a reduction of the hysteresis error by 79.2% and 66.1% in the X- and Y- direction respectively. This level of hysteresis error in the carriage position is acceptable in terms of the required accuracy of the edge-follower system. The slightly higher hysteresis in the Y-direction is attributed to there being more mass attached to movements in the Y-direction that the X-direction.

8.3.2 Gauge Method Hysteresis Measurement (Method 2)

The data for the tests using the gauge are shown in Figure 8.1 to Figure 8.5. Figure 8.1 and Figure 8.2 show the hysteresis for each direction, whilst Figure 8.3 - Figure 8.5 show the detailed investigation into the Y-direction.

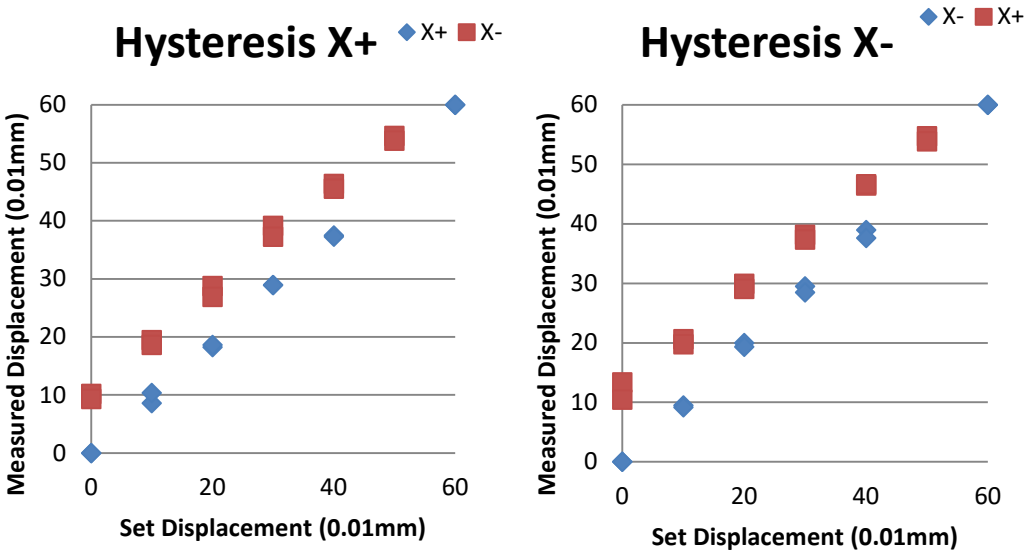

Figure 8.1 X axis hysteresis data.

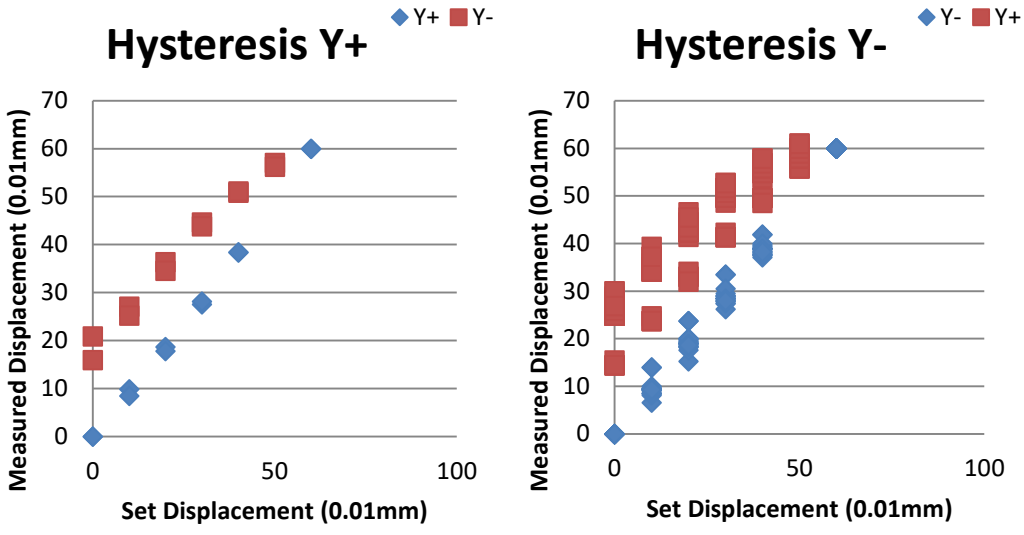

Figure 8.2 Y axis hysteresis data.

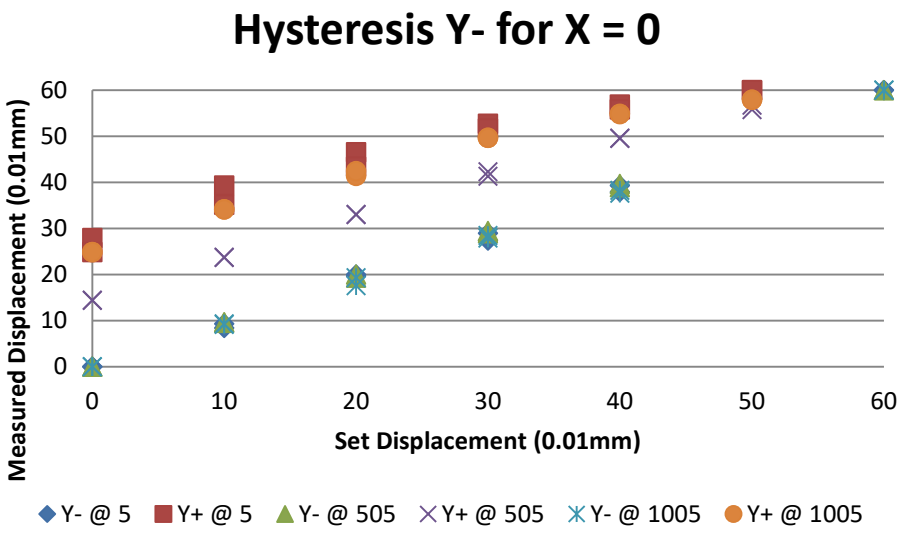

Figure 8.3 Results from hysteresis investigation in the negative Y direction for X = 0mm.

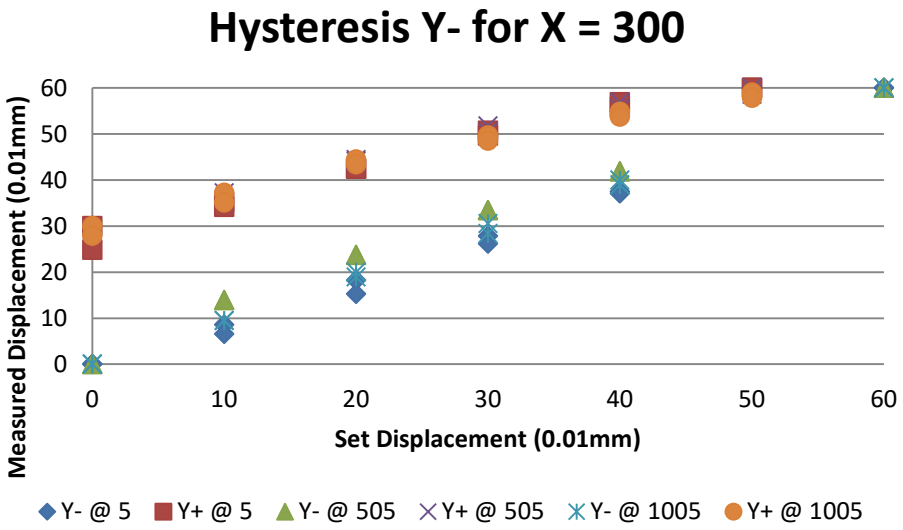

Figure 8.4 Results from hysteresis investigation in the negative Y-direction for X = 300mm.

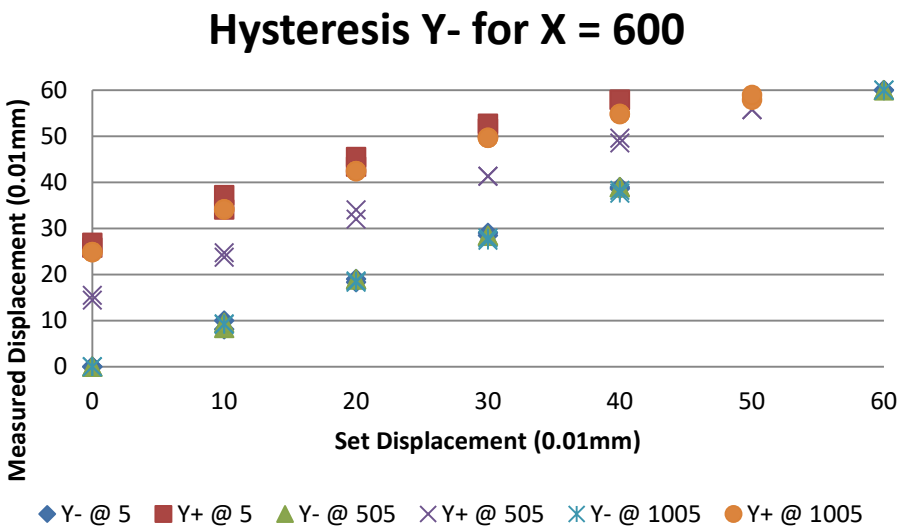

Figure 8.5 Results from hysteresis investigation in the negative Y-direction for X = 600mm.

8.3.2.1 Findings

The test carried out to determine how accurately the machine moved in the absence of hysteresis found that in the X-direction the displacement was about 993mm per 1000mm requested, and in the Y-direction it was 987mm per 1000mm requested.

8.3.2.2 Conclusions

The measurements show the initial hysteresis in the system would make it impossible to meet the desired 0.1mm of accuracy in the edge-follower routine. However, tightening the belts reduced the hysteresis to less than 0.1mm in the X-axis and slightly over 0.1mm in the Y-axis. The reason for the discrepancy in the two axes is that the Y-axis movements move more mass, which would increase the hysteresis due to belt stretch and amplify the effects of the imperfect meshing of the gears. Finally the movement of the bed was found to also have an inherent inaccuracy of approximately 1 percent. This may have arisen from a calibration error in relating encoder pulses from the driving motors to the distance travelled. These inaccuracies will be kept in mind throughout error analyses in this project.

8.4 Appendix B: Vision test rig development

This appendix describes the design of the two vision test rigs developed during this research. This enables the interested reader to further understand aspects of the results, and the reason for the final design. This appendix covers the objectives of the test rigs, the materials and construction methods used, the designs employed and the calibration processes for each.

8.4.1 Objectives

Industrially plasma-arc cutting can perform to an accuracy of 0.1mm, and achieve a class 2 cut (5 degree taper) (ISO, 2017). Therefore, the goal was set to be able to measure parts to an accuracy of 0.1mm. Kerf Ltd. also identified that being able to determine height using the sensing platform could be valuable as the current method uses capacitive sensors and is only accurate to about 0.25mm and can give inaccurate readings depending on the positioning of the torch in relation to its bed.

PAC systems can cut in any direction, so having cameras mounted in such a way that data could be gathered for the majority of the cutting time was another design consideration. Finally, the PAC environment is quite dirty with incinerated metal settling on exposed surfaces, so a mechanism to protect the cameras was also important.

8.4.2 Design: wide-view rig

The designed wide-view test rig used 4 cameras mounted around the torch. Logitech webcam c920s were chosen as they provided a high-quality image, were relatively inexpensive, and software for frame grabbing and pixel manipulation was already available. These cameras were mounted on a base plate that was clamped to the torch roughly 390mm high. This distance was selected because it gave roughly a 100mm window in which 2 cameras could observe the same feature. This would enable stereopsis that could lead to more accurate measurement as well as height detection.

The cameras were encased in a protective case that was 3D printed. This case was designed to allow a pneumatic ram to move a protective shutter to protect the cameras during piercing operations. The design also kept the cameras in a positive pressure environment to avoid contamination by dust. This was done with an air supply, filter and regulator feeding air into the top of the camera casing. The main parts purchased for this rig were:

- Logitech c920 Webcam x4
- Pneumatic Ram x4 – SMC CD85N12-25S-B
- Pressure Regulator x1 – SMC AR20 -01H-B
- Air Filter x1 – SMC AFD20-02-C-A
- Solenoid Valve x1 – SMC VT307-5DZ-01-F

The Logitech c920 Webcam was chosen as the camera for a few reasons. Firstly, it supplied a suitable quality image (1080-pixel resolution) that would be sufficient for the accuracy required. Secondly, they are relatively in-expensive and available (approximately $100). Finally, the university used these cameras for various projects, so expertise and help were available.

The machining of the aluminium for the frame, and the printing of the cases was accomplished in house. Figure 8.6 - Figure 8.9 show the final design for this sensor rig, as well as the constructed product. Slight revisions were made throughout the development and testing of it, most notably a slot was added to allow easier mounting and dismounting, and some strip lighting was placed on the underside of the rig to help offset the shadows the rig was casting.

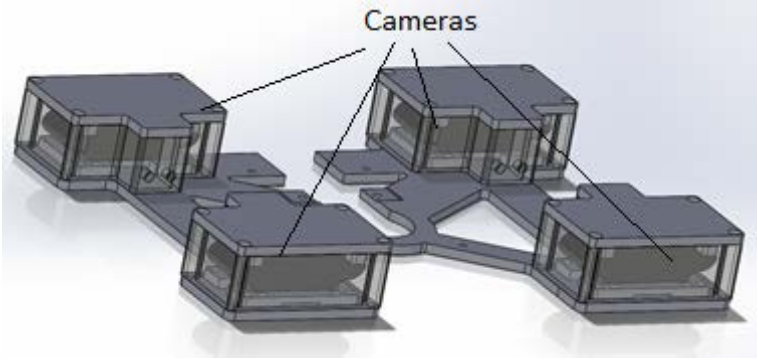

Figure 8.6 SolidWorks™ model of the wide-view, vision showing the 4 cameras and their relative positions.

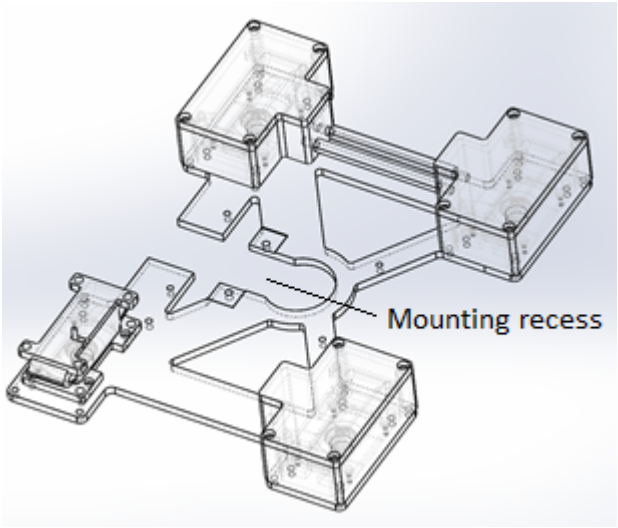

Figure 8.7 SolidWorks™ model showing the mounting of the web cam on the rig.

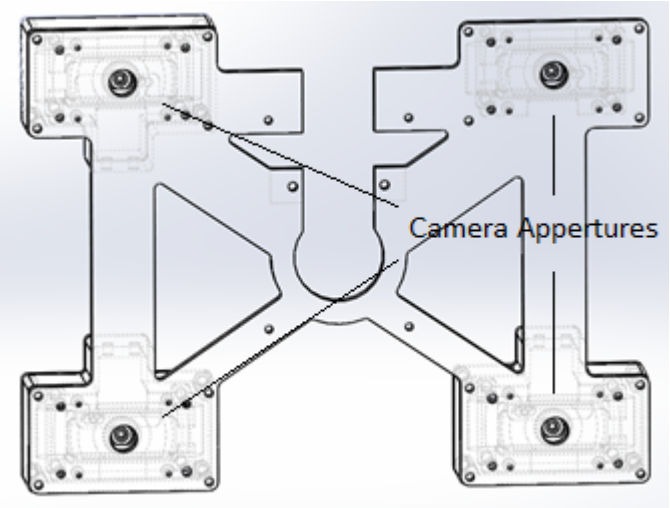

Figure 8.8 SolidWorks™ model showing the vision rig from below.

Figure 8.9 Image of the complete wide-view vision rig.

Calibration

Calibration of a camera set up is always a key part of any application using vision-based metrology. The key parameters identified to calibrate were:

- $ppmm_0, ppmm_h$ (pixels per millimeter) – A measure of the spacial representation of a pixel, and how this varies with respect to height.
- $\vec{c}_o$(mm) – The measure of the offset of the camera centre with respect to the torch in the X and Y axes in millimetres.
- θ_c (radians) – The rotation of the image space about its centre with respect to the plasma carriage system's reference frame in radians.

Calibration Methodology

A procedure was designed to acquire a set of images that could allow the calculation of these parameters. To do this a disc of approximately 49.3mm diameter and 3mm-thick was machined. This disc had a 45-degree tapered edge to simplify edge finding. The disc was painted black and was placed on a white background at the torch's zero position. The camera rig was then moved in 20mm increments over a 300 by 300mm square centred on the zero position (giving a set of images such as Figure 8.10). This passed the disc between the fields of view of all 4 cameras. This was then repeated at a height of 390mm above the field of vision, down to 360mm in 5mm increments which is the height range of the rig that the torch would be expected to operate at. Approximately 6000 images were taken with about 2000 of those containing a disc. During the

development of the calibration algorithm it was discovered that the lowest torch height collided with the disc, so the images from that dataset were discarded.

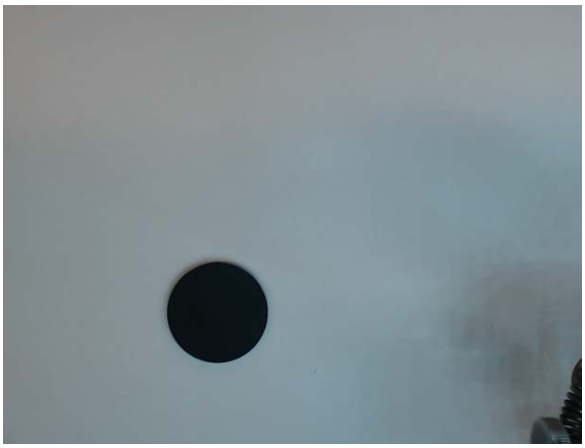

Figure 8.10 Example of an image being taken of the black disc on the white background.

Calibration Algorithm

The data analysis was conducted in three main stages.

1. In each of the 2000 images, edge points of the disc were found (Figure 8.11). This information was then used to calculate the best approximation of a centre point at an I and J value using a simplex regression.
2. This disc centre data was then used to estimate the values of $ppmm_h$ and $ppmm_0$. This was done by regression for a best fit line using the distance travelled between the nominal image locations (20mm increments) and the distances between the disc centers in the corresponding images (about 50 pixels).
3. Next this information, the disc centre locations, and the location of the torch head were used to estimate the camera offsets and rotations. The third regression aimed to minimize the variation in the estimated location of the disc.

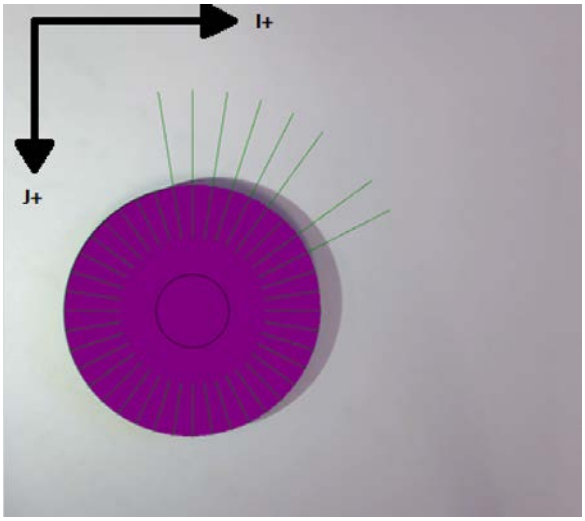

Figure 8.11 Edge point acquisition for the disc.
The estimated circle center is shown in black. The green lines represent searching for edge points. There is an observable region where the edge is not found and that is in the

darkest shadow section.

Regression 1

The first regression initially acquired a selection of edge points around the disc circumference and regressed to find the centre location of each disc, which is a coordinate vector in the image space (I, J) as well as the scaling factor for the pixels. The error calculated is the average deviation of an observed edge point from the predicted location based off a known radius and estimated $\overrightarrow{\boldsymbol{pm_0}}$, $\overrightarrow{\boldsymbol{pm_h}}$ and $\vec{\boldsymbol{c}}$ values for the i^{th} image (equation 8.1).

$$error = \sum_{i=0}^{n} \left| \vec{\boldsymbol{c}} - \vec{\boldsymbol{e}}_i - \frac{49.3}{\overrightarrow{\boldsymbol{pm_0}} + \overrightarrow{\boldsymbol{pm_h}} * h} \right|^2 \tag{8.1}$$

Where:

$\vec{\boldsymbol{c}}$ is the vector representing the disc center being estimated.
$\vec{\boldsymbol{e}}_i$is the vector representing the i[th] edge point on the circle circumference.
r is the radius of the disc in pixels.

There were various problems through this first stage. The torch head could occlude this disc in some images, so it was decided to ignore those images. Further, the shadows around the disc were always changing as the torch was moved, so the edge finding algorithm needed to be tuned to account for this. Therefore, 10 percent of the edge points with the largest contribution to the error function were omitted on the basis that not all the points were necessary, and the edge points with the largest deviation were most likely being influenced by shadowing.

After proceeding to the next regression, a discrepancy arose between the values being reported by this estimation of the pixel scaling factor, and the estimation returned by the next regression. This discrepancy arose from the system being over constrained and the first regression compensating for variations in the edge finding with the pixel scaling factor. Therefore, the scaling factor calculation was omitted from the calculation at this point with the justification that a scaling factor calculated over 300mm of movement would be more accurate than one calculated over 49.7mm. This simplified the error function to:

$$regression\ error = \sum_{i=0}^{n} |\vec{\boldsymbol{c}} - \vec{\boldsymbol{e}}_i|^2 \tag{8.2}$$

The variability of this regression was assessed by taking the average of the errors (equation 8.3) and finding the standard deviation of this estimated radius in pixels. In effect, the value an average estimation of the diameter of the disc will deviate from the actual diameter.

$$regression\ error = \frac{\sqrt{\sum_{i=0}^{n} (\overline{error} - error_i)^2}}{n} \tag{8.3}$$

Regression 2

The second regression estimates the pixel scaling factor and its relationship with height. Logically as the test rig gets closer to the bed, the resolution will increase and the scaling factor will increase. Therefore, an initial scaling factor value, $\overrightarrow{\boldsymbol{pm_0}}$, was chosen as the scaling factor for when the torch height was at its maximum (roughly 390mm above the bed). The scaling factor was then increased by a height dependent scaling factor, $\overrightarrow{\boldsymbol{pm_h}}$, as the torch is lowered, the lowering of the torch has been treated as a positive Z movement. The scaling factor, $\overrightarrow{\boldsymbol{pm}}$, was originally treated as a vector to account for any variation between the I and J directions.

$$\overrightarrow{pm} = \overrightarrow{pm_0} + \overrightarrow{pm_h} * h \tag{8.4}$$

Where:

$\overrightarrow{\boldsymbol{pm}}$ is the scaling factor in pixels per millimeter.
$\overrightarrow{\boldsymbol{pm_0}}$ is the scaling factor at torch's max height.
$\overrightarrow{\boldsymbol{pm_h}}$ is the scaling factor at height, h.
h is the distance travelled down from the max torch height in millimeters.

This regression related the movement of the disc centres in each image to the known distance travelled between the torch positions using the scaling factor relationship. Figure 8.12 shows the

progression of the disc centres as the torch head was moved. The error function (that was minimized) calculates the average distance a disc centre lies from its expected position in millimetres and is calculated as:

$$regression\ error = \frac{\sqrt{\sum_{i=0}^{n-1}\left(\frac{|\vec{c}_i - \vec{c}_{i+1}|}{\overrightarrow{pm}} - 20\right)^2}}{n} \tag{8.5}$$

Where:
$\vec{c}_i$ is the coordinate vector of the i[th] image's disc center.
n is the number of images that contain a disc.

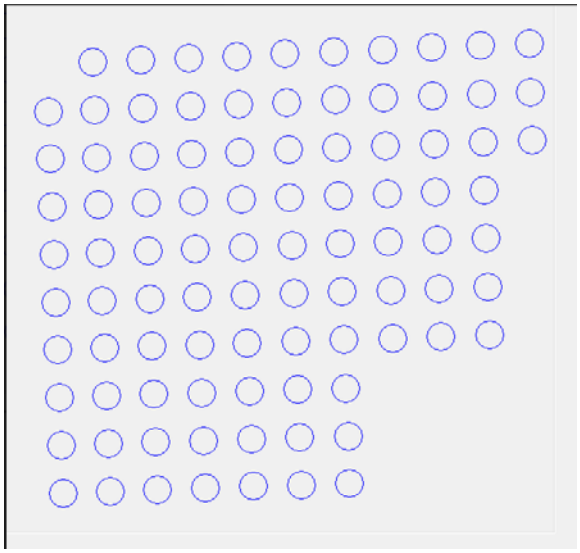

Figure 8.12 Image shows the disc centre moving in camera 1's reference frame as the torch head is moved in its grid pattern.

There were no major problems with this method to estimate the scaling factor. The average error introduced by the scaling factor was calculated at 0.05mm, which meets the accuracy goal. It was found that the components of $\boldsymbol{pm}$ in the I and J axes were within 0.2% of each other, therefore the vector component was neglected in calculations for simplification.

Regression 3

The third regression estimated the camera offset and rotation parameters, t_x, t_y, θ_c. This was done by relating the known location of the disc in the world, and transforming this into a camera's reference frame, and comparing that to the observed position. This transformation makes use of the scaling factor from the second regression and the disc centres from the first regression.

The disc lies at a coordinate vector $\vec{\boldsymbol{d}}$ and is a distance from the coordinate vector of the torch, $\vec{\boldsymbol{t}}$ and the camera offset, $\vec{\boldsymbol{c}}_{\boldsymbol{o}}$. This vector subtraction gives the distance from the disc center to the camera center in millimetres and can be converted to pixels with the scaling factor. Finally this vector needs to be rotated to account for the camera rotation factor.

$$\vec{\boldsymbol{c}} = \frac{|\vec{\boldsymbol{d}} - \vec{\boldsymbol{t}} - \vec{\boldsymbol{C}}|}{\overrightarrow{\boldsymbol{pm}}} * \begin{bmatrix} cos\theta_c & -sin\theta_c \\ sin\theta_c & cos\theta_c \end{bmatrix} \tag{8.6}$$

Where:
$\vec{\boldsymbol{c}}$ Is the coordinate vector of estimated disk center in the camera's reference frame.
$\vec{\boldsymbol{d}}$ is the coordinate vector of the disk location in the plasma cutter's reference frame.
$\vec{\boldsymbol{t}}$ is the coordinate vector of the torch head location in the plasma cutter's reference frame.
$\vec{\boldsymbol{C}}$ is the coordinate vector for the offset of the camera center from the torch head in the plasma cutter's reference frame.
$\overrightarrow{\boldsymbol{pm}}$ is the scaling factor between pixels in the camera's reference frame and

millimeters in the plasma cutter's reference frame.
θ_c is the rotation of the camera about the torch axis.

The regression minimizes the objective function between this estimated disk centre ($\vec{c}_{ei}$) and the observed disk centre. The error returned is the average deviation in pixels an estimated disc centre is away from the actual disc location.

$$regression\ error = \frac{\sqrt{\sum_{i=0}^{n} |\vec{c}_i - \vec{c}_{ei}|^2}}{n} \tag{8.7}$$

The results of the calibration results are presented in the main body.

8.4.3 Design: close-view rig

The first step in developing the close view system was to design and build a test rig that could meet the requirements:

- Provide mounting for 2 Logitech webcams 100mm above the cut face.
- Allow the mounting of lighting to prevent occlusion from shadows.
- Be easily attachable and detachable.
- Provide a sturdy and rigid base that will not move in relation to the torch head.
- Provide protection for the webcams when not being used.

The test rig was designed in SolidWorks™ and is shown in Figure 8.13 and Figure 8.14. The parts were then CNC milled and 3D printed. The parts were designed with the following constraints. The attachment collar (1) and the Logitech C920 webcams are provided parts, so the parts were designed and made to fit them. The cameras are recessed into the plate to aid with alignment. The mounting plate (2) is also recessed for alignment. The 2 fins (3) fit on either side of the Z axis lifter to constrain rotation about the torch, and the attachment collar clamps onto the plasma torch. Lighting is mounted on the underside of the plate. It is placed around the cameras to directly illuminate the area of the image that is of interest.

A clamping piece and a cover were 3D printed. The clamping piece (4) lightly tightens down onto the top of the Logitech webcams, pushing them into their locating recesses. The cover (6) slides over the cameras to protect them from sparks. The mounting plate and the base plate (5) were both machined from aluminium because it was readily available and lightweight. There are 2 benefits to the assembly being light. Firstly, it is more convenient and easier to move. Secondly, the rig mounts to the torch, which is connected with springs to the Z-axis lifter. This is to protect the torch in the case of collision. However, if the vision rig is too heavy it will affect the mounting of the torch, reducing the accuracy of the cutting.

The attachment process was designed to be straight forwards and easy. The clamping collar and mounting plate stay attached to the torch. To attach them, the torch needs to be removed from its holder. The holder fits snuggly over the torch, so unless the clamping part is split into 2 components, this is necessary. Two socket head cap screws release the base plate and attached components from the clamping and mounting pieces, and it is then free to slide out from around the torch. The test rig was found to be not quite parallel with the XY bed of the gantry system. This could potentially result in skewed images, so shim paper was placed between the mounting plate and the base plate to bring it to parallel.

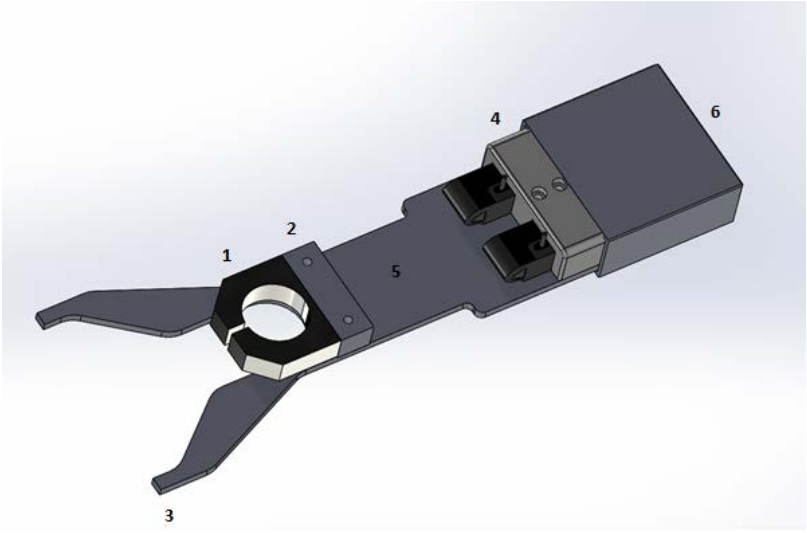

Figure 8.13 SolidWorks™ assembly of the close-view vision rig.

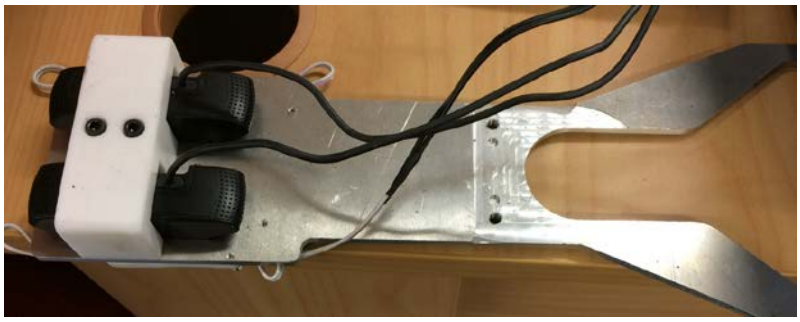

Figure 8.14 Completed assembly of the close-view vision rig, removed from the torch.

Calibration

Calibration is an important part of any vision rig and ensures that observed features in images are accurately transformed into real world data. The key calibration parameters are:

- Camera rotation (θ_c) the amount the camera reference frame has been rotated about its Z axis with respect to the reference frame of the gantry system.
- Camera offset (s_x, s_y) the offset between the camera center and the torch location in millimetres. This offset is along the gantry's reference frame and is in the X and Y direction.
- Pixels per mm initial (pm_0) the initial scaling factor for converting pixels to millimeters when the torch is fully lifted.
- Pixels per mm height (pm_h) the rate the scaling factor for converting pixels to millimeters changes per millimeter of decrease in height.
- Fisheye parameter alpha (α_f) the first constant in the equation for fisheye scaling.
- Fisheye parameter beta (β_f) the second constant in the equation for fisheye scaling.

Calibration Methodology

A steel fiducial calibration plate (Figure 8.15) was designed to allow calculation of the calibration parameters. It was sized to nearly fill the entire field of vision of the camera (200mm wide by 150mm high). A set of slots was then cut into the plate. Two 150mm long cuts were placed horizontally near the top and bottom of the plate, 135mm apart. Two 125mm long slots were

placed vertically near the left and right edges of the plate, 175mm apart. Slots were chosen because they would provide a large amount of edge point data that could be averaged to increase the accuracy of the calculation. Further, calculations of pixels per mm in the X and Y directions become more accurate the larger the distance between the slots.

The part was machined with the CNC plasma cutter and the image Figure 8.15 was taken with the part approximately centred so that the edges were just visible. A set of edge points was then acquired for each side of the slots (left and right for the vertical slots, top and bottom for the horizontal slots). These edge points were averaged to create a set of data points that lay in the middle of the cut slots. A line of best fit was then calculated for each set of slot data using a least squares regression.

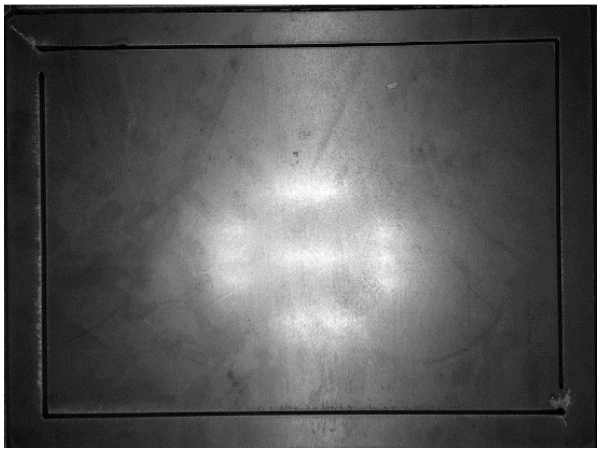

Figure 8.15 The fiducial calibration plate for the close-view vision rig.

All the calibration parameters were calculated from these lines of best fit. The camera rotation was calculated from the slope of the horizontal lines with equation (8.8). This assumes that the slots are perfectly in the reference frame of the gantry. This assumption can be made because the calibration image was taken directly after the slots had been cut, so the reference frame was unchanged. The next parameter to be calculated is the scaling factor pm_0. Initially this was calculated in the X and Y direction; however, it was found to be the same in both directions for this camera, so it was simplified to one value. The pm_0 value is calculated as the ratio of the distance between 2 parallel lines in pixels, over the known corresponding distance in millimetres (135mm for the vertical lines and 175mm for the horizontal lines) as shown in equation (8.9).

$$\theta_c = \text{atan}(\frac{a_1+a_2}{2}) \tag{8.8}$$

Where a_i and a_2 are the slopes of two corresponding lines.

$$pm_0 = \frac{n_{pixels}}{distance} \tag{8.9}$$

The offset parameters were then calculated. The G-Code to cut this part was centred on the plate; therefore, the position of the torch when the image is in the centre is roughly the value of the offsets. The offsets can then be refined by calculating the midpoints between the slots in X and Y, then calculating the distance between these midpoints and the centre of the image (in pixels) and scaling this by pixels per mm and equation (8.10). Equation 8.10 assumes that the best fit lines have been centred on the image centre; however, it can be easily adjusted if this is not the case as showing in equation (8.11). It also assumes that the image that the best fit lines were derived from is at the initial torch height.

$$s_{x,y} = (x,y)_{torch} + correction_{x,y} \tag{8.10}$$

$$correction_{x,y} = \left(\frac{b_{l1}+b_{l2}}{2} - i_c\right) * pm_0 \tag{8.11}$$

Where b_i and b_2 are the slopes of two corresponding lines.

The constants for fish eye distortion were then calculated. To estimate these, the image was

transformed with the relationship (8.12). This lengthens the distance a pixel lies from the centre of the image by a slight amount. Nelder and Meade's simplex regression (Olsson & Nelson, 1975) was then used to maximize the linearity of the 4 sets of data points by regressing for values of α_f and β_f. The values for the fisheye constants turned out to be in the order of 10^{-7} and 10^{-9} showing that the fisheye distortion was negligible. Finally; the relationship between scaling factor and height, pm_h, was determined. This was done by calculating the pm_0 value for calibration images taken at various heights (0mm – 25mm in 5mm steps where height (h) is the distance the torch has been lowered from its highest position). A linear relationship equation (8.13) was then fitted to these values.

$$r' = r(1 + \alpha r + \beta r^2) \tag{8.12}$$

$$pm = pm_0 + h * pm_h \tag{8.13}$$

The results of this methodology are presented in the main body.

8.5 Appendix C: Close-view vision

The data for the 5 test cuts for the close view section is presented in this appendix. Table 8.4 presents the measurements made for each test. Figure 8.16 - Figure 8.20 present the error plots obtained for each test.

Table 8.4 Table of test results for close view experiments.

Test #	Part #	Kerf Width (mm)	Inner measurement (mm)	Outer measurement (mm)	Measurement deviation (mm)
1	1	1.67	0.95	0.72	0.27
	2	1.96	1.01	0.94	0.27
	3	1.92	1.13	0.80	0.28
	4	1.88	0.99	0.89	0.28
	5	1.80	0.96	0.84	0.19
		1.85	**0.29**		
2	1	1.74	0.98	0.76	0.13
	2	1.72	0.86	0.86	0.18
	3	1.69	0.92	0.76	0.15
	4	1.70	0.88	0.82	0.20
	5	1.67	0.88	0.80	0.20
		1.70	**0.07**		
3	1	1.74	0.98	0.76	0.12
	2	1.72	0.86	0.86	0.18
	3	1.69	0.92	0.76	0.15
	4	1.70	0.88	0.82	0.20
		1.71	**0.05**		
4	1	1.95	0.95	1.00	0.17
	2	1.91	0.96	0.95	0.23
	3	2.02	1.03	0.99	0.14
	4		0.94	0.87	0.23
	5	1.91	0.94	0.97	0.27
		1.95	**0.11**		
5	1	1.90	0.93	0.97	0.15

	2	1.73	0.83	0.91	0.22
	3	1.87	0.93	0.94	0.12
	4	1.80	0.92	0.88	0.21
	5	1.83	0.87	0.96	0.15
		1.83	**0.17**		

8.5.1 Test 1 error plots

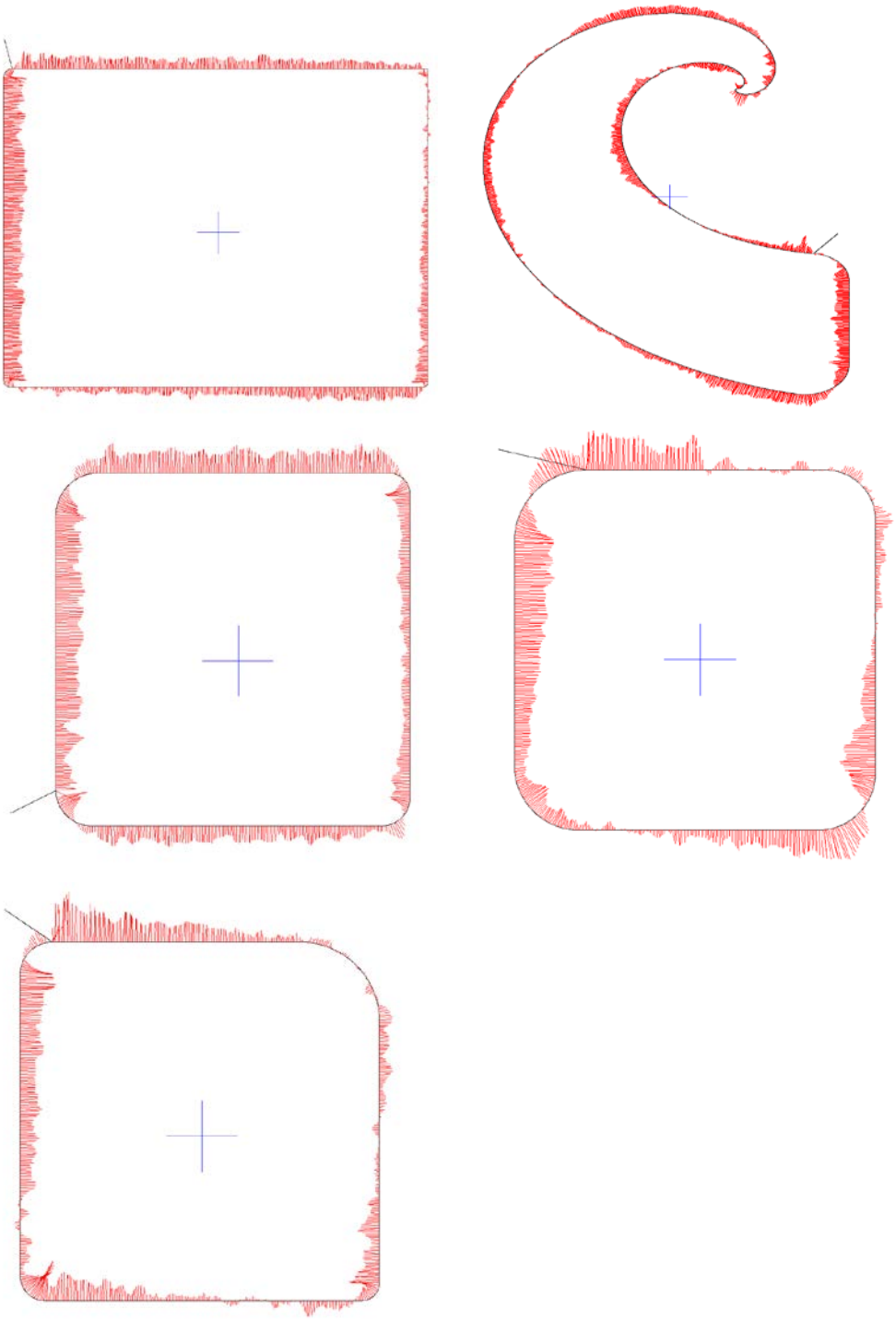

Figure 8.16: error plots from test cut 1.
Plate thickness = 3mm. Black outer line represents the idea cut piece. The red lines represent the magnitude and the direction of the error at that point. The blue cross in the middle shows 1mm in the X and Y directions for the scale of the error. The error is plotted at 50 times the scale of the black line.

8.5.2 Test 2 images

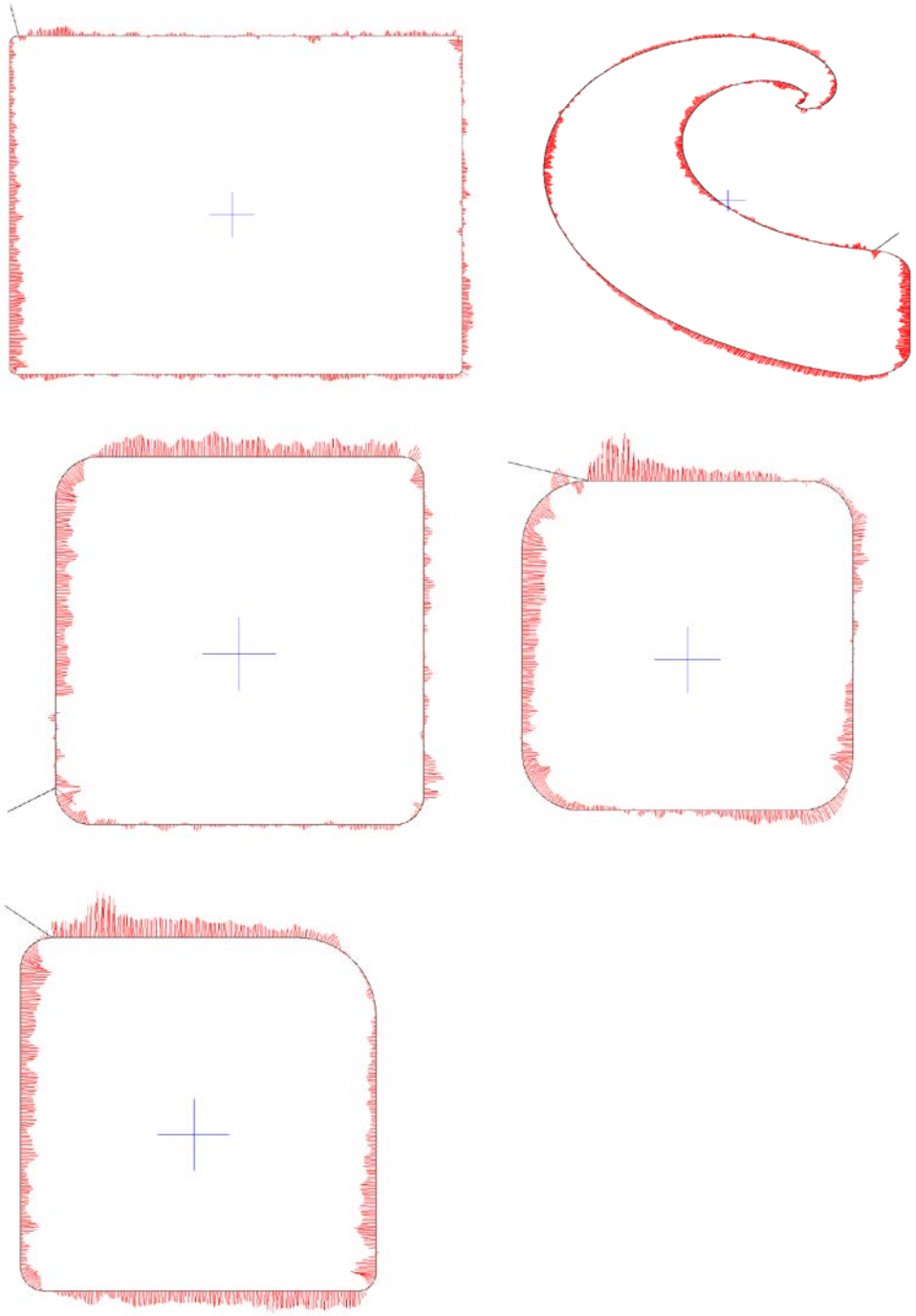

Figure 8.17: error plots from test cut 2
Plate thickness = 3mm. Black outer line represents the idea cut piece. The red lines represent the magnitude and the direction of the error at that point. The blue cross in the middle shows 1mm in the X and Y directions for the scale of the error. The error is plotted at 50 times the scale of the black line.

8.5.3 Test 3 error plots

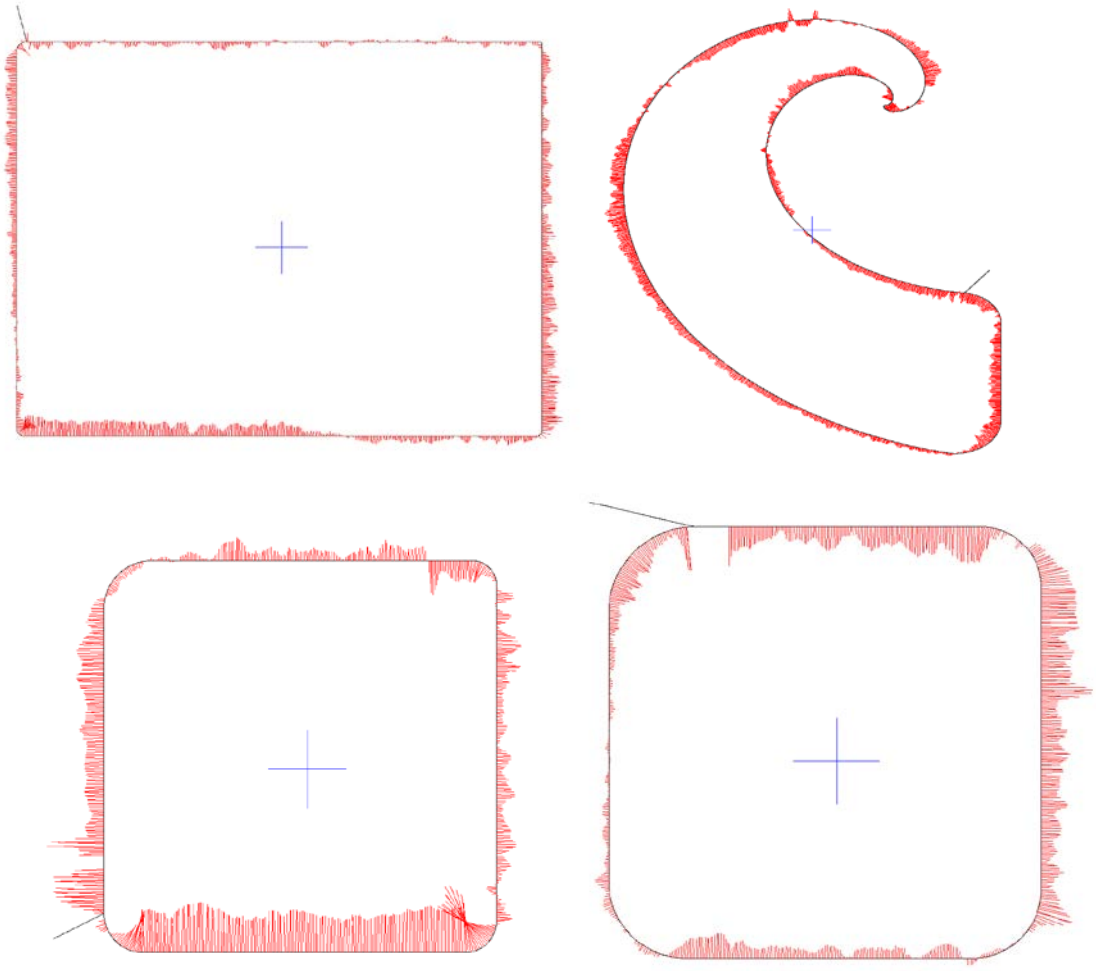

Figure 8.18: error plots from test cut 3
Plate thickness = 3mm. Black outer line represents the idea cut piece. The red lines represent the magnitude and the direction of the error at that point. The blue cross in the middle shows 1mm in the X and Y directions for the scale of the error. The error is plotted at 50 times the scale of the black line.

8.5.4 Test 4 error plots

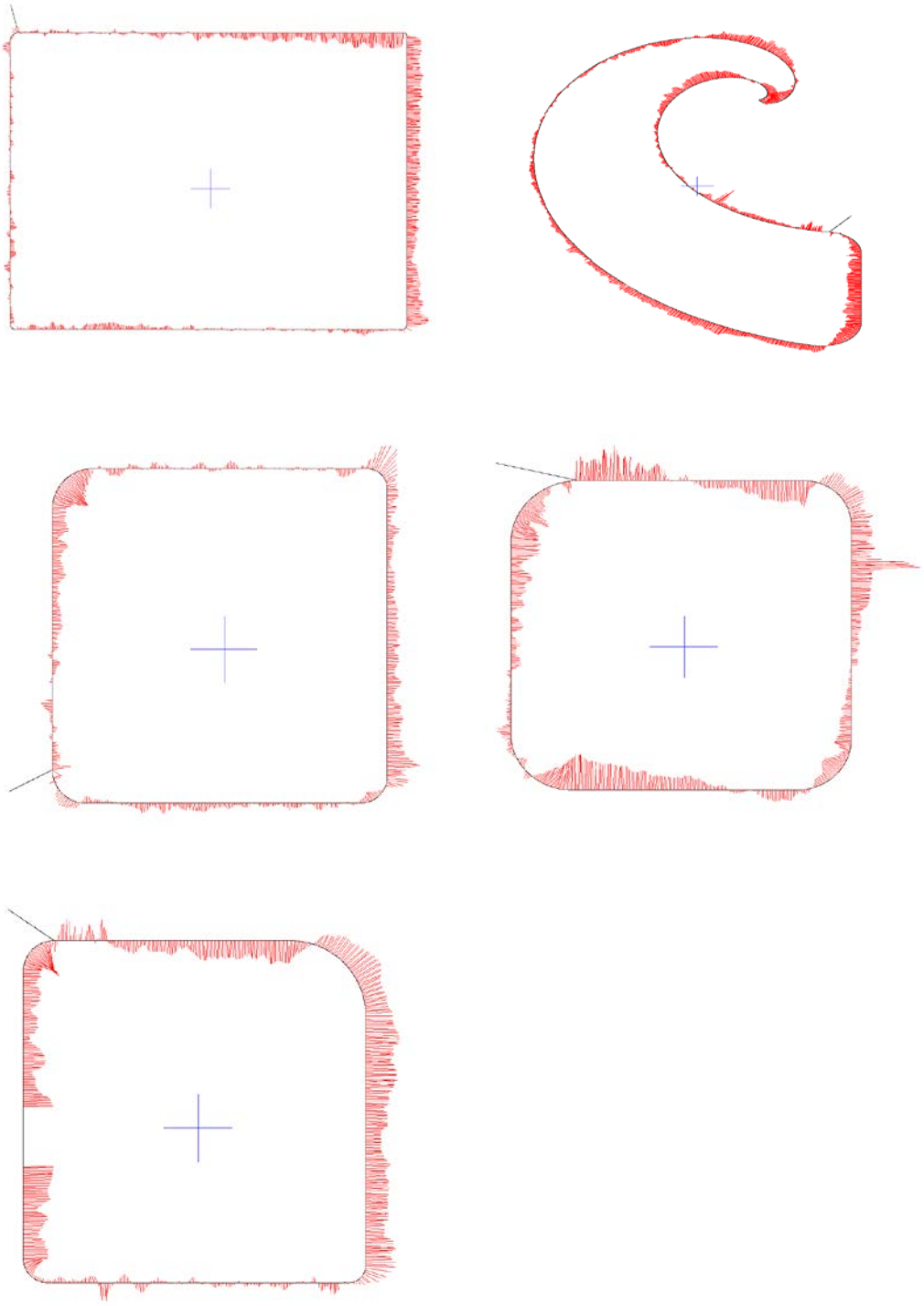

Figure 8.19: error plots from test cut 4
Plate thickness = 8mm. Black outer line represents the idea cut piece. The red lines represent the magnitude and the direction of the error at that point. The blue cross in the middle shows 1mm in the X and Y directions for the scale of the error. The error is plotted at 50 times the scale of the black line.

8.5.5 Test 5 error plots

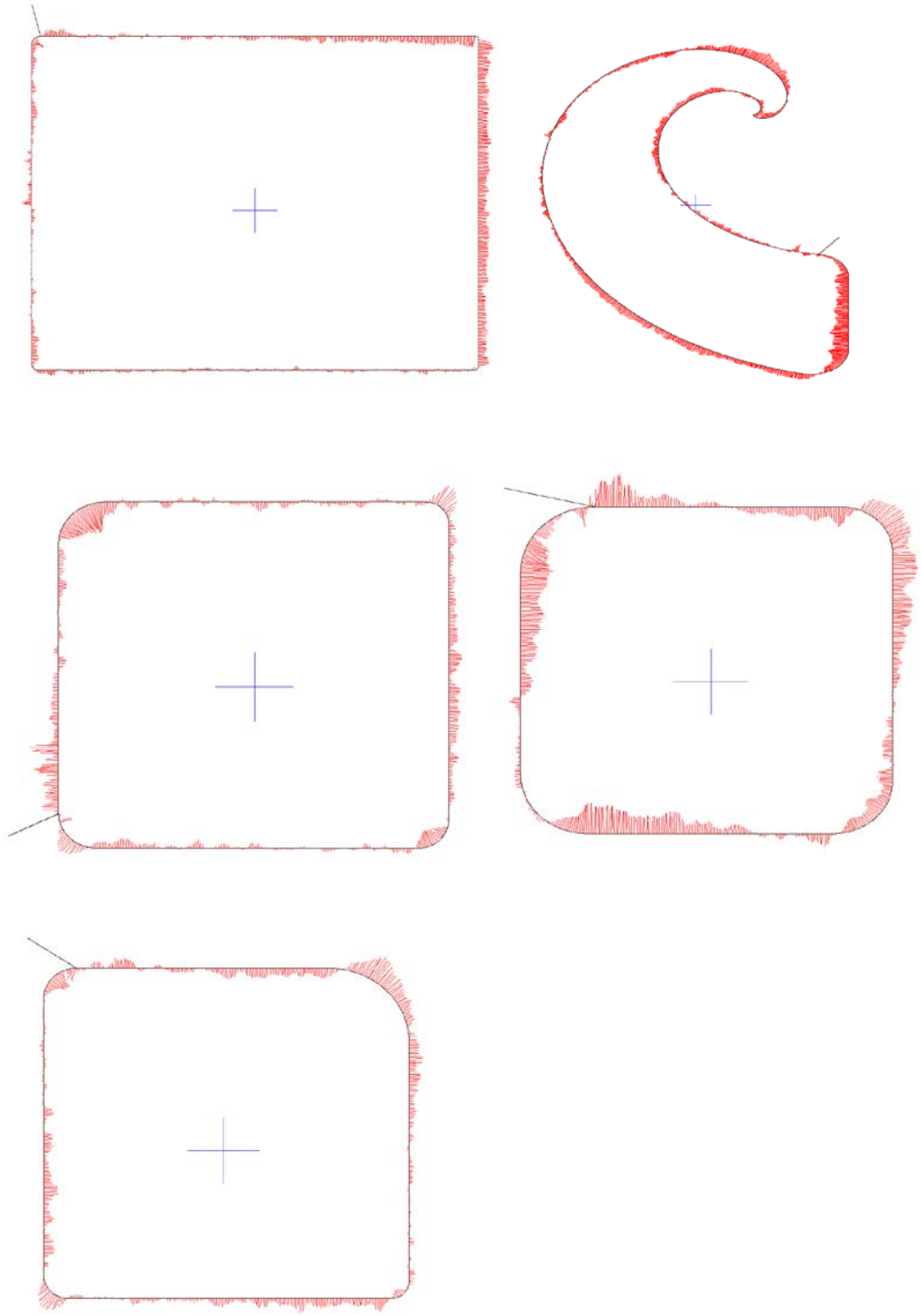

Figure 8.20: error plots from test cut 5
Plate thickness = 8mm. Black outer line represents the idea cut piece. The red lines represent the magnitude and the direction of the error at that point. The blue cross in the middle shows 1mm in the X and Y directions for the scale of the error. The error is plotted at 50 times the scale of the black line.

8.6 Appendix D: Height measurement feasibility results

Table 8.5: Tabulated results for the height feasibility investigation. h = torch height (mm), hp = predicted torch height (mm), j1 = position of common point in the J axis (pixels) for the first camera, j2 = position of the common point in the J axis (pixels) for the second camera, j1 – j2 = the difference between j1 and j2 (pixels), error1 is error calculated using the difference between h and hp, error2 is error1 squared.

T#	h	hp	j1	j2	j1 - j2	error1	error2
1	190	189.93	420.19	180.40	239.79	7.37E-02	5.43E-03
2	189.73	189.68	420.14	180.02	240.12	4.88E-02	2.38E-03
3	189.39	189.37	419.90	179.35	240.54	2.34E-02	5.50E-04
4	189.1	189.06	419.64	178.69	240.95	3.78E-02	1.43E-03
5	188.81	188.78	419.69	178.35	241.34	3.07E-02	9.41E-04
6	188.46	188.46	420.14	178.37	241.77	3.50E-03	1.22E-05
7	188.04	188.06	420.85	178.53	242.33	1.61E-02	2.59E-04
8	187.06	187.08	422.65	178.98	243.67	1.81E-02	3.28E-04
9	186.29	186.29	422.92	178.15	244.77	2.54E-04	6.47E-08
10	185.06	184.99	422.03	175.42	246.61	7.39E-02	5.46E-03
11	182.77	182.78	421.87	172.10	249.78	6.18E-03	3.82E-05
12	180.49	180.46	424.25	171.07	253.18	3.07E-02	9.42E-04
13	180.02	179.96	423.72	169.80	253.92	5.52E-02	3.04E-03
14	175	175.15	425.88	164.55	261.33	1.51E-01	2.29E-02
15	175.51	175.50	425.90	165.12	260.78	1.12E-02	1.25E-04
16	176.21	176.17	425.84	166.12	259.72	3.89E-02	1.52E-03
17	176.71	176.71	425.03	166.14	258.89	3.36E-03	1.13E-05
18	177.07	177.04	424.02	165.65	258.37	2.70E-02	7.31E-04
19	177.54	177.53	423.05	165.43	257.61	6.34E-03	4.02E-05
20	177.96	177.91	422.62	165.59	257.03	4.75E-02	2.26E-03
21	178.42	178.38	422.29	165.98	256.31	3.73E-02	1.39E-03
22	178.78	178.72	422.56	166.77	255.79	5.54E-02	3.07E-03
23	179.13	179.07	422.99	167.72	255.27	6.43E-02	4.13E-03
24	179.73	179.67	423.26	168.91	254.36	5.53E-02	3.06E-03
25	180.25	180.23	424.12	170.60	253.52	1.74E-02	3.02E-04
26	181.14	181.15	424.44	172.29	252.15	1.41E-02	1.99E-04
27	181.84	181.87	423.83	172.73	251.09	3.33E-02	1.11E-03
28	182.54	182.63	422.36	172.38	249.98	9.36E-02	8.77E-03

29	183.13	183.20	421.48	172.32	249.17	6.76E-02	4.57E-03
30	183.77	183.81	421.09	172.80	248.29	3.71E-02	1.37E-03
31	184.33	184.38	421.39	173.93	247.46	5.36E-02	2.87E-03
32	185.05	185.15	421.81	175.44	246.37	9.97E-02	9.95E-03
33	185.68	185.82	422.89	177.47	245.42	1.44E-01	2.08E-02
					average	4.47E-02	3.33E-03

8.7 Appendix E: Slot Data

This appendix contains the experimental results from the kerf angle empirical investigation. A summary and discussion of these results is presented in section 4.4.3. Table.8.6 presents the experimental run performed. Over 35 tests thickness is set at 3, 4, 6, 8 and 10mm-thick; the torch height is set at levels of 1.5mm, 3mm, 7mm, and 10mm; and the feed rate is varied from 400 – 4050mm/min as per recommendations of the operating manual. Tests 4 and 5 examined the use of torch height control with the arc voltage set at 117 and 116V respectively. Their data is included; however they have been omitted from the empirical relationship data.

Table.8.6: Experimental tests showing the process parameters for the Kerf Angle empirical investigation.

Trial data					
Set	Test #	Thickness (mm)	Height (mm)	Feed rate (mm/min)	Voltage (V)
1	1	3	3.8	3550	
	2	3	3.8	3050	
	3	3	3.8	4050	
	4	4	THC	2000	**117**
	5	4	THC	2250	**116**
	6	4	1.5	1800	
	7	4	1.5	2200	
	8	4	1.5	2600	
	9	6	1.5	1000	
	10	6	1.5	1250	
	11	6	1.5	1500	
	12	8	1.5	400	
	13	8	1.5	500	
	14	8	1.5	600	
	15	10	1.5	400	
	16	10	1.5	450	
	17	10	1.5	350	
2	18	10	10	400	
	19	10	7	400	
	20	10	3	400	
	21	8	10	500	
	22	8	7	500	
	23	8	3	500	
	24	6	10	1250	
	25	6	7	1250	

	26	6	3	1250	
	27	4	10	2200	
	28	4	7	2200	
	29	4	3	2200	
	30	3	10	3500	
	31	3	7	3500	
	32	3	3	3500	
	33	3	1.5	3000	
	34	3	1.5	3500	
	35	3	1.5	4000	

THC: Torch height control refers to the torch height being set automatically by maintaining a voltage set-point.

The experimental data was then used in an investigation into the quantification of kerf asymmetry. Two methods were used to estimate kerf asymmetry, and the results of these two methods are presented below.

8.7.1 Symmetrical-kerf method – table of results

Table 8.7 shows the results obtained using the symmetrical-kerf method. The kerf width difference is difference between the kerf widths measured on the top and bottom faces for each test cuts. The standard deviation is the deviation in the difference, and the Kerf-angle measurement calculation is explained in section 4.4.3.1.

Table 8.7 Measurements made on the experimental data using the symmetrical-kerf method.

Results			
T#	KW difference (mm)	Standard deviation (mm)	Kerf Angle (degrees)
1	-0.024	0.021	-0.46
2	0.393	0.076	7.47
3	0.510	0.080	9.64
4	0.487	0.078	6.94
5	0.390	0.086	5.56
6	0.328	0.043	4.69
7	0.344	0.088	4.91
8	0.325	0.077	4.65
9	0.162	0.080	1.55
10	0.183	0.027	1.74
11	0.270	0.047	2.58
12	0.008	0.079	0.06

13	0.062	0.060	0.44
14	0.150	0.046	1.08
15	0.015	0.074	0.09
16	0.263	0.109	1.51
17	-0.014	0.230	-0.08
18	0.893	0.112	5.10
19	0.556	0.073	3.18
20	0.328	0.071	1.88
21	0.728	0.081	5.20
22	0.505	0.126	3.61
23	0.228	0.074	1.63
24	0.851	0.103	8.07
25	0.610	0.086	5.80
26	0.450	0.076	4.29
27	0.736	0.134	10.41
28	0.657	0.090	9.33
29	0.497	0.065	7.08
30	0.559	0.072	10.55
31	0.359	0.188	6.80
32	0.481	0.061	9.11
33	0.291	0.095	5.54
34	0.281	0.088	5.35
35	0.316	0.042	6.01

8.7.2 Slot-end method – Table of results

Table 8.8 shows the results obtained using the slot-end method (described in section 4.4.3.2). This includes the kerf angles calculated for both edges from a line of best fit for both edges, and the parabolas fit to the data to describe the shape of the profiles.

Table 8.8: Table showing the kerf angle results obtained using the slot-end method for both kerf edges, as well as the parabola parameters that describe the shape of both profiles.

Slot-End Method Results								
	Left angle (°)	Right Angle (°)	Parabola Parameters L			Parabola Parameters R		
T#			A	B	C	A	B	C
1	9.4	-0.2	1.18E-02	-2.49E-01	3.57E+00	1.23E-03	-1.09E-01	-1.14E+00
2	15.7	-0.4	2.94E-03	-6.79E-02	3.32E+00	-2.95E-03	-7.97E-02	-9.23E-01
3	14.4	-1.6	8.58E-03	-2.13E-01	4.05E+00	-7.88E-04	-1.12E-01	-5.96E-01
4	-1.1	4.7	2.91E-04	7.43E-02	1.13E+00	-2.87E-03	8.92E-02	-3.54E+00
5	-1.9	3.9	-1.97E-03	1.23E-01	7.49E-01	-3.81E-03	1.22E-01	-3.57E+00
6	1.1	0.7	-7.47E-05	1.37E-02	2.25E+00	-2.82E-03	6.66E-02	-2.47E+00
7	1.9	3.1	9.17E-05	5.20E-02	1.50E+00	-2.99E-03	7.03E-02	-3.00E+00
8	-9.0	6.4	-1.94E-03	1.65E-01	-3.58E-01	-3.93E-03	1.87E-01	-4.77E+00
9	-4.7	0.1	3.50E-03	-1.36E-01	-3.05E+00	1.14E-03	-3.48E-03	1.14E+00
10	2.5	0.2	1.08E-03	-4.03E-02	2.87E+00	4.81E-04	-4.12E-02	-1.89E+00
11	4.2	-0.9	6.64E-05	-1.80E-02	3.29E+00	1.27E-03	-8.69E-02	-1.16E+00
12	-6.5	2.1	-6.09E-04	6.82E-02	-5.64E+00	-1.04E-03	1.12E-01	7.34E-01
13	-6.9	2.4	3.49E-05	3.97E-02	1.15E+00	7.20E-04	2.24E-02	-6.12E+00
14	-2.3	1.7	-8.15E-04	7.20E-02	1.31E+00	1.61E-03	-6.47E-02	-3.69E+00
15	-3.8	1.1	5.48E-05	1.62E-02	1.98E+00	2.98E-04	1.33E-02	-5.68E+00
16	-2.5	0.2	-1.81E-04	1.58E-02	3.16E+00	5.67E-04	-1.54E-02	-4.56E+00
17	-1.1	-0.8	-9.31E-04	4.88E-02	3.75E+00	8.71E-05	3.90E-03	-3.86E+00
18	2.9	4.2	1.98E-04	5.97E-02	2.96E+00	-1.04E-03	4.52E-02	-6.17E+00
19	1.2	3.3	-4.85E-04	9.09E-02	1.69E+00	-6.27E-04	3.31E-02	-5.67E+00
20	-0.9	2.9	-4.06E-04	7.79E-02	1.23E+00	-2.96E-04	2.81E-02	-5.44E+00
21	4.0	3.7	-4.15E-04	8.67E-02	4.22E+00	-4.84E-03	2.21E-01	-6.87E+00
22	1.3	3.1	-2.78E-04	6.81E-02	3.56E+00	-9.86E-04	4.01E-02	-5.87E+00
23	0.4	1.8	-1.23E-03	9.75E-02	3.13E+00	-3.50E-04	1.50E-02	-5.07E+00
24	11.6	5.7	2.34E-03	7.13E-03	2.74E+00	-1.55E-03	-4.27E-02	-2.59E+00
25	8.3	4.4	1.67E-03	1.13E-02	2.46E+00	-3.08E-03	4.67E-02	-3.02E+00
26	3.5	3.8	-9.06E-04	1.01E-01	1.64E+00	-2.02E-03	4.72E-02	-3.58E+00

27	14.1	8.0	3.66E-03	3.69E-02	2.04E+00	-9.32E-03	1.33E-01	-2.80E+00
28	10.6	5.1	3.73E-03	-1.27E-02	2.37E+00	-8.42E-03	1.32E-01	-2.67E+00
29	6.2	3.3	2.90E-03	-2.41E-02	2.36E+00	-1.75E-03	-5.29E-03	-2.33E+00
30	11.3	6.4	1.38E-02	-1.56E-01	2.90E+00	-1.67E-02	2.18E-01	-3.21E+00
31	12.7	4.3	1.17E-02	-1.63E-01	3.03E+00	-9.92E-03	8.69E-02	-2.53E+00
32	9.7	1.2	4.88E-03	-8.44E-02	2.96E+00	-4.48E-03	9.32E-03	-1.85E+00
33	5.4	0.5	8.14E-03	-1.63E-01	3.13E+00	-2.73E-03	9.14E-03	-2.01E+00
34	3.3	2.4	4.30E-03	-4.77E-02	2.38E+00	-3.12E-03	3.53E-02	-2.48E+00
35	11.1	-2.0	5.55E-03	-1.53E-01	3.74E+00	-1.09E-03	-7.55E-02	-1.10E+00

8.7.3 Slot-end method – Profile images.

Figure 8.21–Figure 8.55 show the data acquired from the 35 experimental runs undertaken. Each plot shows the left and right edge points from each of the 9 slots cut with the same process parameters. A parabola is fit to each edge. For each image, t = material thickness in millimetres, H = torch height in millimetres, f = feed rate in millimetres/min. A parabola is fit to each edge's edge points.

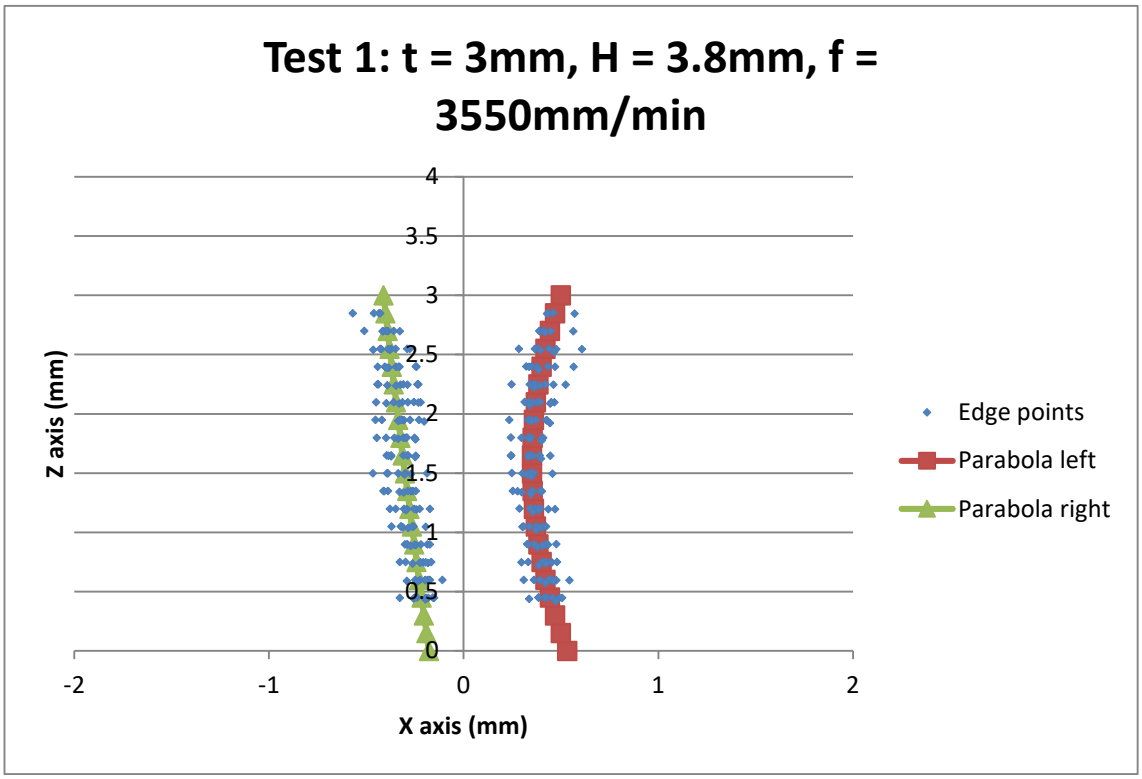

Figure 8.21: Edge points acquired from test piece 1 for kerf angle investigation slot-end method.

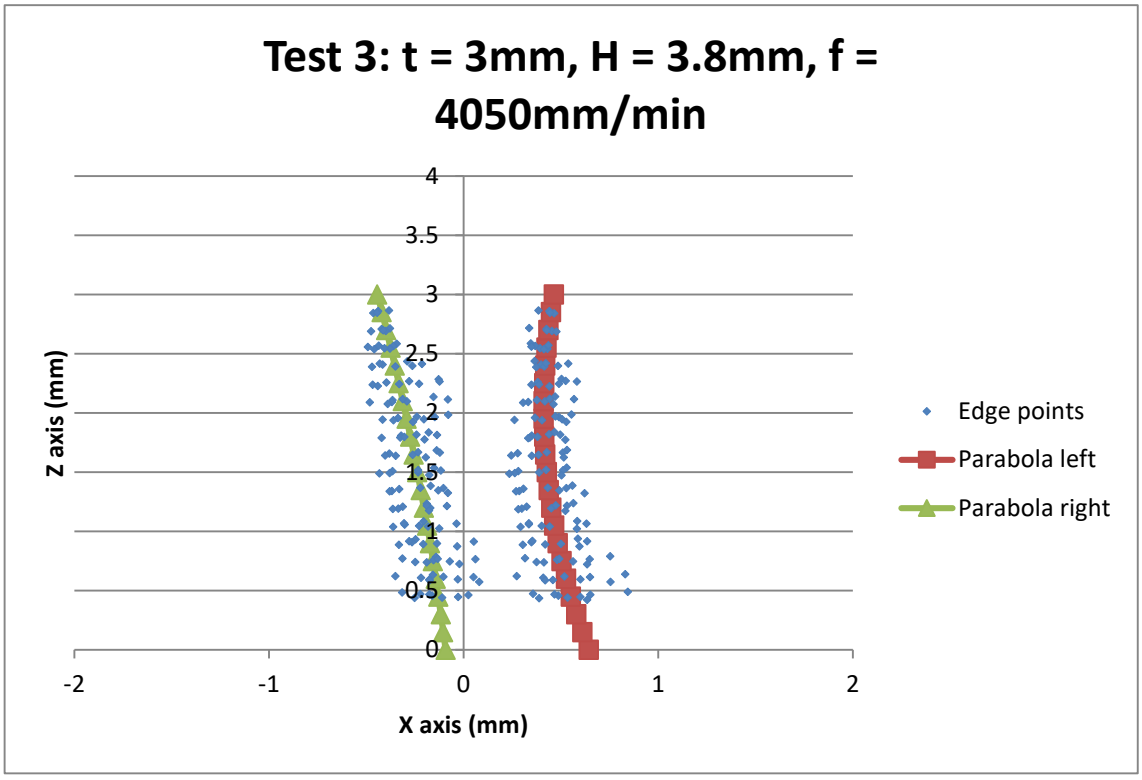

Figure 8.22: Edge points acquired from test piece 2 for kerf angle investigation slot-end method.

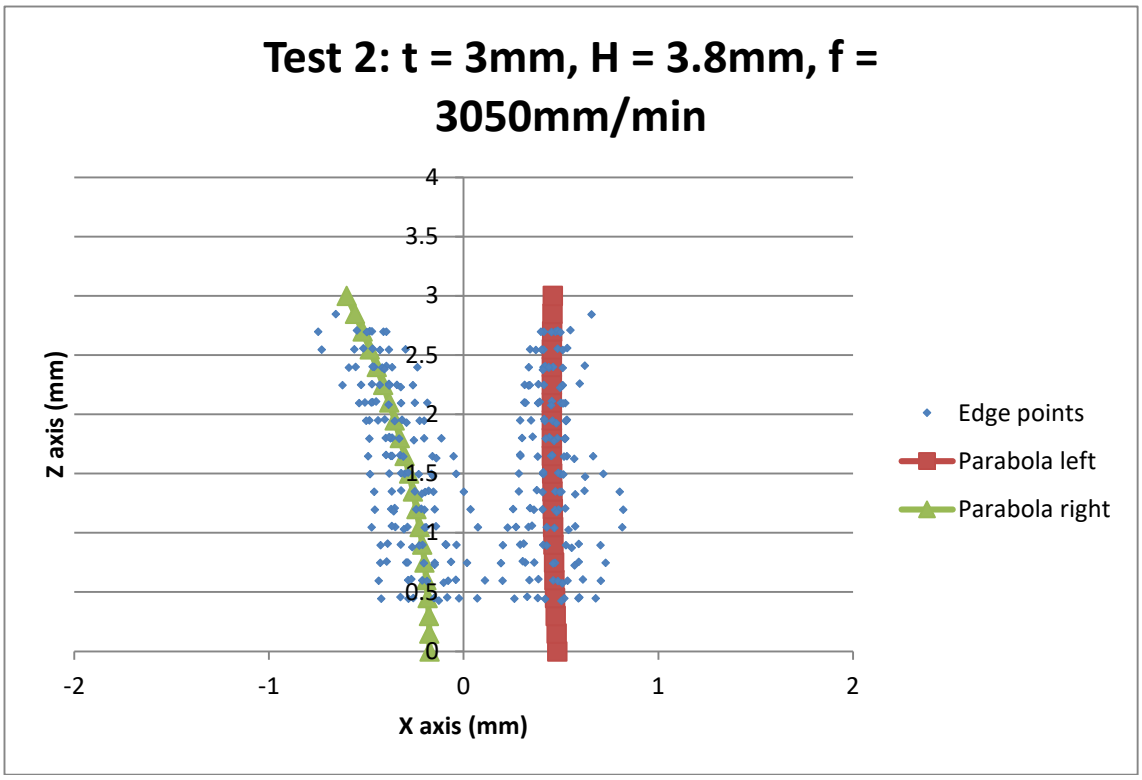

Figure 8.23 Plot of edge points acquired from test piece 3 for kerf angle investigation slot-end method.

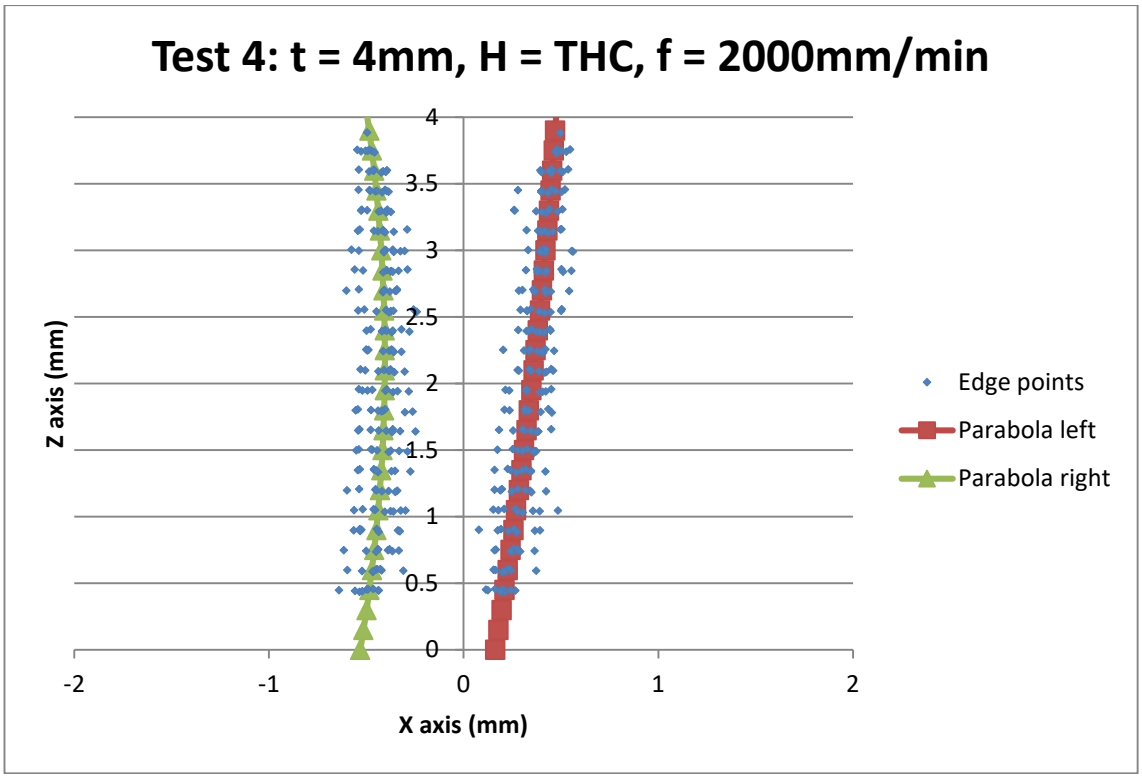

Figure 8.24: Edge points acquired from test piece 4 for kerf angle investigation slot-end method.

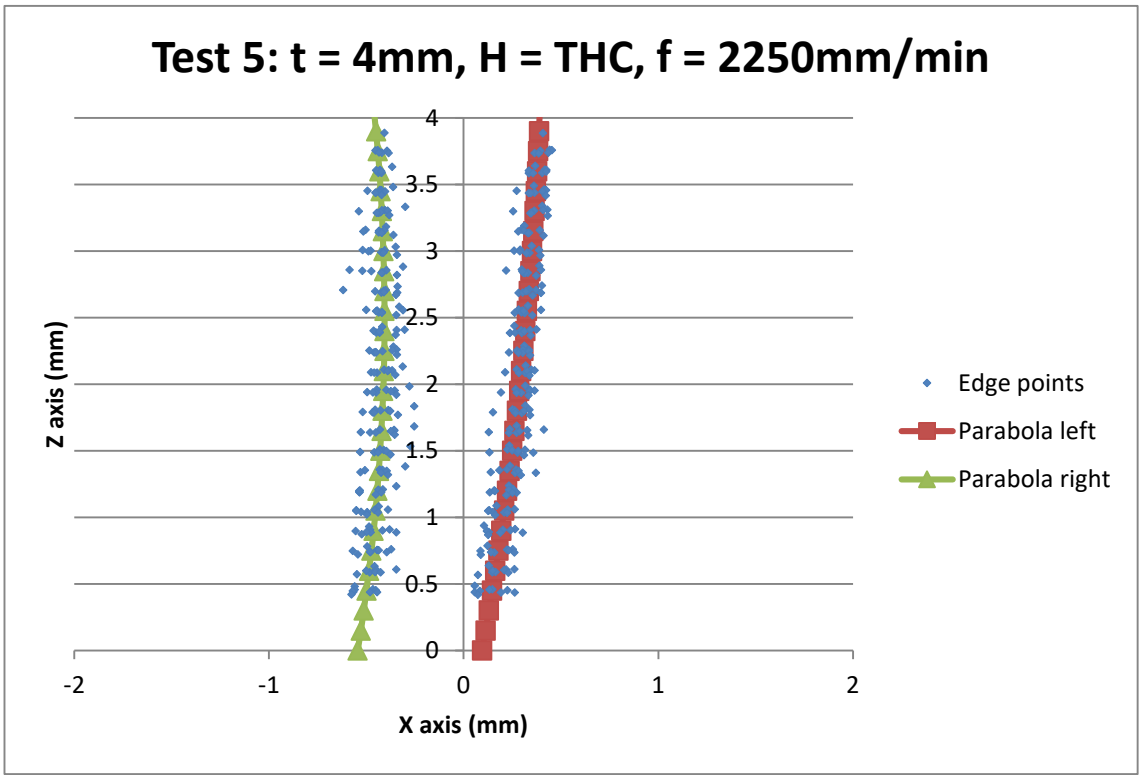

Figure 8.25: Edge points acquired from test piece 5 for kerf angle investigation slot-end method.

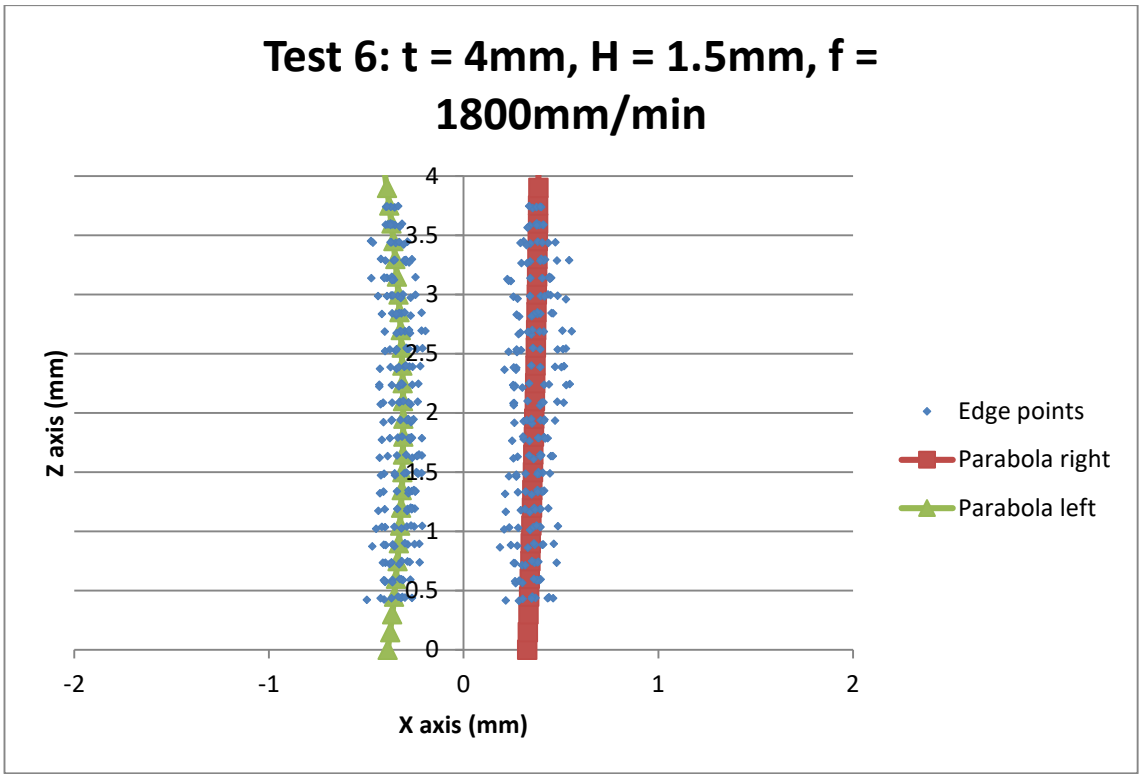

Figure 8.26: Edge points acquired from test piece 6 for kerf angle investigation slot-end method.

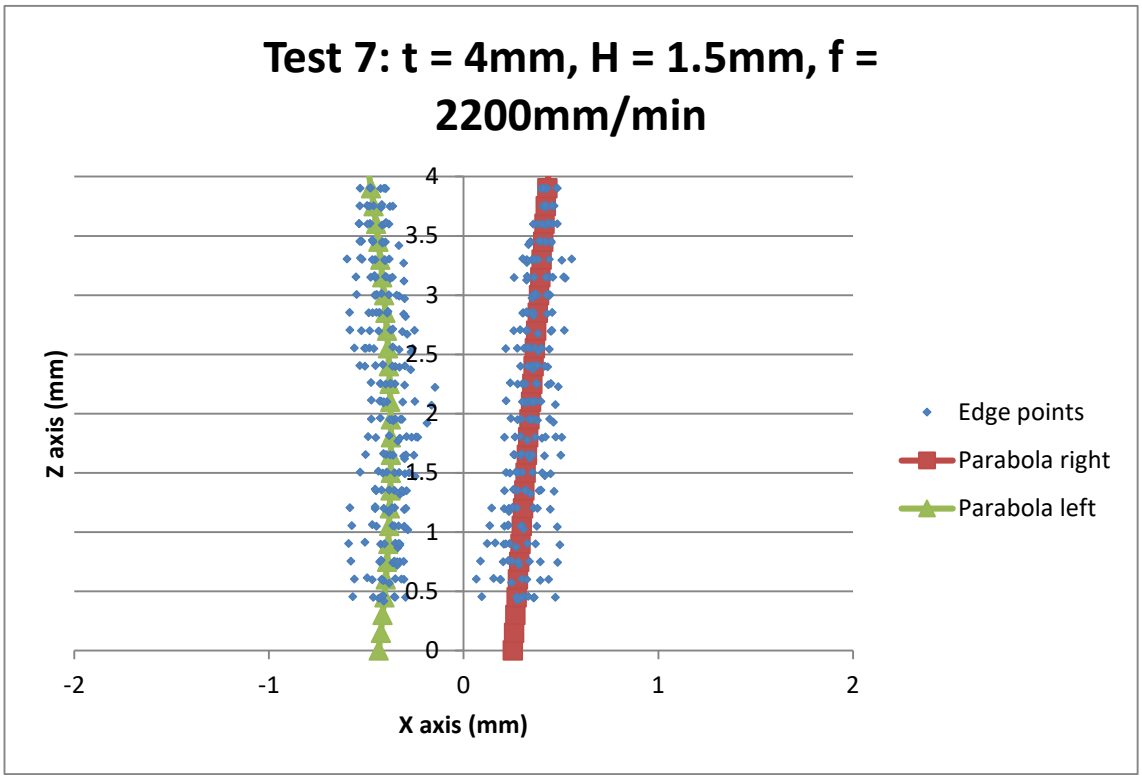

Figure 8.27: Edge points acquired from test piece 7 for kerf angle investigation slot-end method.

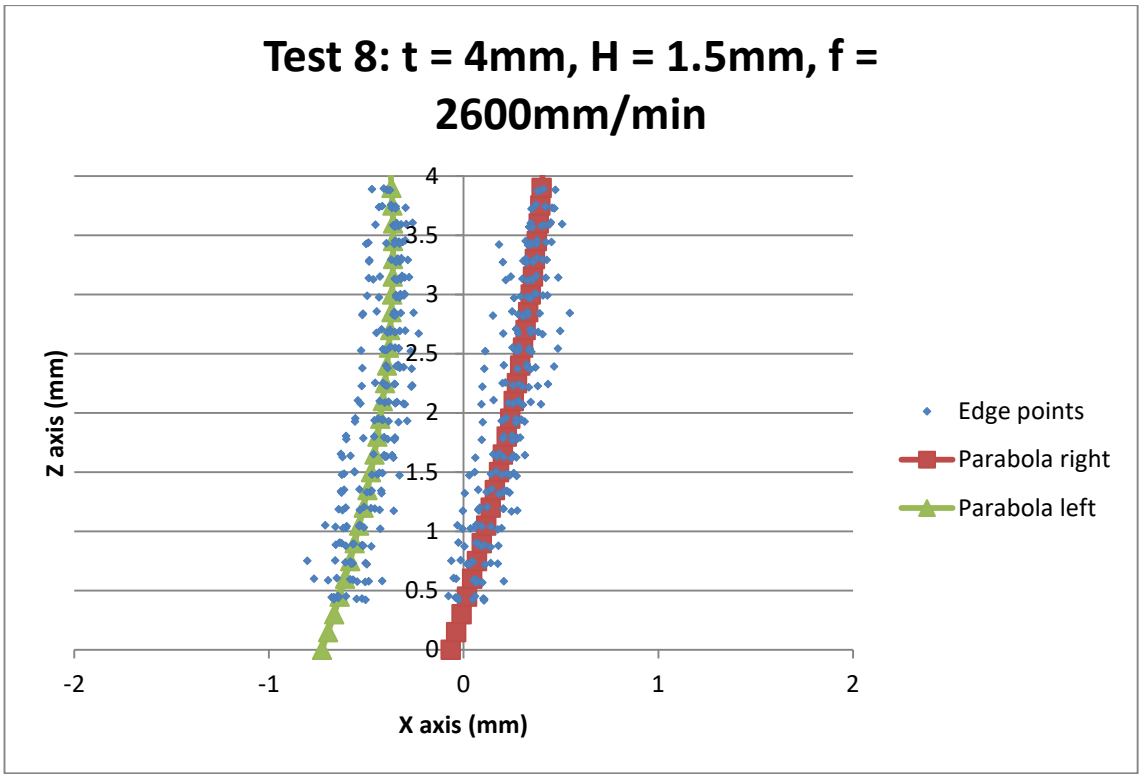

Figure 8.28: Edge points acquired from test piece 8 for kerf angle investigation slot-end method.

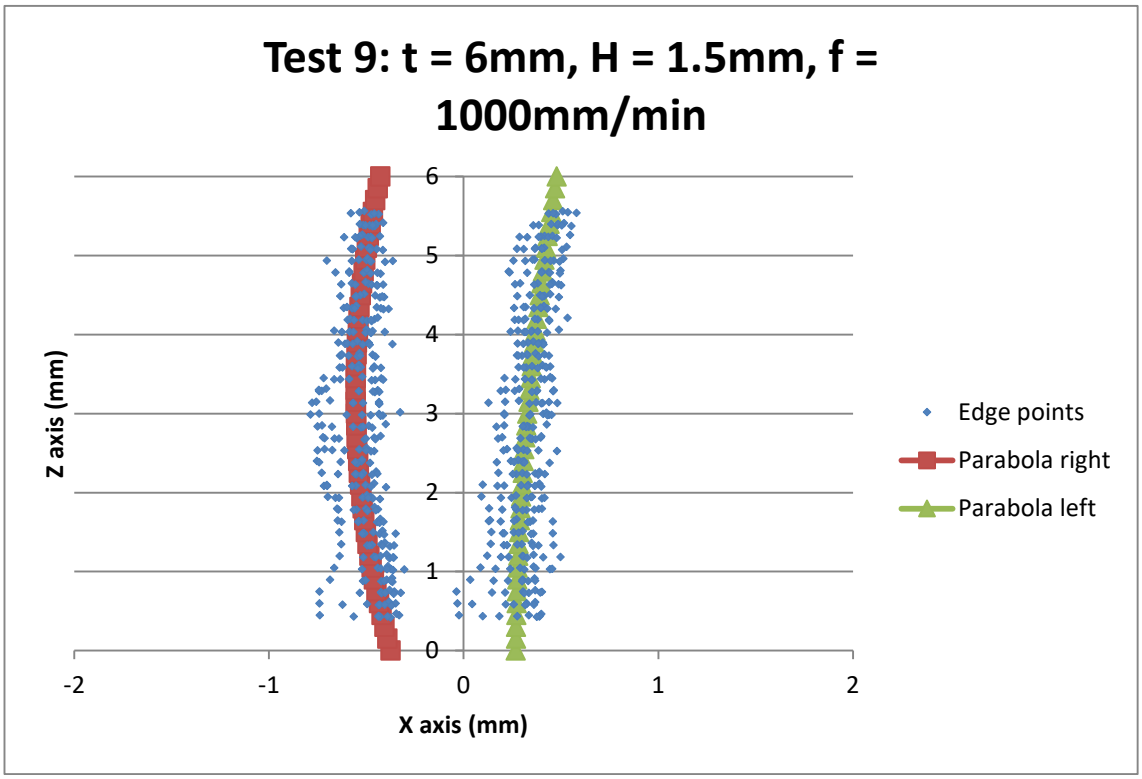

Figure 8.29: Edge points acquired from test piece 9 for kerf angle investigation slot-end method.

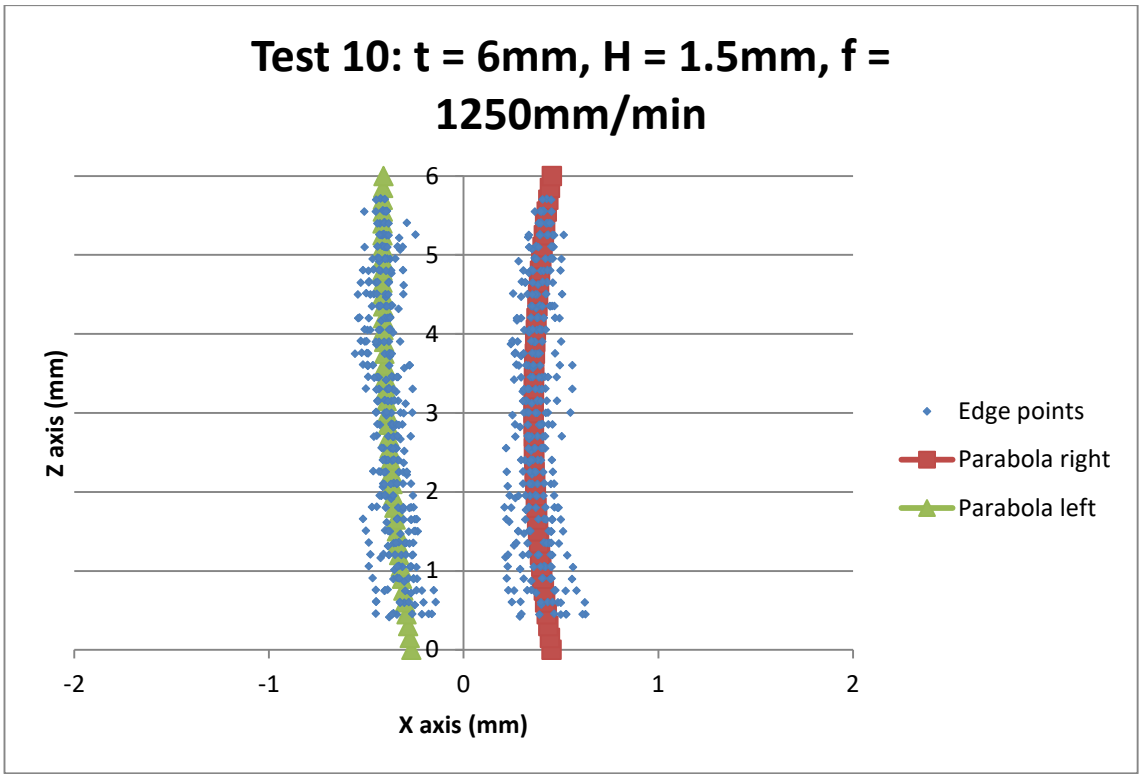

Figure 8.30: Edge points acquired from test piece 10 for kerf angle investigation slot-end method.

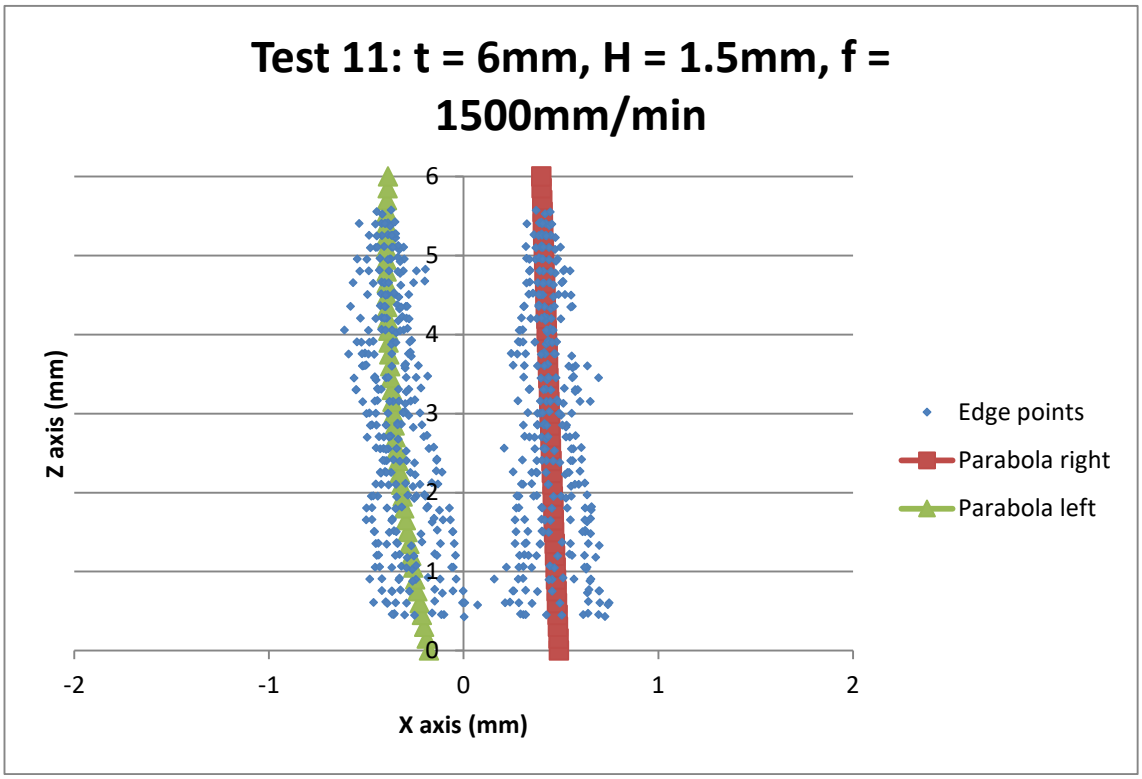

Figure 8.31: Edge points acquired from test piece 11 for kerf angle investigation slot-end method.

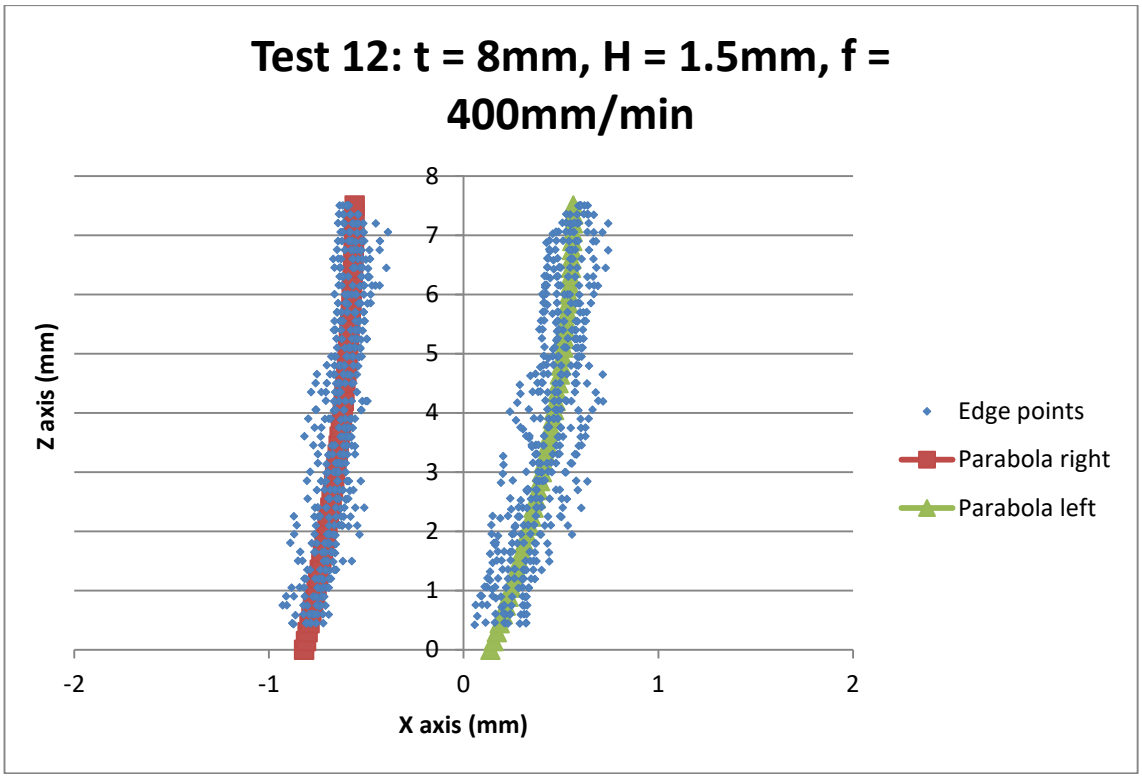

Figure 8.32: Edge points acquired from test piece 12 for kerf angle investigation slot-end method.

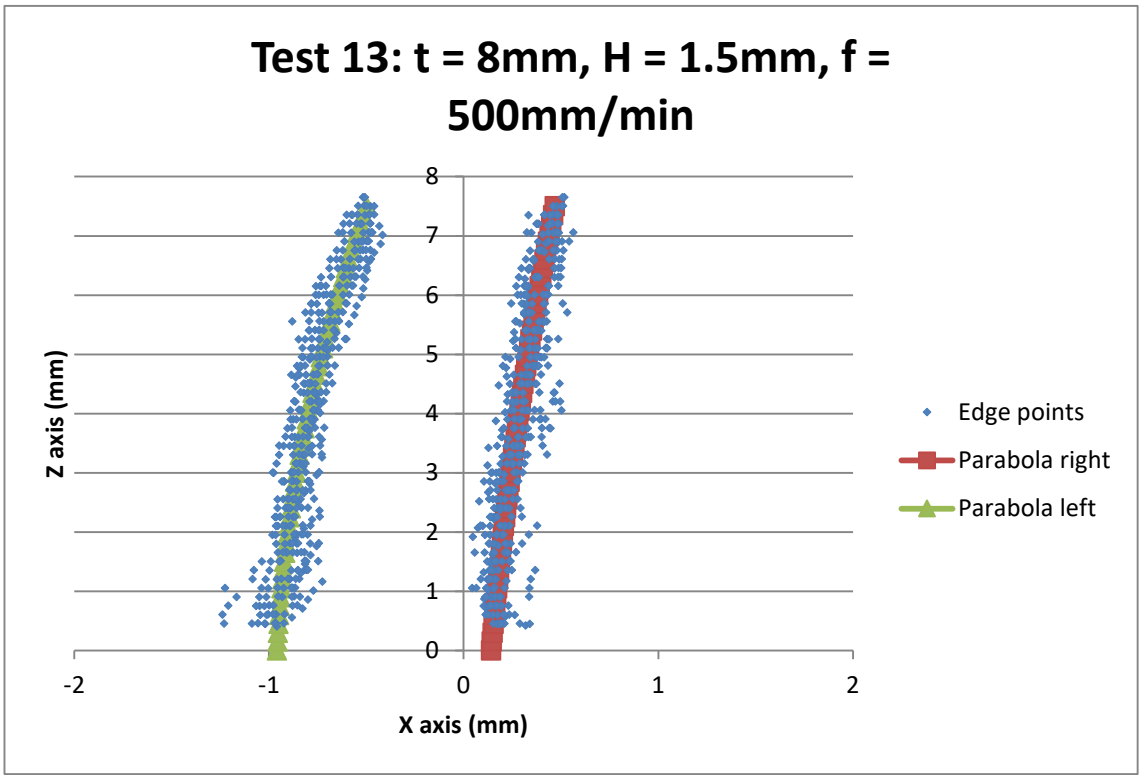

Figure 8.33: Edge points acquired from test piece 13 for kerf angle investigation slot-end method.

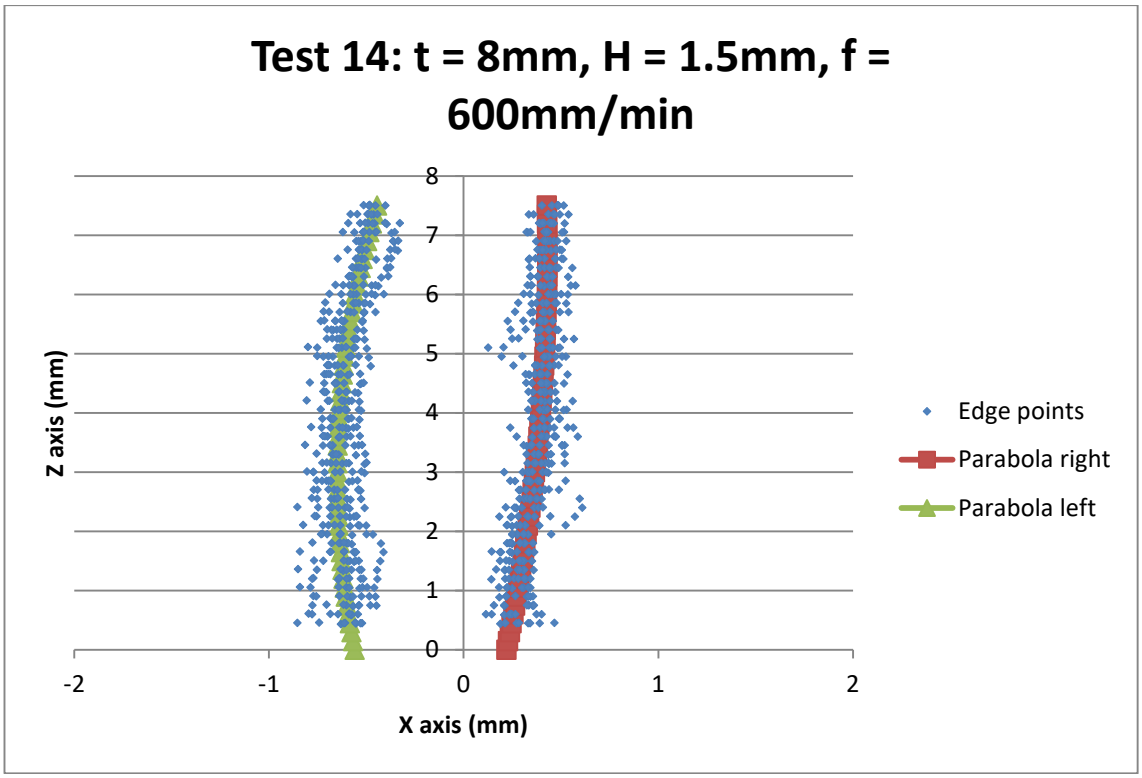

Figure 8.34: Edge points acquired from test piece 14 for kerf angle investigation slot-end method.

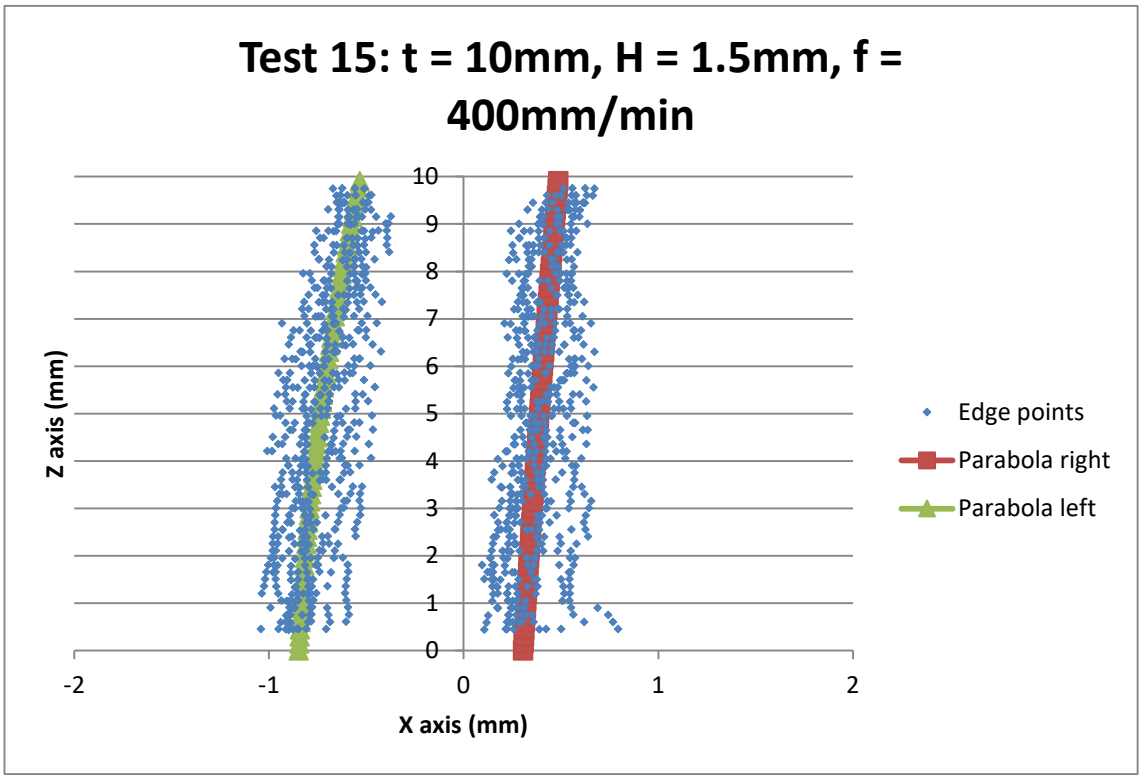

Figure 8.35: Edge points acquired from test piece 15 for kerf angle investigation slot-end method.

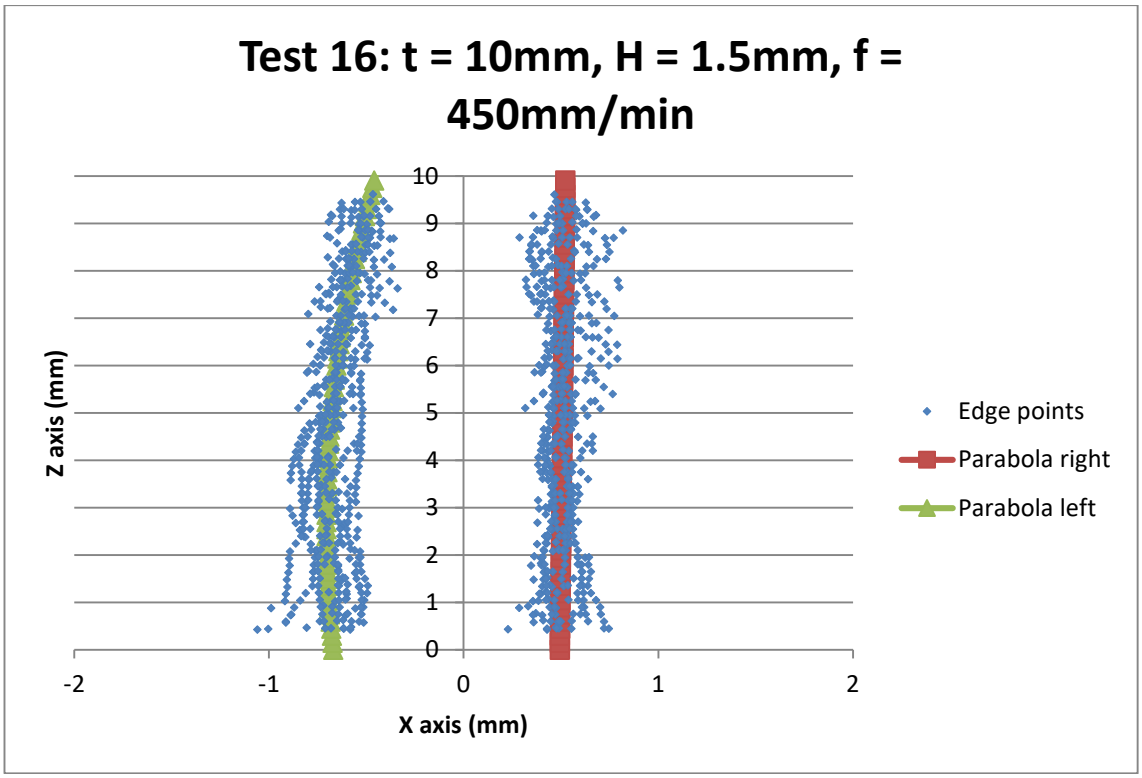

Figure 8.36: Edge points acquired from test piece 16 for kerf angle investigation slot-end method.

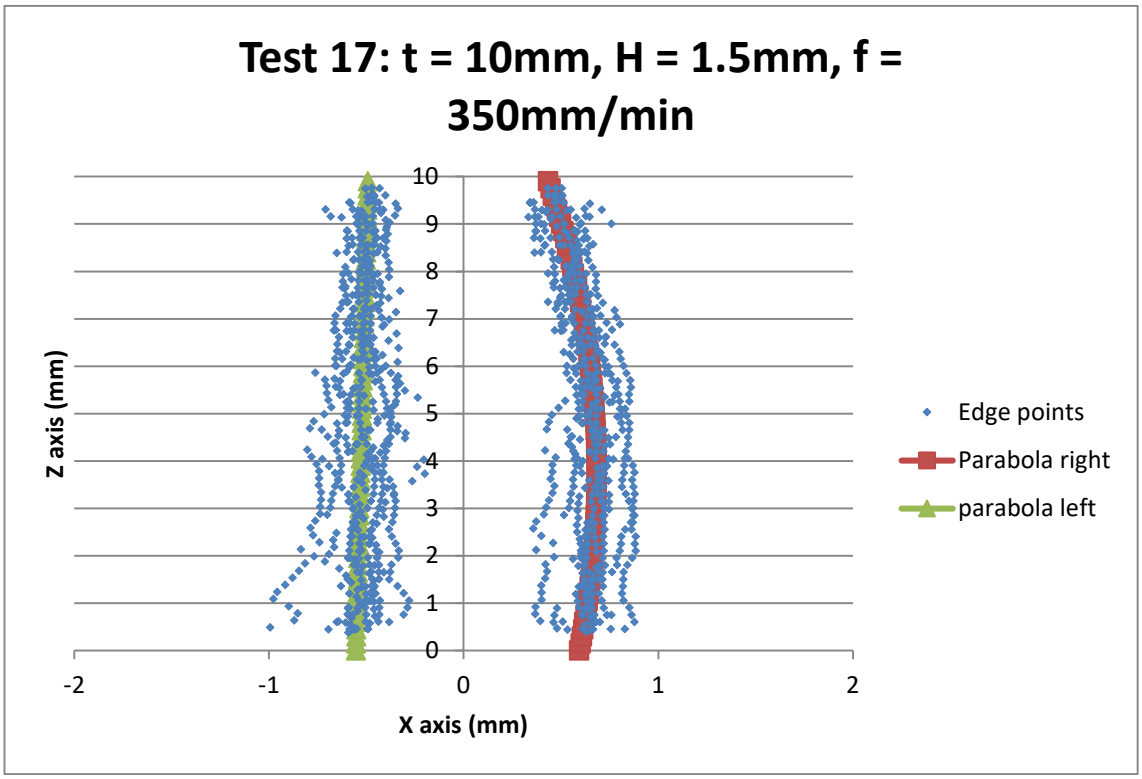

Figure 8.37: Edge points acquired from test piece 17 for kerf angle investigation slot-end method.

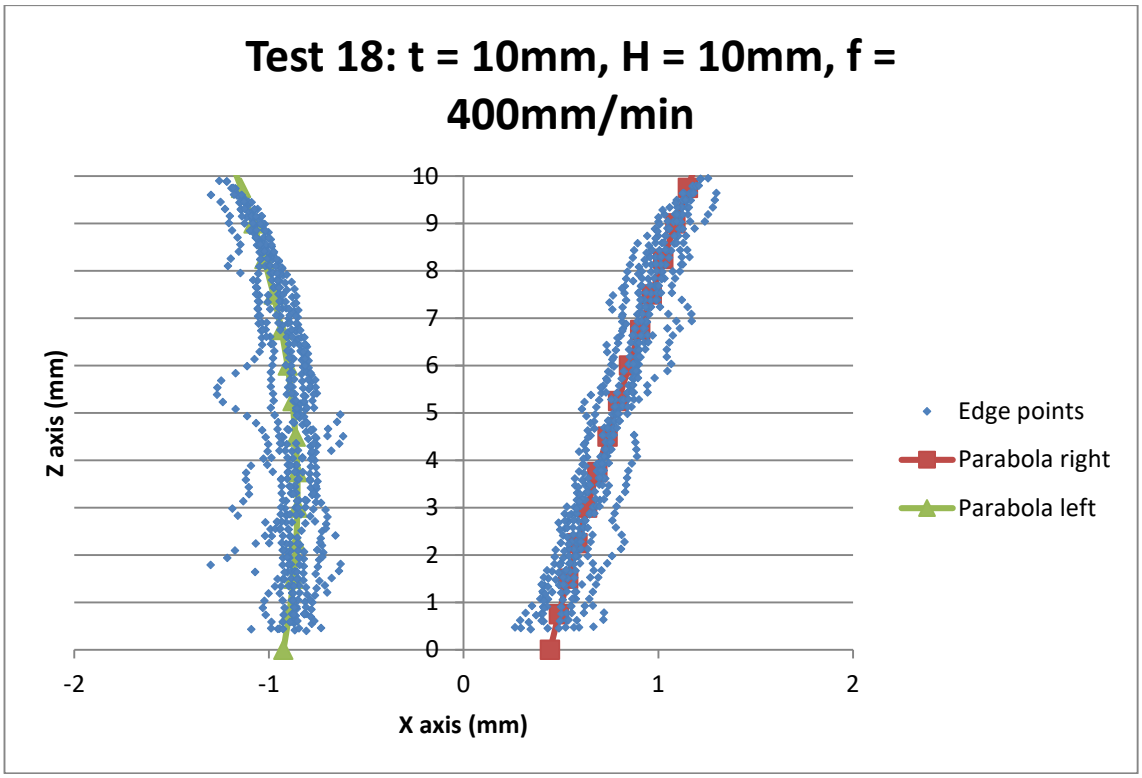

Figure 8.38: Edge points acquired from test piece 18 for kerf angle investigation slot-end method.

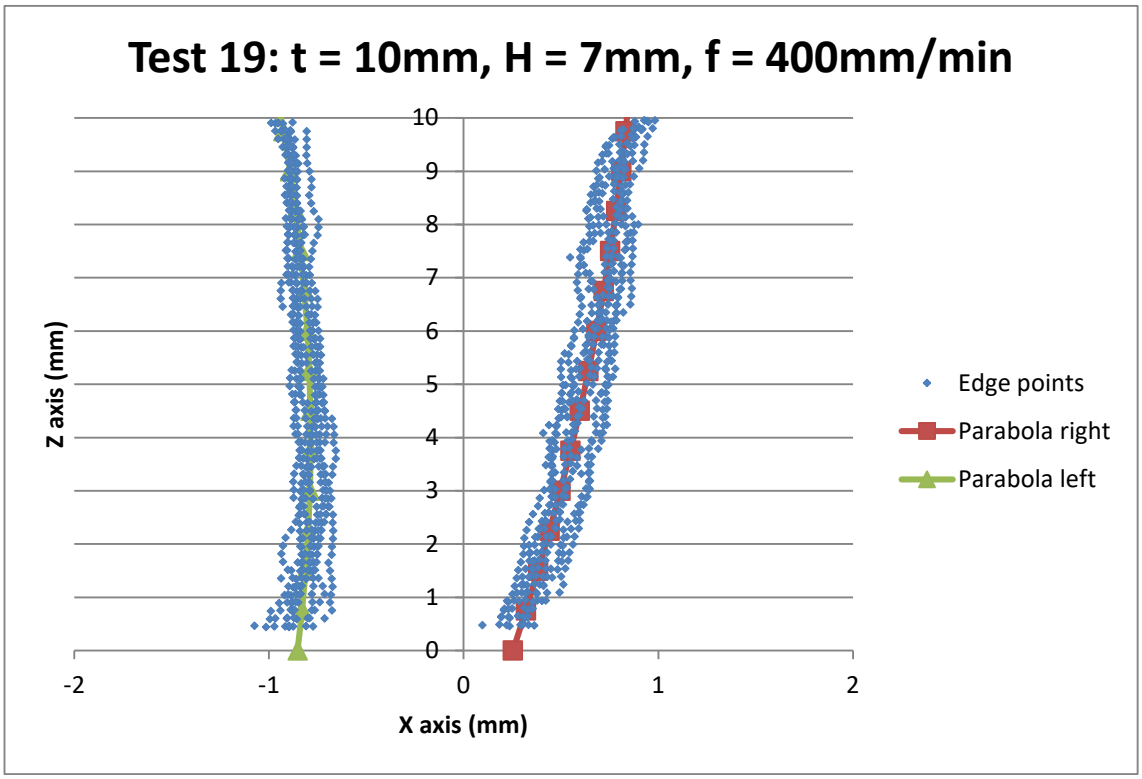

Figure 8.39: Edge points acquired from test piece 19 for kerf angle investigation slot-end method.

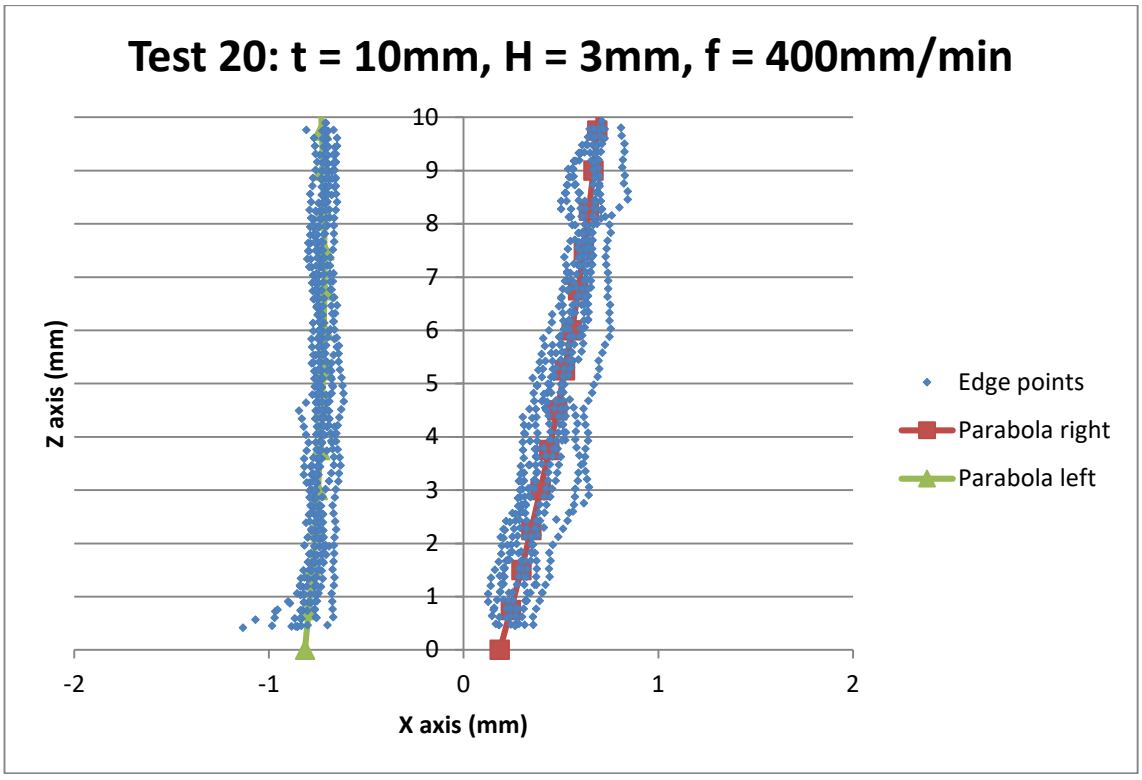

Figure 8.40: Edge points acquired from test piece 17 for kerf angle investigation slot-end method.

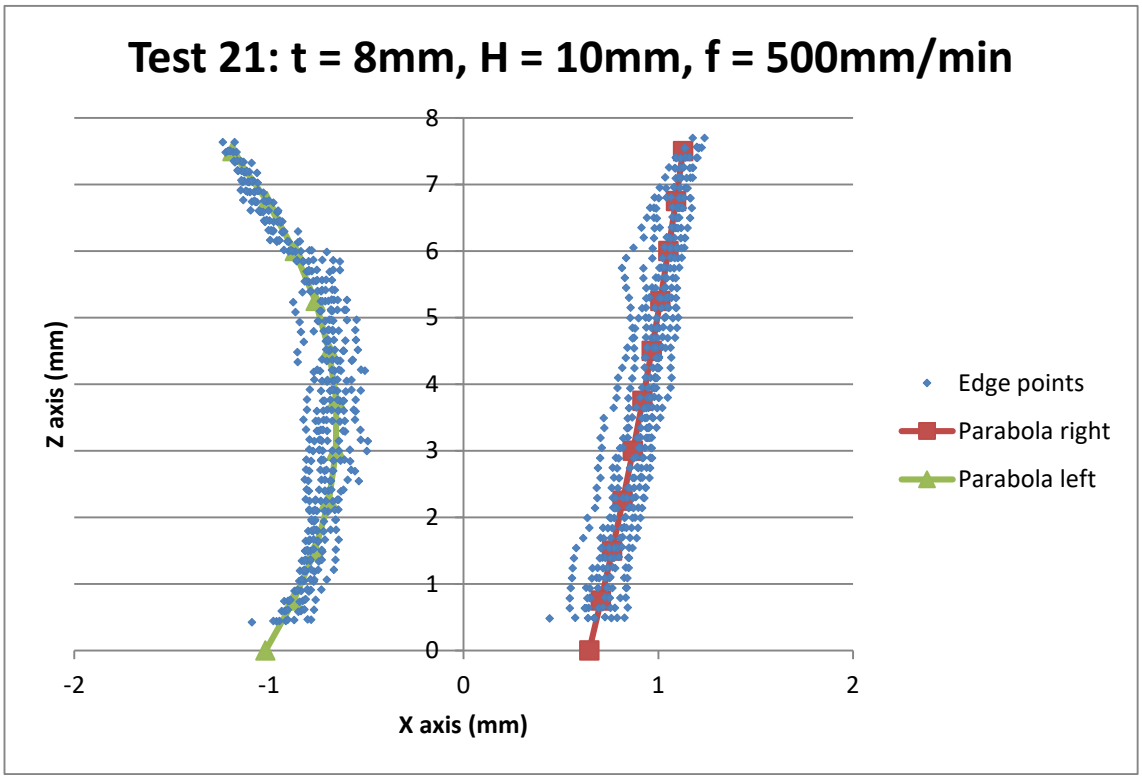

Figure 8.41: Edge points acquired from test piece 21 for kerf angle investigation slot-end method.

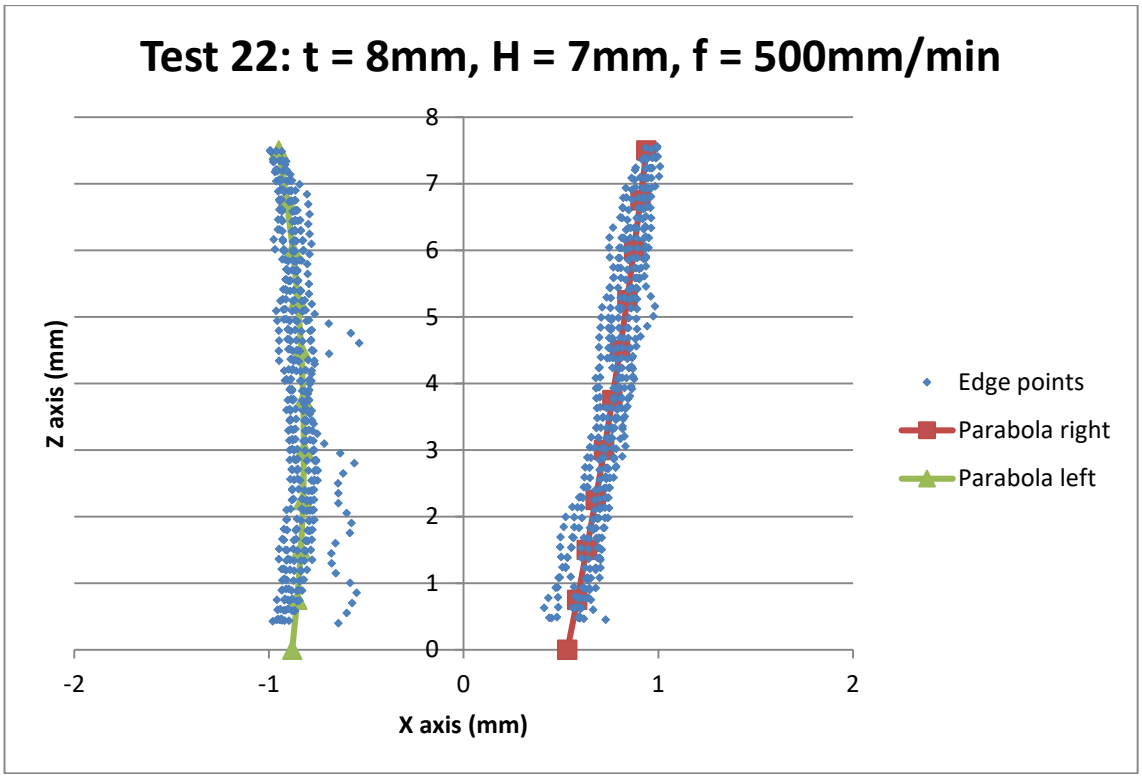

Figure 8.42: Edge points acquired from test piece 22 for kerf angle investigation slot-end method.

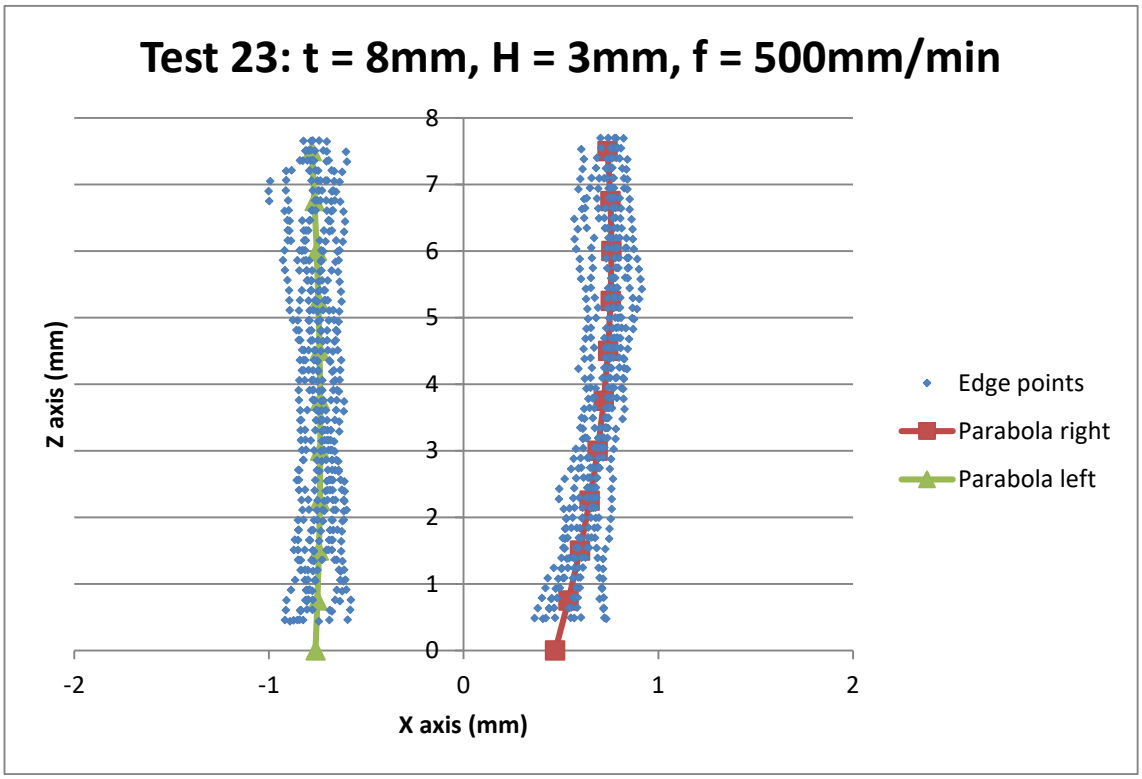

Figure 8.43: Edge points acquired from test piece 23 for kerf angle investigation slot-end method.

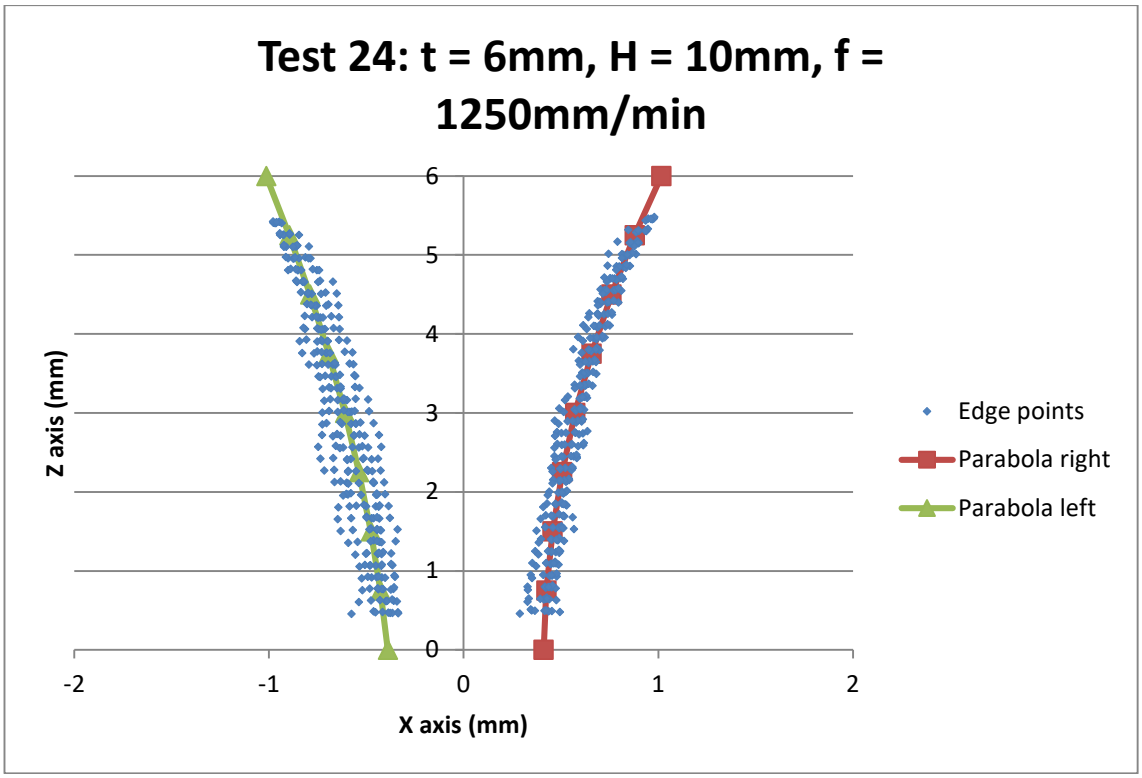

Figure 8.44: Edge points acquired from test piece 24 for kerf angle investigation slot-end method.

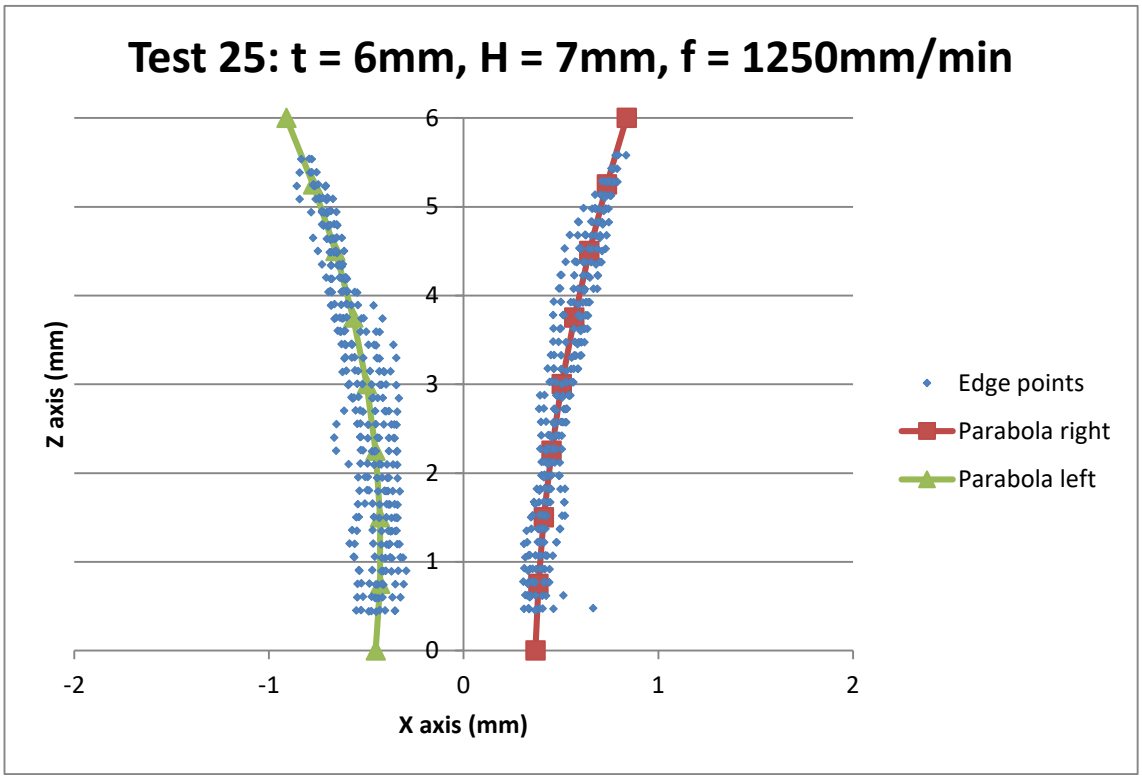

Figure 8.45: Edge points acquired from test piece 25 for kerf angle investigation slot-end method.

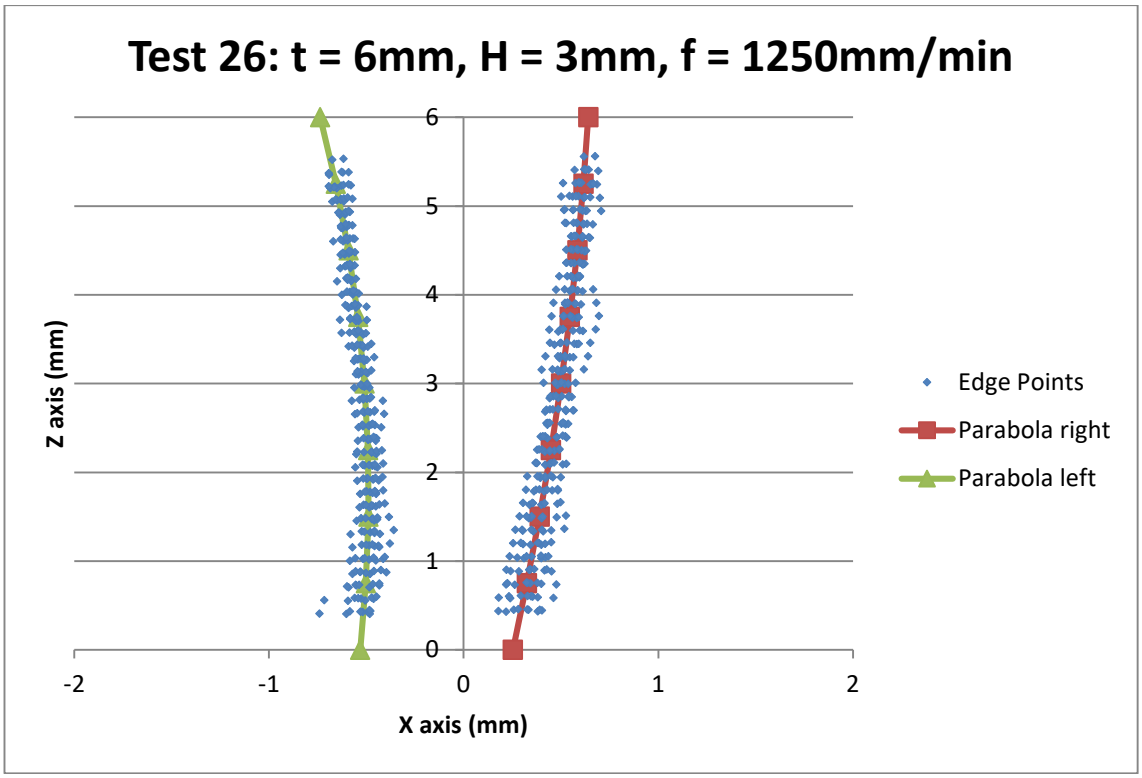

Figure 8.46: Edge points acquired from test piece 26 for kerf angle investigation slot-end method.

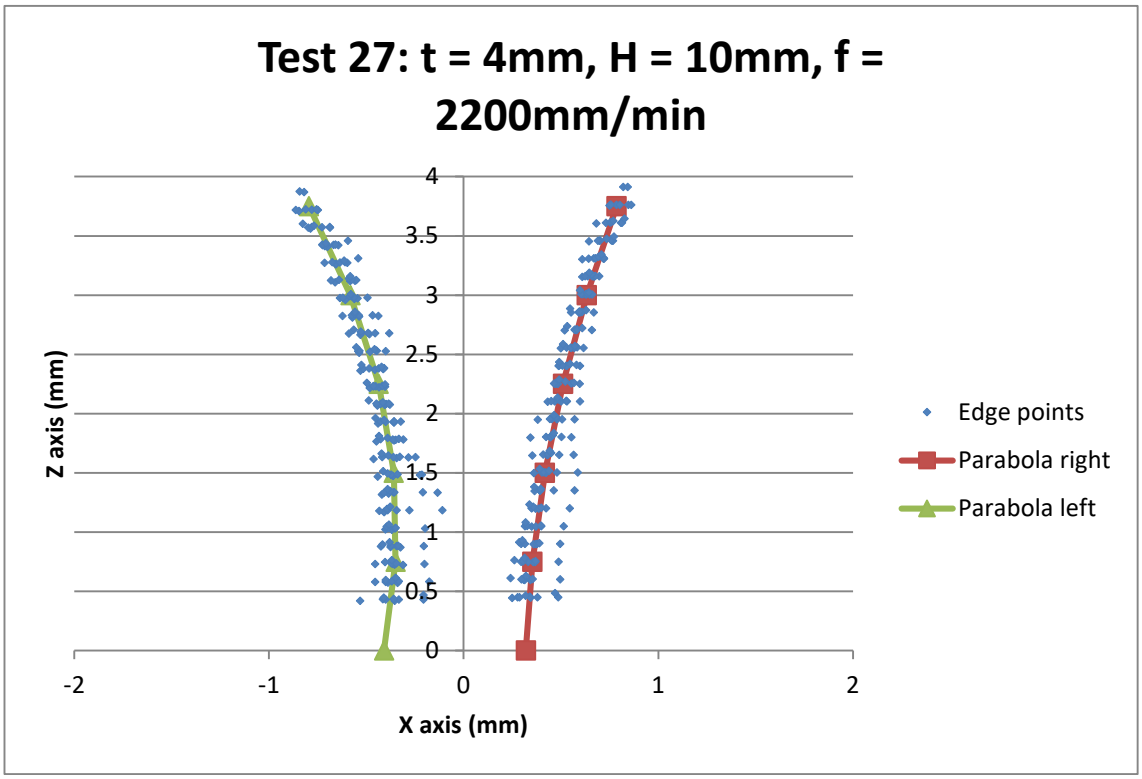

Figure 8.47: Edge points acquired from test piece 27 for kerf angle investigation slot-end method.

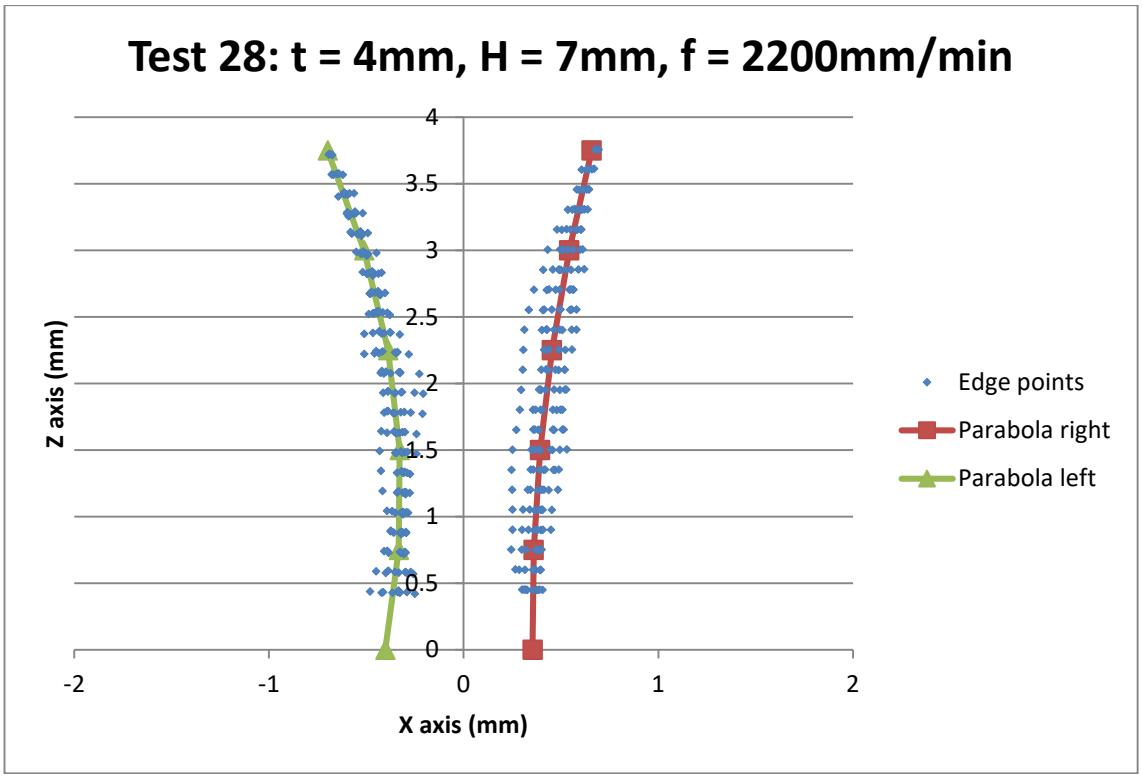

Figure 8.48: Edge points acquired from test piece 28 for kerf angle investigation slot-end method.

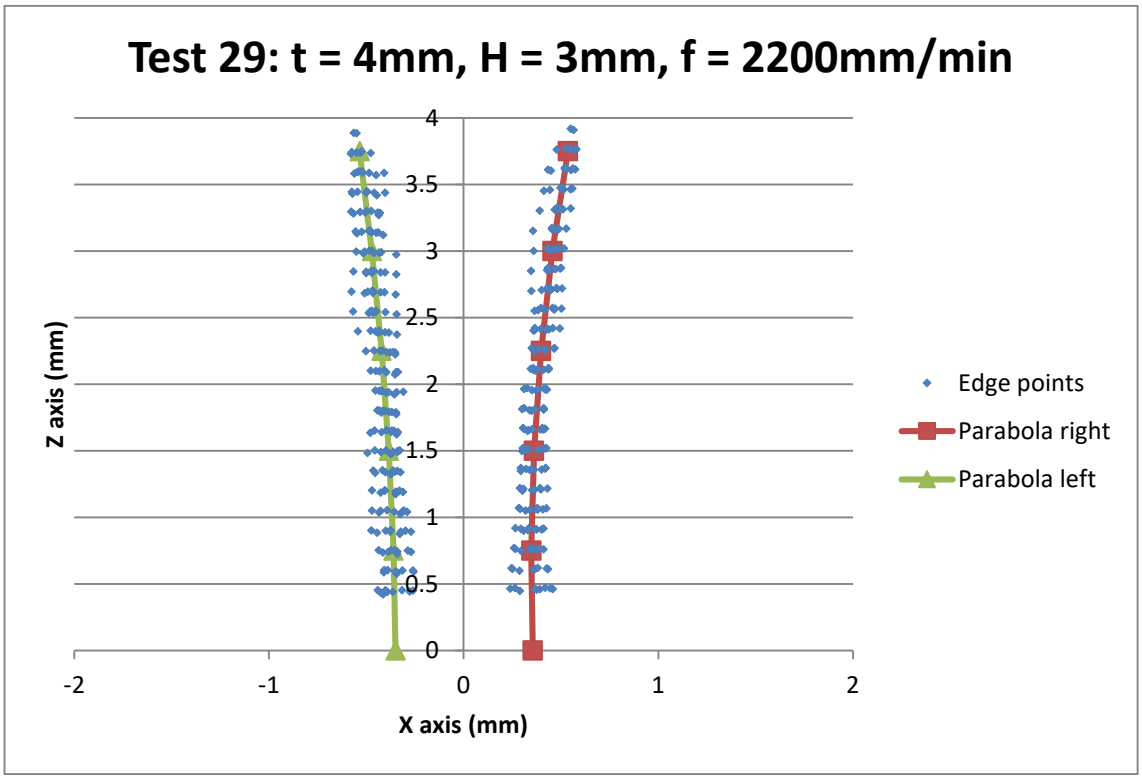

Figure 8.49: Edge points acquired from test piece 29 for kerf angle investigation slot-end method.

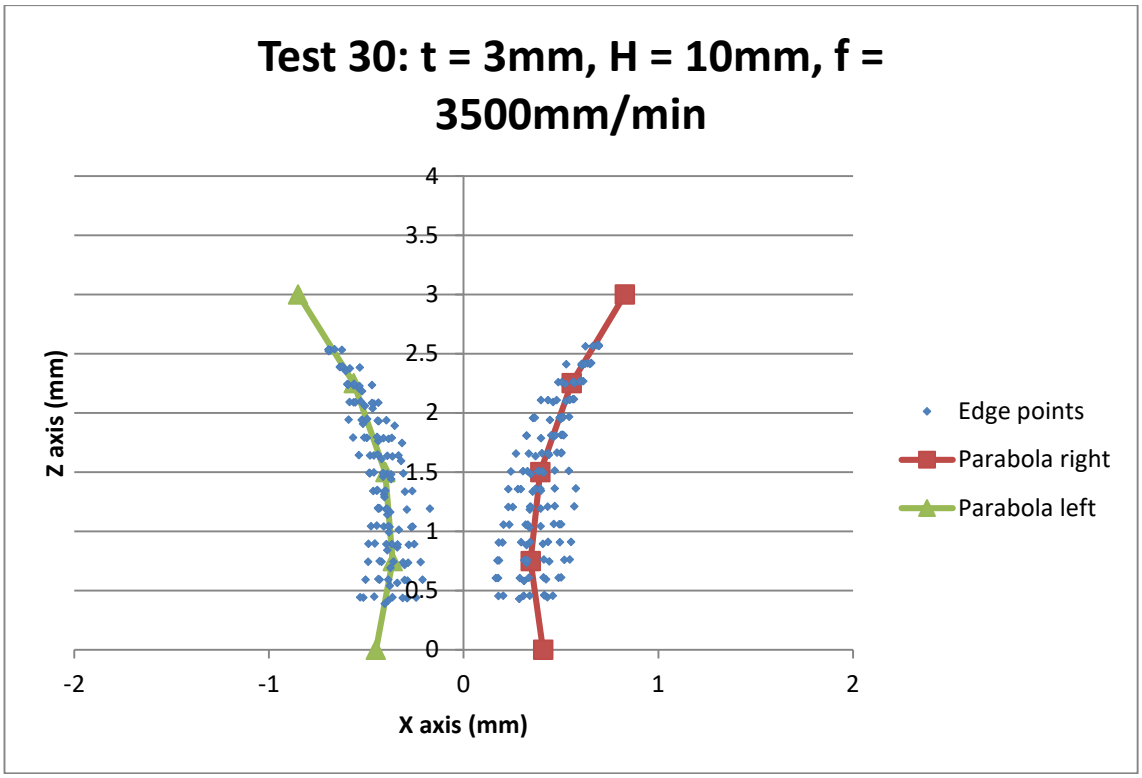

Figure 8.50: Edge points acquired from test piece 30 for kerf angle investigation slot-end method.

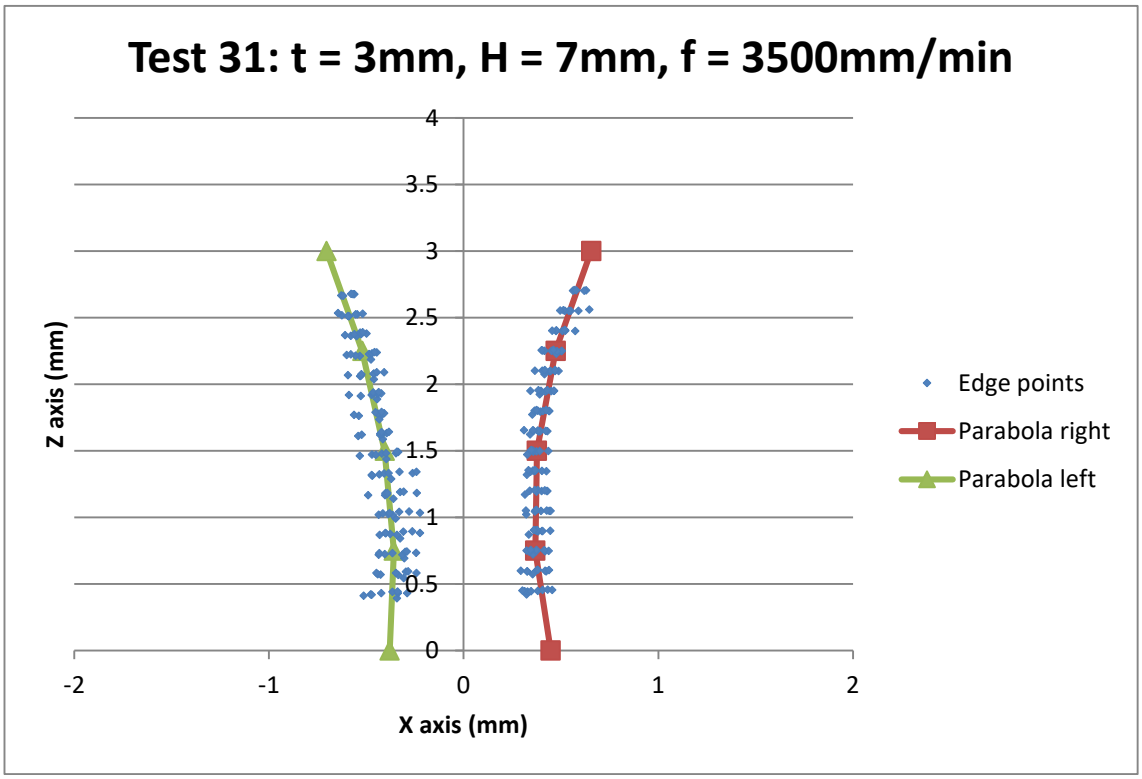

Figure 8.51: Edge points acquired from test piece 31 for kerf angle investigation slot-end method.

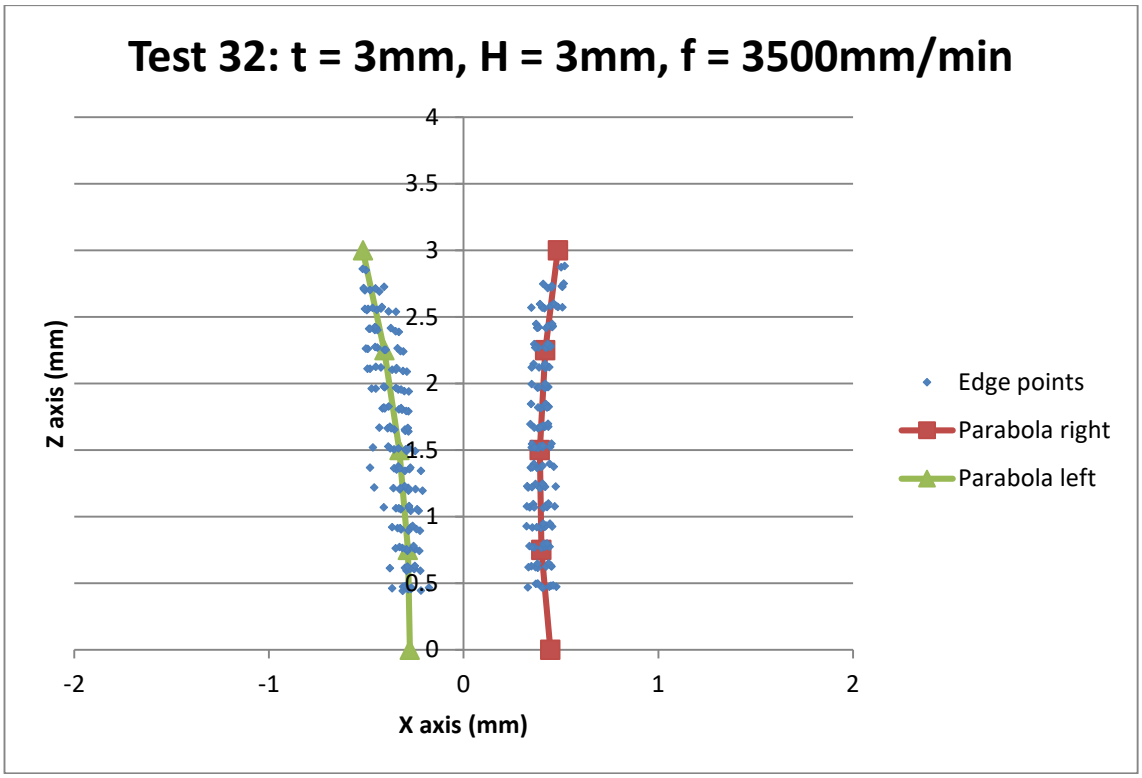

Figure 8.52: Edge points acquired from test piece 32 for kerf angle investigation slot-end method.

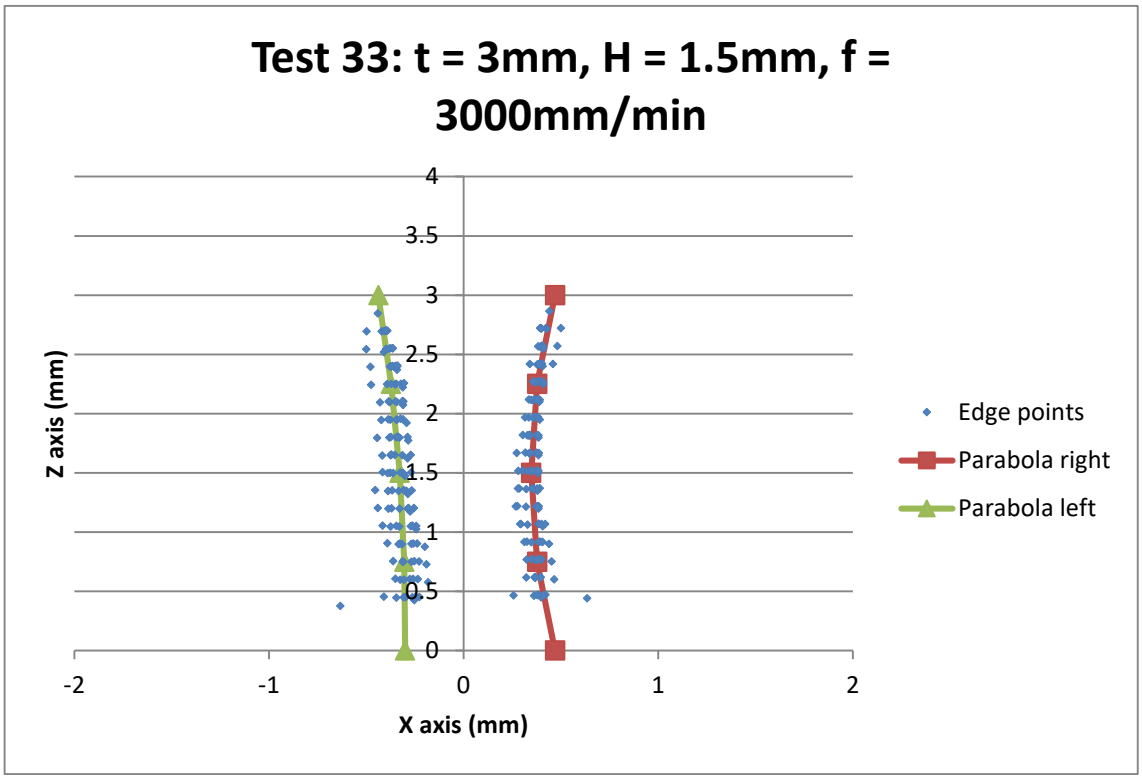

Figure 8.53: Edge points acquired from test piece 32 for kerf angle investigation slot-end method.

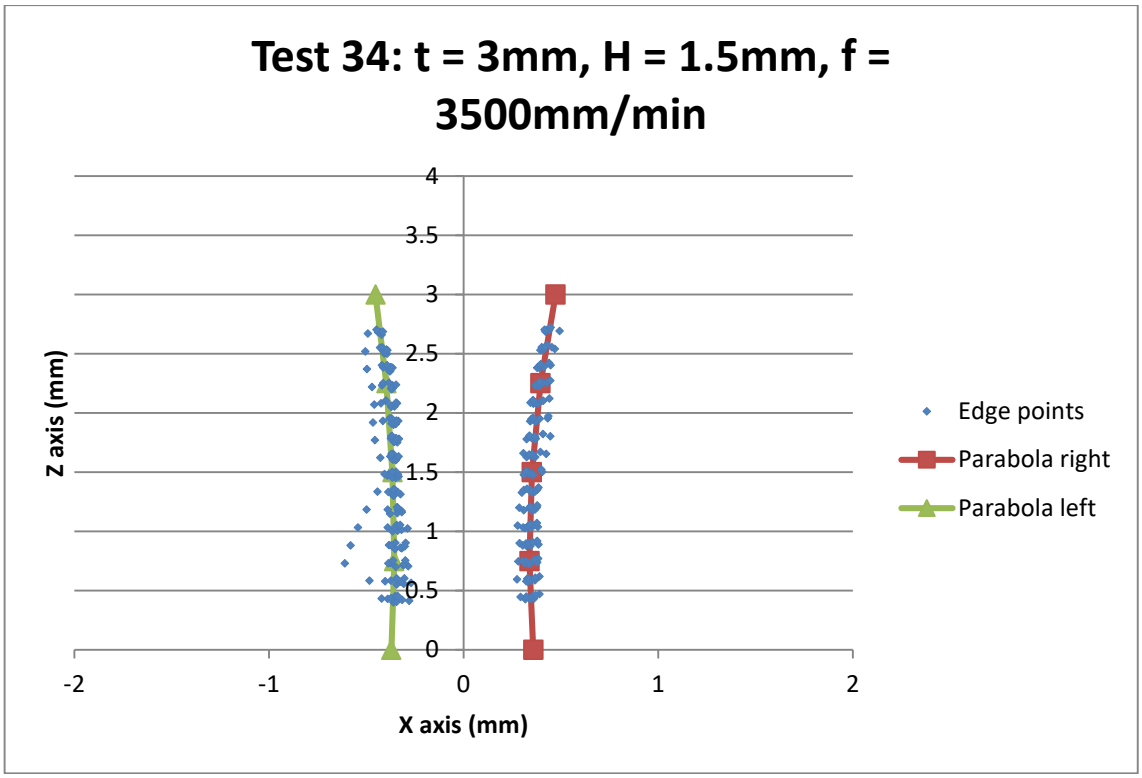

Figure 8.54: Edge points acquired from test piece 32 for kerf angle investigation slot-end method.

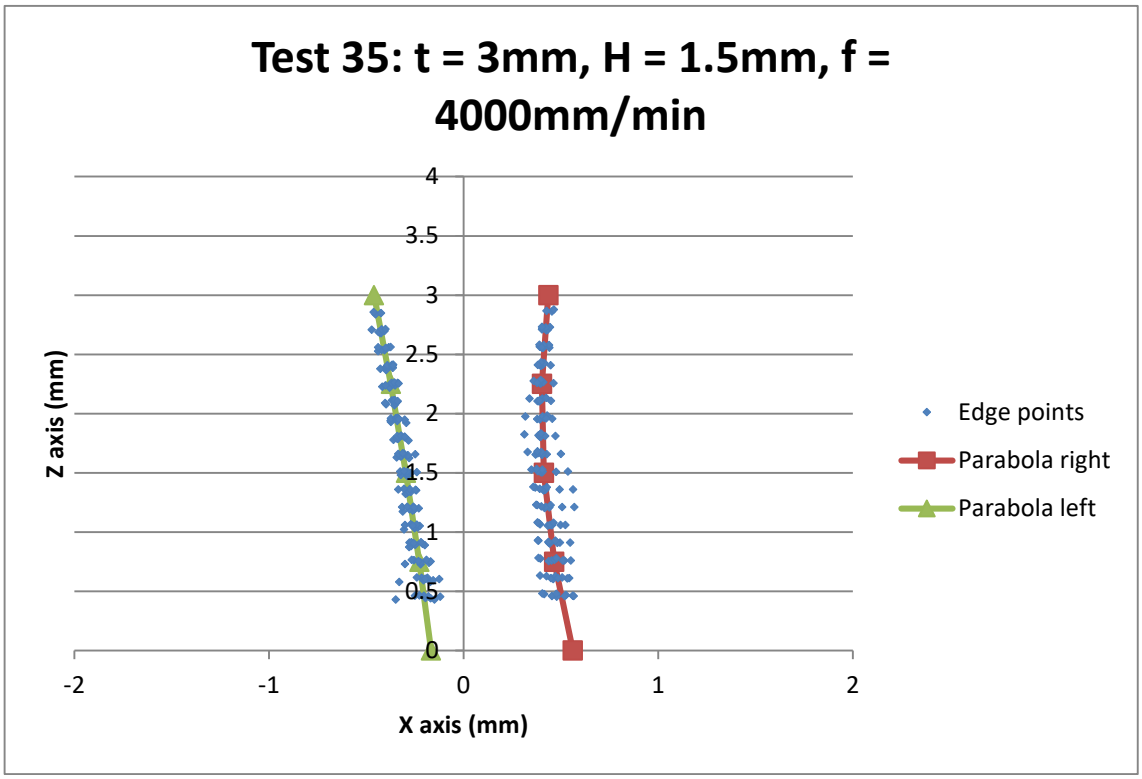

Figure 8.55: Edge points acquired from test piece 32 for kerf angle investigation slot-end method.

8.8 Appendix F: Radiation heat transfer experimental data

This appendix shows the temperature plots for the radiant heat transfer experiments. The methodology for the experiment is described in the main work in section 5.2. For convenience a quick summary of the experiment is given here, followed by the results.

8.8.1 Experimental plan

The goal of this experiment was to quantify the contribution of radiant heat transfer to total transfer to the work piece. In order to do this a system was devised that would limit the potential of conduction and convection to influence a work piece. An arc was established between a water cooled anode and the plasma torch. A work piece was position so that the arc passed through a slot in the work piece. This slot had sufficient widths so that the arc wouldn't short to the test piece.

The arc was maintained for 15s and the temperature of the work piece was measured using RTDs placed at radial distances of 10, 15, 20 and 25mm from the centre of the work piece. A micro controller measured the voltage drop across the RTDs every 0.1s and from this the temperature could be estimated. The accuracy of the temperature measurement was to about 0.3 degrees.

Figure 8.56 shows a plot of the average temperature of each of the 5 test runs. Figure 8.57 shows a plot of the change in average temperature for each of the 5 test runs. The average temperature is calculated as the mean of the 4 temperature measurements at any one time. Figure 8.58 - Figure 8.63 show that as time increases the range between the measurements get within a few degrees, so this is a reasonable approximation. In the first test run the test piece is held 1mm above the arc location and it clearly experiences the most heat transfer. Interestingly as the test piece is raised from 1mm above the anode to 5mm above the anode the amount of energy transferred via radiation is reduced. This is unexpected as the temperature of the jet decreases as it travels away from the nozzle. This could possibly be because the anode is hot and providing a significant amount of heat to the test piece.

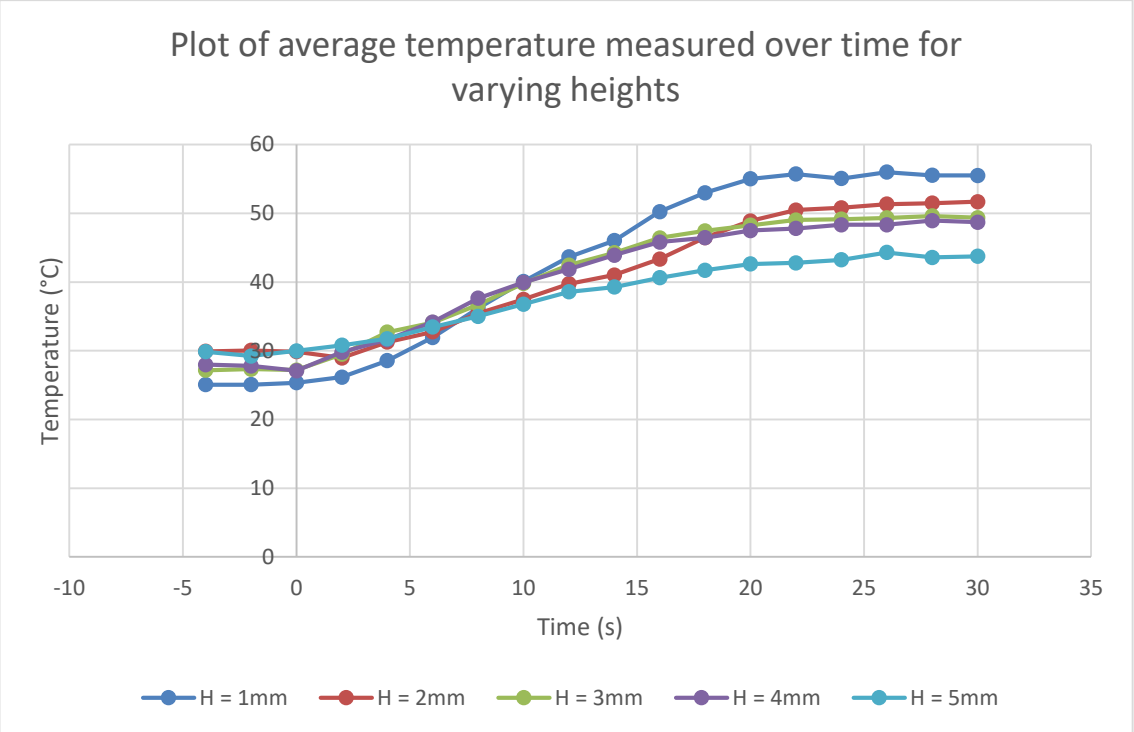

Figure 8.56: a plot of the average temperatures over time of the test piece at the 5 test heights.

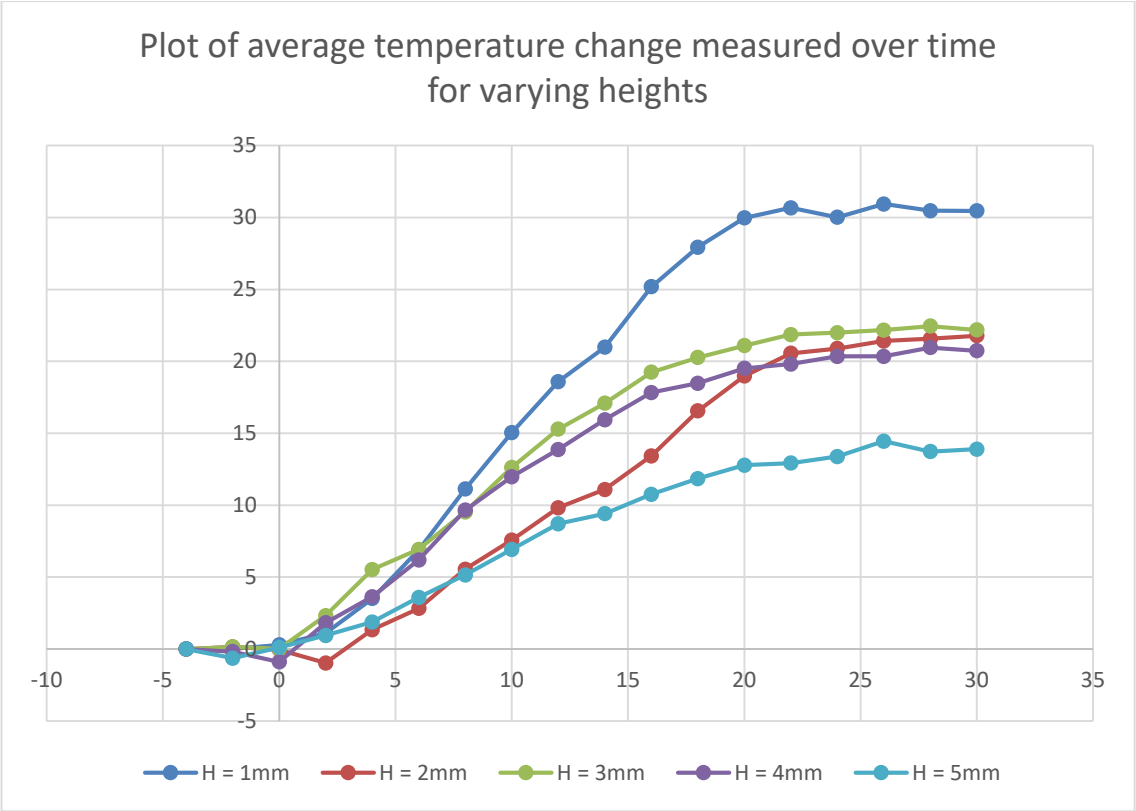

Figure 8.57: A plot of the average temperature change for each of the 5 test heights.

Figure 8.58 - Figure 8.63 show the temperature distribution at each of the 4 sensor positions across the test piece. Figure 3 corresponds to the placing the test piece at a height of 1mm above the anode, and figure 8 corresponds to the test piece being 5mm above the anode. Figure 8.59 shows a replicate of test 1 (Figure 8.58), without the addition of lamp black. The tests were conducted with the test piece being moved up in 1mm increments.

The temperature with the smallest distance from the centre (sensor 1) heats up the most rapidly, and the sensor with the largest radial distance (sensor 4) heats up the slowest. This is to be expected and the presence of this trend gives confidence to the validity of the data.

There is a lag between finishing applying heat with the arc at 15s, and the plate reaching its maximum temperature. This lag is approximately 5 seconds, and is most likely due to three factors. Firstly, it takes time for energy absorbed closer to the arc to be dissipated to the rest of the plate. Therefore the 4 sensors have different rates of temperature increase, and since there is still 5mm of distance between the plate edge and the first sensor 1 would expect that to be reflected. Secondly, it will take time for the hot air where the arc as to decrease back to the temperature of the plate, so there will still be some energy being added to the plate after the arc is extinguished. Finally, the experimental methodology leaves some uncertainty as to when the arc was actually started, so there is potentially a few seconds of leeway in the position of time = 0 in the graphs.

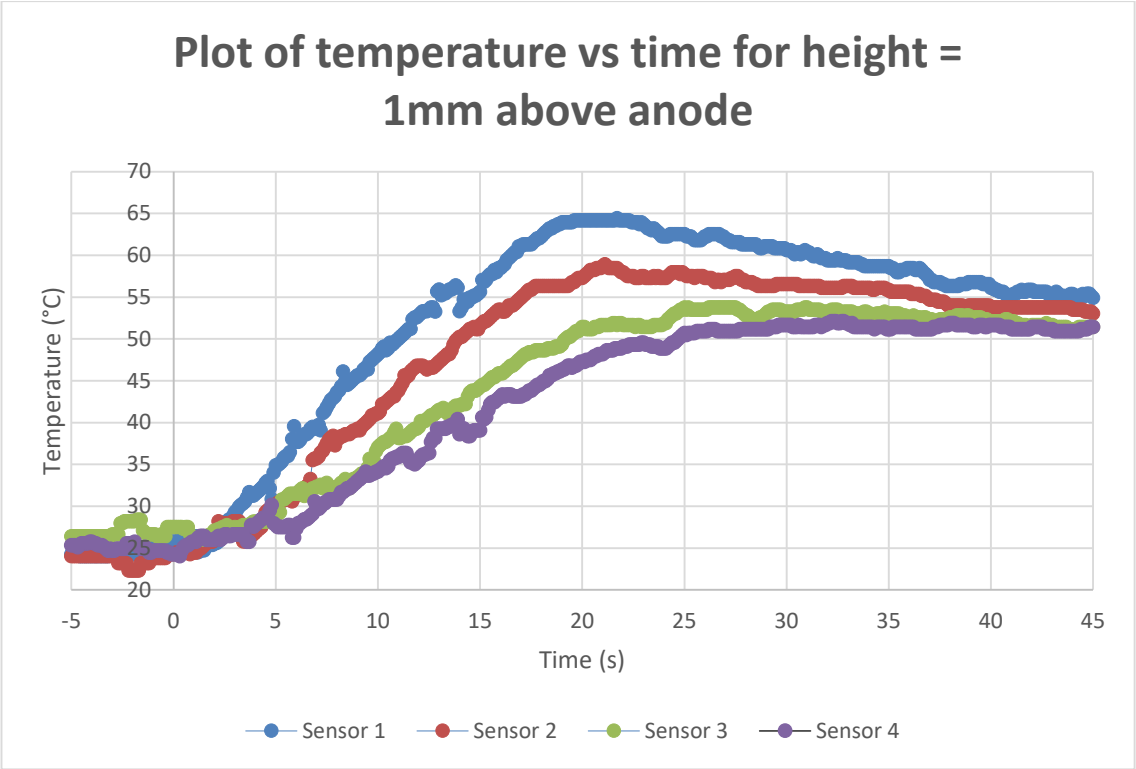

Figure 8.58: A plot of the temperature measured at each of 4 sensor positions over time during the radiant energy test with the test piece at a height of 1mm.

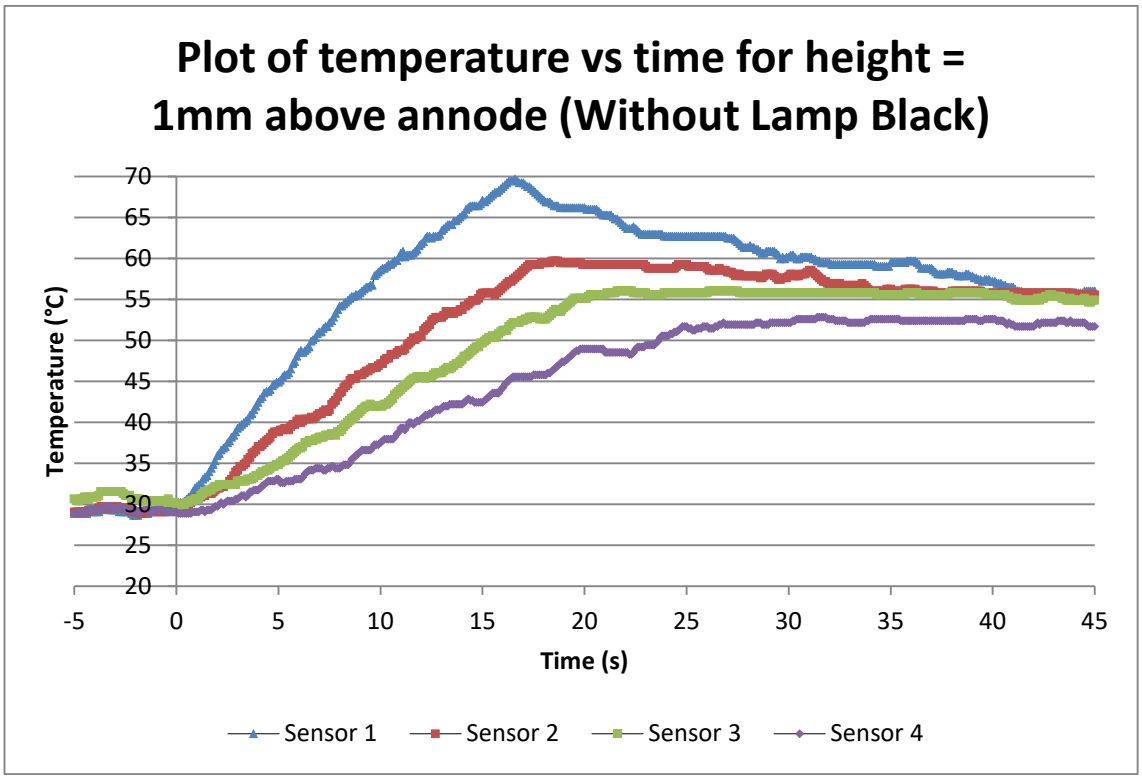

Figure 8.59: A plot of the temperature measured at each of 4 sensor positions over time during the radiant energy test with the test piece at a height of 1mm. The test piece had no lamp black applied to increase absorptivity.

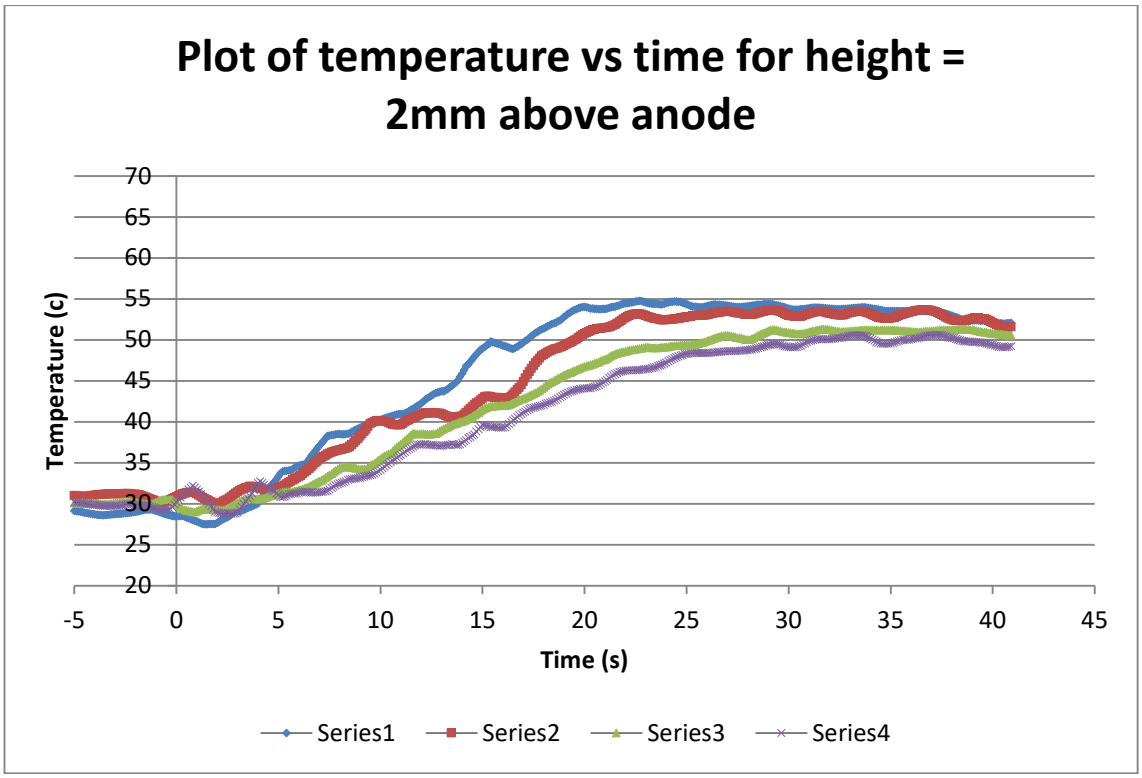

Figure 8.60: A plot of the temperature measured at each of 4 sensor positions over time during the radiant energy test with the test piece at a height of 2mm.

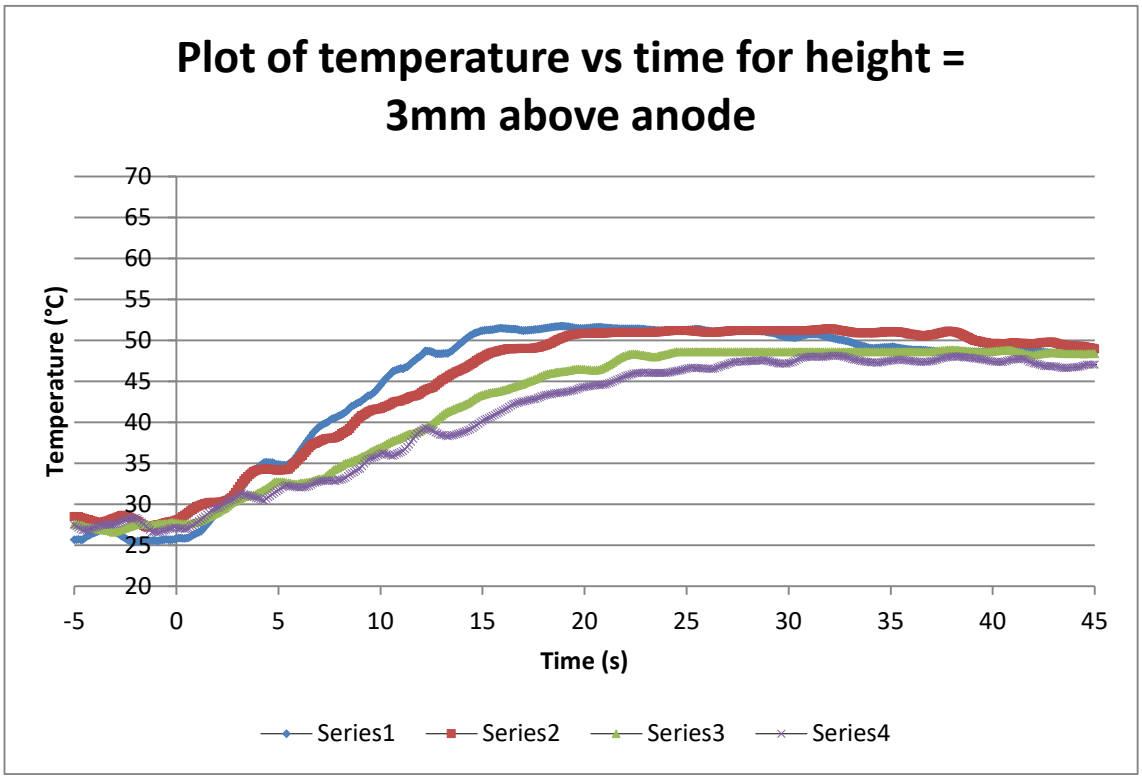

Figure 8.61: A plot of the temperature measured at each of 4 sensor positions over time during the radiant energy test with the test piece at a height of 3mm.

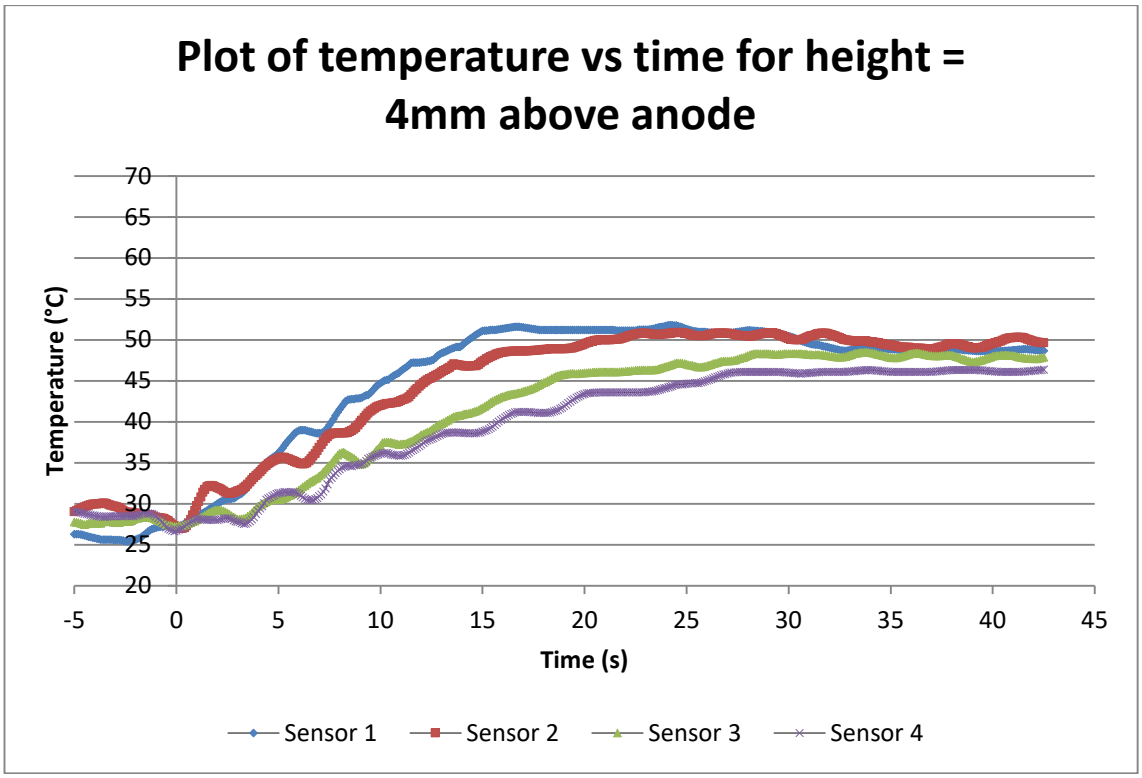

Figure 8.62: A plot of the temperature measured at each of 4 sensor positions over time during the radiant energy test with the test piece at a height of 4mm.

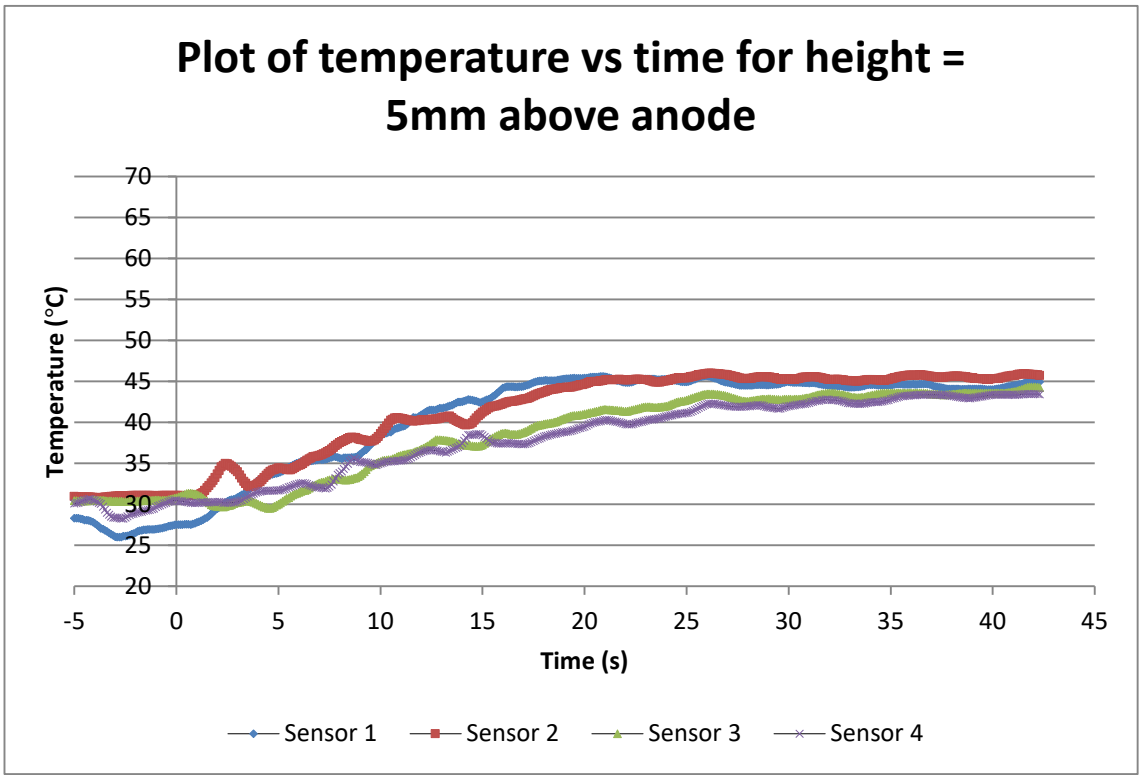

Figure 8.63: A plot of the temperature measured at each of 4 sensor positions over time during the radiant energy test with the test piece at a height of 7mm.

8.9 Appendix G: Profile experiments

This appendix contains the complete set of data obtained from the experiments to obtain the profiles describing the leading edge of the kerf. The appendix is broken into two sections, the data from the first experiment, concerning the section profile of the kerf on the axis, and the second experiment, concerning the profile of the front face.

8.9.1 Experiment 1

The appendix for experiment 1 shows the results obtained from the first experiment. Table 8.9 shows the process parameters used for each test.

Table 8.9: process parameters for the profile experiment test runs.

Profile experiments test parameters			
		Process Parameters	
T#	Thickness (mm)	Feed rate (mm/min)	Torch height (mm)
1	6	2000	1.5
2	6	1800	1.5
3	6	1600	1.5
4	6	1400	1.5
5	6	1200	1.5
6	8	1200	1.5
7	8	1100	1.5
8	8	1000	1.5
9	8	900	1.5
10	8	800	1.5
11	10	800	1.5
12	10	725	1.5
13	10	650	1.5
14	10	575	1.5
15	10	500	1.5

Figure 8.64 - Figure 8.78 show the data points obtained from the edge finding algorithm for each of the 15 sections taken.

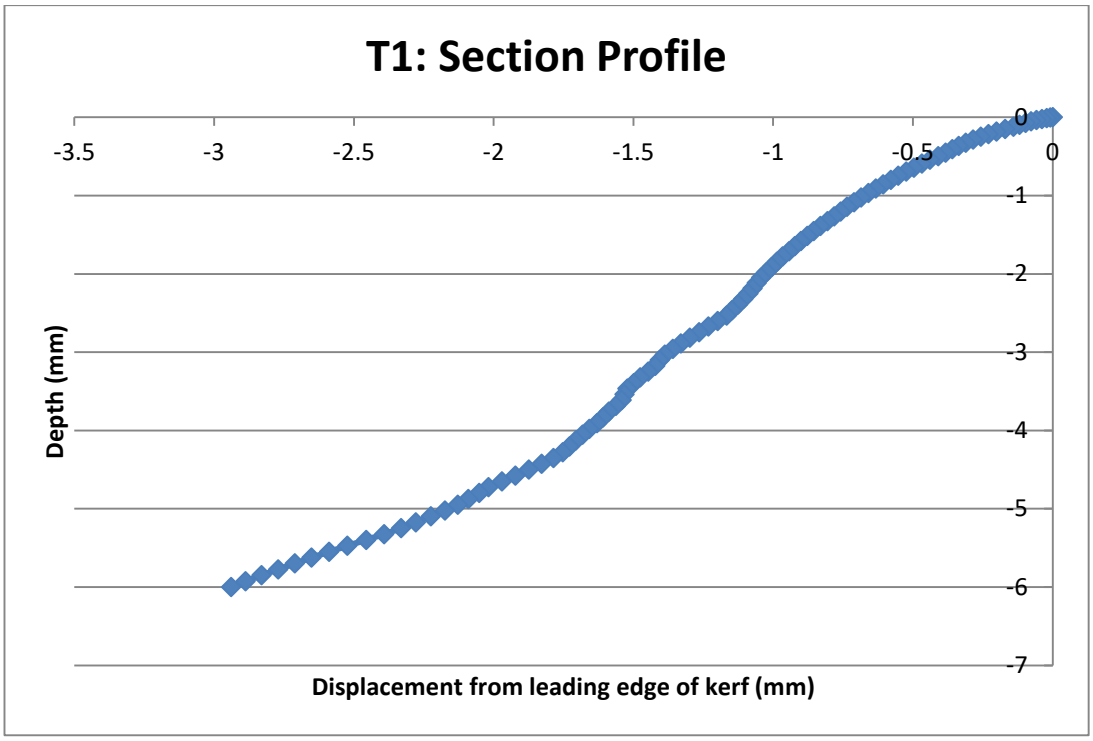

Figure 8.64: T1 of experiment 1. F=2000mm/min, h = 1.5mm,t = 6mm.

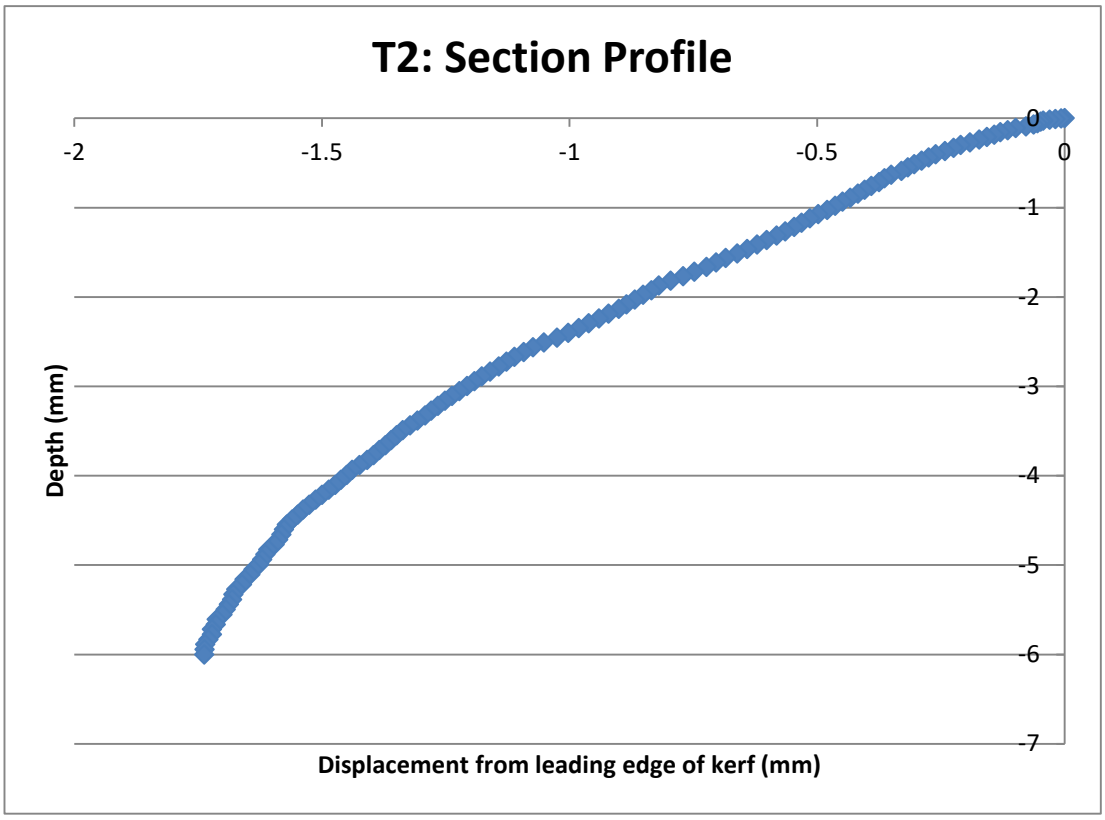

Figure 8.65: T2 of experiment 1. F=1800mm/min, h = 1.5mm, t = 6mm.

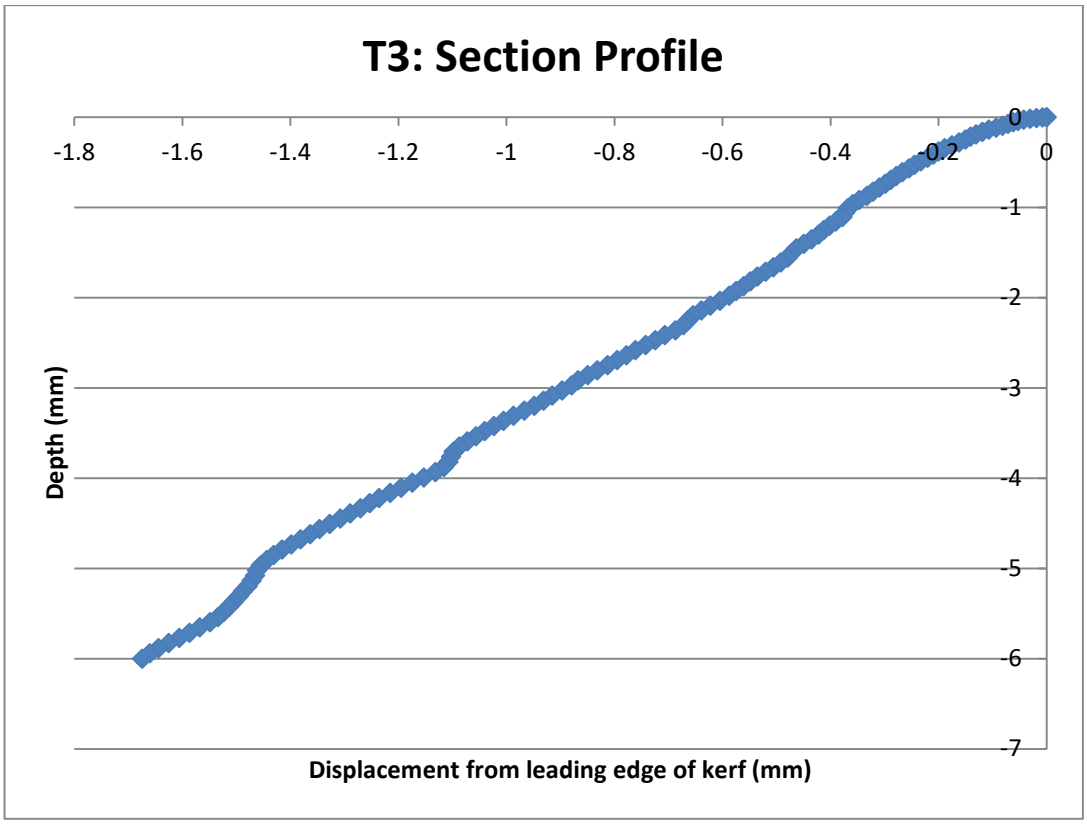

Figure 8.66: T3 of experiment 1. F=1600mm/min, h = 1.5mm, t = 6mm.

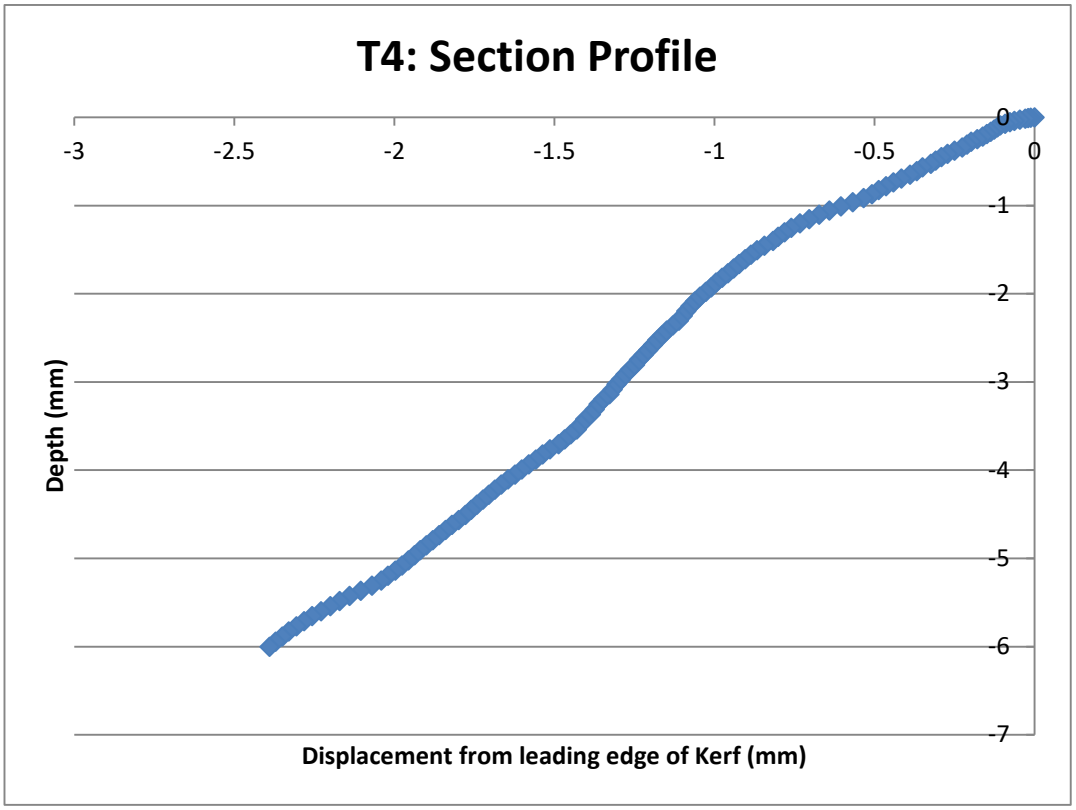

Figure 8.67: T4 of experiment 1. F=1400mm/min, h = 1.5mm, t = 6mm.

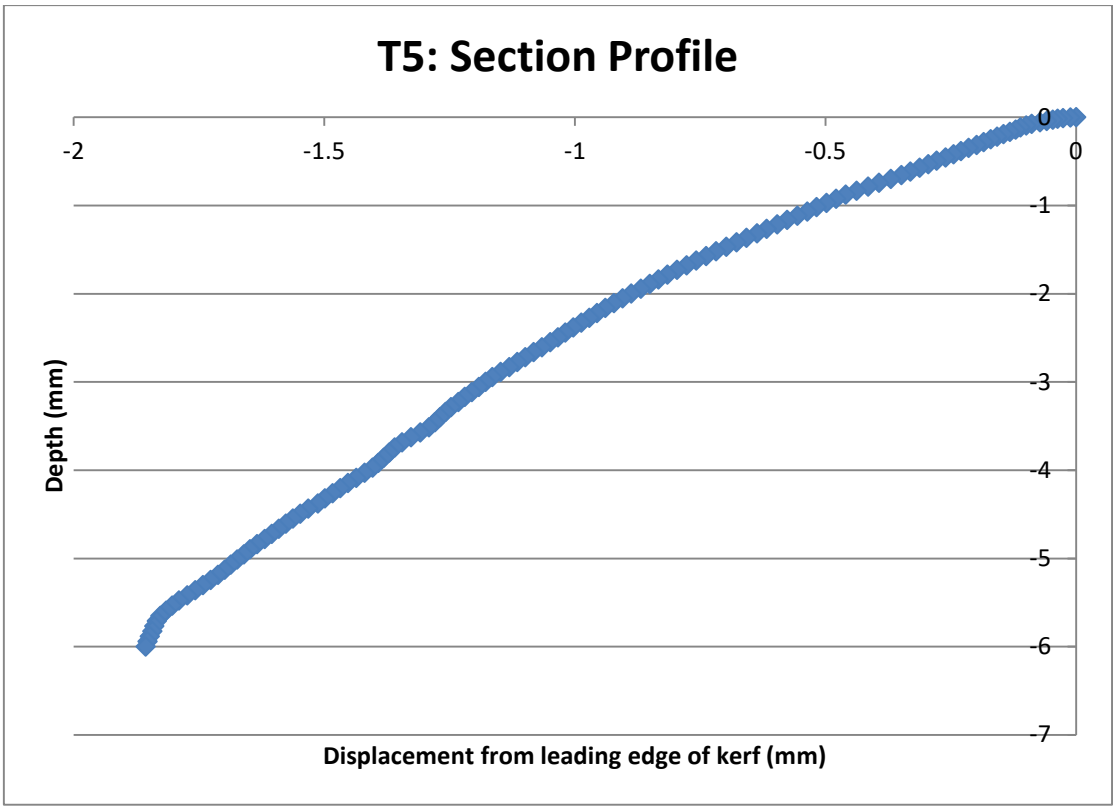

Figure 8.68: T14 of experiment 1. F=1200mm/min, h = 1.5mm, t = 6mm

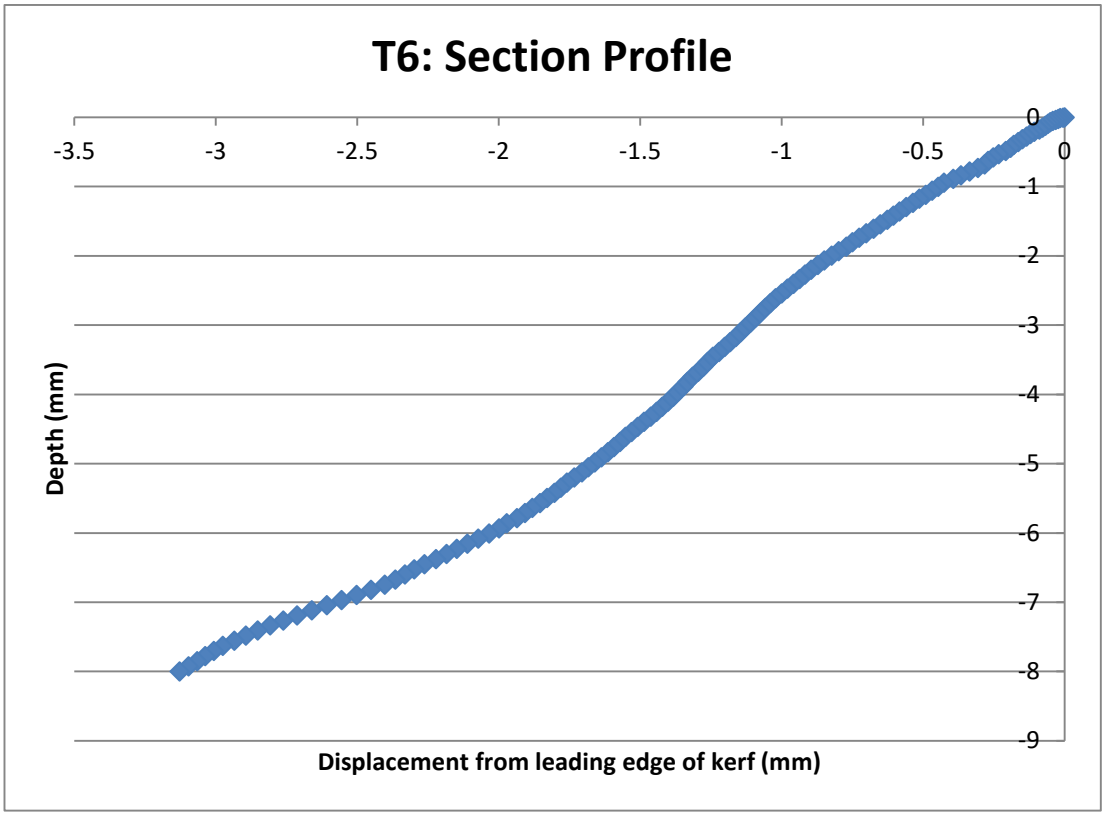

Figure 8.69: T14 of experiment 1. F=1200mm/min, h = 1.5mm, t = 8mm

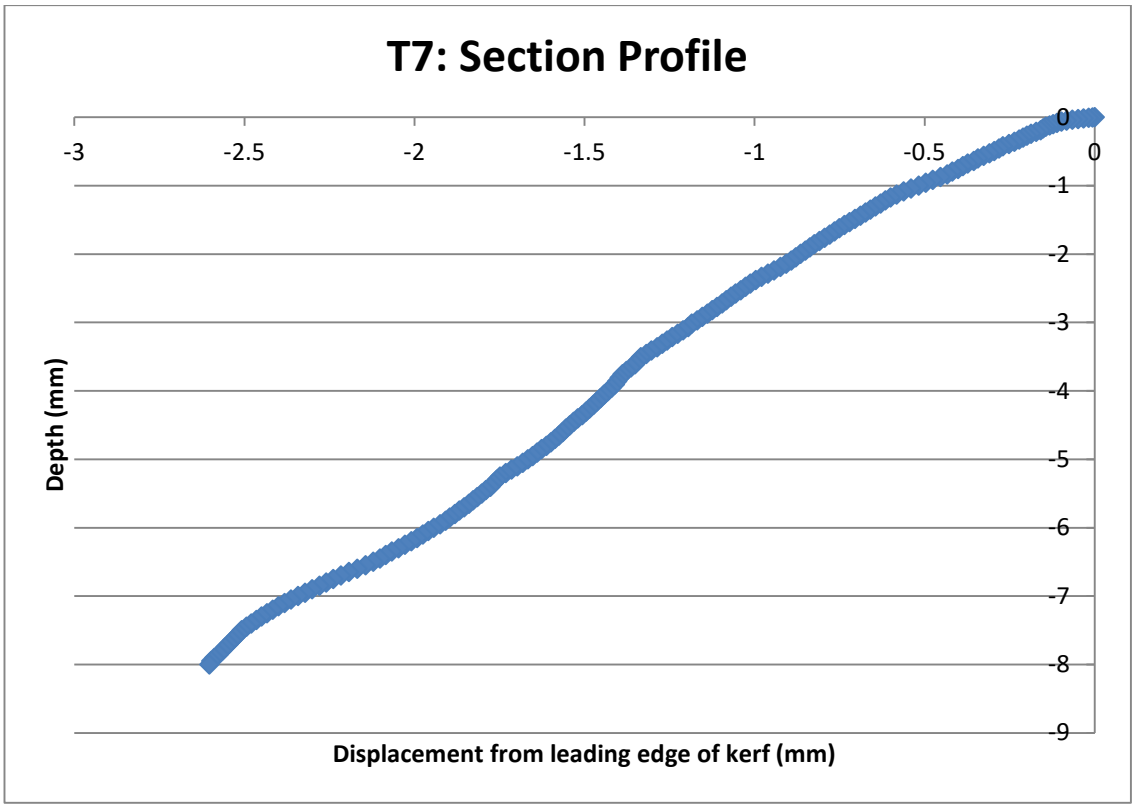

Figure 8.70: T7 of experiment 1. F=1100mm/min, h = 1.5mm, t = 8mm.

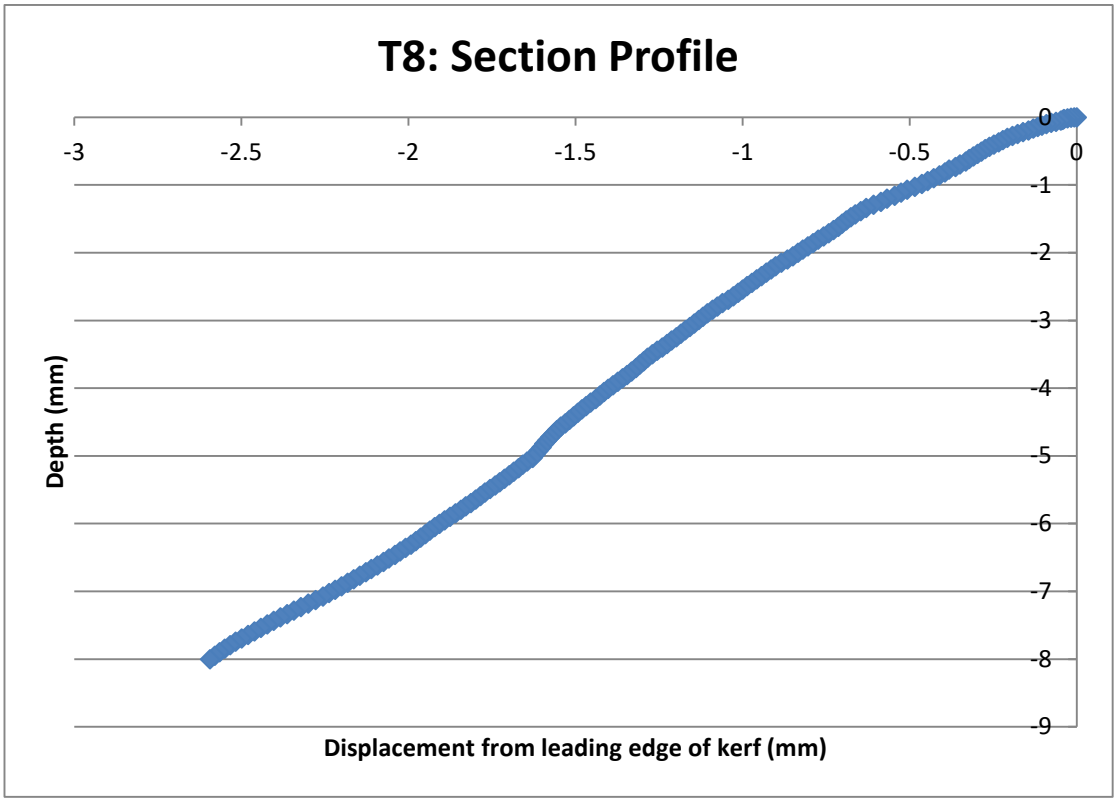

Figure 8.71: T8 of experiment 1. F=1000mm/min, h = 1.5mm, t = 8mm.

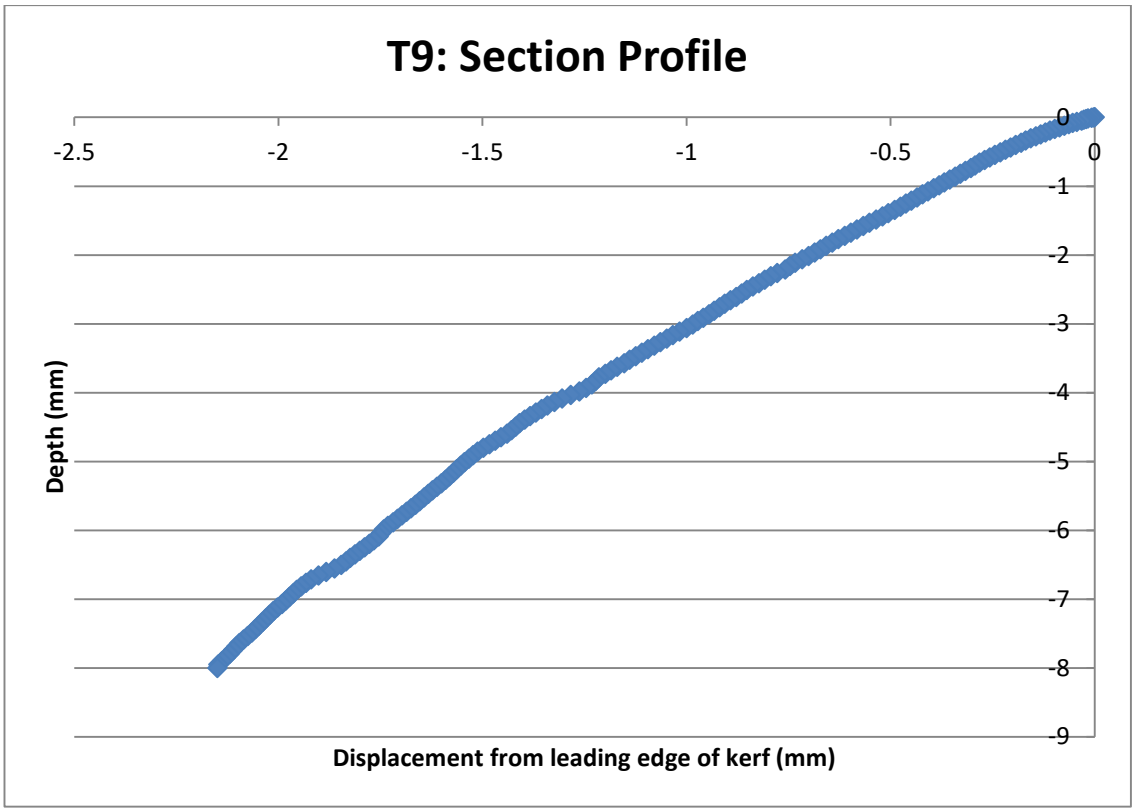

Figure 8.72: T9 of experiment 1. F=900mm/min, h = 1.5mm, t = 8mm.

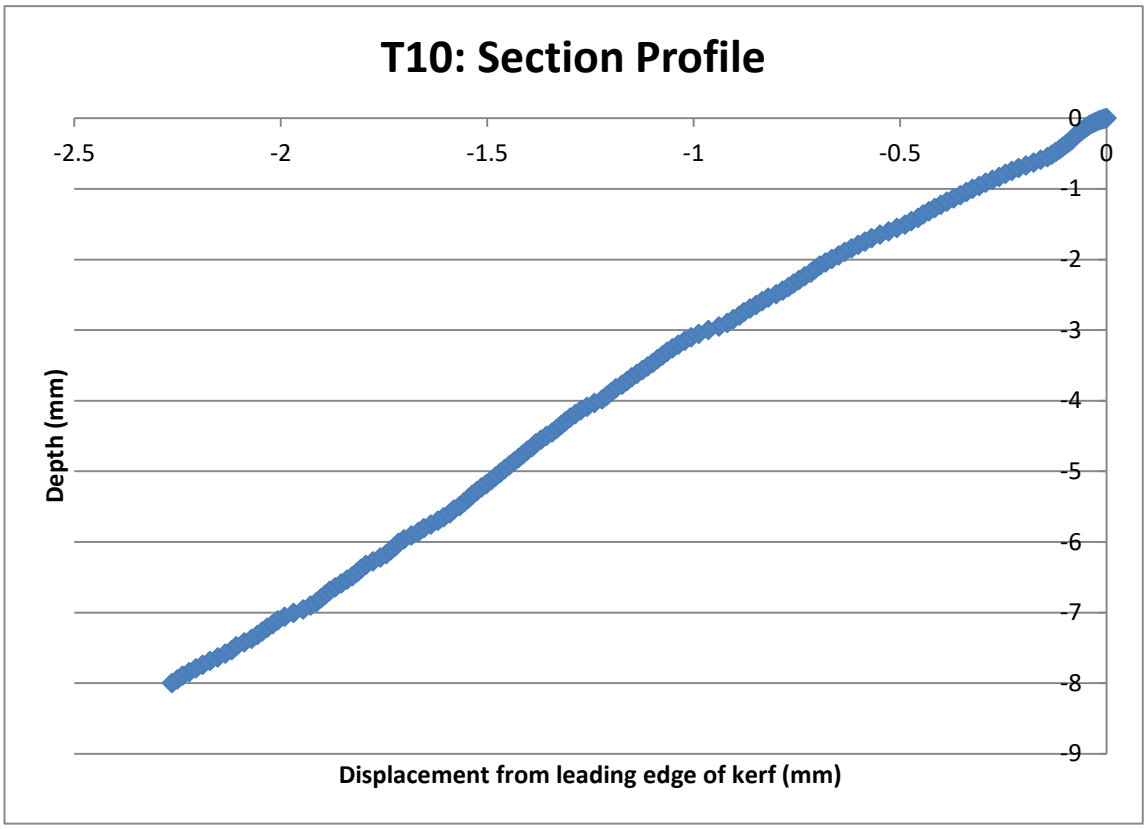

Figure 8.73: T10 of experiment 1. F=800mm/min, h = 1.5mm, t = 8mm.

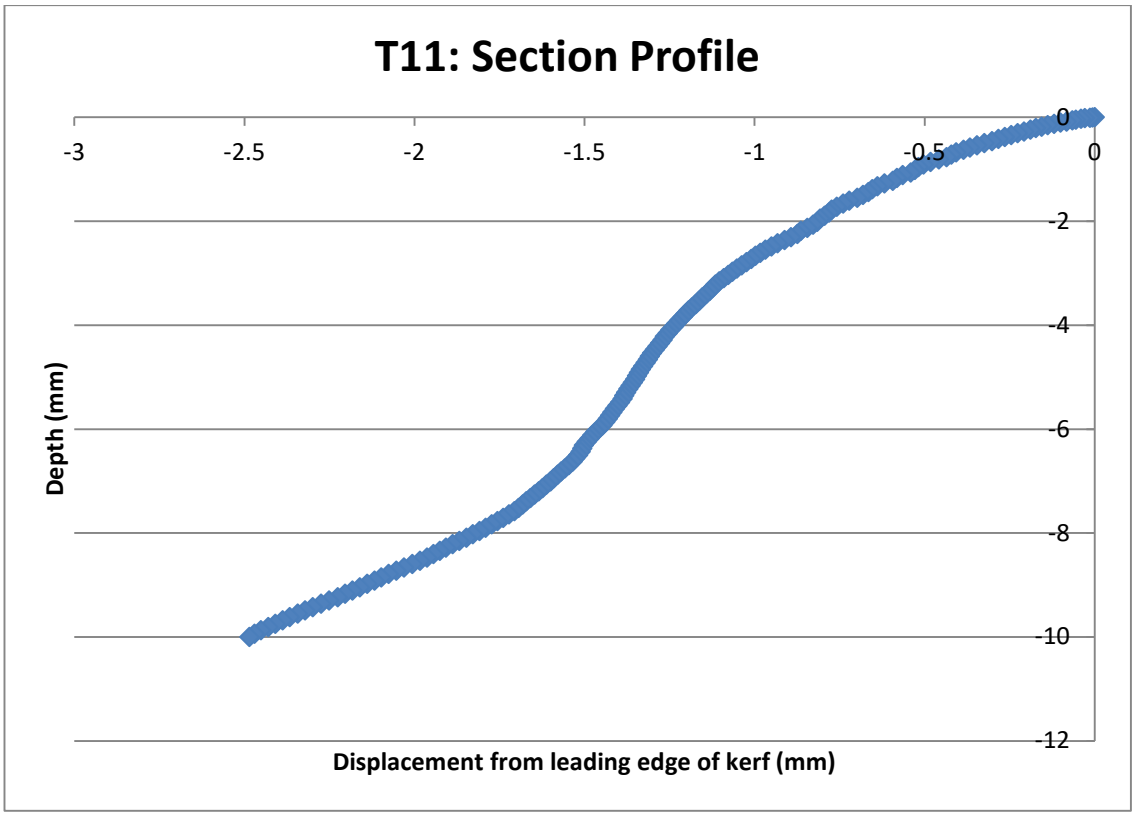

Figure 8.74: T11 of experiment 1. F=800mm/min, h = 1.5mm, t = 10mm

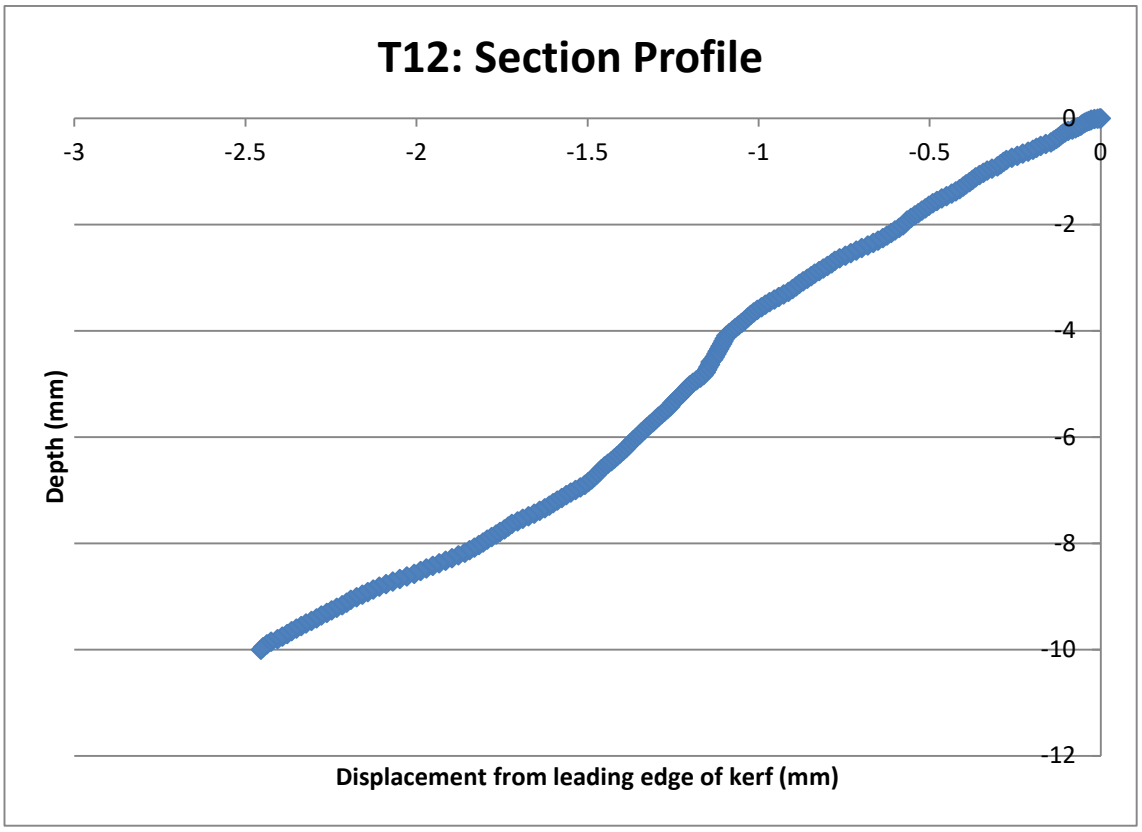

Figure 8.75: T12 of experiment 1. F=725mm/min, h = 1.5mm, t = 10mm.

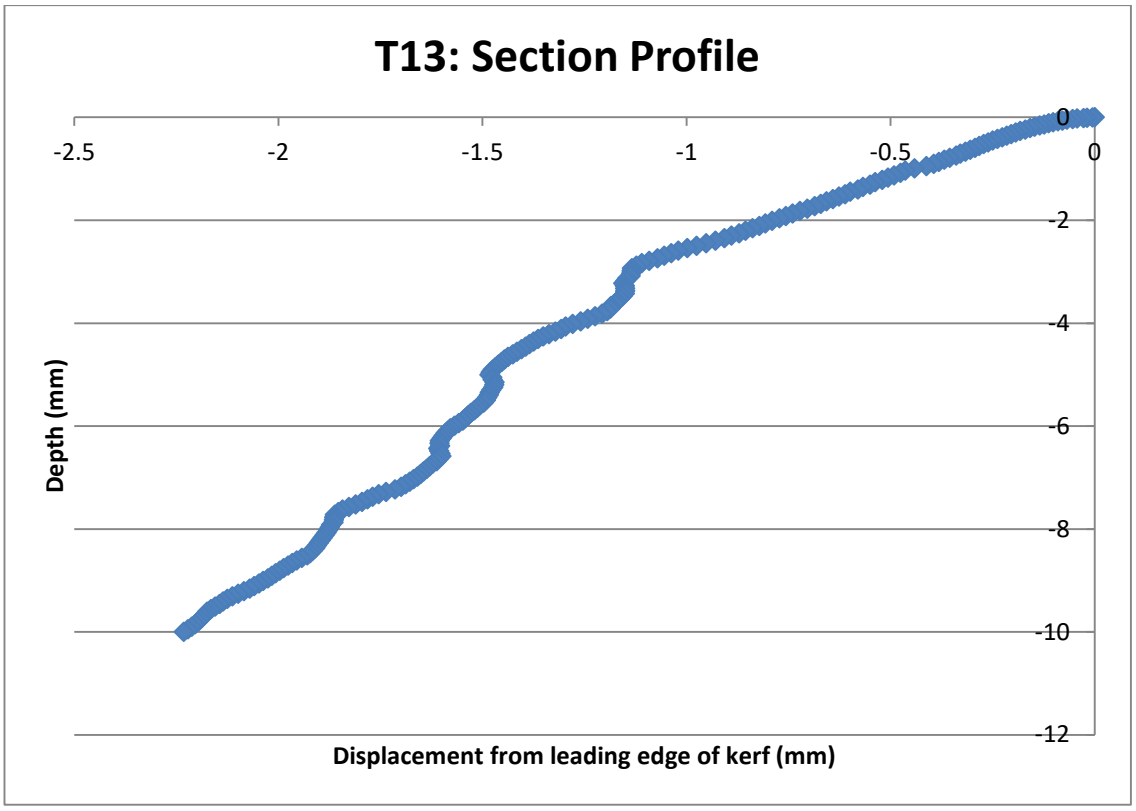

Figure 8.76: T13 of experiment 1. F=?650mm/min, h = 1.5mm, t = 10mm.

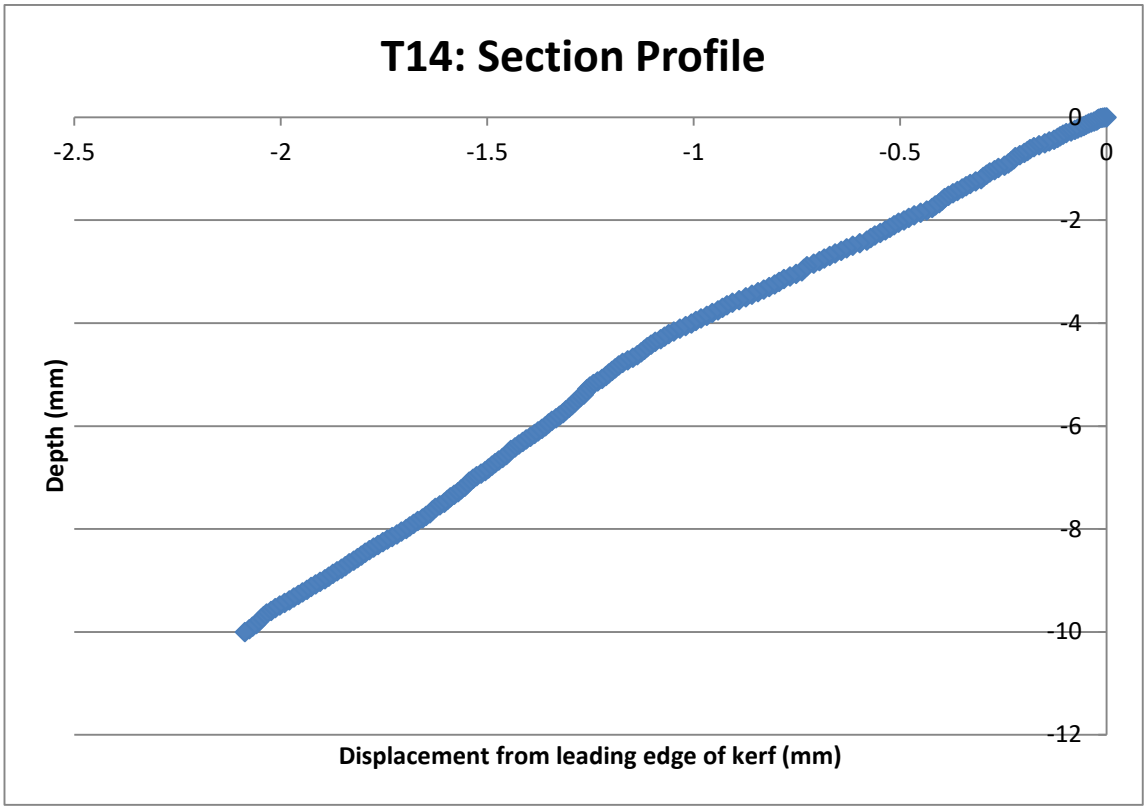

Figure 8.77: T14 of experiment 1. F=575mm/min, h = 1.5mm, t = 10mm.

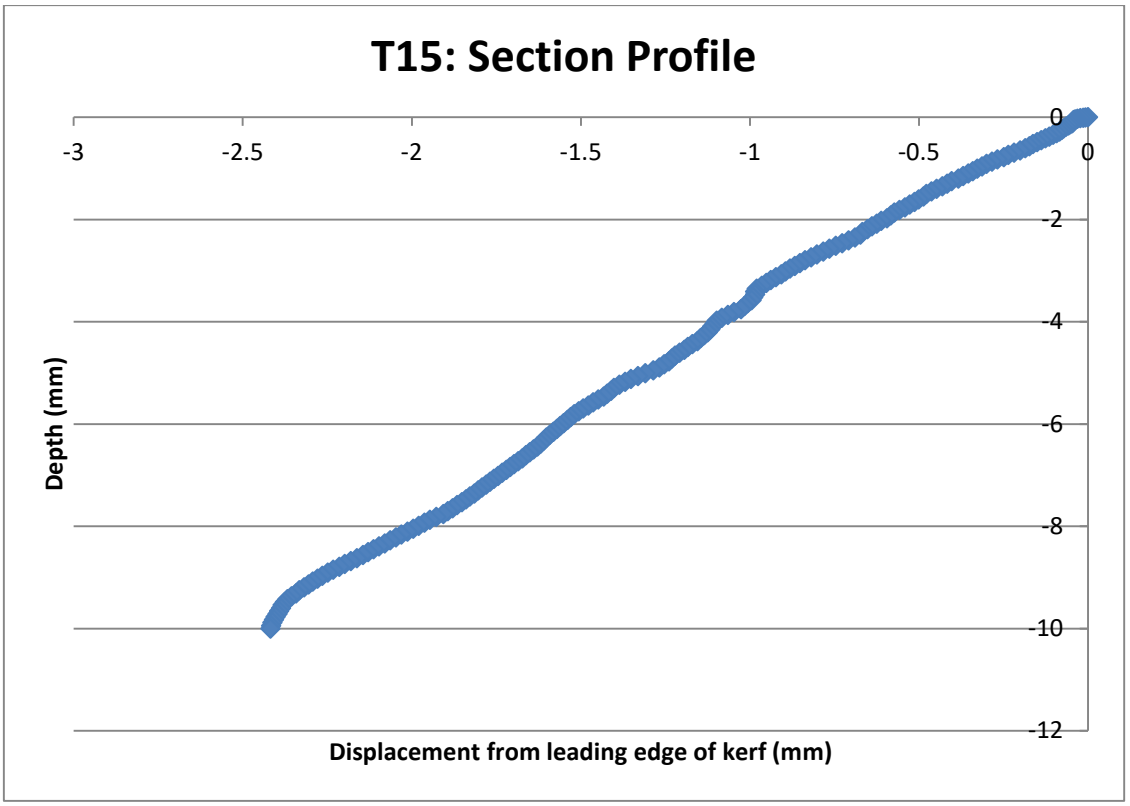

Figure 8.78: T15 of experiment 1. F=500mm/min, h = 1.5mm, t = 10mm.

8.9.2 Experiment 2

The appendix for experiment 2 shows the data points obtained that describe the front profile edge. Table 8.10 shows the process parameters for the experimental runs. Figure 8.79 - Figure 8.102 shows plots of the data that allow visualization of the shape of the front edge. All tests were performed with a torch height of 1.5mm.

Table 8.10: Summary of profile experiment 2 process parameters and results. (I# = image number, Pm = pixels per mm, KW = kerf width)

Profile experiment 2: Test results									
Test piece	Test	I#	Feed rate (mm/min)	Thickness (mm)	Offset (mm)	Height (mm)	Width (mm)	Pm	KW (mm)
1	1	1	650	10	0	10	18.69	18.62	1.48
1	2	3	650	10	2.17	7.83	18.82	16.50	1.46
1	3	5	650	10	4.22	5.78	18.95	16.68	1.27
1	4	6	650	10	4.18	4.18	19.05	16.72	1.13
1	5	4	650	10	1.95	1.95	19.19	16.56	1.17
1	6	2	650	10	0	0	19.31	18.80	1.24
2	7	7	550	10	0	10	18.69	18.79	1.84
2	8	9	550	10	2.21	7.79	18.82	16.39	1.39
2	9	11	550	10	3.9	6.1	18.91	16.43	0.85
2	10	12	550	10	3.78	3.78	19.04	16.50	1.57
2	11	10	550	10	2.12	2.12	19.14	16.63	1.25
2	12	8	550	10	0	0	19.26	18.78	1.35
3	13	13	450	10	0	10	18.50	19.05	1.52
3	14	15	450	10	2.02	7.98	18.53	16.64	1.56
3	15	17	450	10	4.05	5.95	18.56	16.55	1.32
3	16	18	450	10	3.86	3.86	18.60	16.53	1.19
3	17	16	450	10	2.53	2.53	18.62	16.60	1.15
3	18	14	450	10	0	0	18.66	18.99	1.30
4	19	19	2000	6	0	6	18.12	15.34	2.15
4	20	21	2000	6	1.9	4.1	18.34	15.63	1.26
4	21	22	2000	6	1.97	1.97	18.60	15.61	1.64
4	22	20	2000	6	0	0	18.83	15.69	1.62
5	23	23	1600	6	0	6	18.37	15.24	2.40
5	24	25	1600	6	1.83	4.17	18.48	15.80	1.74
5	25	26	1600	6	1.92	1.92	18.61	15.59	1.70
5	26	24	1600	6	0	0	18.72	15.70	1.63
6	27	27	1200	6	0	6	18.11	15.44	2.53
6	28	29	1200	6	1.77	4.23	18.30	16.04	1.75
6	29	30	1200	6	1.89	1.89	18.56	15.77	1.55
6	30	28	1200	6	0	0	18.77	15.28	2.02

Figure 8.79 - Figure 8.102 show plots of the data points for each piece. Three plots show 3d scatter plots with various views of the data points to show the shape while the last plot for each test piece shows a scatter plot in X and Y to demonstrate the spread of the profiles at each depth.

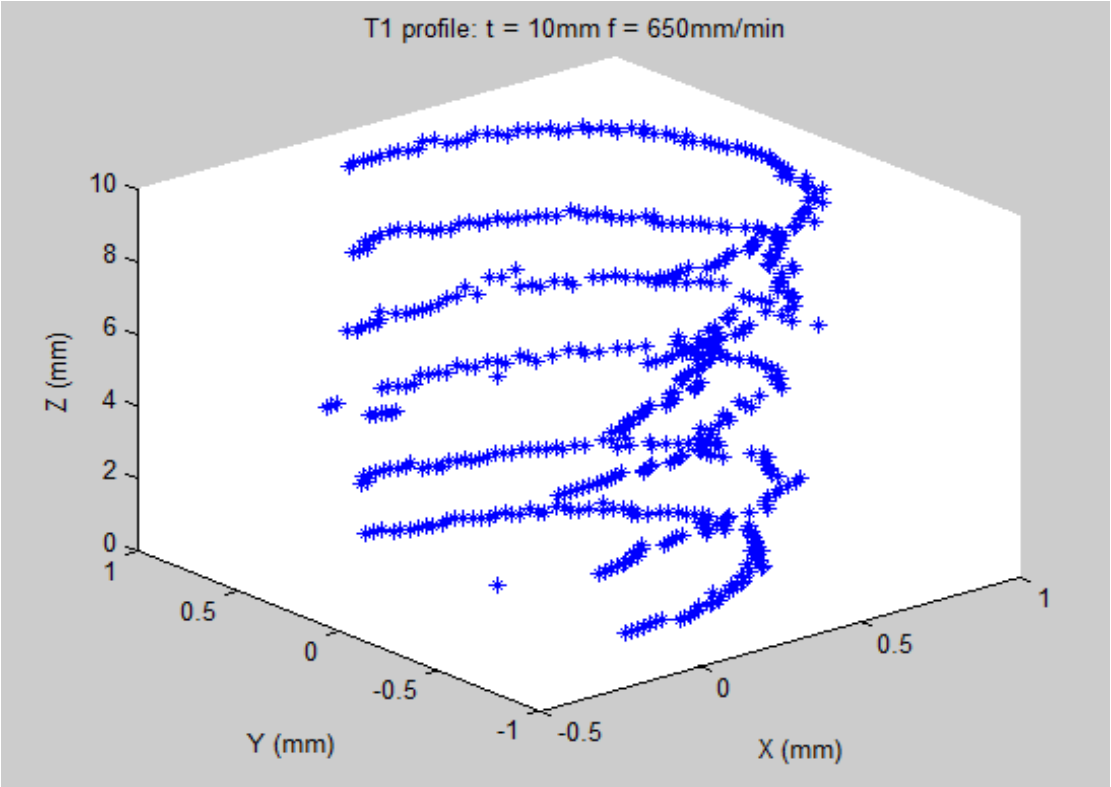

Figure 8.79: Test piece 1 data points where elevation is 30 degrees and azimuth is at 30 degrees.

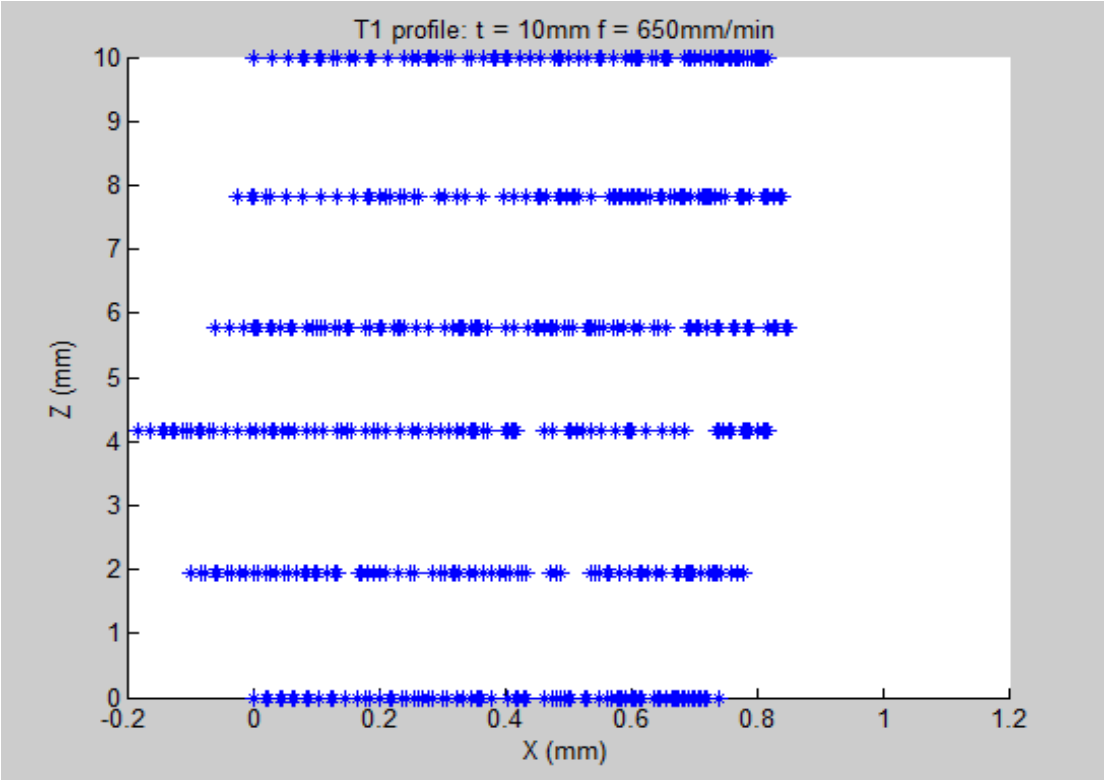

Figure 8.80: Test piece 1 data points where elevation is 0 degrees and azimuth is at 0 degrees.

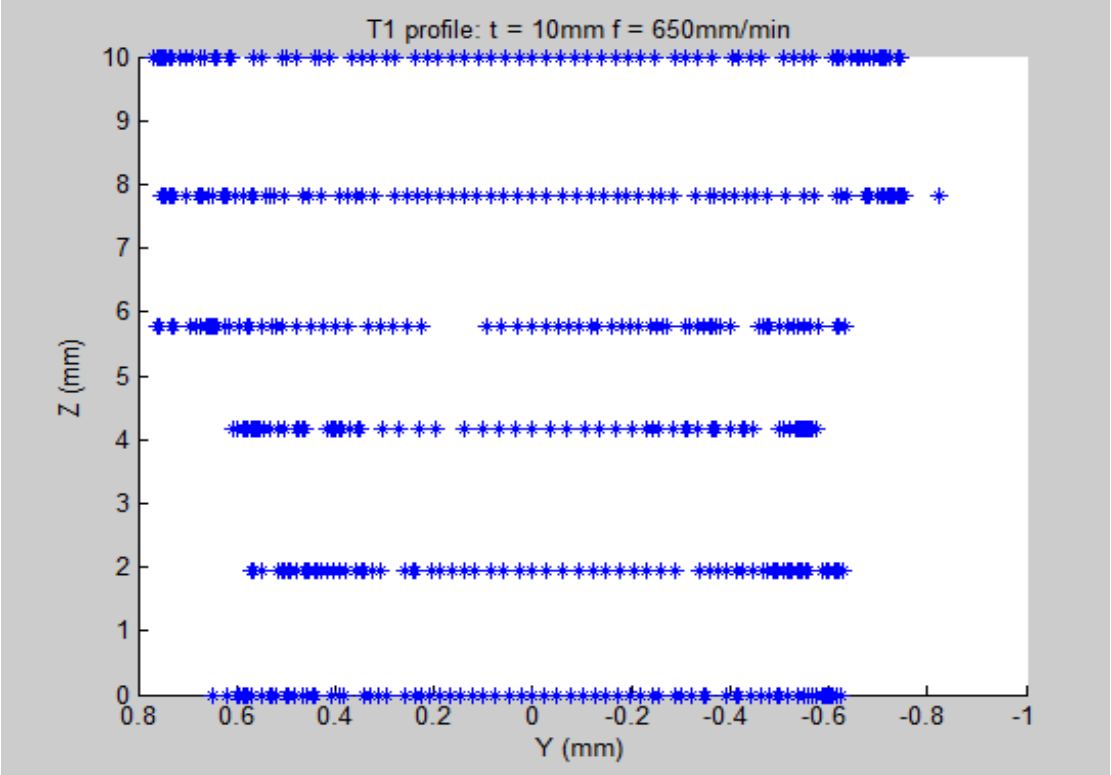

Figure 8.81: Test piece 1 data points where elevation is 0 degrees and azimuth is at 90 degrees.

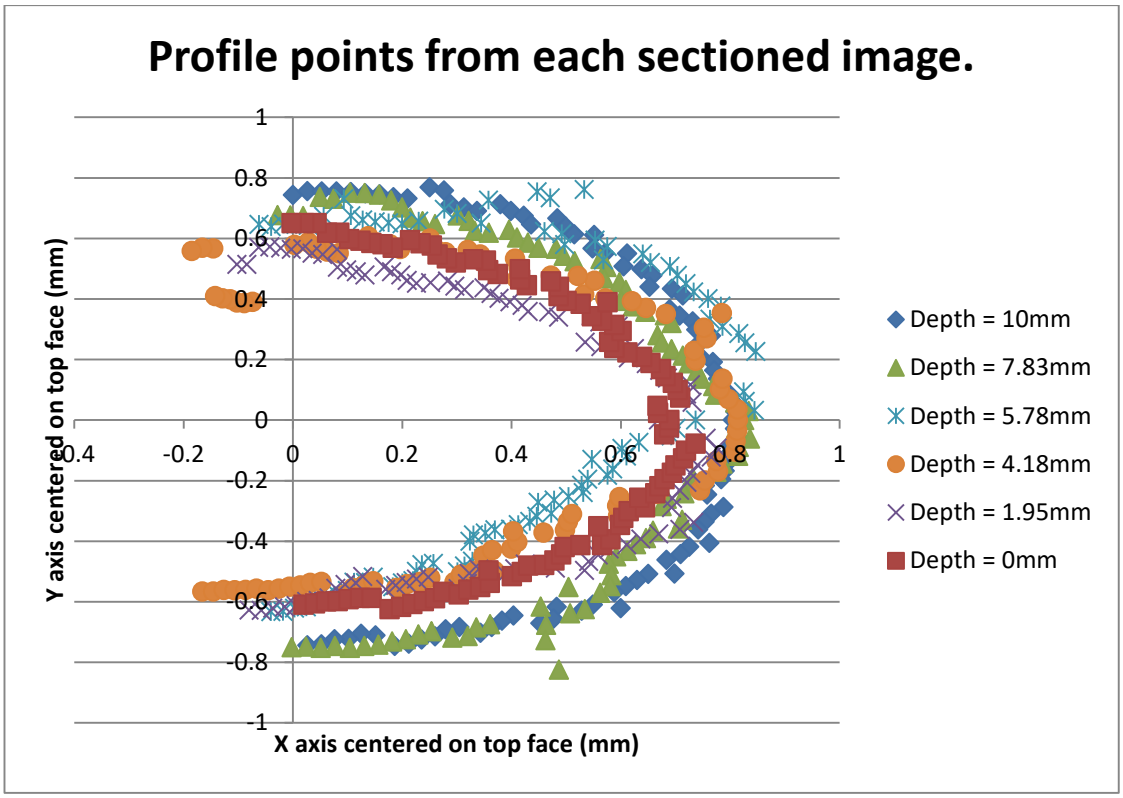

Figure 8.82: Scatter plot of test piece 1 data points for each depth view from above.

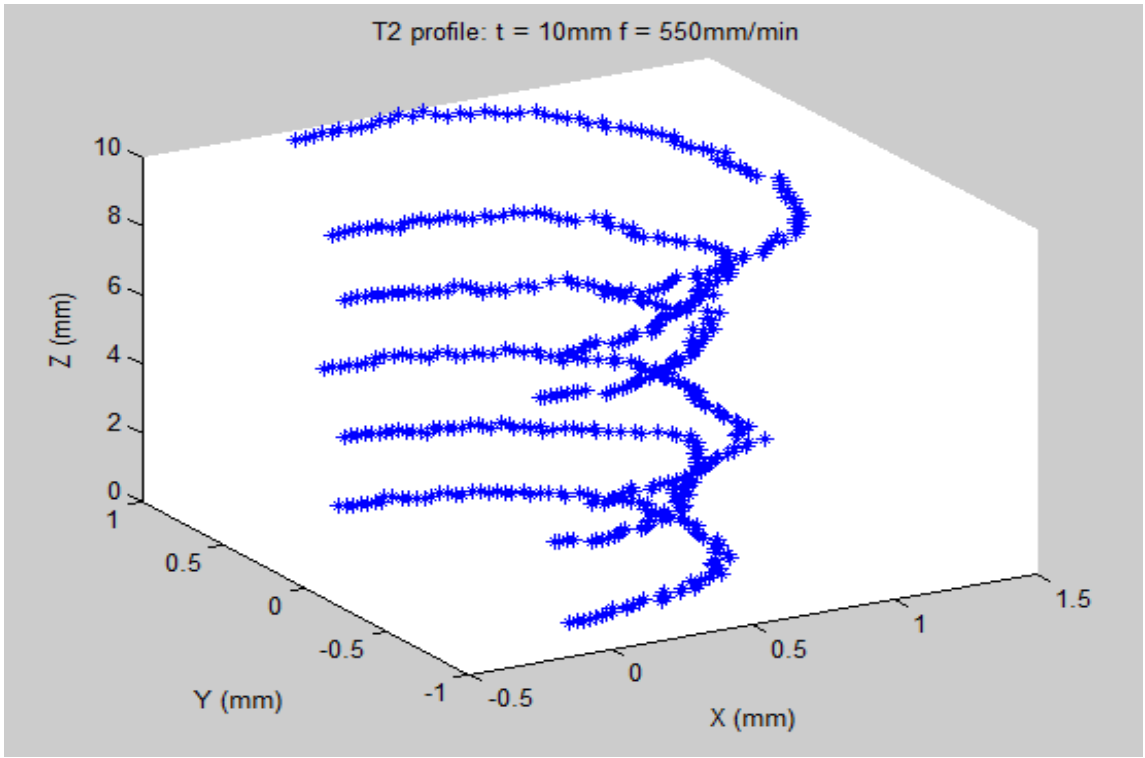

Figure 8.83: Test piece 2 data points where elevation is 30 degrees and azimuth is at 30 degrees.

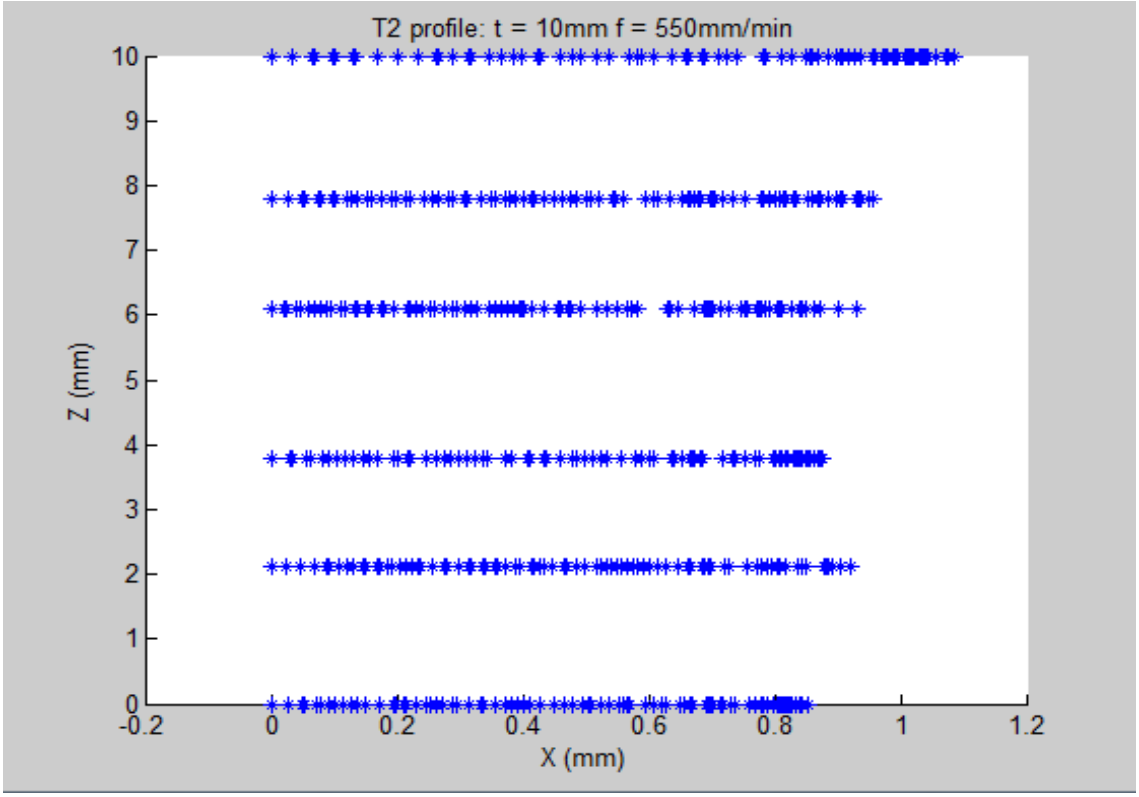

Figure 8.84: Test piece 2 data points where elevation is 0 degrees and azimuth is at 0 degrees.

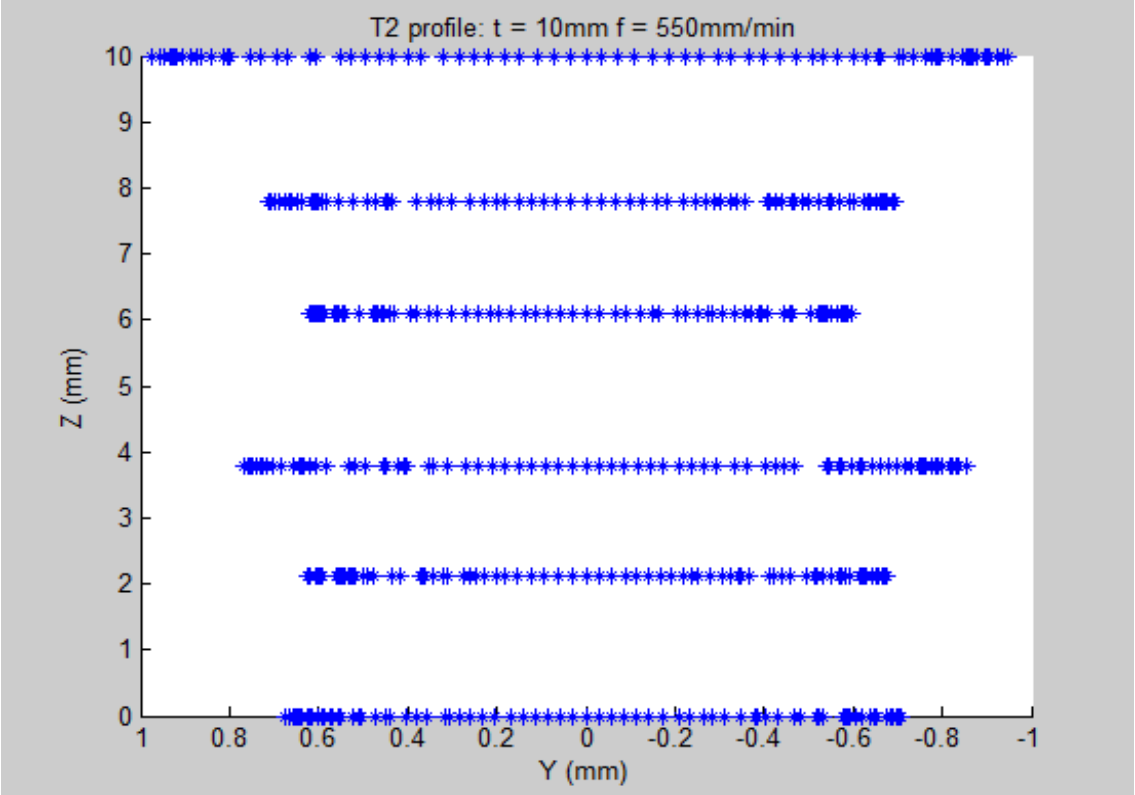

Figure 8.85: Test piece 2 data points where elevation is 0 degrees and azimuth is at 90 degrees.

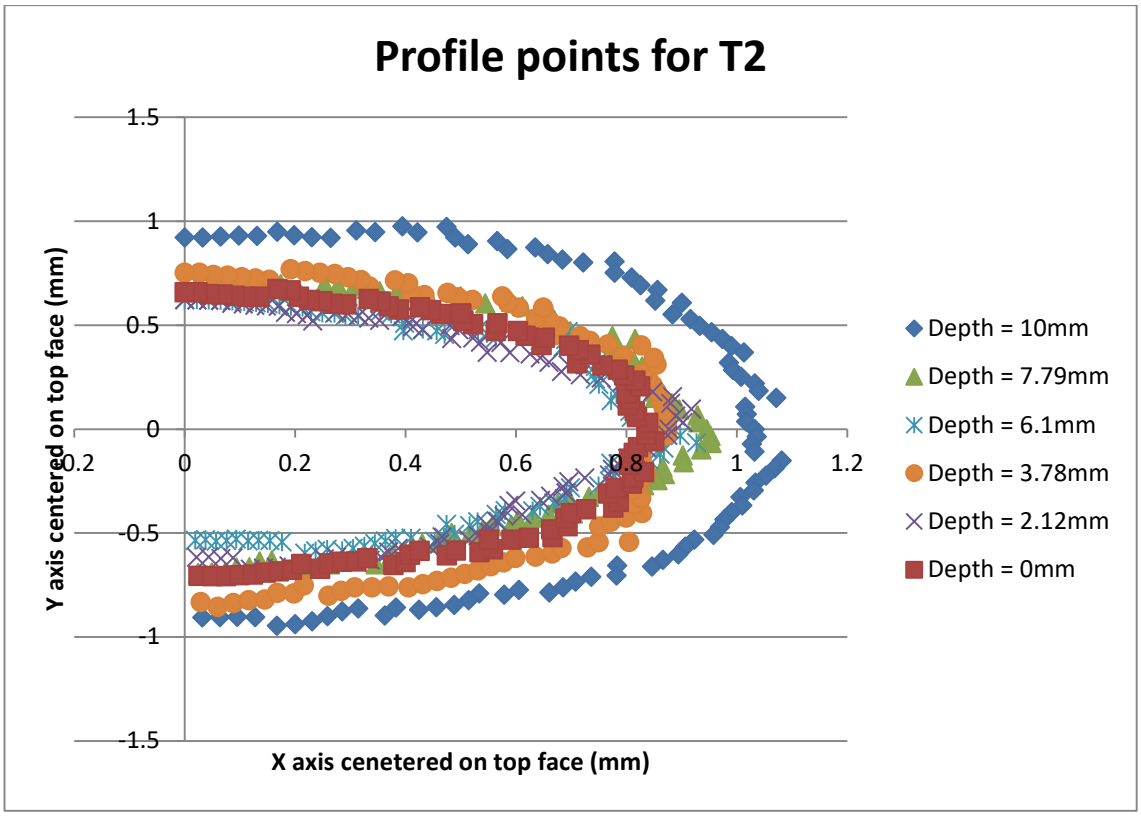

Figure 8.86: Scatter plot of test piece 2 data points for each depth view from above.

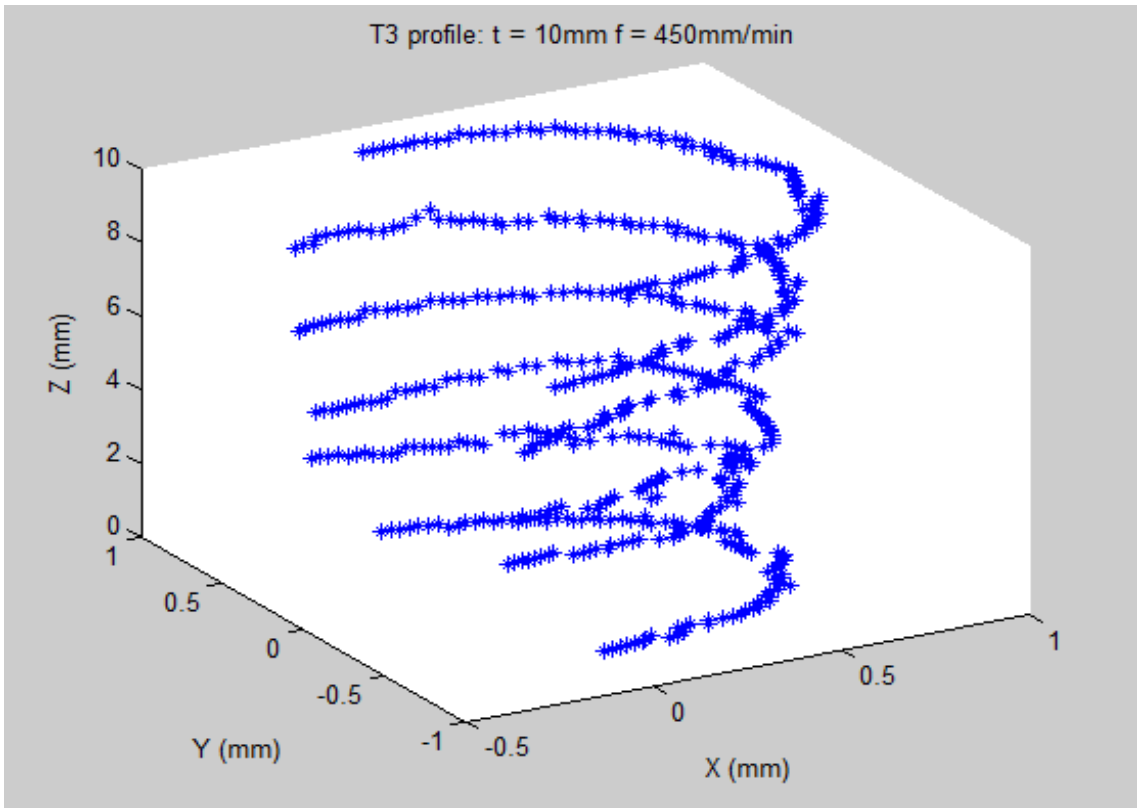

Figure 8.87: Test piece 3 data points where elevation is 30 degrees and azimuth is at 30 degrees.

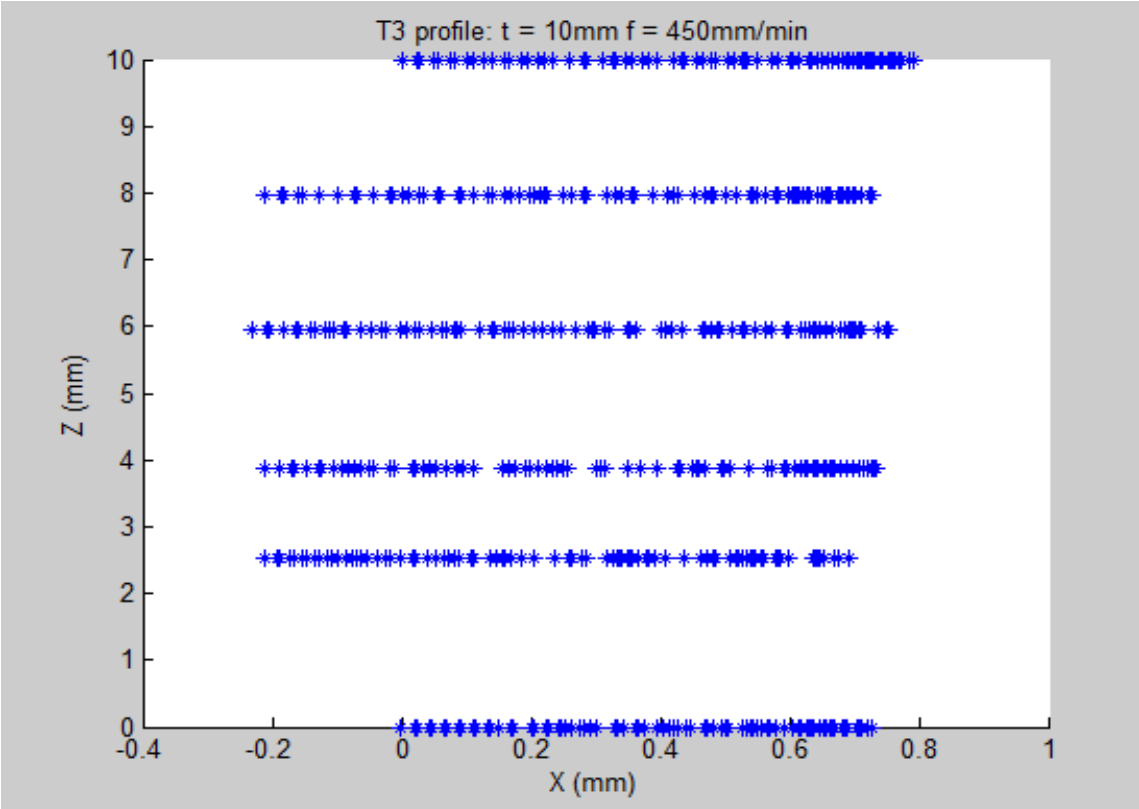

Figure 8.88: Test piece 3 data points where elevation is 0 degrees and azimuth is at 0 degrees.

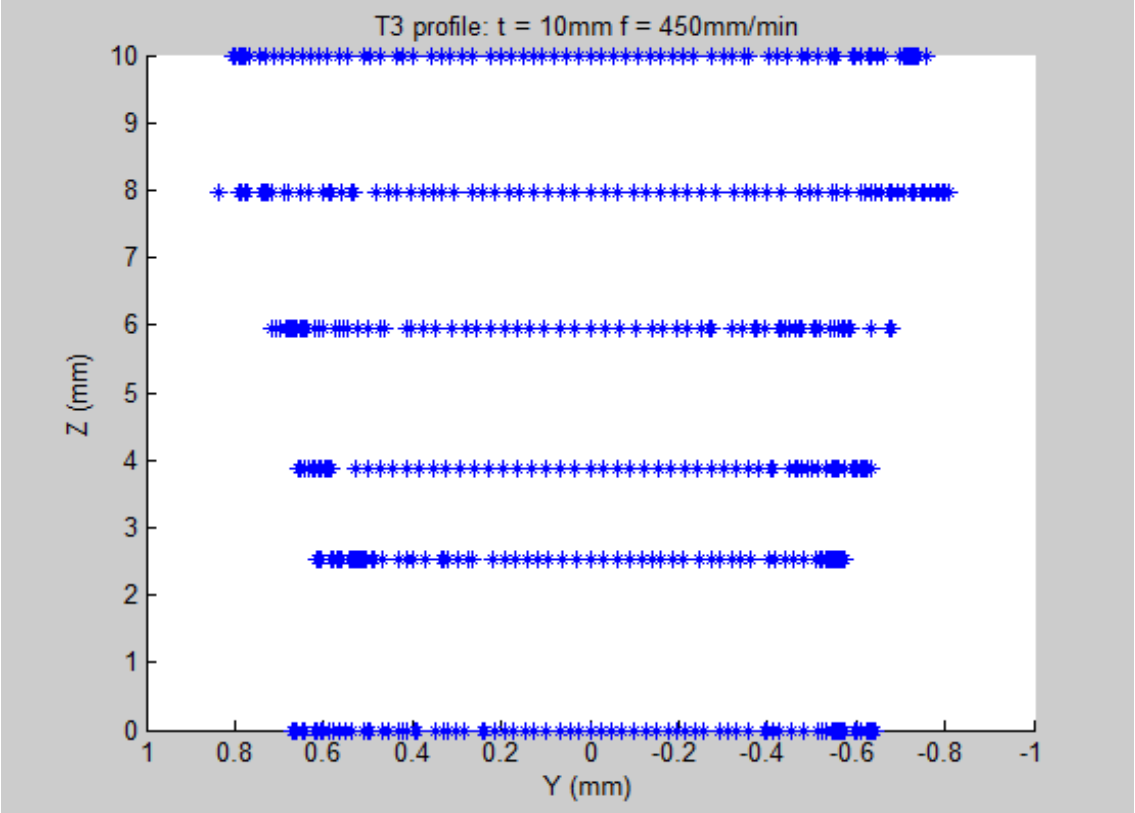

Figure 8.89: Test piece 3 data points where elevation is 0 degrees and azimuth is at 90 degrees.

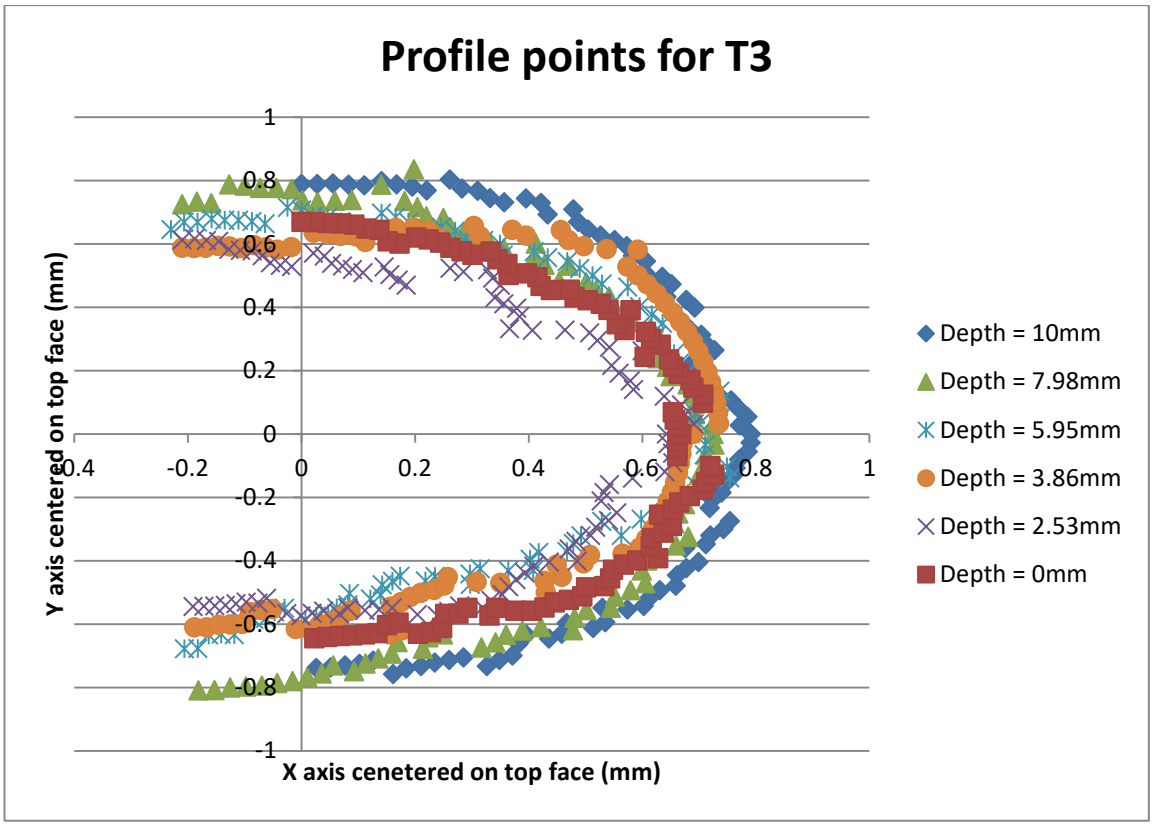

Figure 8.90: Scatter plot of test piece 3 data points for each depth view from above.

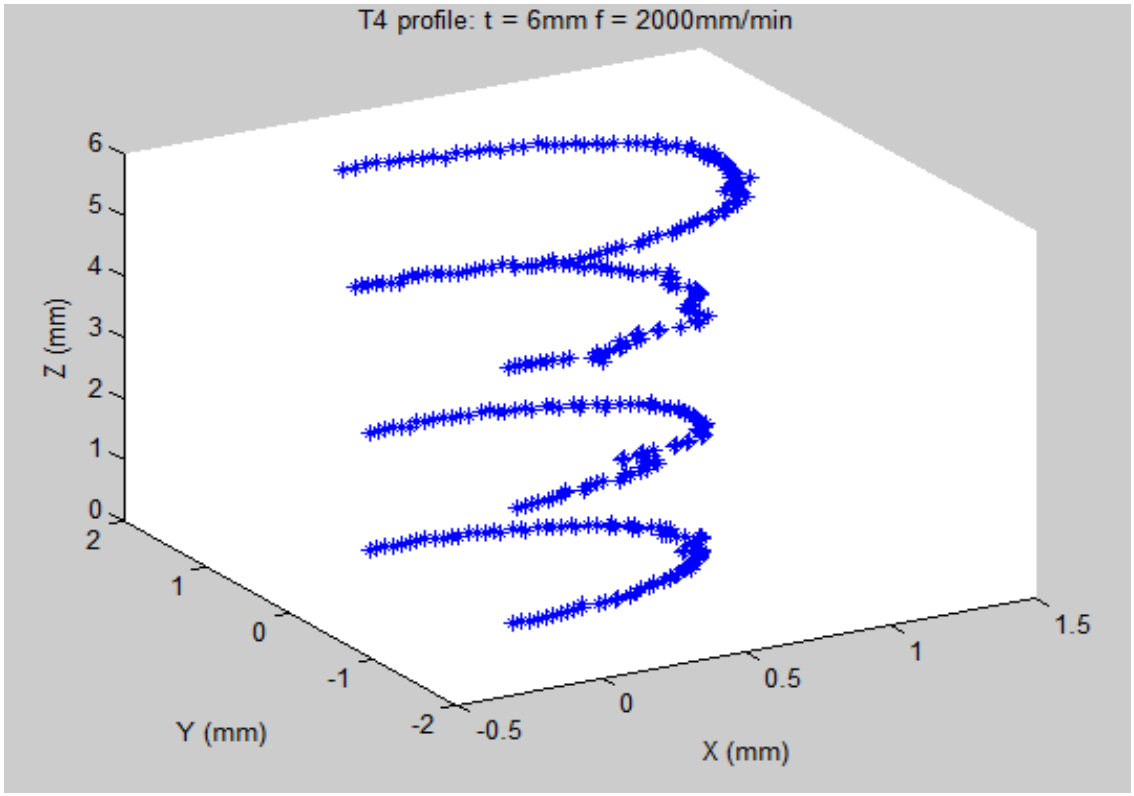

Figure 8.91: Test piece 4 data points where elevation is 30 degrees and azimuth is at 30 degrees.

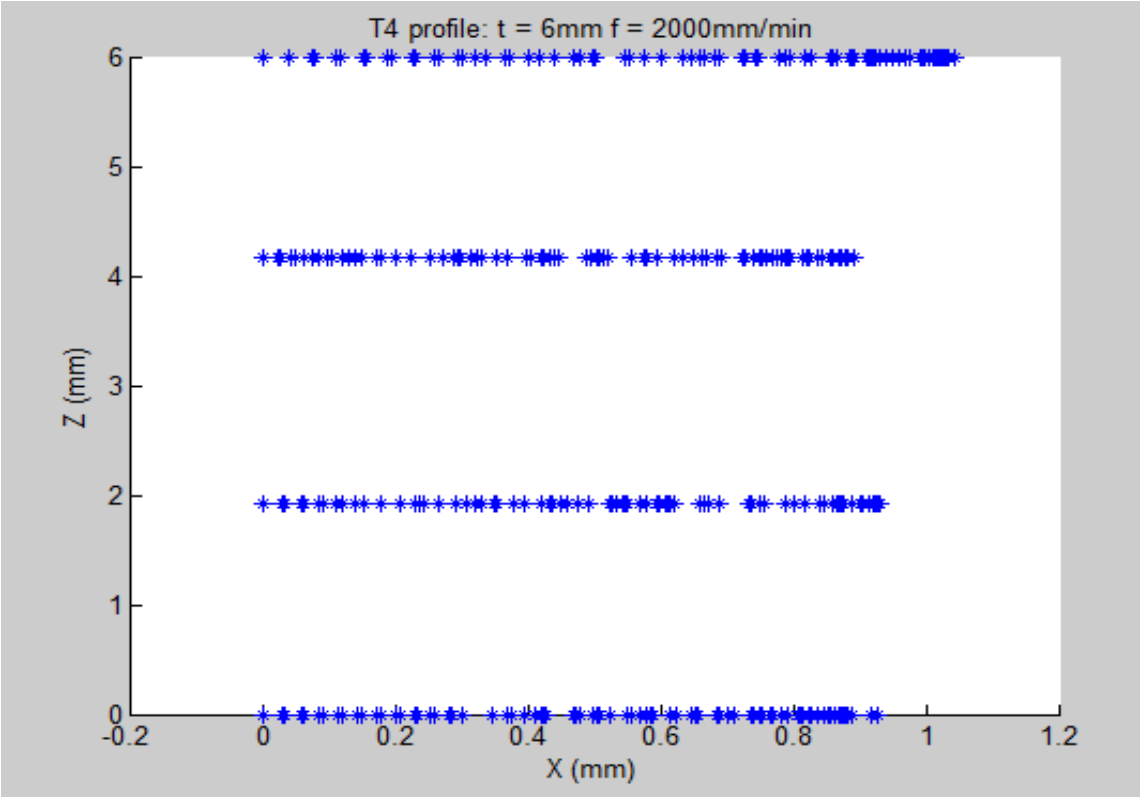

Figure 8.92: Test piece 4 data points where elevation is 0 degrees and azimuth is at 0 degrees.

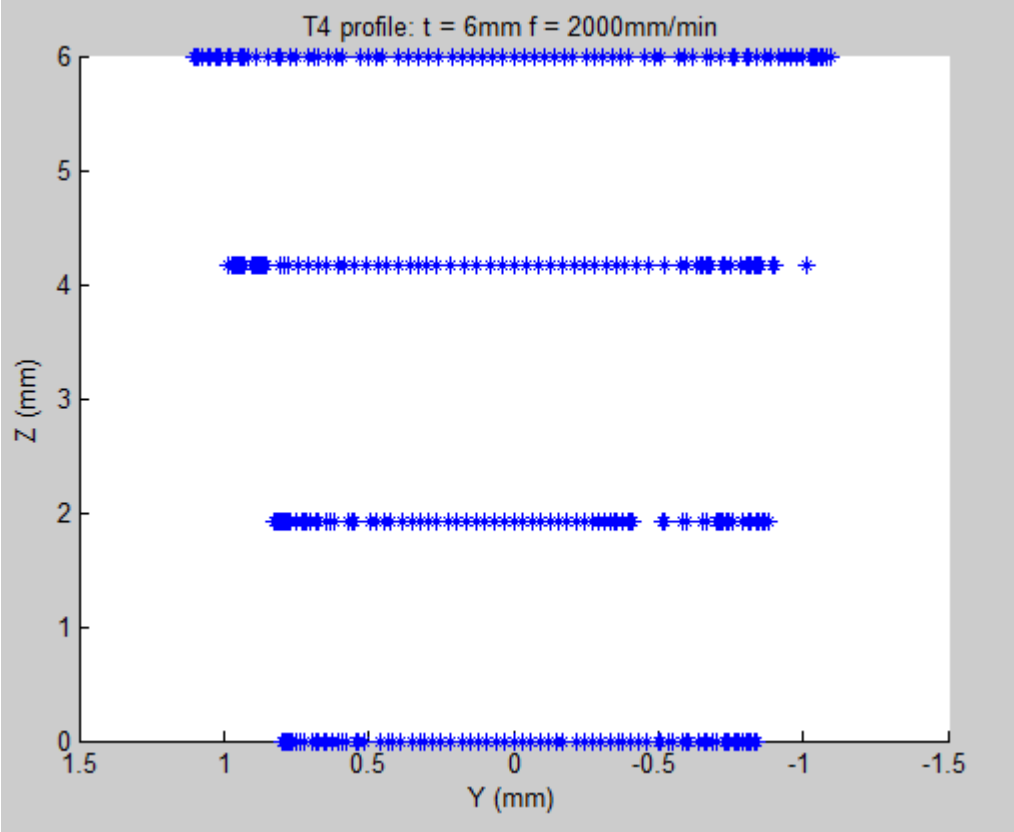

Figure 8.93: 3D plot of test piece 4 data points where elevation is 0 degrees and azimuth is at 90 degrees.

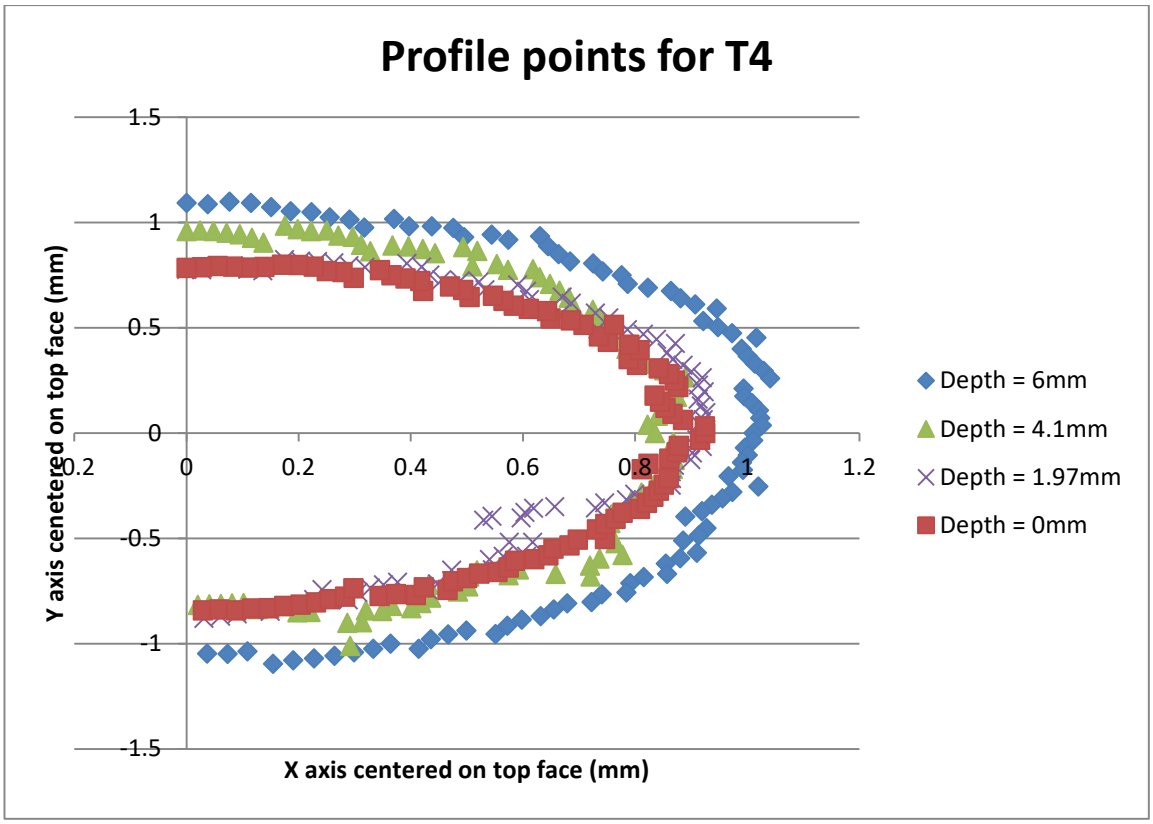

Figure 8.94: Scatter plot of test piece 4 data points for each depth view from above.

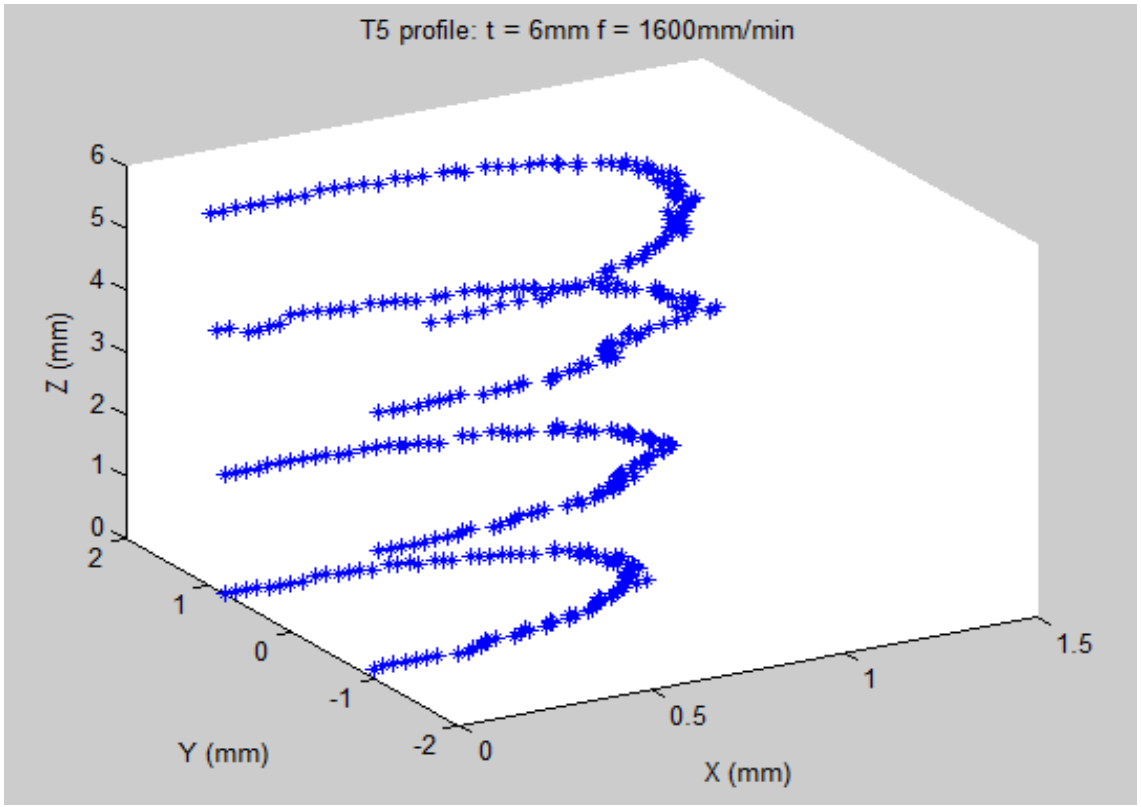

Figure 8.95: 3D plot of test piece 5 data points where elevation is 30 degrees and azimuth is at 30 degrees.

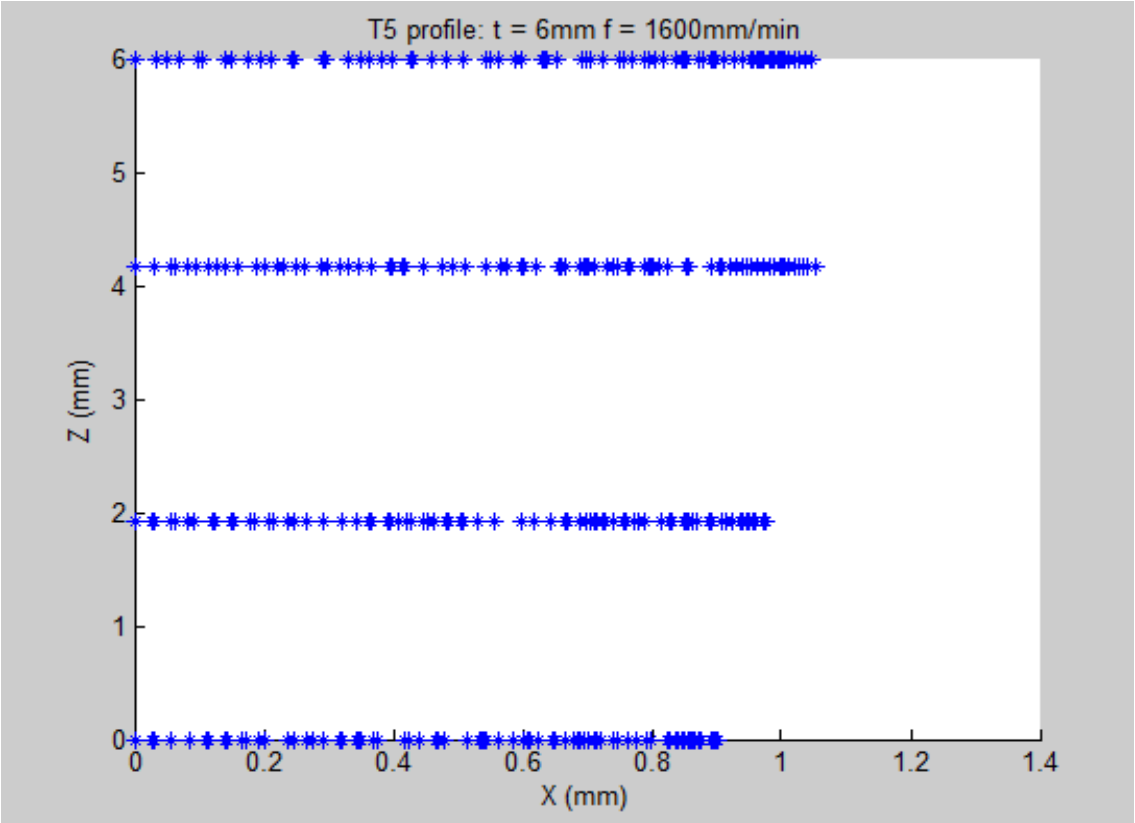

Figure 8.96: 3D plot of test piece 5 data points where elevation is 0 degrees and azimuth is at 90 degrees.

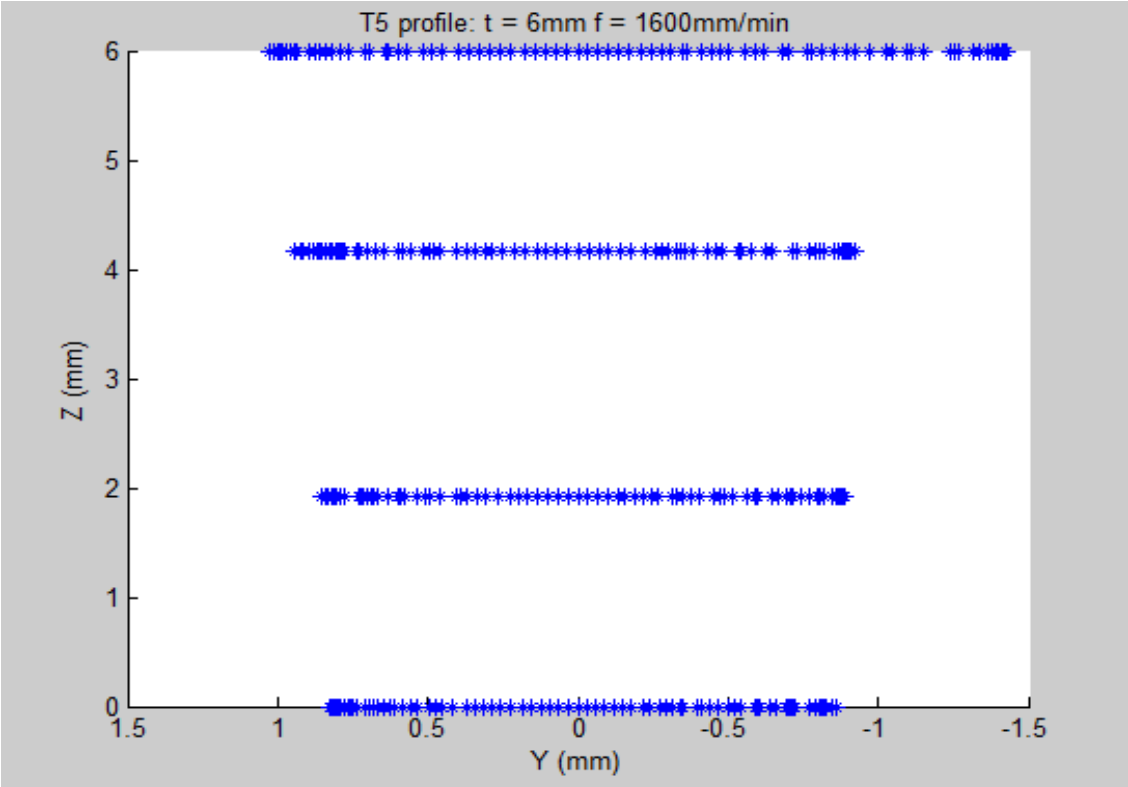

Figure 8.97: 3D plot of test piece 5 data points where elevation is 0 degrees and azimuth is at 0 degrees.

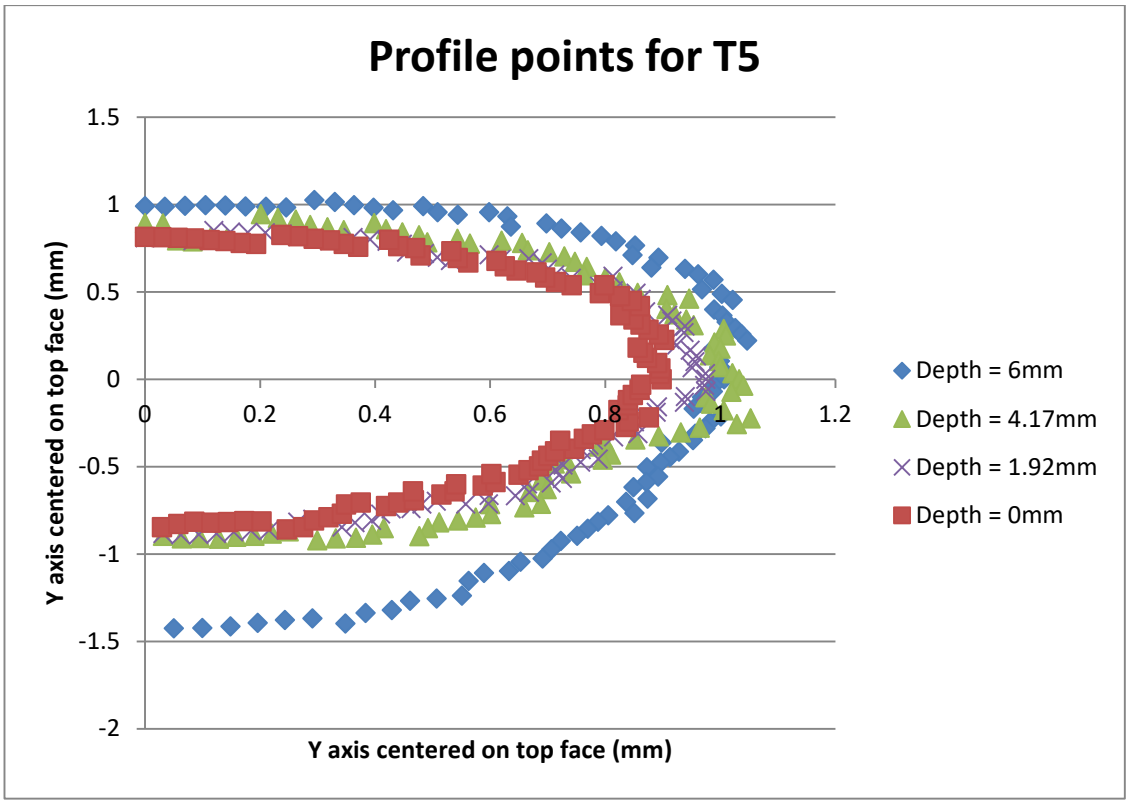

Figure 8.98: Scatter plot of test piece 5 data points for each depth view from above.

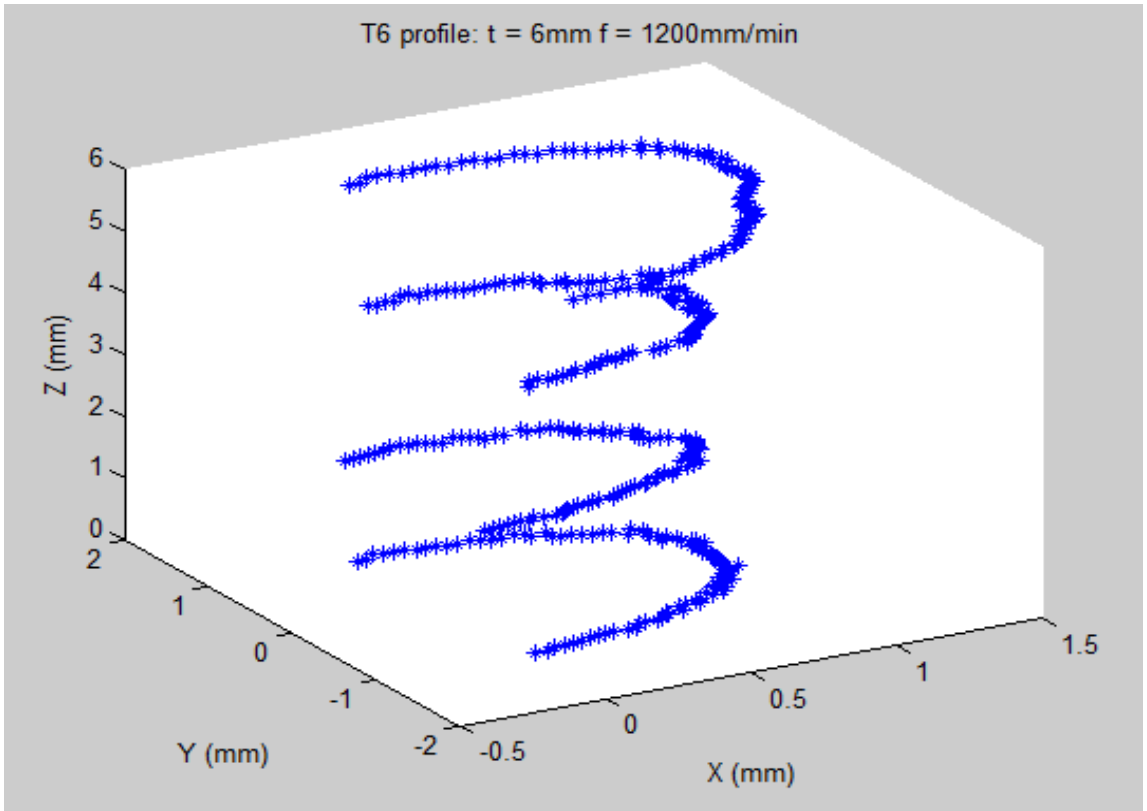

Figure 8.99: 3D plot of test piece 6 data points where elevation is 30 degrees and azimuth is at 30 degrees.

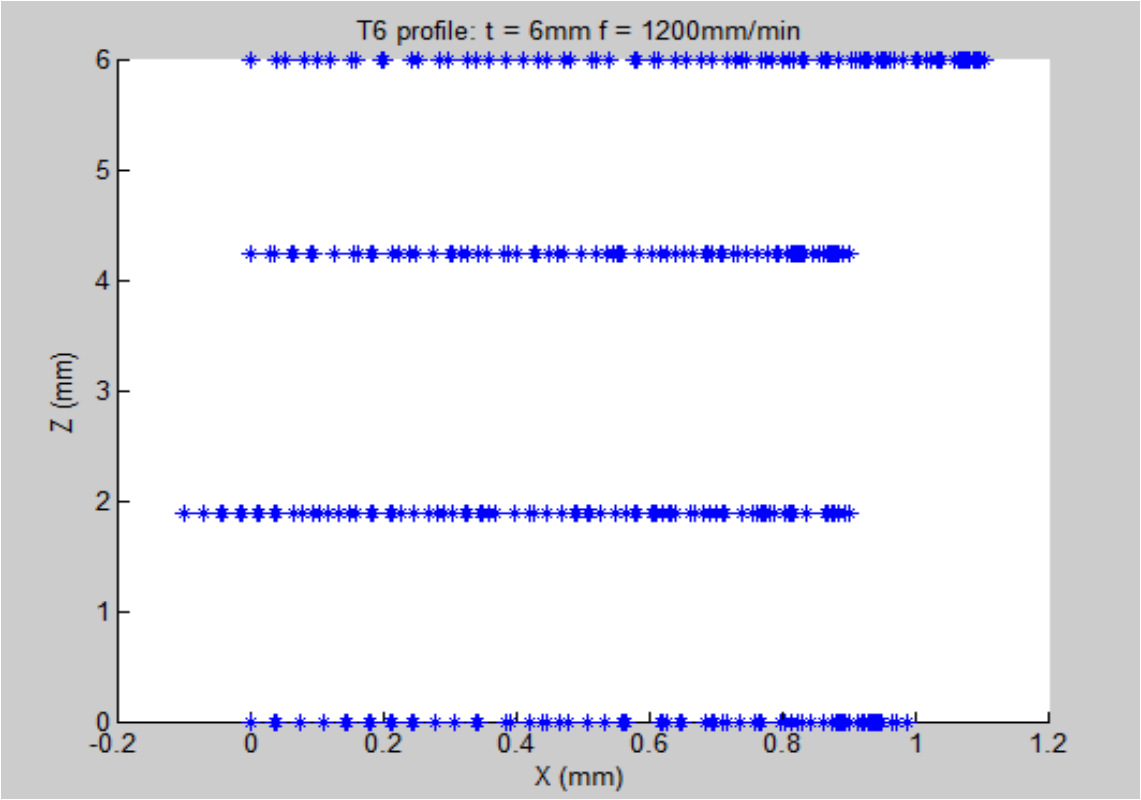

Figure 8.100: 3D plot of test piece 6 data points where elevation is 0 degrees and azimuth is at 90 degrees.

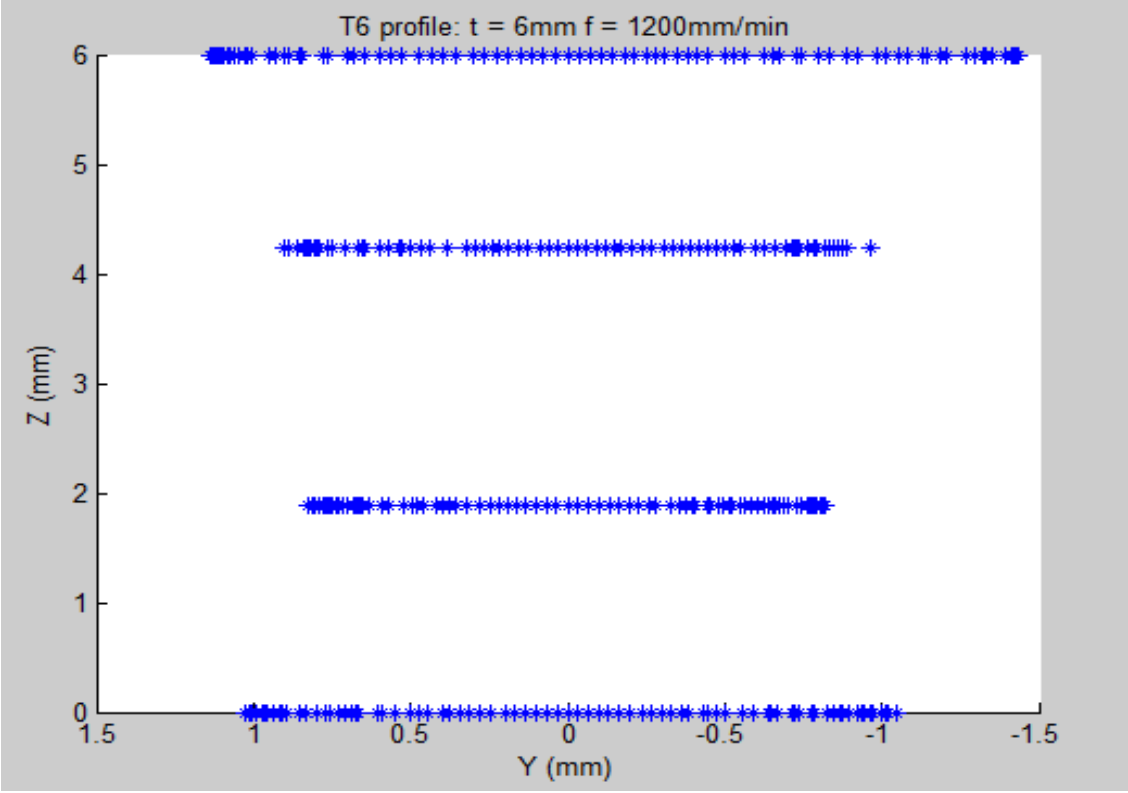

Figure 8.101: 3D plot of test piece 6 data points where elevation is 0 degrees and azimuth is at 0 degrees.

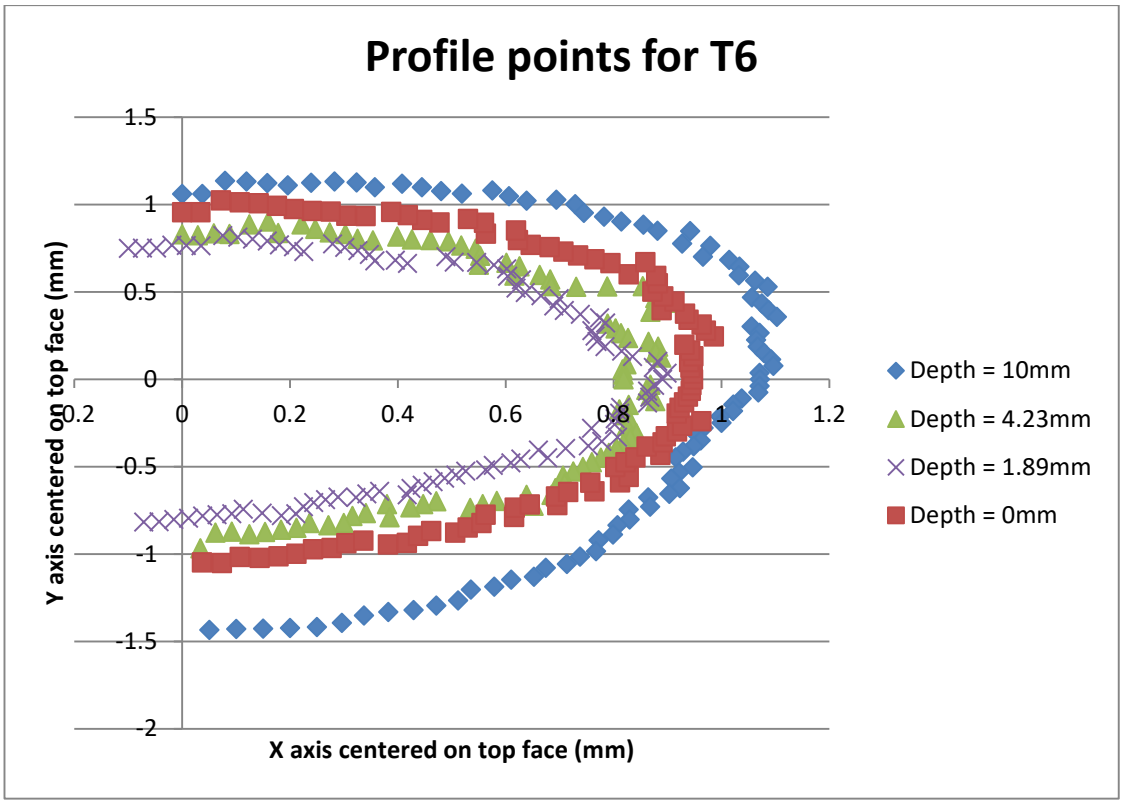

Figure 8.102: Scatter plot of test piece 6 data points for each depth view from above.

8.10 Appendix H: Plasma jet characteristics

This appendix presents the normalized relationship between Distance from the plasma torch, radius from the centre of the jet (both normalized with respect to nozzle diameter) and temperature (normalized with respect to maximum temperature). The data points were calculated from data presented in the literature for confined arcs. For each image, Normalized Temperature = Temperature (T) / Maximum temperature of the jet (Tmax). Normalized radius = Distance from the centre of the jet (r)/ Nozzle diameter (D). Normalized depth = Distance along the Z axis from the torch (Z)/ Nozzle diameter (D).

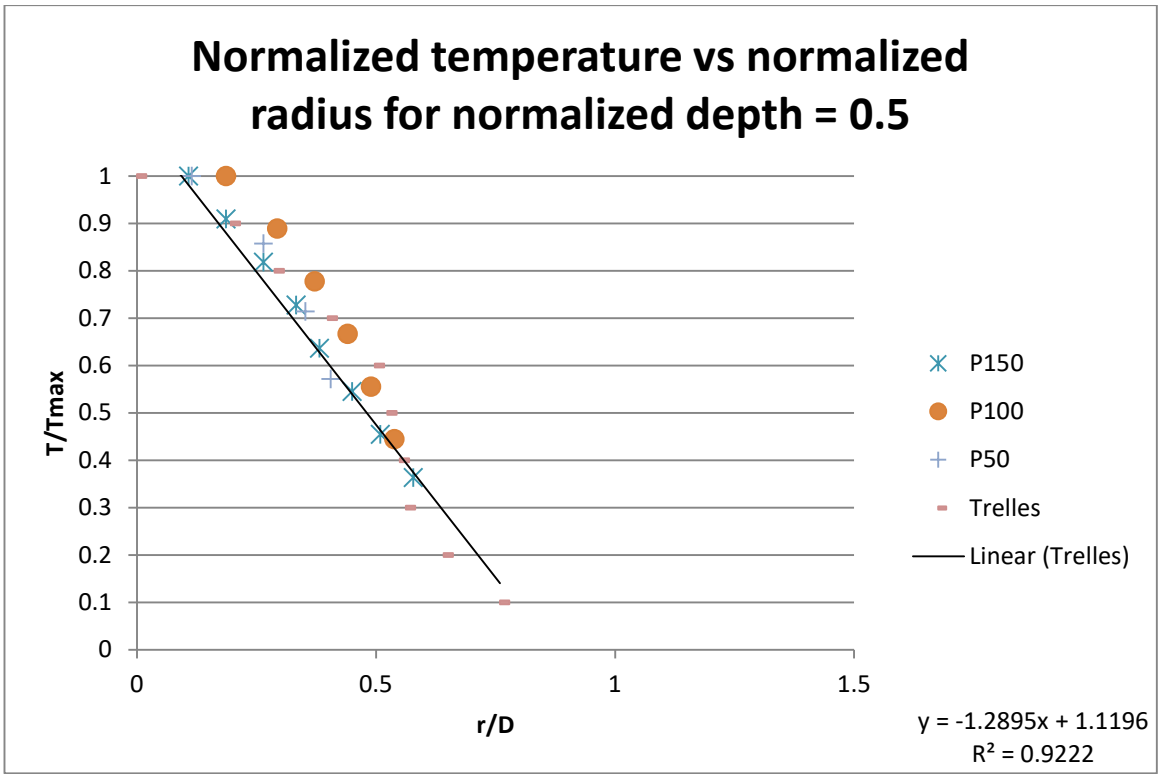

Figure 8.103 Plot of Normalized temperature vs normalized radius for a normalized depth = 0.5.

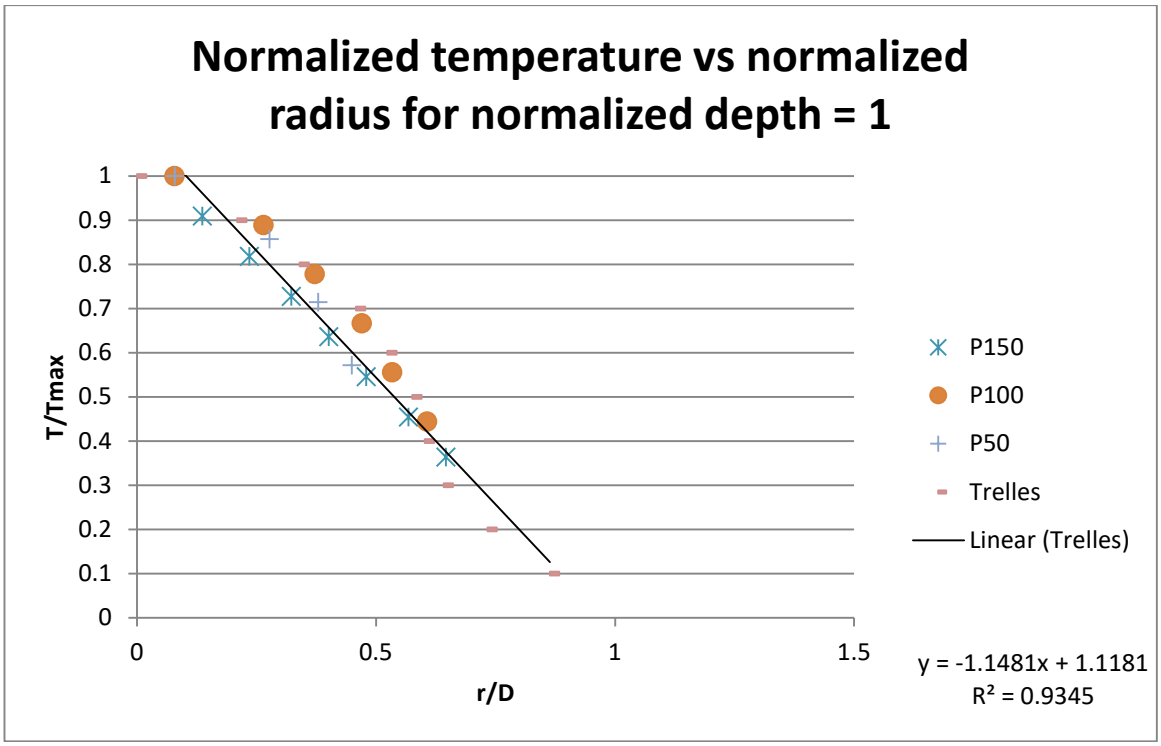

Figure 8.104 Plot of Normalized temperature vs normalized radius for a normalized depth = 0.5.

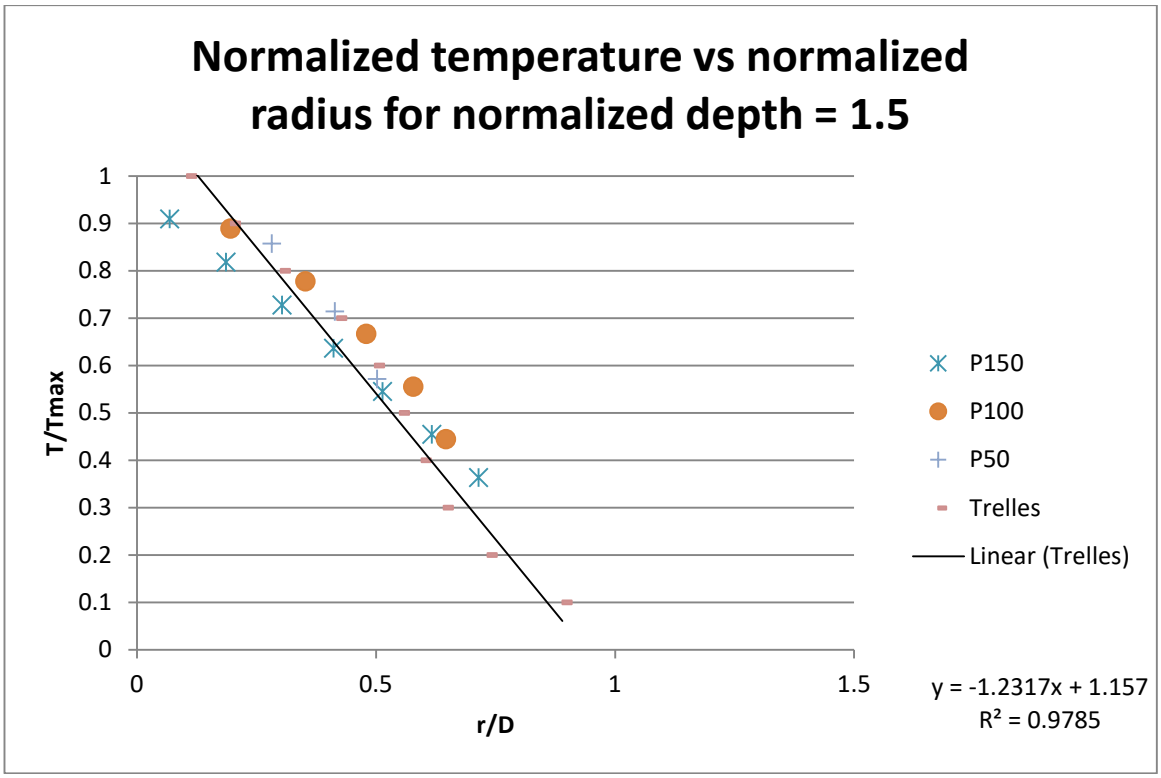

Figure 8.105 Plot of Normalized temperature vs normalized radius for a normalized depth = 1.5.

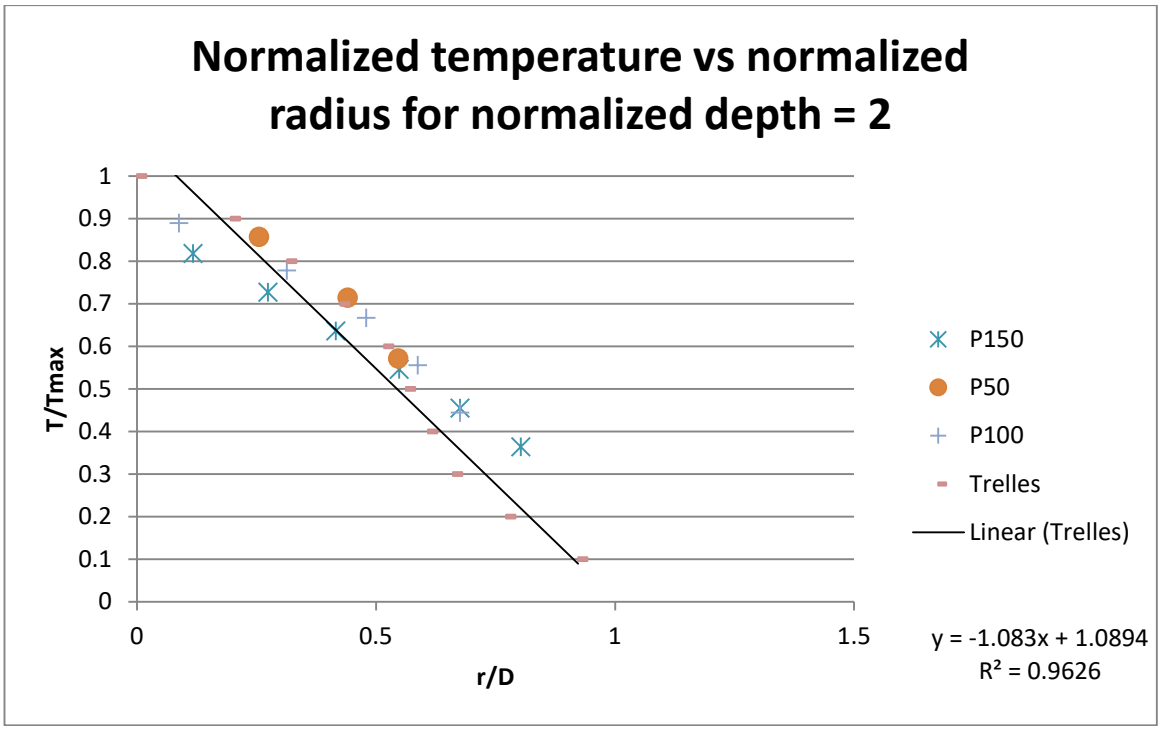

Figure 8.106 Plot of Normalized temperature vs normalized radius for a normalized depth = 2.

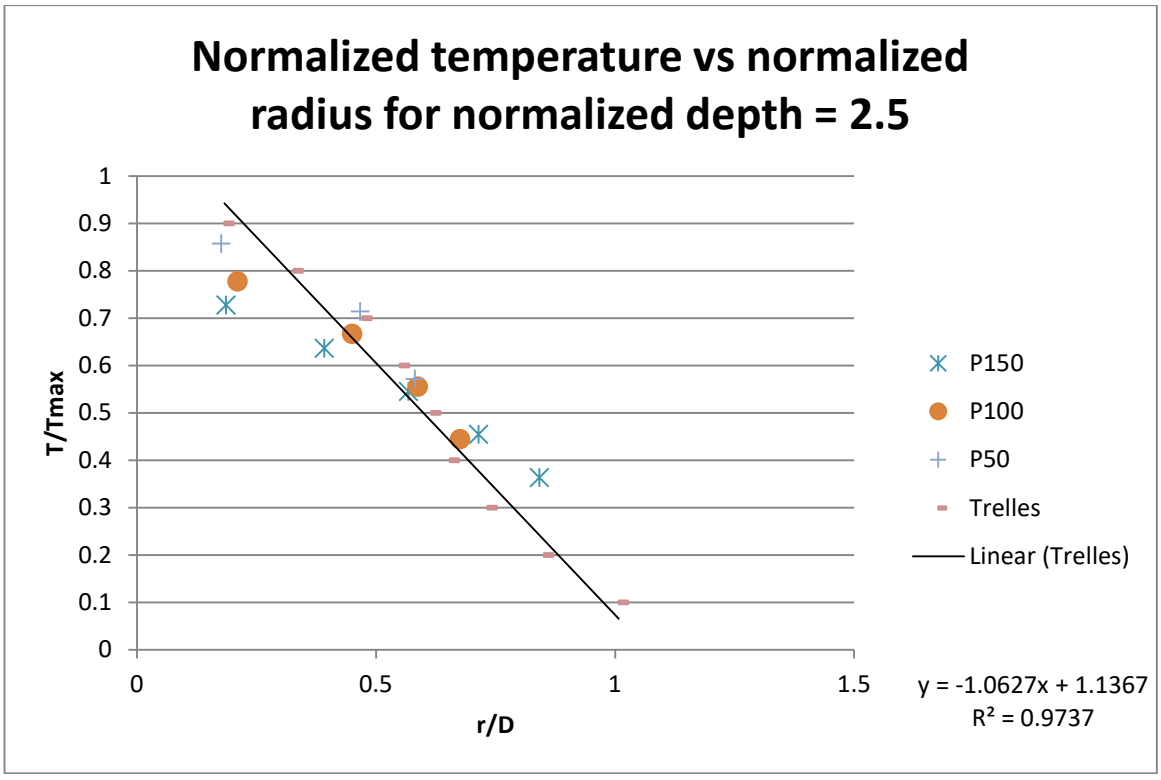

Figure 8.107 Plot of Normalized temperature vs normalized radius for a normalized depth = 2.5.

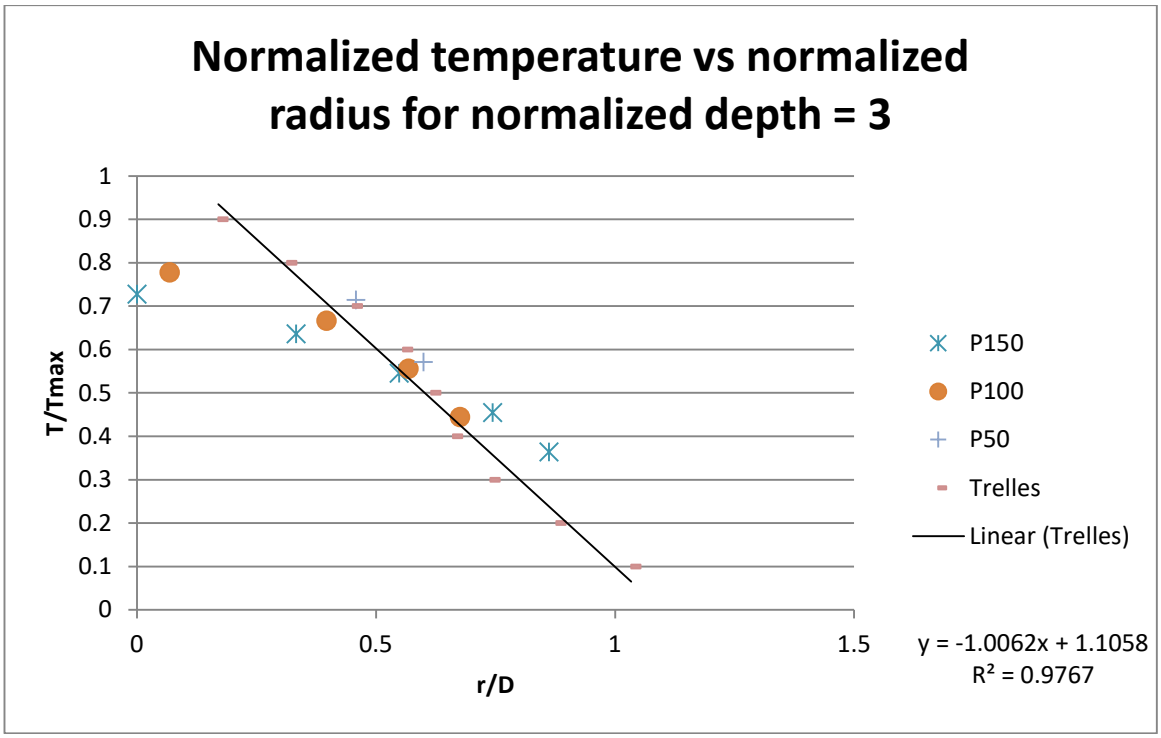

Figure 8.108 Plot of Normalized temperature vs normalized radius for a normalized depth = 3.

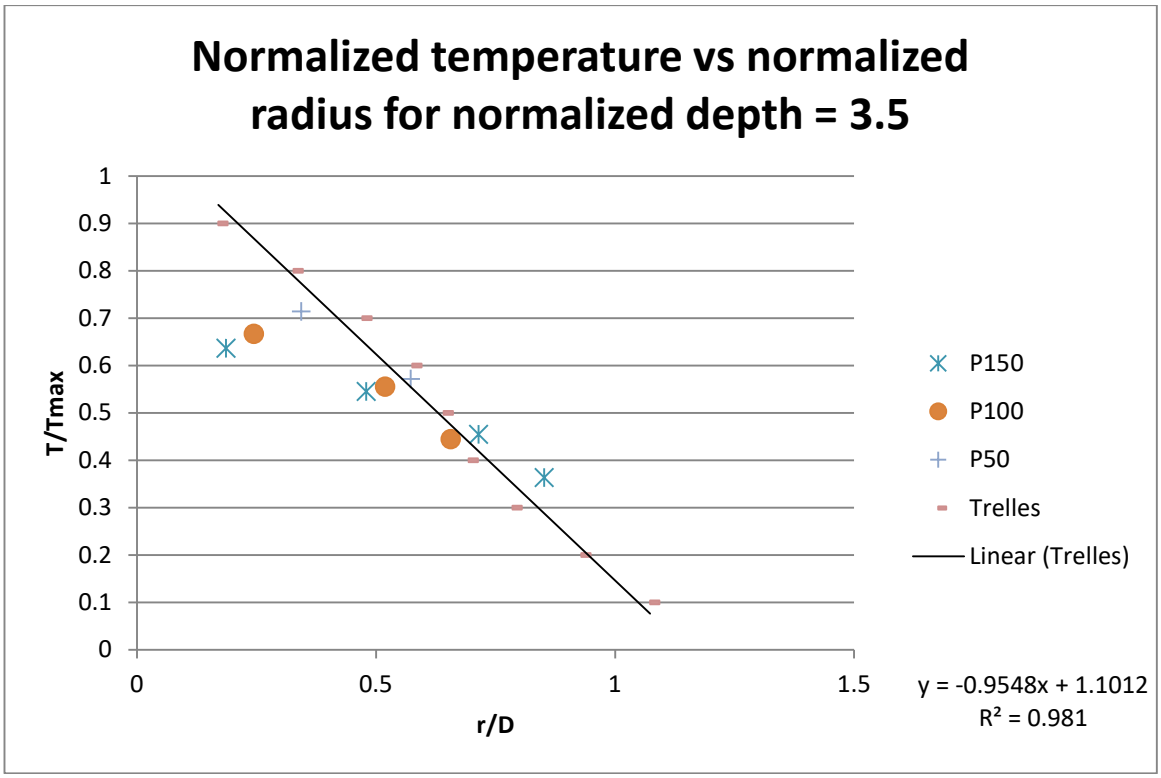

Figure 8.109 Plot of Normalized temperature vs normalized radius for a normalized depth = 3.5.

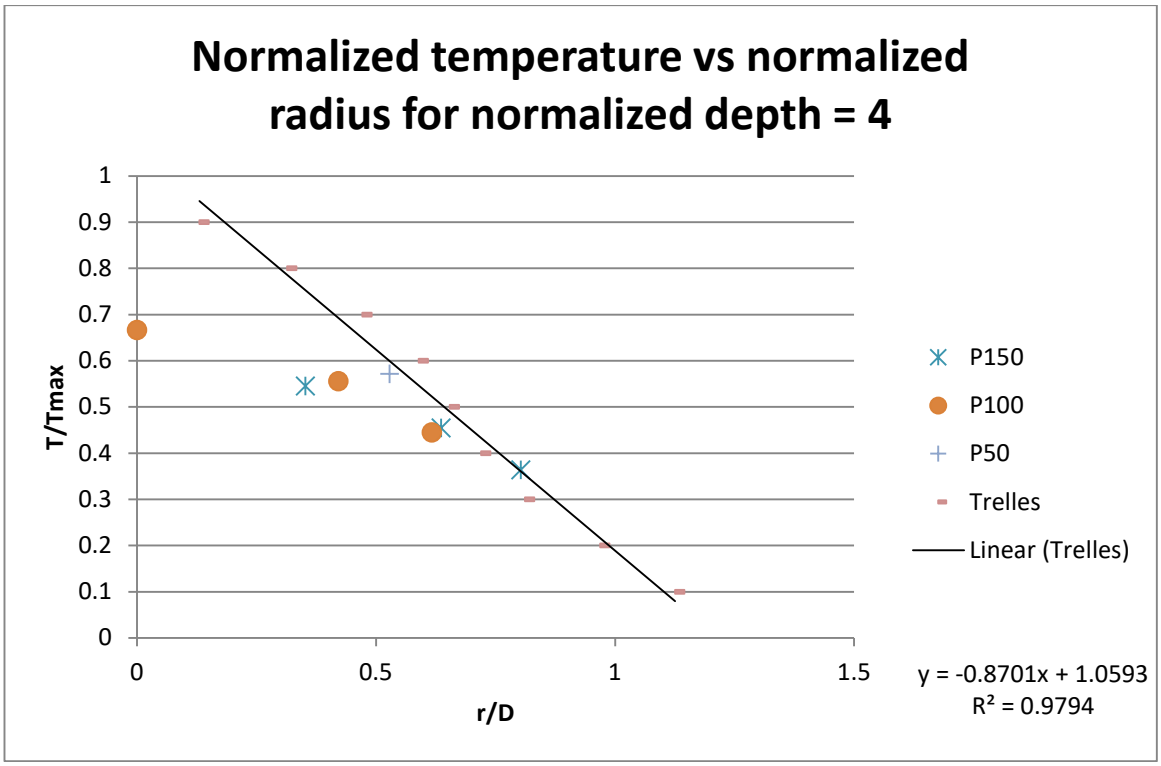

Figure 8.110 Plot of Normalized temperature vs normalized radius for a normalized depth = 4.

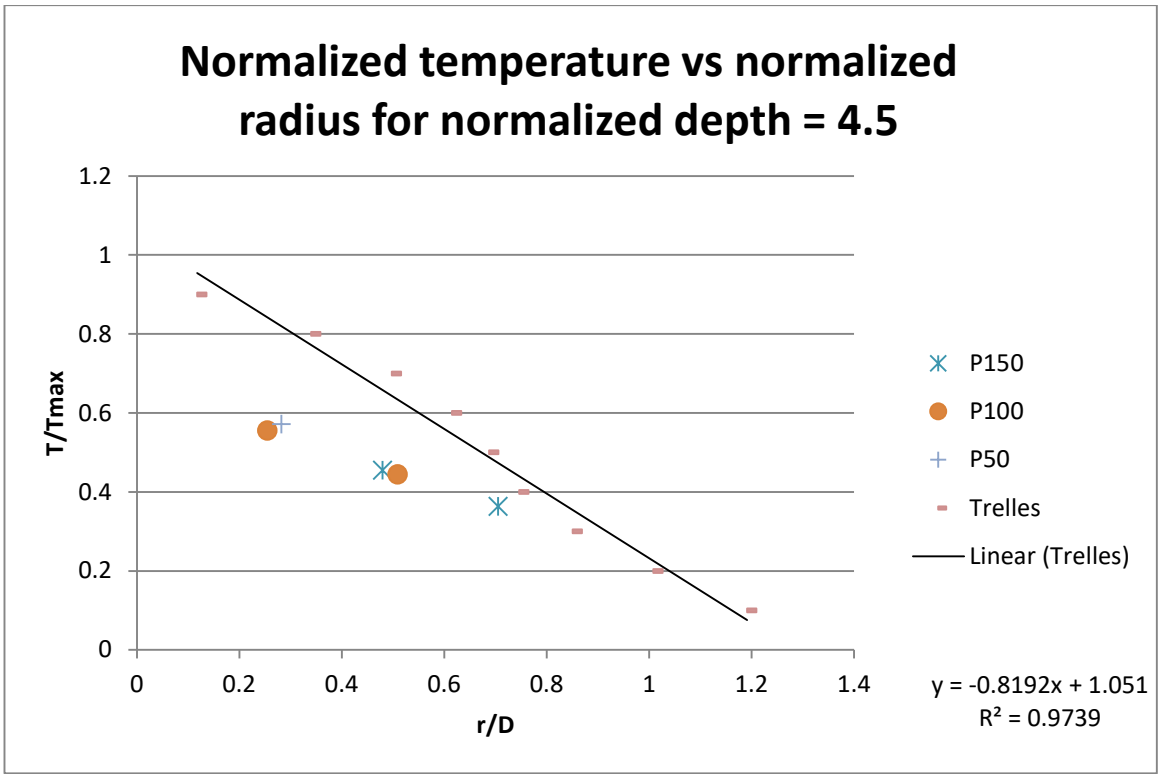

Figure 8.111 Plot of Normalized temperature vs normalized radius for a normalized depth = 4.5.

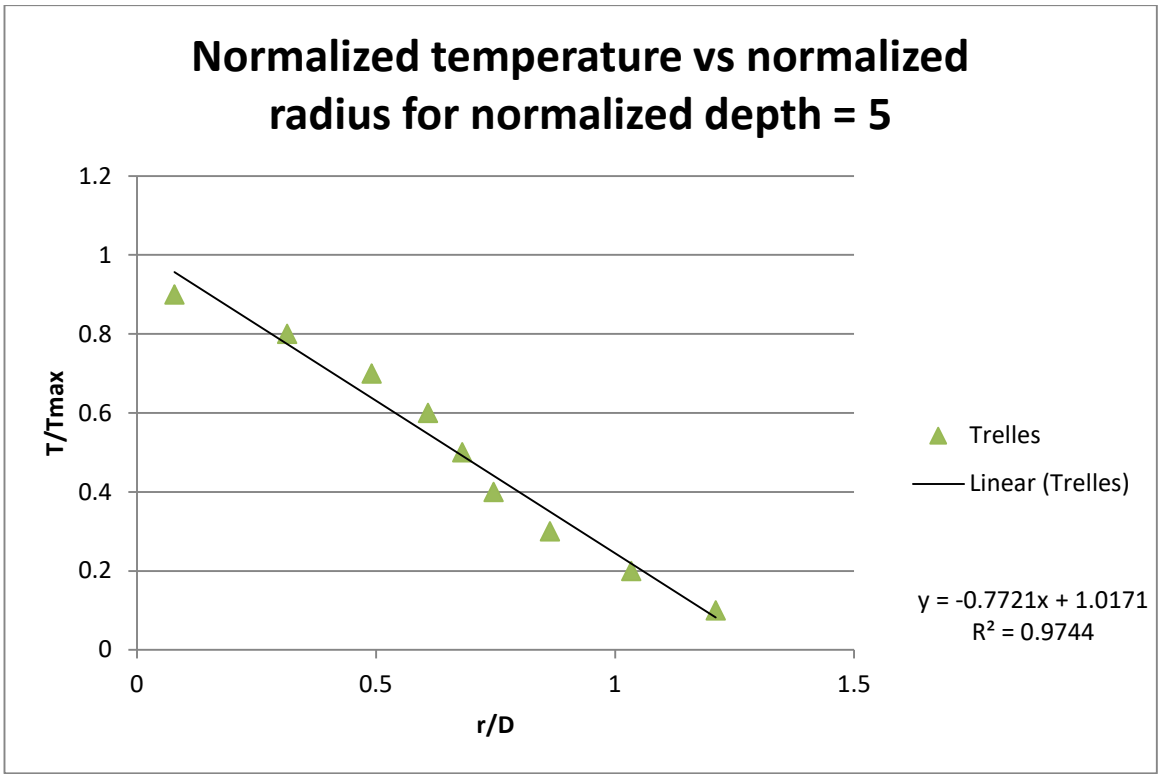

Figure 8.112 Plot of Normalized temperature vs normalized radius for a normalized depth = 5.